Towards a Standard Methodology for Determining Hydrogen Storage in Nanoporous Materials

Hruzewicz-Kolodziejczyk, Anna

Award date:
2013

Awarding institution:
University of Bath

TOWARDS A STANDARD METHODOLOGY FOR DETERMINING HYDROGEN STORAGE IN NANOPOROUS MATERIALS

Anna Hruzewicz-Kołodziejczyk

A thesis submitted for the degree of Doctor of Philosophy

University of Bath

Department of Chemical Engineering

April 2013

DECLARATION OF AUTHORSHIP

This is all my own work except where I have indicated otherwise via references or other forms of acknowledgement.

Signature:

Date:

ABSTRACT

Hydrogen has a great potential to become a wide-scale, carbon free, sustainable energy carrier of the future. However its implementation and final utilization especially in mobile applications is still limited because of several technological and socio-economical barriers, mainly to do with safe, efficient storage of hydrogen with high gravimetric and volumetric storage capacities. Physisorption into nanoporous materials is an attractive option as it benefits from rapid, fully reversible adsorption/desorption and can store significant amounts of hydrogen at more moderate temperature and pressures conditions than conventional liquefaction (20.3 K) or compression (350–700 bar). Nevertheless, the critical challenge exists to define the experimental methods that allow accurate hydrogen sorption determination and reduce discrepancies in measurements between different laboratories.

This thesis presents an investigation of the experimental methodology of hydrogen sorption in porous materials. A set of nanoporous samples and characterisation techniques have been tested rigorously to explore experimental uncertainty and provide universally reproducible procedures. The validity of the standard methods and some new approaches for experimental data collection and analysis are presented. High repeatability of gas sorption isotherms measured gravimetrically and volumetrically at 77 K on reference TE 7 III carbon beads sample has been demonstrated in-house. A study has been conducted between seven laboratories to evaluate the reproducibility of nitrogen/hydrogen isotherms at 77 K according to a defined test protocol. Statistical analysis yields very good agreement between nitrogen and hydrogen sorption results. The Brunauer-Emmett-Teller surface area of 777.8 ± 6.2 m^2 g^{-1} and Dubinin-Radushkevich micropore volume of 0.3766 ± 0.0078 cm^3 g^{-1}, have been determined. The excess hydrogen sorption capacities are found to be 1.65 ± 0.04 wt% and 2.33 ± 0.007 wt% for 1 bar and 20 bar hydrogen pressure, respectively. This study concludes that the accuracy of hydrogen sorption measurements have been pushed forward and methodology proposed here could contribute to improvements in certification of future hydrogen sorption methods.

ACKNOWLEDGMENTS

Firstly and foremost, I would like to deeply thank my supervisor Dr. Tim Mays for his help and guidance through this PhD. I have been very happy to work with someone who always demonstrates high level of professionalism and is never run out of the great ideas. I will be forever grateful to him for the success of my PhD.

I would like to acknowledge the funding support provided by University of Bath.

I cannot afford not a acknowledge my research group colleges, especially Dr. Valeska Ting for bringing precious help and friendly relationship, being always available when I need her to problem solving, for her understanding and priceless help with correcting my thesis. Would like to express thanks to Mr. Nuno Bimbo for his friendship and help with adsorption data modeling. Thanks are also due to Miss. Jessica Sharp for her careful proof-reading of this thesis. Many thanks must also go to Mr. Antonio Noguera Díaz, who has provided help with designing and testing of filtration chamber used in our laboratory to improve hydrogen stream purity. I would like also express my gratitude to the technicians and administrative staff in the Chemical Engineering Department, especially Mr. Fernando Acosta, for his assistance and help in the laboratory.

Such a comprehensive study cannot be accomplished without the contributions of some collaboration. That was a great honor for me to collaborate with Prof Steve Tennison from MAST Carbon, who was kindly supported me with testing materials. Thanks must go to all interlaboratory study participants for their contribution made in testing new experimental methodology.

On a more personal level, I would like thank all people around me, especially my family, my husband Paweł Kołodziejczyk and my little daughter Natalie for their love, support and constant reminder of how proud they are of me.

I would like to dedicate this work to memory of my loving mother, Danuta Neczaj - Hruzewicz, who died on March 6th 2007.

CONTENTS

CHAPTER 6: CONCLUDING REMARKS

SUPLEMENTRY INFORMATION

LIST OF FIGURES

LIST OF TABLES

NOMENCLATURE

a	Particle Radius
a_{db}	Ash Content (on the Dry Basis)
a_s	Brunauer Emmett Teller Specific Surface Area
a_s^o	Reference Value of Brunauer Emmett Teller Specific Surface Area
C	Brunauer Emmett Teller Constant
d	Molar Diameter
d_c	Diffusion Coefficient
D	Dubinin-Radushkevich Empirical Constant
E_1	Heat of Adsorption in the First Layer
E_L	Heat of Adsorption for the Second and Higher Layers (Equal to Heat of Liquefaction)
E_0	Dubinin-Radushkevich Characteristic Energy of Adsorption
$f(h)$	Pore Size Distribution
$f_{buoyancy}$	Mass Change Due to Buoyancy
g	Acceleration Due to Gravity
k	Kinetic Rate Constant
L	Avogadro's Constant
m_1	Mass of the Empty Crucible
m_2	Mass of the Crucible Plus Sample Before Drying
m_3	Mass of the Crucible Plus Sample After Drying
m_{ad}	Moisture Content
m_f	Final Sample Mass after Second Transformation
m_i	Initial Sample Mass
m_k	Final Sample Mass after First Transformation
m_s	Sample Mass
M	Molar Mass
n_1	Initial Mass Uptake at $t=t_1$
n_2	Equilibrium Mass Uptake at $t\rightarrow\infty$
n	Actual Mass Uptake

n_a	Amount of Gas Adsorbed/Desorbed
n_m	Monolayer Capacity (Maximum Capacity)
n_a^{max}	Amount of gas Adsorbed Corresponding to Micropore Volume
p	Equilibrium Pressure
p/p^o	Relative Pressure
p^o	Saturation Pressure of Gas at T
P_s	Sample Chamber Pressure
P_r	Reference Chamber Pressure
P_{sys}	System Pressure
$\Delta\%p$	Change in Equilibrium Pressure
R	Gas Molar Constant
R^2	Square of Correlation Coefficient
T	Temperature
T_c	Critical Temperature
T	Time
V	Volume of Gas Adsorbed at p/p^o
V_o	Volume Needed to Fill Micropores
V_c	Chamber of Known Volume
V_x	Sample of Known Volume
V_r	Reference Chamber of Known Volume
v_p	Micropore Volume
v_{closed}	Volume of Closed Pores
v_s	Skeletal Volume
v_{solid}	Volume Occupied by Sample
$\Delta wt\%$	Total Change in Gas Uptake
x_d	Particle Diameter
n	Number of Data Point
$\overline{x}$	Mean of Value x
$(x_i - \overline{x})$	Deviation from Mean
$(x_i - \overline{x})^2$	Square of Deviation from Mean

Abbreviations

ASAP	Accelerated Surface Area and Porosimetry
BDDT	Brunauer Deming Deming and Teller
BE	Bioenergy
BET	Brunauer Emmett Teller
BIP-H_2	Ultra-Pure Hydrogen
BS	British Standard
BP	British Petroleum Company
CDC	Carbide-Derived Carbons
Cu-BTC	Copper-Benzene-1 3 5-Tricarboxylate
COF	Covalent Organic Framework
DFT	Differential Functional Theory
DOE	Department of Energy
DR	Dubinin-Radushkevich
EDX	Energy Dispersive X-ray Spectroscopy
EIA	Energy Information Administration
EOS	Equation of State
FC	Fuel Cell
GHG	Green House Gasses
HCP	Hypercrosslinked Polymer
HTP-1	High Temperature and Pressure Analyser
IAEA	International Atomic Energy Agency
ICE	Internal Combustion Engine
IEA	International Energy Agency
IGA	Intelligent Gravimetric Analayser
IPCC	Intergovernmental Panel on Climate Change
IRMOF	Inorganic Metal-Organic Framework
ISO	International Organisation of Standarization
IUPAC	International Union of Pure and Applied Chemistry
LDF	Linear Driving Force
LH_2	Liquid Hydrogen

MIL	Matérial Institut Lavoisier
MOF	Metal-Organic Framework
MWCNT	Multi-Walled Carbon Nanotubes
NIST	National Institute of Standards and Technology
NMR	Nuclear Magnetic Resonance
PAF	Porous Aromatic Framework
PEM	Proton Exchange Membrane
PEME	Proton Exchange Membrane Electrolyser
PEMFC	Proton Exchange Membrane Fuel Cell
PIM	Polymer of Intrinsic Microporosity
POX	Partial Oxidation
PSA	Pressure Swing Adsorption
PV	Photovoltaic
RE	Renewable Energy
SEI	Secondary Electron Images
SEM	Scanning Electron Microscopy
SG-H_2	Standard Grade Hydrogen
S-I	Sulphur-Iodine Cycle
SMR	Steam Methane Reforming
STP	Standard Temperature and Pressure
SWCNT	Single Walled Carbon Nanotubes
TGA	Thermogravimetric Analysis
TEPCO	Tokyo Electric Power Company
TEM	Transmission Electron Microscopy
UK	United Kingdom
UK-SHEC	UK Sustainable Hydrogen Energy Consortium
US DOE	United States Department of Energy
WEC	World Energy Council
WEO	World Energy Outlook
XRD	X-ray Diffraction
RT	Room Temperature

Greek Symbols

ρ_g	Gas Density
ρ_s	Sample Density
β	Dubinin-Radushkevich Affinity Coefficient
$v(h, p/p^o)$	Excess Volume of Gas at p in Pore of Size h
σ	Adsorptive Molecular Cross Sectional Surface Area

DISSEMINATION

1) The work presented in this thesis has been disseminated as follows:

Bimbo, N., Ting, V.P., Hruzewicz-Kołodziejczyk, A. and Mays, T.J. (2011). Analysis of hydrogen storage in nanoporous materials for low carbon energy applications, Journal Publication, Faraday Discussions, 151, 59-74.

Hruzewicz-Kołodziejczyk, A., Ting, V.P., Bimbo, N. and Mays, T.J. (2012). Improving comparability of hydrogen storage capacities of nanoporous materials, Journal Publication, International Journal of Hydrogen Energy, 37, 2728-2736.

Neczaj-Hruzewicz, A., Overview of Hydrogen Storage, Talk, Presented at 2nd UK-SHEC Researchers Workshop, Biannual, UK, July 2009.

Hruzewicz-Kołodziejczyk, A., Bimbo, N., Ting, V.P., Fisher, L. and Mays, T.J., Improving Comparability of Hydrogen Storage Capacities of Nanoporous Materials, Presented at the 2010 Annual Meeting of American Institute of Chemical Engineers (AIChE), Salt LakeCity, UT, USA, November 2010.

Hruzewicz-Kołodziejczyk, A., Banchmarking methodology for hydrogen sorption in nanoporous materials, Talk, Presented at 3rd UK-SHEC Researchers Workshop, Bath, UK, September 2011.

Ting, V.P., Hruzewicz-Kołodziejczyk, A., Bimbo, N., There is plenty of room at the bottom – Nanoengineered materials for hydrogen storage, Talk, Presented at Bath Royal Literary and Scientific Institution Speaking of Research, Bath, UK, October 2011.

Hruzewicz-Kołodziejczyk, A., Accurate methodology for determining hydrogen sorption in nanoporous solids, Talk, Presented at Department of Chemical Engineering, Bath, UK, February 2012.

Ting, V. P., Bimbo, N., Hruzewicz-Kołodziejczyk, A., Fisher, L. C., Mays, T. J., Towards practical hydrogen storage materials: Synthesis, measurement and analysis of hydrogen storage materials at the University of Bath, Poster, Presented as part of the EPSRC International Energy Review, in Oxford, UK, October 2010.

Hruzewicz-Kołodziejczyk, A., Ting, V.P., Bimbo, N. and Mays, T.J. Investigating accuracy of hydrogen sorption in nanoporous materials, Poster, Presented at Hydrogen Showcase, Birmingham, UK, April 2011.

Bimbo, N., Hruzewicz-Kołodziejczyk, A., Ting, V. P., Mays T. J., High-pressure experimental data collection, analysis and modeling of hydrogen storage on

nanoporous materials, Poster, Presented at 10th International Materials Chemistry Conference, Manchester, UK, July 2011.

2) The author has received the following awards:

Royal Academy of Engineering International Travel Grant to attend the AIChE Annual Meeting in Salt Lake City, UT, USA (£600 award).

Royal Society of Chemistry Conference Bursary to attend Faraday Discussions 151 – Hydrogen Storage Materials (£150 award).

CHAPTER 1

INTRODUCTION

1.1 Context of Research

Growing concerns about fossil fuel depletion, climate change and energy security in this century and beyond create a serious challenge for the forthcoming decades. New more sustainable, secure and environmentally friendly alternatives are desperately needed to supply energy as the world's population grows and gets richer. Hydrogen is at present one of the prime candidates as a future energy vector to provide an alternative option to the current fossil fuel generation. It has a variety of social, economic and environmental benefits, such as its capability to reduce global world pollution and greenhouse gas emissions hence protecting our health and ecosystem.

Currently hydrogen is used in a variety of industries mainly for ammonia production, crude oil refining and in metallurgical processes. However in the long term (15+ years) hydrogen is expected to play a major role as a clean energy carrier for transportation, electronics and stationary applications such as storing intermittent renewable electricity for example for solarphotovoltaic (PV) and wind. Because of the high energy density per unit mass hydrogen is a very attractive and competitive fuel at the same time it is not harmful to environment, because it is carbon free if produced form sustainable processes. It can be burned in a modified internal combustion engine or in a gas turbine, as a clean synthetic fuel without direct emission of carbon dioxide or can be converted into electricity in a fuel cell with just water as a co-product.

One of the key features is that hydrogen is the most abundant and least complex element in the universe. However it does not occur naturally on earth as molecular

hydrogen (H_2) but instead is bonded in water, fossil fuels and biomass (Häussinger et al., 2000c). Moreover, hydrogen like electricity is not an energy source but it is an energy vector meaning that energy must be put in for it to be produced. Presently, most hydrogen is produced from fossil fuels by steam reforming of natural gas (Häussinger et al., 2000a, Press, 2009), but in the future it can be extracted from more sustainable resources such as biomass and water with input from renewables (e.g. sunlight, wind, wave and hydro-power) which will lower the carbon footprint (Gosselink, 2002, Dincer, 2012).

Another barrier to the successful implementation of hydrogen as an energy carrier is the ability to efficiently store it for later use. Due to the very low density of hydrogen, large storage spaces are required. This is a major issue especially in mobile applications where 5 kg of hydrogen (required to achieve a driving distance of ~ 300 miles) would occupy ~ 60 m^3 at ambient temperature and pressure, which is about three times the volume of a road car. Storage of H_2 via physisorption in nanoporous materials is a very promising option as the process is reversible, fast (rapid ad- and desorption) and can operate at reasonable temperatures and pressures compared with currently available storage techniques such as liquid (< 33 K) and as compressed gas (350–700 bar). However, such technologies are still in the intensive research stage.

With the constantly growing need for advanced nanoporous materials which can store significant amount of the hydrogen, accurate characterisation methodology is necessary. As a matter of fact, at present no standard method exists and hydrogen sorption data are collected and analyzed without any systematic routine. Consequently real materials properties cannot be duplicated in other laboratories, which have led to confusing reports of hydrogen storage capacity of many nanoporous materials (Yurum et al., 2009). Recent round robin gas sorption experiments across a number of different laboratories have highlighted the large variations in the results collected in a non-standard way (Zlotea et al., 2009). Research must be carried out to develop a reliable and accurate methodology which helps researchers to validate their data and to verify previous claims in the literature.

1.2 Research Scope

It is essential that the methodology that we use to determinate hydrogen storage capacities is thoroughly understood. Determination of the precise experimental set up, optimal experimental conditions, detailed analysis of uncertainties, consistent data presentation and interpretation are a major step in the better understanding of accurate hydrogen sorption characteristics. With the driving need to improve hydrogen sorption capacities, rigorous and qualitative analysis become more critical to ensure the correct selection of promising materials for US Department of Energy (DOE) requirements for hydrogen storage in motor vehicle. As a matter of fact, nowadays there are only few descriptions of accurate hydrogen sorption measurements in literature (Broom, 2007, Zhang et al., 2004, Gross, 2012, Kiyobayashi et al., 2002, Blackman et al., 2006, Broom and Moretto, 2007). Much of the recent research focuses on developing new high capacity materials, with less emphasis on the rigor and accuracy of data. Descriptions of analysis methods are often very general which does not always enable researchers to repeat experiments.

In this context, we are looking into understanding the areas where problems are likely to occur in the measurement and analysis of hydrogen uptake. It is important to recognize that a major barrier when comparing data from the literature is that the sample preparation and analysis conditions are not always well controlled or documented. A consequence is that results obtained may not always be easily compared between laboratories. Many of these issues are dealt with thoroughly in this thesis. Literature studies are used to collect relevant background information on hydrogen sorption methodology to identify the potential factors affecting experiments, but also to study information about method approval and validation. Reproducible methods for sample preparation and analysis are developed in order to reduce the uncertainly as much as possible. Uptake methods include volumetric and gravimetric gas sorption as complementary techniques. A number of commercially available nanoporous materials are analysed as potential reference materials for sorption measurements validation. The structural properties are assessed to correlate the results and make reasonable judgments on their suitability for hydrogen storage. A reference material is chosen and used for data comparison and validation.

Experiments are carried out using different gas sorption apparatus available at Bath to ensure results reproducibility. Major sources of error affecting experiments are identified and appropriate recommendations for improvement are made. Reference sample, data analysis protocols and experimental procedures are sent to external laboratories, including both universities and commercial organizations to validate our methodology and check their reproducibility. Statistical analysis is applied to all collected data and final results communicated to participants. Final recommendations for improving sorption experiments are made and the best methodology for this type of measurementis detailed.

Based on the above discussion, the main aim of this thesis is to improve reproducibility of hydrogen sorption measurements with the assessment of standard experimental methodology. To our knowledge, there does not exist any standard methodology (in the public domain) to determine hydrogen sorption in nanoporous materials at 77 K. An investigation into method standardization will lead to a better understanding of fundamental hydrogen sorption behaviour. Furthermore, research into new methods also provides an opportunity to identify possible sources of measurement errors and provide better grounds and recommendations for future work. Finally, we believe that this research is interesting, particularly to academia and organizations such as British Standard (BS) and International Organisation of Standardization (ISO) interested in standard materials and methods.

1.3 Thesis Structure

This thesis consists of six chapters. Chapter 1 (this one) is an introduction which briefly brings the research into context, describes the scope, purpose and structure of the thesis. Chapter 2 contains important background information in the area of the research such as energy supply and security problems, environmental pollution and climate change, and presents some future sustainable energy solutions with a major role of hydrogen as a renewable energy vector. A complete review of the current status of hydrogen energy, including production, storage and final use is also presented. Particular attention is paid to hydrogen storage methods, especially to the concept of molecular hydrogen stored via physisorption in nanoporous materials.

Some recent approaches to produce standard hydrogen storage methodologies are reviewed. Chapter 2 concludes with a final statement of the aims and objectives of this research.

Chapter 3 gives a detailed description of the experimental methods adopted for the characterisation of the nanoporous materials. It provides information on the materials selected and the experimental techniques used in their analysis. This includes details of the experimental set-up, apparatus design, operational and calibration standard procedures and particularly experimental variables which are critical in accurate measurements.

Chapter 4 presents the materials characterisation and the nitrogen/hydrogen sorption results, obtained in-house by methods described in Chapter 3. In the first part general materials characterisation is investigated, with attention on the purity, skeletal density, homogeneity, BET specific surface area and porosity. A brief discussion of the determination of the most appropriate sample degassing conditions is also given. The influence of main experimental variables, such equilibration time, data corrections, hydrogen purity and sorption kinetics are then carefully investigated. Analyses of the nitrogen and hydrogen storage results are presented along with discussions on the measurement quality and accuracy. Uniformity of the nitrogen and hydrogen sorption results is firstly evaluated using in-house measurements and then methodology is approved by interlaboratory study as discussed in the following section.

Chapter 5 is dedicated to an interlaboratory study of hydrogen sorption with external groups. Participants from all over the world took part in the same measurements of nitrogen/hydrogen sorption at 77 K in their own laboratories to ensure of our methods asses. The detailed description of the program design and experimental protocol is given. Statistical methods are applied to the uncertainty of the results. All the details are given and the final methodology for determination hydrogen storage in nanoporous materials is proposed.

Finally, in Chapter 6, a summary and conclusions of the work in this thesis are given. Some suggestions for future work are also proposed.

CHAPTER 2

BACKGROUND

2.1 Introduction

This Chapter provides a summary of the background and motivation of this thesis. Section 2.2 is a brief discussion on the global energy situation, resource availability and the impact of the energy provision on the environment. The global energy scenario used in this section follows the most up-to date reports published by the International Energy Agency (IEA, 2012) and British Petroleum Company (BP, 2012a) and shows the trend for current global energy consumption and projected demands up to 2030 and beyond. Section 2.2 concludes that future energy systems must be based on more sustainable alternatives then fossil fuels. While sustainability is defined in different ways, here we accept the most famous one expressed in the United Nations report which is that " sustainable development meets the needs of the present without compromising the ability of future generations to meet their own needs" (World Commission on Environment and Development, 1987). Renewable energies in the context of clean, sustainable energy solutions are covered in the Section 2.3. This is followed by Section 2.4 where hydrogen is identified as a wide-scale energy vector to address world energy needs and to provide massive reductions in CO_2 emission. The relevant properties of elemental and molecular hydrogen are reviewed in Section 2.4.1. Hydrogen production methods, including from conventional fossil fuels and 'green', sustainable technologies are discussed in Section 2.4.2. Hydrogen storage presented in Section 2.5 is the central topic of this thesis and mainly focuses on hydrogen physisorption in nanoporous materials as the most favourable storage solution (Section 2.6). The problems with accuracy and reproducibility of hydrogen sorption measurements in different laboratories are discussed in Section 2.7. The chapter concludes in Section 2.8 with the aims and objectives of the thesis.

2.2 Energy and the Environment

Clean and low cost energy supply is essential for world socio-economic development, improved life quality, global stability and peace around the word. The critical energy scenario in the mid 21st century includes security of energy supply for a population of 9.3 billion and removed of environmental damages caused by greenhouse gasses (GHG) emissions from fossil fuel combustion (Midilli et al., 2005, Veziroglu and Sahin, 2008). To deal with these issues, additionally motivated by natural energy resource depletion, there is significant push on the world energy transformation to more sustainable alternatives with improved efficiency, applicability and environmental protection (Hidy et al., 2012).

Energy is used almost everywhere, for transportation, household work, agriculture, industry and manufacturing, service, buildings, and more (Orhan et al., 2012). At present, approximately 81 % of all primary energy consumption comes from fossil fuels, because of their availability and convenient use, however there are serious uncertainties in how the energy market is likely to be in the future (IEA, 2012). To address this point a number of the industrial and governmental organisations such as BP (BP, 2012a), Shell (Shell International BV., 2008), International Energy Agency (IEA) (IEA, 2012) , the US Energy Information Administration (EIA) (EIA, 2011), the International Atomic Energy Agency (IAEA) (IAEA, 2009) and the World Energy Council (WEC) (Schiffer, 2008) make attempts to shape the baseline for the future demographic, socioeconomic and the energy trends.

According to BP estimates (BP, 2012a) global primary energy consumption is projected to increase by remarkable 32 % in the period between 2010 to 2030, from nearly 13 000 million tonnes of oil equivalent (Mtoe) to around 17 000 Mtoe (see Figure 2.1). Fossil fuels continuously dominate the energy market worldwide, however their share in the global energy mix will be slightly different by the end of 2030. Coal remains the main energy contributor, accounting for almost 39 % and natural gas will stay at pretty much a stable level of around 31 % through the next 20 years. Renewables, nuclear and hydro together are projected to deploy rapidly,

with a significant shift from around 20 % today to 34 % by the end of 2030 year (BP, 2012).

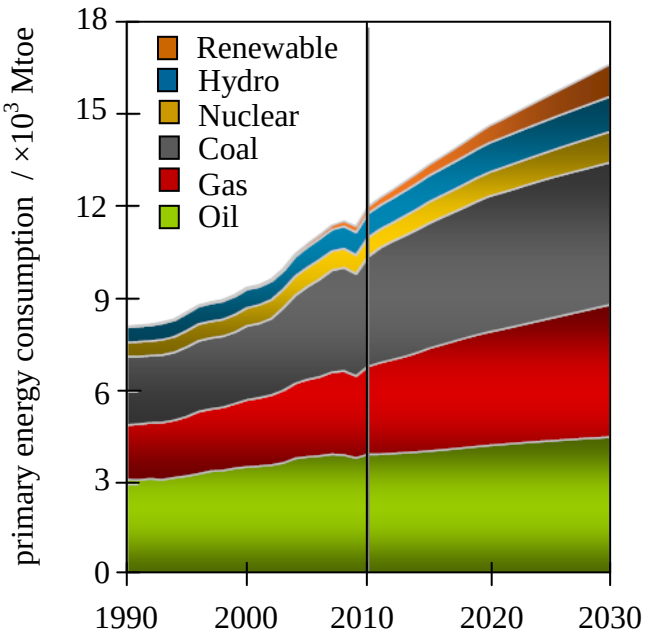

Figure 2.1: Primary global energy consumption growth between the years 1990 and 2030. Adapted from (BP, 2012a).

However, the trend in fossil fuel use cannot continue forever since their resources are declining. Predictions indicate that reserves of oil proven for about 1662.1 thousand million barrels are expected to last for next 50–75 years. Natural gas reserves totalling 208.4 trillion cubic metres are predicted to last for 60 years. Coal reserves proven for 860 938 million tonnes, on the other hand are sufficient to supply the next 112 years (BP, 2012b). More than 70 % of these reserves are found within the so called 'strategic ellipse' of countries extending from Saudi Arabia in the south, over Iraq and Iran, up to Russia. Considering these two facts together, then it becomes clear how explosive the supply situation for the 'energy-hungry West' may become in the foreseeable future (Muller-Steinhagen and Nitsch, 2005).

In addition energy supply and security problems, there are growing fears about irreversible environmental damage caused by fossil fuel technologies. The most notable ones include the anthropogenic climate change, acid rain formation, stratospheric ozone depletion and air pollution (King, 2004, Dincer, 1998, Dincer, 1999). A main issue with fossil fuel use is that pollutants like carbon monoxide

(CO), carbon dioxide (CO_2), methane (CH_4), nitric oxide (NO) and nitrogen dioxide (NO_2), nitrous oxide (N_2O), sulphur dioxide (SO_2), chlorofluorocarbons (CFCs) and ozone (O_3) are formed during their combustion, which are emitted into the atmosphere (Dincer, 1999). The atmospheric concentration of GHG, defined as CO_2, CH_4, N_2O, CFCs and aerosols results in the absorption of infrared energy radiated by the Earth's surface into the atmosphere and re-radiates this energy back to Earth, making the positive or negative changes in the energy balance causing the atmospheric temperature rise or decrease (Veziroglu and Sahin, 2008, Dincer, 1999). Present estimates show that from the beginning of large scale industrialization in the 18^{th} Century, and the rapid rise in fossil fuel consumption, the carbon dioxide concentration in the atmosphere increased from 280 ppm to 392 ppm (parts per million) causing the mean temperature to rise by 0.8 ^{o}C (Dyne, 2013). The Intergovernmental Panel of Climate Change (IPCC) raised these concerns, showing that in the future the mean temperature is expected to rise in the range of 2.0 ^{o}C to 4.5 ^{o}C by the end of the 21^{st} century (IPCC, 2007).

It is not easy to precisely predict the environmental impact of temperature increase on the Earth's atmosphere, however the expected critical results can include sea levels rise, more frequent extreme weather conditions and a shift in climate and vegetation zones (Steffen, 2009). To keep the temperature rise within reasonable limits, the current concentration of CO_2 in the atmosphere must not be allowed to rise above 500 ppm before the end of this century (Dyne, 2013). To comply with these targets, the greatest world-wide priority should become the switch to more sustainable, clean energy alternatives which could reduce CO_2 and other GHG emission and stop reliance on fossil fuels. Renewable energies are necessary components in achieving such goals (see Section 2.3). Nuclear power is another important resource that has been greatly promoted to support future energy needs. However there are enormous environmental risk, safety uncertainties, and concerns with nuclear power following the accident at the Tokyo Electric Power Company in Fukushima, in Japan in March 2011 (Ministry of the Environment Government of Japan, 2011).

2.3 Renewable Energies

Due to interest in reducing environmental impacts associated with harmful CO_2 emission and to sustain natural energy resources in the future there is a significant push for the development of renewable energies (RE), particularly (1) bioenergy (2) hydropower, (3) wind, (4) solar and (5) geothermal, since they serve a wide range of energy services to supply electricity, thermal and mechanical energy as well to produce fuels (Bilen et al., 2008). As can be seen from Figure 2.2 on the global scale, the RE share is relatively small and accounted just for 12.9 % of the total primary energy supply in 2008, with the largest contribution provided from bioenergy (10.2 %) and hydropower (2.3 %), and just around 0.4 % from other renewable sources (IEA, 2010) however their future share in the global energy mix can be very different (Moriarty and Honnery, 2012). For example, referring to the IEA World Energy Outlook 2012 (WEO) New Policies Scenario projections, renewables are expected to deploy rapidly, from 1 684 Mtoe in 2010 to almost 3 080 Mtoe by the end of 2035, with the highest input from solar energy helping to mitigate climate change by reducing overall CO_2 emission by almost 4.1 Gt (IEA, 2012). Some experts even say that in principle renewable energies could meet about half of global energy consumption by the year 2050 (Martinot et al., 2002).

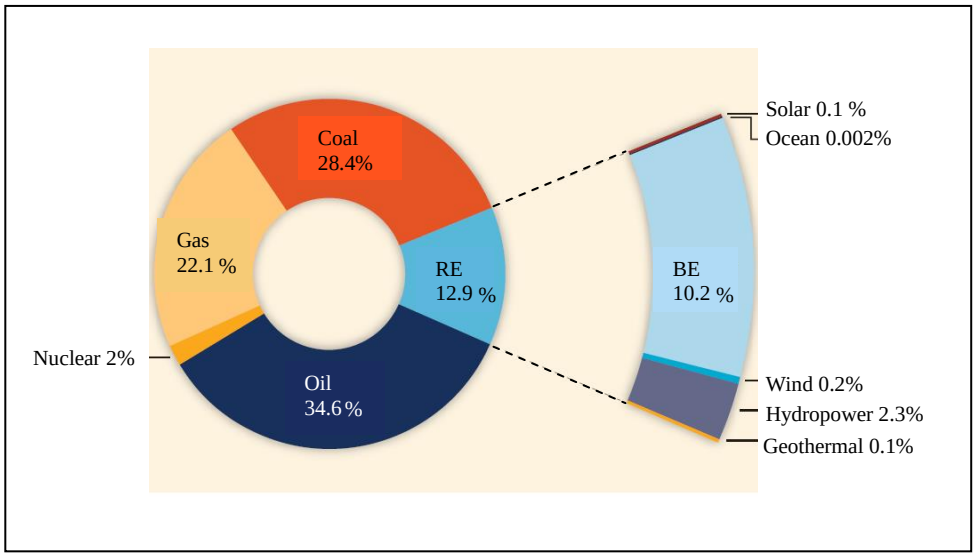

Figure 2.2: Shares of energy sources in total global primary energy supply in 2008 (492 EJ). Modern biomass contributes 38 % to the total biomass share. Data source: IEA (2010). Adapted from Special Report of the Intergovernmental Panel on Climate Change (Figure 1.10), (IPCC, 2011).

As mentioned earlier bioenergy (BE) is currently one of the largest RE resources supplying almost 50.40 EJ (EJ=exajoule=10^{18} J), of the annual global primary energy needs in the form of biomass feedstock and biogas to generate electricity and heat or can be converted into gaseous, liquid or solid fuels. According to estimates, BE share in global energy mix is likely to increase especially in the largest industrialized countries, such USA, Canada, Germany, France, Japan, Italy, UK and Russia) through the use of so-called modern biomass forms (e.g., via combustion or insulation). It is important to mention here that presently, BE technologies are at different deployment stages, with some like small and large scale boilers, domestic pellet-based heating systems or ethanol production from sugar and starch hydropower considered as commercially available, while for example liquid biofuels produced from algae and some other biological conversion still at research and development stage. While the use of bioenergy has many benefits such as security of energy supply, lower GHG emissions and the support for agriculture evolution there are also some limitations, for example the direct and indirect land-use change, possible biodiversity loss, challenges to water supply and food security and human rights violations (IEA, 2009, Hennenberg et al., 2010, Berndes, 2002, Gerbens-Leenes et al., 2009).

While hydropower is considered as a mature technology, hence, with limited potential, it is still predicted to grow at 2 % until 2030 (IEA, 2008) mainly because of modernization and expansion of current power plants. Other kinds of renewable energies such as wind energy, PV solar energy and geothermal are considered as 'new' sources and there is still a huge potential for exploring and developing these technologies. Long-term prospects for these new sources are very hopeful, and significant advances in raw materials usage, production and efficiency are expected, making electricity generation by these sources very competitive (Muller-Steinhagen and Nitsch, 2005, Dincer, 2000).

Definitely renewable energies are strong candidates for sustainable energy development, such all represent natural resources and not limited accessibility for all people in the world for many years over (Resch et al., 2008). Unfortunately under the 'business as usual' RE alone cannot completely resolve growing energy demand without policy support and a variety of technological, and socio-economic

breakthroughs (IPCC, 2007, Verbruggen et al., 2010). One major issue with RE is that their resources are not uniformly distributed on the globe and therefore like solar on wind are variable and not always available when needed (Painuly, 2001). For example, wind energy comes just from five counties with less than 10 % of the global population (Honnery and Moriarty, 2009). Therefore in principle renewables should be manufactured in sufficient geographical locations to provide maximum and continuous energy output, like for example the geothermal sources should be located in the areas called 'ring of fire' around the Pacific or where earthquakes and volcanoes are concentrated (Duffield, 2003). Also, variation in climate change can produce future uncertainty for example the results in dry years for hydro, poor crop yields for biomass, increased cloud cover and materials costs for solar, and variability in annual wind speeds (Awerbuch, 2005). Table 2.1 below summarize the potential negative environmental impacts caused by use of renewable energy sources.

Table 2.1: Summary of renewable energy sources and their potential negative impacts on the environment. Adapted from (Azarpour et al., 2013) with kind permission from Springer.

RE sources	potential impact on environment
wind	bird and bat deaths, noise and vibration pollution, possible climate-change, potential habitat loss;
solar	pollution from PV production (toxic heavy metals and rare earth minerals), landscape change, reduce solar irradiation for plants and vegetation ;
hydro	change in the local eco-systems and local weather conditions, social impact, induction of earthquakes
geothermal	landscape change, could cause water and air pollution, cooling of earth core;
biomass	produced yield affected by biomass crop, loss of biodiversity, elimination of current biomass use;
tidal/wave	landscape change, reduction water motion/ circulation, deterioration of the water quality

2.4 Hydrogen Energy

Among possible sustainable energy alternatives, hydrogen seems to receive particular attention since it offers a clean, sustainable and secure long-term solution

for the global energy needs. In principle, hydrogen can replace all available forms of energy used today and provide clean services for all energy sectors, including mobile, stationary and portable. It can be stored for later use in a liquid or gaseous form or can be transported over long distance using pipelines, tankers or rail trucks to meet the time and geographical demands (Johnston, 2005). Despite these strong arguments several technical, economical and social barriers need to be overcome before widespread use of hydrogen as a sustainable energy vector (Edwards et al., 2008). The priority areas need to focus on the large-scale 'green' hydrogen generation (see Section 2.4.2), safe, and low-cost and efficient hydrogen storage (see Section 2.5) and the proper infrastructure to use hydrogen in the electric grid, efficient and affordable fuel cells or heat engines development (discussed in next pages of this section).

At present, worldwide hydrogen production accounts for approximately 50–60 million tons per year, and approximately 97 % of this captive or internal production with only about 3 % categorised as "merchant" and delivered elsewhere (Moniba Energy Develpment Initiative, 2003). Currently, hydrogen is mostly used in a variety of industrial processes for synthesis of chemical compounds such ammonia and methanol, in refineries for crude oil hydrogenation and in metallurgy as a reducing or protection gas (Häussinger et al., 2000b). Several approaches for hydrogen use have been proposed. For example, one approach involves use of hydrogen in the transportation sector by mixing it with hydrocarbons as a fuel for internal combustion engines (ICE) which is a way to increase engine performance and decrease CO_2 pollution. Another approach involves production of hydrogen at central locations and its distribution to refuelling stations, where it will be pumped into vehicles for use in the fuel cell (FC) and other power plants (Midilli et al., 2005). However, in the long-term future the hydrogen holds the promise to provide a secondary energy carrier together with the efficient FC as the most competitive low-carbon energy alternative, when combined with right hydrogen sources.

Hydrogen and FC can be used in different applications ranging from portable devices (such as mobiles phones, laptops) through transportation in light-duty vehicles, delivery trucks, buses, ships, as well as heat and power generators in stationary use. The main interest in the hydrogen FC systems is motivated by their high efficiency,

stability and lower noise than ICE (McNicol et al., 2001). There are two classes of hydrogen fuel cells, depending on their operation temperature: a low temperature FC (60–250 ^{o}C) and high temperature FC (600–1000 ^{o}C). The low temperature FC is mainly used in the transportation sector due to its quick start, compact volume and low weight, while the more efficient high temperature FC is mainly chosen for stationary use. The proton exchange membrane FC (PEMFC) is considered for commercial transportation use, mainly due to its low operating temperature, and performance level necessary for wide scale commercialisation (Wee, 2007). The PEMFC in principle works as the reverse of electrolysis. The hydrogen (from fuel) and oxygen (from air) are recombined electrochemically to produce electricity as long as hydrogen is supplied (see Figure 2.3). The only by-product is water and heat and no pollutants are produced when hydrogen is used (Züttel et al., 2008). However, at present this technology is still in the early stage of commercialisation and does not offer sufficient end-use mainly due to high price compared to conventional ICE. The drawbacks associated with the fuel cell are the need for a very expensive platinum catalyst, fuel cell durability, and sensitivity to impurities in the input hydrogen gas (Dincer, 2008).

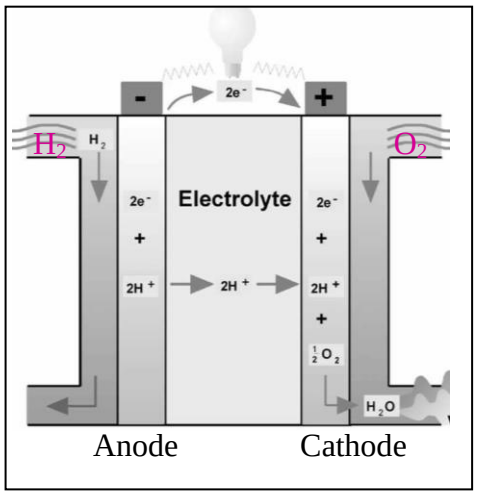

Figure 2.3: Schematic of PEMFC operation. Adapted from (Mourato et al., 2004) with kind permission from Elsevier.

Figure 2.4 depicts a network of hydrogen with production, storage, and its distribution until it is finally used in a fuel cell, combustion engine or other applications to extract electrical and mechanical energy. As shown below, in order to

alleviate the problems of global warming and climate change in long-term energy sustainability, hydrogen generation must be based on renewable sources such as wind, solar, hydro, bioenergy not on the conventional fossil fuels (Gosselink, 2002).

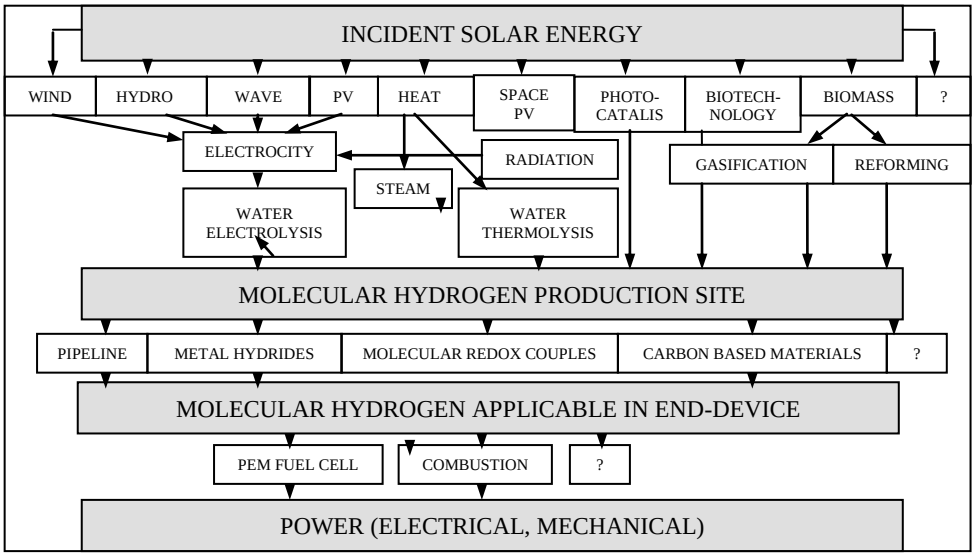

Figure 2.4: Sustainable hydrogen chain. Adapted from (Gosselink, 2002) with kind permission from the International Association of Hydrogen Energy.

2.4.1 Hydrogen Properties

Hydrogen is the lightest and most plentiful element in the universe making almost 75 % by mass and over 90 % by volume of all matter (Midilli et al., 2005). Because of its high reactivity hydrogen on Earth is nearly always combined with other elements and can be found in water, all living organisms, hydrocarbons and several other natural and artificial compounds (Armaroli and Balzani, 2011). In its free form it can be found in the atmosphere but at less than 1 ppm concentration. A hydrogen atom is composed of a single electron and single proton and its ordinal number in the periodic table is one. Hydrogen has three natural isotopes called protium (^{1}H), deuterium (^{2}D) and tritium (^{3}T), all having the same proton number (equal to one), but different number of neutrons in the nucleus. Its ordinary isotope protium (atomic mass 1.007822 u), with no neutrons is the predominant form on the Earth (99.985 %). The second stable isotope is deuterium (atomic mass 2.01410178 u), with one neutron accounts just for around 156 ppm of hydrogen found in oceans.

The third, radioactive tritium (atomic mass 3.0160492 u) with two neutrons is unstable with a half-life of around 12.33 years. Tritium is extremely rare on Earth, and just traces can be found into atmosphere (Greenwood, 1997). All hydrogen isotopes, because of their single electron in the atom can react together and form covalent molecules of H_2, D_2 and T_2 as well as mixed species such as HD. Hydrogen in its molecular form is composed of two hydrogen atoms, which can coexist as two spin isomers known as para- and ortho-hydrogen, due to differences in their spins orientations. As can be seen from Figure 2.5 the equilibrium proportions of both forms in a hydrogen mixture depends on the temperature. For example at ambient temperature (298 K) the equilibrium mixture concentration is about 75 % ortho- (parallel spins) and 25 % para-hydrogen (anti-parallel spins), and this form is called the 'normal' hydrogen. At lower temperatures below 80 K para-hydrogen is the more stable form (50 %), and at 19 K almost all equilibrium mixture contains pure para-hydrogen (99.75 %). Some properties of the para- and ortho isomers show significant differences especially in thermodynamic properties, such as enthalpy, entropy and heat capacities (Jacobsen et al., 2007).

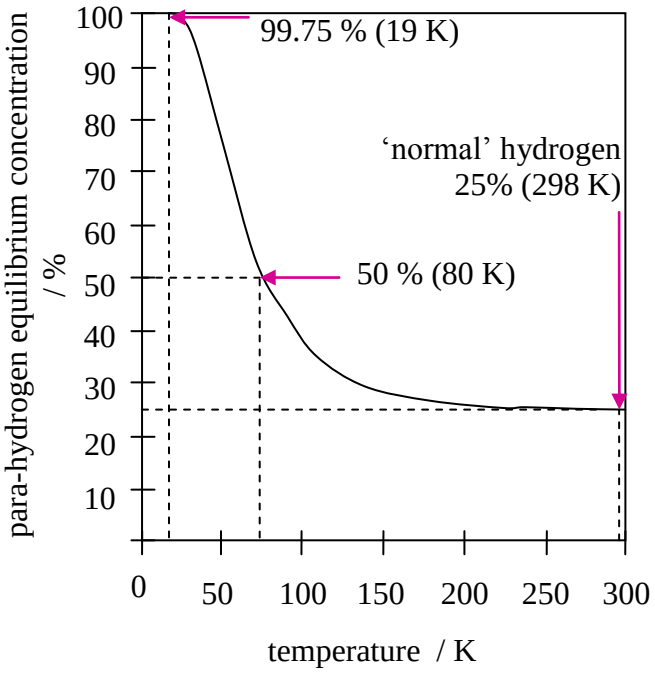

Figure 2.5: Para- and ortho-hydrogen equilibrium concentration ratios as a function of temperature. Adapted from (Jacobsen et al., 2007) with kind permission from Springer Science.

The physical properties of hydrogen are illustrated in the phase diagram in Figure 2.6. As can be seen the hydrogen molecules can be found in different forms (gaseous, solid, liquid) depending on the temperature and pressure. For example at very low temperatures of around 11 K, hydrogen is in a solid state with density of 70.6 kg m^{-3}. At standard conditions (STP, 273 K and around 1 bar) hydrogen is a gas with a density of 0.089886 kg m^{-3}. In small regions starting at the triple point (21 K) and ending at critical point (33 K) hydrogen liquefied with a density of 70.8 kg m^{-3}.

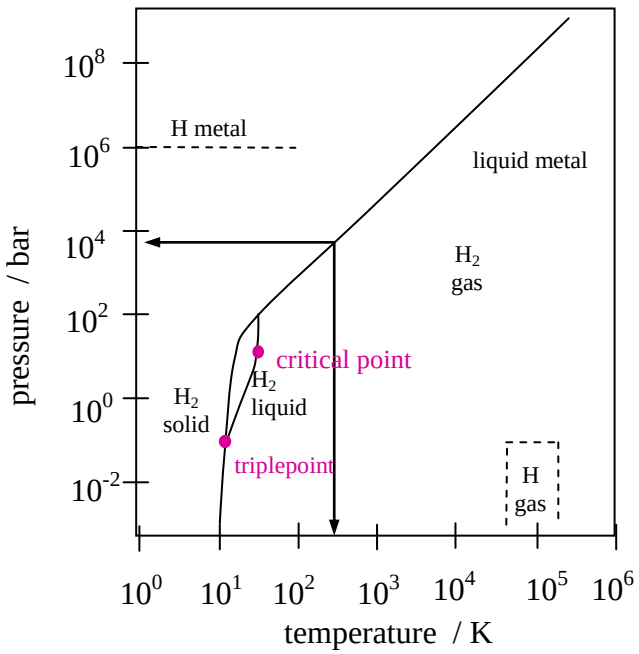

Figure 2.6: Primitive phase diagram for hydrogen. Adapted from (Leung et al., 1976) with kind permission from Elsevier.

At ambient temperature (298 K) hydrogen is odorless, colourless and non-toxic gas. It can be combusted in oxygen with no harmful emissions other than considerable amounts of heat and water. When burned in air some small amounts of nitrogen oxides can be released at very high temperatures (< 2300 K) (Demirbas, 2002). Hydrogen is highly flammable with a wide flammability range between 4–75 %, meaning that just a little as 4 % of hydrogen in air can produce a highly combustible mixture (Balat, 2007). Hydrogen also possesses very high diffusivity, on account of its small size and low mass and can mix in air very rapidly, diluting its concentration below flammable level when hydrogen leaking occurs (Balat, 2007). A fundamental attraction is that hydrogen has the highest gravimetric energy density among conventional fuels with a lower heating value of 120.0 MJ kg^{-1}, exceeding gasoline

by almost a factor of three (43.0 MJ kg^{-1}). In contrast its volumetric energy density is very low, making hydrogen difficult to store under ambient conditions (Weidenthaler and Felderhoff, 2011). This is a specially demanding problem for vehicular use, which generally requires low mass, low volume components. In order to increase the hydrogen volumetric density there are several methods including hydrogen compression and liquefaction, which are currently an option andother promising alternatives under development such as hydrogen storage in the highly porous materials (Weidenthaler and Felderhoff, 2011). Hydrogen storage in solids is the main topic of this thesis and will be covered in more detail in Section 2.5 of this thesis.

2.4.2 Hydrogen Production

Hydrogen, like electricity is an energy carrier or vector, not an energy resource, meaning that energy is needed to obtain it from other materials rich in hydrogen since does not occur naturally on the Earth as H_2, apart from a few hydrogen rich natural gas wells in Kansas (Sherif, 2005). Many ways to produce hydrogen exist including both fossil fuel and sustainable resources available almost everywhere, making hydrogen the most universal fuel (Rosen and Scott, 1998). As listed in Table 2.2, approximately 96 % of hydrogen available on the market right now is produced from fossil fuel conversion, through steam methane reforming (SMR) of natural gas, partial oxidation of heavier oil fractions (POX) and coal gasification, providing relatively low-cost production routes but still associated with high CO_2, emission, which must be captured and stored to ensure processes sustainability (Turner, 2004, Häussinger et al., 2000, Press, 2009). On the other hand electrolysis, which accounts just for less than 4 % is clean but very expensive because large amounts of electricity are required for hydrogen generation (Ewan and Allen, 2005). Meanwhile, there are different promising ‘green’ technologies to produce hydrogen from renewable sources, such as biomass and photocatalysis, which together with virtually unlimited sunlight, wind, wave of hydropower processes are believed to be capable of reducing the world’s carbon footprint (Momirlan and Veziroglu, 2002, Adamson, 2004).

Table 2.2: Annual world hydrogen production share by source. Adapted with kind permission from (Balat, 2008). Copyright 2008 International Association of Hydrogen Energy.

sources	share / %
methane steam reforming	48.0
partial oxidation of oil	30.0
coal gasification	18.0
electrolysis	3.9
other	0.1
total	100

As seen in Table 2.2 roughly 48 % of the world's hydrogen production is based on SMR, which is the cheapest and most common industrial method of producing hydrogen, with a low energy consumption rate of about 1.23–1.35 GJ-natural gas/GJ-H_2 (Jin et al., 2008). Endothermic SMR is heat intensive process and requires a high temperature source (750–900 ^{o}C) which is mainly provided from burning natural gas (Yildiz and Kazimi, 2006). A rich in hydrogen reformat (70–75 %) is produced, along with smaller amounts of CH_4 (2–6 %), CO (7–10 %), and CO_2 (6–14 %) via a three-step process. Firstly methane is catalytically reformed at elevated temperature and pressure to produce a syngas mixture of H_2 and CO. Then a catalytic shift reaction is carried out to combine CO and H_2O and to produce the additional H_2. Finally the hydrogen products are purified by the adsorption methods and industrial grade hydrogen is obtained (99.99 %). The reforming steps can be described by the following reactions (McHugh, 2005):

$$CH_4 + H_2O \rightarrow CO + 3H_2 \quad (2.1)$$

$$CO + H_2O \rightarrow CO_2 + H_2 \quad (2.2)$$

Another major source of hydrogen is partial oxidation of heavier oil fractions, such as natural gas or other fossil fuels which when combusted with limited oxidant supplies (air or pure oxygen) and steam yield carbon monoxide and hydrogen (see Equation 2.3).

$$2C_8H_{18} + 2H_2O + 9O_2 \rightarrow 12CO + 4CO_2 + 20H_2 \quad (2.3)$$

In this process heat is produced in an exothermic reaction so any external energy source is needed for the reactor (Kothari, 2004). Produced hydrogen is separated and purified using shift reactors similar to SMR and pressure swing adsorption (PSA) systems. The carbon monoxide can be further converted to hydrogen as earlier (Equation 2.2).

Hydrogen can be also produced from coal by the gasification processes, and while less mature than SMR, this technology is relatively well established. It is noteworthy that hydrogen from coal accounts only for 18 % of the world's hydrogen production, and that the complex and expensive gasification process it undergoes presents the greatest drawback for its widespread production. Its energy consumption is about 1.54–1.69 GJ-coal/GJ-H_2 (Jin et al., 2008). A typical reaction for the coal gasification is given in Equation 2.4 where carbon is converted to a synthesis gas mixture. Since the process is endothermic additional heat is required. The water vapour (steam) shift reaction can be further introduced to carbon monoxide to produce extra hydrogen (Equation 2.5):

$$\text{C (carbon source)} + H_2O \rightarrow CO + H_2 + \text{impurities} \quad (2.4)$$

$$CO + H_2O \rightarrow H_2 + CO_2 \quad (2.5)$$

Now it is clear that the production of hydrogen via all these methods cannot be a long-term solution since all result in carbon dioxide co-production, which is assumed to be the main greenhouse effect contributor. To enhance the vision of clean, zero-emission hydrogen economy the idea of using more sustainable, 'green' hydrogen production routs which can be used directly to supply hydrogen fuel additionally reducing environmental impact is developed (Orhan et al., 2012).

There is a remarkable number of reviews of hydrogen production from clean, sustainable resources in the literature (Das and Veziroglu, 2008, Joshi et al., 2011, Turner et al., 2008, Miltner et al., 2010, Dincer, 2011). According to a recent paper published in the International Journal of Hydrogen Energy by Dincer (Dincer, 2012), there are four kinds of 'green' pathways, namely electrical, thermal, photonic, biochemical or their combination like *e.g.* electrical+ thermal, electrical + photonic, to extract hydrogen in a sustainable manner. As can been seen from Figure 2.7 the

forms of ‘green’ energies can be derived from various conversion routes, based on the renewable (solar, wind, biomass, geothermal, hydro, ocean and tides and waves), nuclear or recovery energy sources (Dincer, 2012).

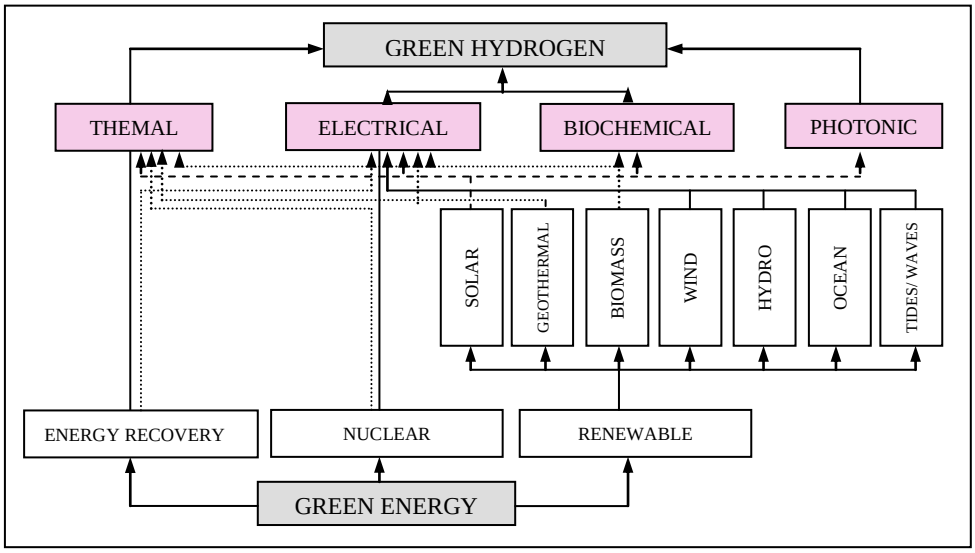

Figure 2.7: Paths for green hydrogen production. Adapted from (Dincer, 2012) with kind permission from International Association of Hydrogen Energy.

A very promising near-term ‘green’ solution for deriving hydrogen is electrolysis of water. Electrolysis is the process where direct currents passing through the two electrodes into water solution splitting water to hydrogen and oxygen. The most common electrolyser today is based on the electrolysis of the alkaline solution (e.g. 30 % potassium hydroxide or sodium hydroxide), where the water is dissociated into hydrogen and hydroxyl ions (OH^-) at the cathode (Equation 2.6). The mobile OH^- anions pass through the electrolytic material to the anode, where oxygen is formed (Equation 2.7) (Bicakova and Straka, 2012). The process is relatively cheap since it does not require expensive catalysts, since typically carbon steel coated with nickel is used. The purity of generated hydrogen is higher than 99.7 % (Orhan et al., 2012).

Cathode: $2H_2O + 2e^- \rightarrow H_2 + 2OH^-$ (2.6)

Anode: $4OH^- \rightarrow O_2 + 2H_2O$ (2.7)

Total: $H_2O \rightarrow H_2 + 1/2O_2$ (2.8)

Electrolysis can also be used together with proton exchange membrane (PEM) systems, which typically use platinum, iridium, ruthenium, and rhodium for

electrode catalysts and a perfluorosulfonic acid polymer membrane (trade name NAFION) for electrode separation (Turner et al., 2008, Pettersson et al., 2006). In PEME (proton exchange membrane electrolysers) water is fed to the anode where it is broken into protons and oxygen (Equation 2.9) (NAS, 2004). Then protons pass through the polymer membrane to the cathode, where they are recombined into molecular hydrogen (Equation 2.10) (NAS, 2004). The total hydrogen production is presented in Equation 2.11.

$$\text{Anode: } 2H_2O \rightarrow O_2 + 4H^+ + 4e^- \quad (2.9)$$

$$\text{Cathode: } 4H^+ + 4e \rightarrow 2H_2 \quad (2.10)$$

$$\text{Total: } H_2O \rightarrow H_2 + 1/2O_2 \quad (2.11)$$

One of the biggest advantages of PEME is that the generated hydrogen is of ultra high purity (> 99.999 %), which is required for some fuel cell vehicles in order to protect their platinum catalyst (NAS, 2004). In addition, because the hydrogen is produced on site, no transportation and storage is needed, which makes electrolysed hydrogen more competitive then delivered hydrogen (NAS, 2004). Although, the PEME is the most expensive process of producing hydrogen today, mainly because of high NAFION membrane cost (approximately £400 per m^2) and expensive cathode metals (such as Pt, Ru, Ir).

Intensive efforts have been made to produce clean hydrogen via thermochemical methods in which water is split into hydrogen and oxygen using a series of chemical reactions, initiated by heat or electrical energy (Bicakova and Straka, 2012). The conceptually simplest version of the thermal technique is direct water conversion by heating to very high temperatures (over 2500 K), but stable materials and heat sources are not yet easily available (Holladay et al., 2009). Over 300 examples of water cracking cycles can be found in literature, but many of them are still at the experimental stage, since some of the technical issues related to product separations and the infrastructure development needs to be overcome first (Momirlan, 1999). Three steps Sulphur–Iodine (S-I) cycle written below (Equation 2.12) is the most promising water cracking system for the hydrogen production, but required high temperatures over 1143 K (Orhan et al., 2012).

(1) $I_2+SO_2+2H_2O \rightarrow 2HI+H_2SO_4$ (2.12)

(2) $2HI \rightarrow I_2+H_2$

(3) $H_2SO_4 \rightarrow H_2O+SO+1/2O_2$

Other promising approaches to producing hydrogen are biological processes namely bio-photolysis and bacteria fermentation (Bicakova and Straka, 2012). Both processes are controlled by enzymes producing hydrogen. Bacteria fermentation is an anaerobic process that transforms organic matter into hydrogen and oxygen in the absence of sunlight or oxygen and provides the most common method to produce bio-hydrogen. By contrast, bio-photolysis is a process that uses sunlight and water in combination with some algae or cyanobacteria to generate hydrogen and oxygen (Bicakova and Straka, 2012). Currently, both processes are in laboratory scale testing, but have the potential for low-cost, larger-scale hydrogen technologies.

Another important feedstock for hydrogen is biomass, since it is renewable, abundant and can be converted into hydrogen via different ways (Goswami et al., 2003). Methods for producing hydrogen from biomass include: (1) gasification in steam, air/oxygen or catalyst to produce rich in hydrogen gas (about 40–60 %), and other gaseous by-products which can be further oxidised to yield more hydrogen (Equation 2.13), (2) pyrolysis where via decomposition processes biomass is transformed into bio-oil (Equation 2.14) which followed by (3) catalytic steam reforming method produce hydrogen (Equation 2.15). It is, important to note that in all biomass processes hydrogen must be separated from the explosive, high temperature and pressure gaseous mixture because of the safety and practicality constraints (Ni et al., 2006).

(1) Gasification of biomass $\rightarrow H_2 + CO_2 + CO + N_2$ (2.13)

(2) Pyrolysis of biomass $\rightarrow H_2 + CO_2 + CO +$ hydrocarbons (2.14)

(3) Catalytic steam reforming of bio-oil $\rightarrow H_2 + CO_2 + CO$ (2.15)

Clearly, all biomass conversion methods are very promising technologies for sustainable hydrogen production development and according to the recent US National Research Council statement it is expected that biomass gasification will be

the most possible commercial route for the long-term renewable hydrogen production (2015–3035) (NRC, 2008).

Geothermal power also holds promise for electrolytic hydrogen production, for example in Iceland, Vanuatu, and Hawaii. Other longer-term options include wave and tidal energy. But areas where cheap hydroelectricity exists – Brazil, Canada, Iceland, Norway and Sweden – may be where renewable electrolysis happens first on a large scale (Ni et al., 2006). Furthermore, the use of nuclear energy sources, particularly linked with S-I thermochemical cycles can certainly provide the technology for the high hydrogen demand. However this is still accompanied by radioactive waste generation (Orhan et al., 2012).

2.5 Hydrogen Storage

One of the biggest challenges that needs to be overcome in the transition towards a hydrogen energy system is efficient, safe, low-weight, low-cost and high energy density hydrogen storage (Harris, 2004, Crabtree et al., 2004, Satyapal et al., 2007). Due to the low energy content of hydrogen on a volume basis (8.7 MJ L^{-1}) at ambient conditions, large volume containment is required. This is a major issue especially in vehicular (mobile) applications where 4 kg of hydrogen occupies around 45 m^3 at ambient temperature and pressure (298 K and around 1 bar) and is required to achieve a practical driving distance of 500 km (Satyapal et al., 2007a). There is still a great deal of research to be done to explore hydrogen storage methods and to provide on-board storage systems that will be competitive with conventional vehicles available on the market. Existing hydrogen storage methods can be mainly divided into three categories: physical storage, chemical storage and Kubas type quasi-molecular hydrogen bonding (see Figure 2.8). In physical storage (Figure 2.8 (a)), hydrogen remains molecular (H_2) and interacts weakly with a storage medium via van der Waals forces with energies in the range of typically 1–10 kJ mol^{-1}. Hydrogen is stored reversibly with little heat or reduction in pressure to be fully released. Here, physical storage of hydrogen includes liquid (20 K), high pressure compressed gas (350–700 bar) and physisorbed gas into highly porous sorbents. In the case of chemical storage (Figure 2.8 (b)) hydrogen molecules

dissociate into individual atoms (H^o) and can bond into materials either covalently or ionically. The interaction energies lie in the range of 50–200 kJ mol^{-1} but this form of hydrogen storage is typically not reversible, and requires very high temperature for desorption. However, in some cases the hydrogen atom can exist in the dissociated form in so-called interstitial hydrides, where atoms occupy the octahedral or tetrahedral interstices in the metal or alloy framework (Züttel, 2003). The bonding between the hydrogen atom and the metal is highly delocalized, with a multi-centre, multi-electron bond similar to metallic bonding. Some examples of these interstitial hydrides are PdH, (V, Ti, Fe)H_2 and $LaNi_5H_x$ (Gross, 2008). An a interesting bridge between physical and chemical storage is the so called 'Kubas' mechanism (Figure 2.8 (c)) (Kubas, 1988), where a transition metal (like Sc, Ti and V) supported on a nanostructured material can bind hydrogen into a quasi molecular form and slightly stretched its bond, but not enough to break it. Typical binding energies associated with Kubas mechanism are in the range of 10–80 kJ mol^{-1} (Jena, 2011).

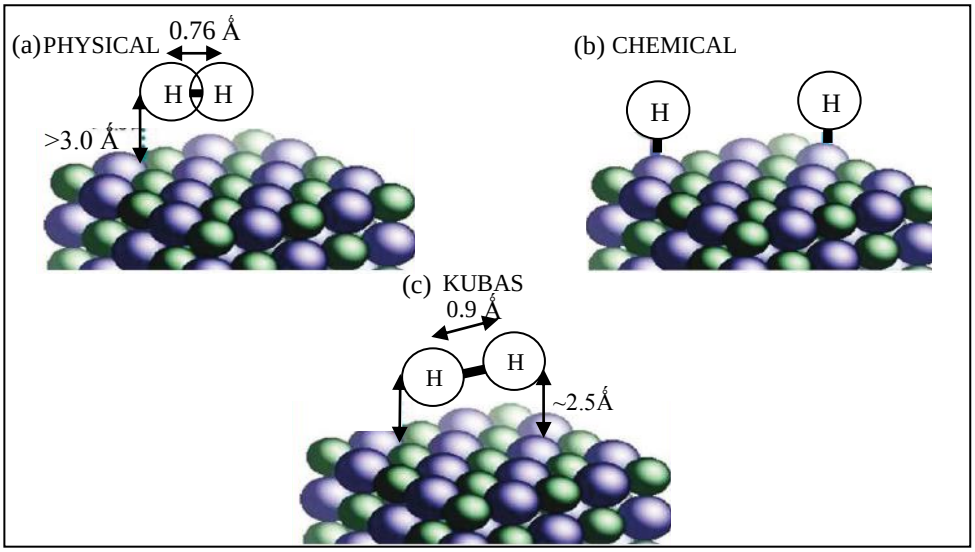

Figure 2.8: The existing hydrogen storage methods, depending on the hydrogen binding mechanism: (a) physical, (b) chemical and (c) quasi-molecular in the Kubas type. Reprinted with permission from (Jena, 2011). Copyright 2011 American Chemical Society.

In order to frame storage requirements, the US Department of Energy (DOE) established a set of technical requirements for on-board hydrogen storage for light-duty vehicles, as a useful benchmark for storage methods (DOE, 2009). The most up-to date DOE targets published in September 2009 are tabulated in Table 2.3. It is

important to emphasize here that listed values are the system level targets, which incorporate material and other system components such as tanks, valves, regulators, piping, regulators, mounting brackets, insulation and added cooling capacity and are suitable for the 500 km driving range distance on the single hydrogen fill. As can be observed below, in order to achieve the compacting requirements of 5.5 wt% and 40 g L^{-1} in 2015 (or ultimately 7.5 wt% and 70 g L^{-1}) the storage material capacity itself must be significantly higher. Furthermore, there are other performance requirements, including the operational pressure and temperature for the hydrogen storage and delivery, fuel cost, efficiency and kinetics for the system refuelling, and fuel purity. For example, the temperatures targets shown below refer to –40 and 85 ^{o}C in 2015 (or –40 / 95–105 ^{o}C in ultimate) are the requirements for the cold weather and the fuel cell operation. Another important parameter highlighted below is acceptable operating pressure, which should be targeted at 5–12 bar in 2015 (or 3–12 bar in ultimate) and 35–100 bar respectively for the fuel cell and ICE system. Furthermore, as listed above the hydrogen storage system is expected to provide fuel with 90 % efficiency and with targeted refilling time (assuming 5 kg hydrogen fill) of 3.3 minute in 2015 (2.5 minute in ultimate). Another critical factor is fuel cost, which should be in the range 2–6 dollars per gallon of gasoline equivalent (gge) (2015) to be competitive with conventional petroleum fuels (DOE, 2009).

Table 2.3: Summary of DOE hydrogen storage system targets for the light-duty vehicles established in September 2009. Adapted from (DOE, 2009).

storage parameter	units	2015	ultimate*
system gravimetric capacity	wt%	5.5	7.5
system volumetric capacity	g H_2 L^{-1}system	40	70
delivery temperature	^{o}C	– 40/85	– 40/95–105
operating pressure	bar	5–12 (FC) 35–100 (ICE)	3–12 (FC) 35–100 (ICE)
system efficiency	%	90	90
life cycle (1/4 tank to full)	cycles	1500	1500
system filling time (5 kg fill)	min	3.3	2.5
fuel cost	$/gge at pump	2–6	2–3
fuel purity (from storage)	% H_2	99.75	99.75

*Ultimate targets are intended to facilitate the introduction of hydrogen-fuelled propulsion systems across the majority of vehicle classes and models.

Figure 2.9 shows the current status of hydrogen storage technologies for different materials types updated recently by US DOE (DOE, 2008). As can be seen, at this time no hydrogen storage materials and technology exist to meet the 2015 DOE criteria required for on-board application. However, there is enormous research activity in both materials and engineering field to explore suitable hydrogen storage materials as will be addressed in the following sections of this thesis.

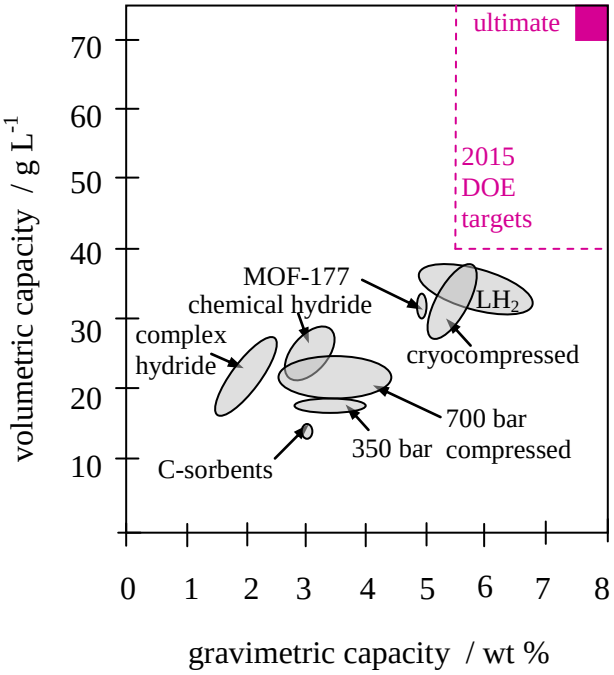

Figure 2.9: Current status of hydrogen storage technologies updated by US DOE. Adapted from (DOE, 2008).

2.5.1 Physical Storage

As mentioned earlier, the physical storage of hydrogen can be regarded as having three subtechnologies: compression, liquefaction and physisorption into highly porous materials. Compression is one of the most mature, commercially available technologies which involve increasing of pressure typically up to 350 or 700 bar at ambient temperature and storing compressed hydrogen into cylinders or spherical vessels. Compression is an obvious choice for storing of hydrogen, since it can decrease its storage volume by 99.6 % at 350 bar (Hosseini et al., 2012). At ambient temperature, the densities of compressed hydrogen is approximately 22.9 kg m^{-3} at 350 bar and 39.6 kg m^{-3} at 700 bar (Zhang et al., 2005). Clearly, working with such

high pressures requires specially designed storage vessels. There are different types of commercial high pressure hydrogen cylinders available on the market, mostly categorised into four types. Type I are made of stainless steel or aluminium with pressure ranging up to 200 bar and maximum 1 wt% of hydrogen to be stored is mainly used for the industrial or medical applications (Hosseini et al., 2012). Type II and Type III composite based cylinders, are made from a metal liner wrapped with resin–fibre (Type II) or carbon-fibre (Type III) which show slightly different storage characteristics. Type II with a pressure up to 850 bar has a very poor weight performance and is mainly used in stationary applications such as a fuelling station buffer. While Type III vessels are rated to 700 bar, which achieves significant gravimetric storage density of 6 wt% (volumetric storage density of 30 kg m^{-3}) and are successfully applied in automotive, mobile and stationary sectors (Irani, 2002). The last Type IV cylinders are also composites-based. They also reach high storage capacities of around 5 wt% and additionally use much lighter polymer liners for thermal isolation than Type II and III.

The main advantages of compressed hydrogen storage systems are that they are relatively simple and the filling of a vehicle tank is completed in a short time. Because of these advantages it is favourably adopted in many prototype fuel-cell vehicles. The main disadvantages are its low volumetric and gravimetric densities compared to other storage methods, which fall short of the DOE 2015 goals. Another shortcoming of compressed hydrogen is the public perception of safety concerns associated with extremely high operating pressures. However, recent test results have indicated that 700 bar composite vessels may actually be safer than their low pressure counterparts widely used in industry, primarily because of thicker tank walls (Zhang et al., 2005). The process of compressing hydrogen from atmospheric pressure to 700 bar consumes a large amount of energy. Another important heat-transfer issue for compressed hydrogen storage is the temperature increase during fast tank-filling processes (Newell, 2004). Hydrogen exhibits a reverse Joule-Thomson effect at room temperature, i.e., throttling processes from a high pressure stationary tank to a tank being filled causes heating of the gas instead of cooling. During rapid filling (1 kg H_2 min^{-1}), the temperature rise inside the tank can be as high as 50 °C and overheating can adversely affect the integrity of the composite tank (Richards, 2002). Further, with increasing temperature, the tank carries less

hydrogen at a given pressure. Another barrier to wide scale use is cost of compressed hydrogen, which is mainly driven by expensive carbon-fibre composites and large assembly cost (Jorgensen, 2011). For these reasons it seems that this method is not likely to be used in the future.

Liquefaction is another commercially available technology for physical storage of hydrogen (Jorgensen, 2011), where liquid hydrogen (LH_2) can be stored at atmospheric pressure in cryogenic tanks (20.3 K) with a density of 70.8 kg m^{-3}, almost twice as compressed hydrogen at 700 bar (39.6 kg m^{-3}). The simplest liquefaction cycle is the Joule-Thompson cycle in which hydrogen gas is first compressed to a high pressure (e.g., 100 bar) and then cooled in a heat exchanger before passing through a throttling valve, where it undergoes an enthalpic Joule-Thomson expansion and produces liquid. The cooled gas is separated from the liquid and returned to the compressor through a heat exchanger. Because the inversion temperature (i.e., the temperature below which throttling produces a cooling effect) of hydrogen is only approximately 200 K, expansion at room temperature will not induce a cooling effect, and liquid nitrogen (77 K) is often used to pre-cool hydrogen before expansion. LH_2 tanks can be filled in a relatively short time and preferably in much safer way then than high-pressure hydrogen cylinders. The main disadvantages with LH_2 are the high energy consumption associated with liquefaction processes stated to be in the range of 30 % of the total chemical energy stored in the liquid hydrogen (Eberle et al., 2009). Another important point that limits its future application is relatively large boil-off during storage (typically of 0.4 % per day for 50 m^3 tank), which can be minimised by implementation of capture systems but is unpractical as it increases overall storage system cost (Zuttel, 2004, Eberle et al., 2009). Another drawback is that storage of LH_2 requires highly insulated cryogenic tanks. To minimize heat losses, the multilayer vacuum insulation consisting of 30–80 layers of aluminium foil as radiation shields is required (Zhang et al., 2005). Due to all these fundamental problems, LH_2 storage is not likely to the used in massive on-board application.

An intermediate process between compression and liquefaction, which can revolutionize the hydrogen storage market, is physisorption into highly nanoporous materials. Please note, the term nanoporous cited here refers to materials with pore

sizes between 0.1–100 nm (Mays, 2007). The advantage of physisorption is that it does not require the direct input of energy associated with hydrogen liquefaction, and offers fast and completely reversible storage. Nevertheless, physisorption could be an attractive alternative to liquid and compressed storage since hydrogen can be simply adsorbed into nanoporous structure with a little heat or pressure decrease to fully desorb. Physisorption is the main subject of this research and more detailed analysis will be addressed in next pages of this thesis.

2.5.2 Chemical Storage

Chemical storage concerns technologies where molecular hydrogen dissociates in solid surfaces into individual hydrogen atoms and is chemically bound (covalently or ionically) into hydride–type compounds, in contrast to physical storage (physisorption), where molecular hydrogen is only weakly physically adsorbed onto the materials surface or into porous structure (for illustration see Figure 2.10) (Eberle et al., 2009). From the practical point of view, the most distinct difference between physical and chemical storage is operational temperature. Hydrides, because of their high stability often require elevated temperature typically about 500 K for thermal decomposition and consequent hydrogen release (Eberle et al., 2009). There is also some reversibility problems, meaning that not all hydrogen can be recovered by desorption. By contrast most physisorption systems require very low temperatures of about 77 K, but is reversible (van den Berg and Arean, 2008).

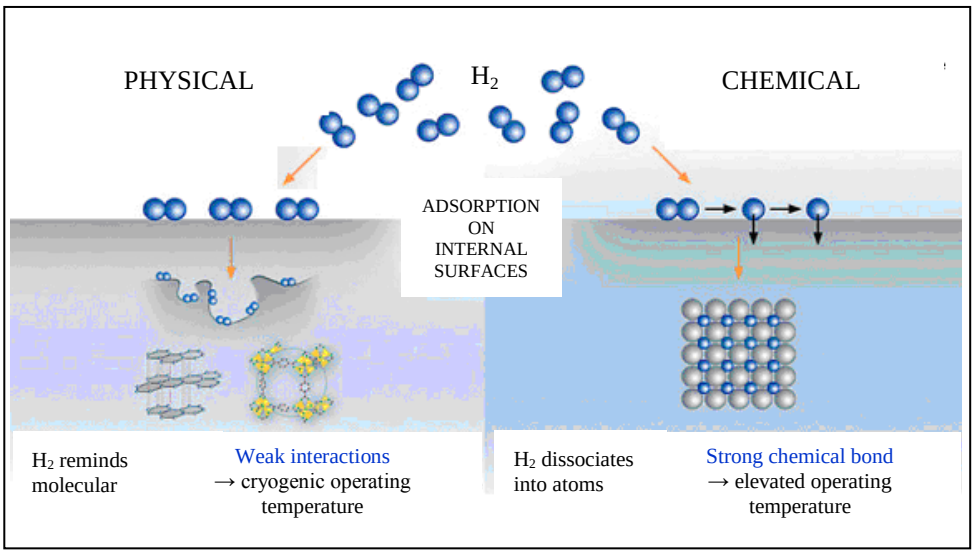

Figure 2.10: Differences between physisorption and chemisorption of hydrogen Adapted from (Eberle et al., 2009) with kind permission from John Wiley and Sons.

Among chemical storage materials, families of conventional metal hydrides, complex hydrides and chemical hydrides have been widely investigated for over a century (Grochala and Edwards, 2004, Züttel et al., 2008, Yang et al., 2010, Broom, 2011). Conventional metal hydrides, compounds that contain hydrogen and a metal or metal alloys and form a metal hydride, are usually stable at ambient temperature and pressure. These materials have been extensively studied for on-board hydrogen use because of safety and volume-efficiency, but the main drawback apart their cost is its low gravimetric hydrogen uptake and slow desorption kinetics (Yang et al., 2010). Complex hydrides are ionic hydrogen compounds which have a metal cation (usually a lightweight alkali or alkaline earth Li, Na, Mg or Ca) and hydrogen "complex" anions, such as borohydrides (BH^{4-}), alanates (AlH^{4-}) and amides (NH^{2-}), where the hydrogen atoms are covalently bonded to the central atoms (Yang et al., 2010). Examples of promising complex hydrides include lithium borohydride ($LiBH_4$), sodium alanate ($NaAlH_4$) and lithium amide ($LiNH_2$). These classes of hydrides have attracted much attention in the hydrogen storage field mainly because of their remarkable hydrogen capacities, estimated to reach up to 18.5 wt% (120 g H_2 L^{-1}) for $LiBH_4$ (Yang et al., 2010). However, the main limitation of this materials include high desorption temperature, sensitivity to air and moisture, and the ammonia formed upon dehydrogentaion, which can poison the fuel cell (Broom, 2011a, Kojima et al., 2004). The use of magnesium hydrides, sodium alanates and the borohydrides is also the subject of current research, all considered

such as safe and practical medium for storing of hydrogen for on-board use (Broom, 2011, Kojima et al., 2004, Amendola et al., 2000). However, the main barriers associated with these classes of materials are irreversibility and energy inefficiency. Nonetheless, hydride storage is a very active field of research and could provide interesting solutions for hydrogen storage. Table 2.4 shows examples of the hydrogen uptake results for some promising hydride systems. More detailed information regarding the chemical hydrogen storage can be found elsewhere (Sandrock, 1999, Grochala and Edwards, 2004, Sakintuna et al., 2007, Orimo et al., 2007).

Table 2.4: Hydrogen storage uptakes obtained for some promising hydrides.

material	gravimetric hydrogen uptake, n_a / %wt	volumetric hydrogen uptake, n_a / g H_2 L^{-1}	References
$Mg(BH_4)_2$	14.8	146	(Orimo et al., 2007).
$LiBH_4$	13.9	93	(Vajo et al., 2005, Siegel et al., 2007)
AlH_3	10.0	148	(Wolverton et al., 2004)
MgH_2	7.7	109	(Siegel et al., 2007)
NH_3BH_3	6.5	96	(Miranda and Ceder, 2007)
$NaAlH_4$	3.7	52	(Bogdanovic et al., 2000)
$LiNi_5H_{6.5}$	1.5	100	(Sandrock, 1999)

2.6 Physisorption Storage

Hydrogen physisorption arises from the van der Waals interaction between hydrogen molecules (adsorbate) and the surface of the porous material (adsorbent). In the absence of relatively strong polarizing centres, interaction between the adsorbent and non-polar hydrogen molecules relies on the weak London dispersion type forces, which are typically in the order of 1–10 kJ $mol^{-1}$for most materials – based on low operating temperatures, e.g., 77 K (Yang et al., 2010).

According to the International Union of Pure and Applied Chemistry (IUPAC) (Sing et al., 1985) the experimental physisorption isotherms determined for any porous system can be categorised into six types, depending on materials structure

and interaction types (Figure 2.11). Fully reversible Type I isotherm is characteristic for purely microporous materials having relatively small pores (below 2 nm in diameter), or can be an indication of sub-monolayer chemisorption into non-porous materials. Both are sub-critical systems, below the adsorptive critical temperature. The Type I isotherm can also occur for super-critical systems, which is reflected by densification of fluid near the material surface with increasing pressure. Type II isotherms are usually found for non-porous or macroporous materials (pores greater than 50 nm), where mono- or multilayer adsorption occurs. Type III isotherms are very uncommon, but can occur when adsorbent–adsorptive interactions are weak and adsorptive-adsorptive interactions dominate (e.g. nitrogen adsorption on polyethylene). Type IV isotherms are typical for mesoporous materials having pores between 2–50 nm and show a characteristic hysteresis loop due to capillary condensation. Hysteresis and capillary condensation are also present in Type V isotherms, but differs from Type IV because of its initial part which is related to the

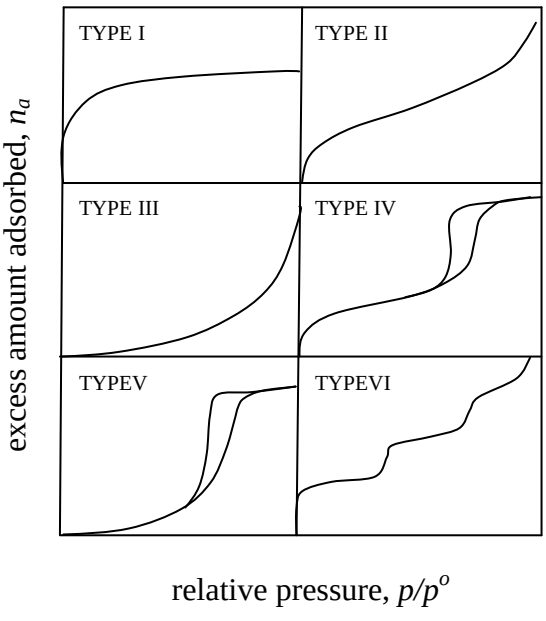

Figure 2.11: Types of physisorption isotherms according to IUPAC classification. Adapted from (Sing et al., 1985) with kind permission from Pure and Applied Chemistry.

Type III, again being an indicative of weak adsorbent–adsorptive interactions. Finally, the Type VI isotherms show the stepwise multilayer adsorption which

occurs for uniform, non-porous surfaces (e.g. argon or krypton adsorption on graphitised carbon blacks at 77 K) (Sing et al., 1985).

The main advantages of hydrogen physisorption when compared with high pressure compression and liquefaction is that it offers lower pressure and higher temperature storage, increased safety, design flexibility and reasonable volumetric/ gravimetric storage efficiency and reduced mechanical requirement of insulation vessels. Unfortunately, so far the hydrogen sorption capacities at moderate temperature and pressure for well known physisorbed materials are too low for practical use (Yurum et al., 2009). The reported hydrogen capacities are limited to around 0.6–0.8 wt% of hydrogen at 298 K and around 100 bar, including capacities of MOF-177 of 0.6 wt% at 298 K and 100 bar and MIL-101 less than 0.5 wt% at 298 K and 80 bar, claimed to have some of the best hydrogen capacities at 77 K (Ferey et al., 2005, Latroche et al., 2006, Chae et al., 2004, Furukawa et al., 2007, Li and Yang, 2008, Li and Yang, 2007).

However, this technology remains a very attractive research area. Hope of enhancing hydrogen storage capacities lies in the increasing strength of adsorbent-adsorptive interaction, preferably to be greater than 15 kJ mol^{-1} (Yang et al., 2010). To realise this several methods are proposed, such as doping (e.g. boron doped carbons) (Chung et al., 2008), surface chemistry modifications (e.g. open metal sites in MOFs) (Wang et al., 2008), and optimizing pore size and shape (Yang et al., 2010). So-called spillover mechanism is attracting much attention as a potential route for improving hydrogen storage performance in carbon based and metal organic framework nanostructures (Wang and Yang, 2008, Cheng et al., 2008). Generally, the hydrogen spillover mechanism relies on the use of supported metallic catalyst to dissociate molecular hydrogen and surface diffusion to store atomic hydrogen in the host substrate. One interesting example of hydrogen spillover is so called ‘carbon bridge building’ method proposed by Yang (Yang, 2006), where dissociated hydrogen atoms migrate from the metal catalyst to the nanostructured carbons by physical ‘bridges’ which are built of carbonizated glucose molecules and diffuse through the entire bulk solid (Figure 2.12) (Lachawiec et al., 2005). Further information regarding the hydrogen spillover mechanism can be found elsewhere (Wang and Yang, 2008).

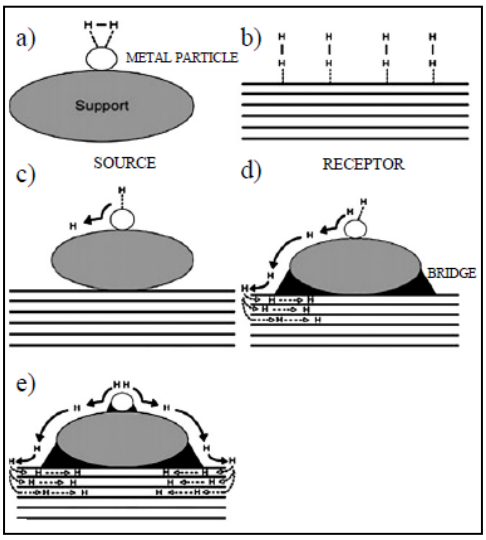

Figure 2.12: Hydrogen spillover into supported catalyst system: (a) adsorption of hydrogen on a supported metal particle; (b) the low-capacity receptor; (c) primary spillover of atomic hydrogen to the support; (d) secondary spillover to the receptor enhanced by a physical bridge; (e) primary and secondary spillover enhancement by improved contacts and bridges. Reprinted with permission from (Lachawiec et al., 2005). Copyright 2005 American Chemical Society.

Recently, the use of physisorption into nanoporous materials has increased noticeably. This optimisation depends on the synthesis of new materials exhibiting ultrahigh surface areas and narrow microporosity, especially pore widths of 0.6–0.7 nm (Gogotsi et al., 2009). There are several comparative studies on the dependence of the hydrogen storage capacities of various sorbents on their BET specific surface areas (Thomas, 2007, Panella and Hirscher, 2005, Zhou, 2005). Typically all agree on a roughly linear scaling of the storage capacity with increasing specific surface area and increasing micropore volume. The most important classes of porous adsorbents being considered for hydrogen storage comprise (1) carbon based materials, (2) zeolites, (3) organic polymers and (4) metal-organic frameworks and all will be covered in the following pages of this thesis. Table 2.5 summarise the best ten results obtained to date for hydrogen storage into porous materials via physisorption.

Table 2.5: Summary of the best ten results obtained for hydrogen storage in porous materials via physisorption.

material	surface area, a_s / m^2g^{-1}	excess hydrogen uptake, n_a / %wt	absolute hydrogen uptake, n_a / %wt	volumetric hydrogen uptake, n_a / g L^{-1}	operation conditions (p and T)	References
NU-100	6143	9.95	14.3	45	56 bar, 77 K	(Farha et al., 2010)
$Be_{12}(OH)_{12}$	4030	–	9.2	–	100bar, 77 K	(Sumida et al., 2009)
MOF-210	6240	8.6	17.6	43	80 bar, 77 K	(Furukawa et al., 2010)
MOF-177	4630	7.3	11.3	32	52 bar, 77 K	(Furukawa et al., 2007)
COF-102	4650	7.24	–	40	40 bar, 77 K	(Furukawa and Yaghi, 2009)
NOT-103	2929	7.2	–	–	60 bar, 77 K	(Lin et al., 2009)
MOF-5	3800	7.1	11.5	42	40 bar, 77 K	(Kaye et al., 2007, Yaghi et al., 2003)
PAF(P2)	5640	7.0	10.7	66	48 bar, 77 K	(Ben et al., 2009)
MWCNT	—	–	10.7	–	148bar, 238 K	(Zuttel et al., 2002)
SWCNT	—	–	6.3	–	60 bar, 77 K	(Zuttel et al., 2002)

Apart from high gravimetric hydrogen storage capacities, the volumetric capacity of materials, which represent the amount of hydrogen adsorbed per unit volume (eg., g L^{-1}) is also a critical parameter to consider. As can be seen from data tabulated in Table 2.5 the volumetric capacities of some MOFs and other porous sorbents are slightly higher than the density of compressed H_2 at 700 bar and 300 K (39 g L^{-1}). Important to note that the volumetric capacities of such nanoporous materials are typically converted from gravimetric uptakes and crystallographic densities of each material, so that in order to improve the volumetric performance both parameters should increase. For example, MOF-5 having a high crystallographic density of 0.61 g cm^{-3} and a high gravimetric hydrogen uptake of 7.1 wt% is reported to have the best excess and absolute volumetric capacities (42 g L^{-1} and 66 g L^{-1}) among porous sorbents. It is well known that the density of hydrogen can be improved by liquefaction at 20 K (70.8 g L^{-1}), however the main problem is large energy consumption and high boil-off which make this method unattractive for on-board use. In fact, many complex hydrides have hydrogen densities greater than the liquid hydrogen, however these materials suffer from poor reversibility and high temperature requirement for hydrogen desorption.

2.6.1 Carbon Based Materials

Carbon based materials have been studied extensively as potential hydrogen storage media due to their low density, extensive pore structure, chemical inertness, wide variety of structured forms, good chemical stability and the ability to modify the structures using a wide range of preparation, carbonization and activation processes (Sakintuna and Yurum, 2005). Since early reports indicating high hydrogen storage capacities on carbon nanotubes (Dillon et al., 1997, Liu et al., 1999) various different forms of carbons have been tested, including activated carbons (Dillon and Heben, 2001, Chahine and Bose, 1994), graphite, carbon nanofibres (Poirier et al., 2006, Strobel et al., 2006, de la Casa-Lillo et al., 2002) and templated carbons (Strobel et al., 2006, Zhao et al., 2005b). Adsorption/desorption of hydrogen on the nanostructured carbons usually offers no or very little hysteresis and very fast kinetics enable quick recharging and discharging of hydrogen storage system (Thomas, 2007, Zhao et al., 2005a). Mainly because of these advantages nanoporous carbons are very attractive materials for hydrogen storage.

The wide ranges of experimental hydrogen uptakes determined on carbon based materials have been reported in the literature, scattering from negligible to extremely high. Some of the best results are presented in Table 2.6 and more detailed description will be given below.

Table 2.6: Summary of the best hydrogen storage capacities obtained on carbon based materials.

material	surface area, a_s / m^2 g^{-1}	hydrogen uptake, n_a/ %wt	operation conditions (p and T)	References
polypyrrole-based-KOH activated carbon	3500	7.0*	20 bar, 77 K	(Sevilla et al., 2011)
ZTC CB850h	3150	6.9*	20 bar, 77 K	(Yang et al., 2007)
MWCNT	—	6.3**	148 bar, 238 K	(Hou et al., 2002)
Zr-CDC-KOH-900	2447	6.2*	20 bar, 77 K	(Sevilla et al., 2010)
AX-21	2780	5.2*	40 bar, 77 K	(Weinberger and Lamari, 2009)
SWCNT	—	3.3	1.3 bar, 77 K	(Ioannatos and Verykios, 2010)
MWCNT	—	2.29	16 bar, 298 K	(Ioannatos and Verykios, 2010)

*excess
**absolute

Activated carbons are of great importance for hydrogen physisorption, because they are cheap and accessible for large commercial scale, moreover they represent large structural complexity and heterogeneity. There has been much research on hydrogen sorption into activated carbons and one popular example is superactivated AX–21, proposed as a benchmark to fully meet DOE targets (Anton and Motyka, 2011). This highly microporous carbon exhibiting a high BET surface area of 2780 $m^2 g^{-1}$ can reach up to 5.2 wt% hydrogen uptake at 77 K and 40 bar. See reference (Weinberger and Lamari, 2009) for a comprehensive listing of observed hydrogen storage capacities for AX–21. The remarkable hydrogen uptake of 7.03 wt% translated to 37 g H_2 L^{-1} (at 77 K and 20 bar) was recently reported on ultrahigh surface area (3000–3500 $m^2 g^{-1}$) polypyrrole-based one-step KOH activated carbon (Sevilla et al., 2011).

Another class of promising carbon nanostructures for hydrogen sorption are carbon nanotubes. Depending of the wall structures carbon nanotubes can be found in two different forms: single walled carbon nanotubes (SWCNT) and multi walled carbon nanotubes (MWCNT) (Darkrim et al., 2002). SWCNT typically consist of a graphene sheet rolled up into a cylinder of a few nanometers diameter and several microns length, while MWCNT are an arrangement of coaxial tubes of graphite sheets ranging in number of 2–50, where the carbon atoms are ordered in a helical fashion along the tube axis (Darkrim et al., 2002). MWCNT have diameters from a few to a few tens of nanometers and length of 1 μm (Darkrim et al., 2002). Initial optimism have been given to solve the hydrogen storage problem, by Dillon et al. in 1997 (Dillon et al., 1997), who appeared to show that SWCNT can potentially store up to 10 wt% of hydrogen at ambient temperature. Soon after it was shown (Hirscher et al., 2001) that the disparity observed in the Dillon report was due to sample impurities, such as cobalt catalyst and amorphous carbon in the SWCNT structure. Hydrogen storage in carbon nanotubes is still of interest, however despite initial excitement regarding high capacities reported in the literature recent studies show that the maximum hydrogen storage capacities are of the order of 4 wt% at 77 K and less than 1 wt% at ambient tempertaure (Poirier, et al., 2004, Panella, et al., 2005). Graphitic nanofibres are another group of carbon nanostructures studied extensively for hydrogen storage. The nanofibres consist of graphene layers ordered in parallel, perpendicular or intermediately angled (so-called herringbone)

configurations depending on the fibre axis (Yurum et al., 2009). Carbon nanofibres display remarkable hydrogen storage capacities even at ambient temperature (Chambers et al., 1998, Browning et al., 2000, Gupta et al., 2000), but again probably due to impurities present in the fibres, which typically correspond to the catalyst from fibre synthesis (Yurum et al., 2009).

Graphene is another candidate that can be considered for hydrogen storage processes (Tozzini and Pellegrini, 2013). Graphene is a two-dimensional, one-atom thick crystal composed of carbon atoms, which are arranged in a honeycomb geometry, and it possesses extraordinary properties, including strength, flexibility and electronic conduction (Tozzini and Pellegrini, 2013). The properties of graphene make it an ideal material with many applications and particularly interesting candidate for hydrogen storage. According to Tozzini et al., (Tozzini and Pellegrini, 2013) if only a monolayer of hydrogen is formed on the surface of graphene, the gravimetric hydrogen capacity of 3.3 wt% (at low temperature and high pressure) can be obtained, which can be doubled if the two sides of the graphene are considered. Evidently the hope lies in synthesis of novel three-dimension nanostructured materials with tailored porosity, such as pillared graphene which additionally doped with lithium ion can reach hydrogen storage capacity of 7.6 wt% (70 g L^{-1}) at 77 K and 100 bar pressure, as predicted from Grand Canonical Monte Carlo simulations (Dimitrakakis et al., 2008).

Templated carbons are also of interest to store hydrogen. These materials are created via introducing a carbon precursor (such as sucrose or acetonitrile) into pores of an inorganic template, and its later removal to obtain the well defined pores structure. To date, the highest hydrogen storage capacity of 6.9 wt% (at 77 K and 20 bar), with estimated maximum around 8.33 wt% for was reported a zeolite templated carbon by Yang et al., (Yang et al., 2007). Another type of templating materials are so called carbide-derived carbons (CDCs), synthesised from carbide precursors (such as SiC, TiC, Mo_2C, VC). These materials are very valuable for hydrogen storage, since have the microporous structures with very well defined pore sizes (Gogotsi et al., 2005, Gogotsi et al., 2009). As reported by Gogotsi et al., (Gogotsi et al., 2009) the CDCs can display hydrogen capacities of 4.7 wt% at 60 bar and 77 K, but its potential is expected to be much higher.

2.6.2 Zeolites

Zeolites are a type of highly crystalline aluminosilicate (or aluminophosphate) frameworks that posses well defined pore structure (typically between 0.3 and 1.5 nm) and large internal surface area (> 1000 m^2 g^{-1}) providing prominent candidates for many applications. These cheap, highly stable materials are widely used in fundamental research and industrial processes mainly for the gas sorption, separation, ion exchange, purification and catalysis. Typically, the experimental hydrogen storage capacities obtained on zeolites are found to be < 2 wt% at cryogenic and < 0.3 wt% at ambient temperatures (Weitkamp et al., 1995). For example, Zecchina et al. (Zecchina et al., 2005) reported the hydrogen uptake of 1.28 wt% at 77 K and around 1 bar on the H-SSZ-13 zeolite. Also it was reported that at cryogenic and 15 bar conditions, a Ca exchanged X zeolite can physisorb up to 2.19 wt% of hydrogen (Regli et al., 2005, Langmi et al., 2005). However, even at 60 bar ambient temperature hydrogen uptake on zeolites is still less than 0.5 wt% (Kayiran and Darkrim, 2002). These results suggest that zeolites themselves are not likely to be a material of choice for practical hydrogen storage. However, they can be ideal materials for systematic studies of hydrogen binding to a large variety of metal cationcenters, and those studies could inform and guide for other hydrogen adsorbent systems.

2.6.3 Organic Polymers

Organic polymers, such as Polymers of Intrinsic Microporosity (PIMs), Hyper-crosslinked Polymers (HCPs) and Covalent Organic Frameworks (COFs) are another type of interesting materials for reversible hydrogen storage. PIMs are fused-ring, rigid but controlled polymers that cannot fill space efficiently and create enclosed interconnected cavities with large surface area of about 500–1100 m^2 g^{-1} (McKeown and Budd, 2006, Budd et al., 2007). The maximum hydrogen capacity value of around 2.71 wt% (at 77 K and 10 bar) was reported for a triptycene-based polymer (trip-PIM) (Budd et al., 2007). HCPs are highly rigid cross linked polymers with small pore volumes and high surface areas, ranging from 700 to 1500 m^2 g^{-1} (Dawson et al., 2012). HCPs are capable to adsorb of 3.04 wt% of hydrogen at 77 K

and 15 bar (Lee et al., 2006). Covalent-Organic Frameworks (COFs) are crystalline networks formed in similar way as MOFs but instead metal centre incorporate light elements (such hydrogen, boron, carbon, oxygen and silica), that are linked by strong covalent bonds (Cote et al., 2005). The highest surface areas COFs, named COF-102 (3620 m^2 g^{-1}) and COF-103 (3530 m^2 g^{-1}) are capable to adsorb respectively 7.16 wt% and 6.98 wt% (at 77 K and 40 bar), respectively (Furukawa and Yaghi, 2009).

2.6.4 Metal-Organic Frameworks (MOFs)

Metal-Organic Frameworks (MOFs) are porous crystalline materials consisting of metal ions or small metal-containing clusters joined by organic linkers (Rowsell and Yaghi, 2004, Rosseinsky, 2004). Similar to zeolites, most MOFs have a three-dimensional framework that encloses uniform pores which are inter-connected forming an ordered network of channels. MOFs are synthesized by a self assembly process in which different combinations of organic linkers and metal centres lead to materials having a wide range of porous characteristics (Rowsell and Yaghi, 2004). After removal of retained solvent from synthesis, MOFs can exhibit a very high surface area, making them ideal candidates for hydrogen storage. Values in the range of 1500–3000 m^2 g^{-1} are typical, but even values higher than 6000 m^2 g^{-1} were reported for some MOFs (Furukawa et al., 2010). MOFs pore volume usually ranges from 0.2 to 0.8 cm^3 g^{-1}, but values over 1.1 cm^3 g^{-1} were also reported (Collins and Zhou, 2007, Wong-Foy et al., 2006, Latroche et al., 2006). Outstanding BET surface areas and pore volumes give MOFs considerable potential as hydrogen storage media. In contrast to activated carbons, MOFs have well-defined crystal structures, resulting in a system of uniform pore sizes (about 0.5–2 nm) for each particular material.

Moreover, the wide range of possible topologies and chemical composition holds the promise for rational design of chemical synthesis aimed at optimizing hydrogen adsorption properties. Some new approaches involve interweaving of isoreticular 3D networks and pillaring of MOFs (i.e., connecting two-dimensional layers with appropriate pillars) (Eubank et al., 2011). As also found for carbons, maximum

hydrogen capacities (at 77 K) in MOFs are approximately proportional to surface area and microporous volume (Rowsell and Yaghi, 2005) and that explains why initial experimental work is aimed at increasing these parameters. Table 2.7 summarises several promising metal organic framework materials for reversible, high capacity hydrogen storage at 77 K. For example, one of the highest value of excess uptake of 7.5 wt% (32 g L^{-1}) at 77 K and 70 bar was reported for MOF-177, which composed of Zn_4O clusters and 4,4',4"-benzene-1,3,5-triyltribenzoate (BTB) linker units (Furukawa et al., 2007). MOFs synthesized from carboxylate ligands, such as MOF-5 based on the octahedral Zn-O-C clusters with 1,4-benzene-dicarboxylate (BDC) also show high excess hydrogen capacity of 7.1 wt % at 77 K and 40 bar (Li et al., 1999, Kaye et al., 2007, Yaghi et al., 2003). From a series of isoretricular MOFs, IRMOF-20 derived from linking $Zn_4O(CO_2)_6$ units with various dicarboxylic acids, shows the highest uptake on volumetric basis of 34 g L^{-1} (6.7 wt%) at 77 K and 80 bar (Wong-Foy et al., 2006). However, one of the most promising results have been reported for MOF-210, which consists of $Zn_4O(CO)_6$ groups joined with BTE/biphenyl-4-4-dicarboxylate (BPDC) linker, where BTE is 4,4',4"-(benzene-1,3,5-triyltris(ethyne-2,1-diyl))tribenzoate (Furukawa et al., 2010). The authors found that excess H_2 uptake of this MOF is 8.6 wt% (absolute 17.6 wt%) at 77 K and 80 bar. MIL-101, chromium and di- or tricarboxylates based MOF, outlined in Table 2.7 also shows a high excess hydrogen uptake of 7.1 wt% at 77 K and 80 bar (Latroche et al., 2006).

Table 2.7: Hydrogen sorption capacities for some promising MOFs at 77 K.

material	surface area, a_s / m^2g^{-1}	pore volume, v_p/ cm^3g^{-1}	hydrogen uptake, n_a/ wt% (T, p)	References
MOF-177	4630	1.69	7.3 (77 K, 52 bar)	(Chae et al., 2004), (Furukawa et al., 2007)
Mn(btt)	2100	0.80	6.9 (90 bar)	(Collins and Zhou, 2007)
IRMOF-20	4580	—	6.7 (70 bar)	(Wong-Foy et al., 2006)
MIL-101	4230	2.15	6.1 (77 K, 80 bar)	(Latroche et al., 2006, Llewellyn et al., 2008)
MOF-5	3800	1.55	7.1 (77 K, 40 bar)	(Yaghi et al., 2003, Kaye et al., 2007)
Cu-BTC	2175	0.75	3.6 (10 bar)	(Collins and Zhou, 2007)
IRMOF-11	2180	—	3.5 (34 bar)	(Wong-Foy et al., 2006)
MIL-100	2800	1.0	3.28 (26 bar)	(Collins and Zhou, 2007)
MOF-210	6240	3.6	8.6 (77 K, 80 bar)	(Furukawa et al., 2010)

In summary, it should be recognized that, despite the huge efforts being put into developing promising materials for hydrogen storage, there is no storage system so far that fully meet DOE requirements for light-duty vehicular use. Therefore, there is a need to develop materials with an improved hydrogen storage performance.

2.7 Accuracy of Physisorption Measurements

As discussed in the previous section, hydrogen storage via physisorption has received much attention as a competitive medium for on-board hydrogen storage applications. However, some promising results reported in the literature were disputed due to problems with data reproducibility between different laboratories (Dillon et al., 1997, Chambers et al., 1998). In most cases, the observed disagreement was caused by experimental errors involved in both analytical procedures and instruments calibration, but also lack of fundamental understanding of the hydrogen physisorption mechanism. To address this point, a number of reviews and best practices were published, all hoping to guide the research efforts to reliably determine hydrogen uptakes (Gross, 2012, Broom, 2011, Broom and Moretto, 2007, Zhang et al., 2004, Blackman et al., 2006, Tedds et al., 2011, Morris et al., 2013, Gross, 2008). Particularly, there is still a great importance to examine measurements accuracy and to define more rigorous criteria on how to monitor the performance between individual laboratories. To address this point, there is a new DOE Hydrogen and Fuel Cell Program requirement under development, which states the following: "Capacity measurements for hydrogen-storage materials must be based on valid and accurate results to ensure proper identification of promising materials for DOE support" (Parilla, 2012). This means that the precision of the testing procedures becomes more important, particularly in aspect of preventing confusion and wasting research time and money.

A useful way to check accuracy of experimental results and to establish measurements standards is by performing an interlaboratory study (also known as round robin tests), where the experimental method on the chosen sample is compared between different labs. There is description of round-robin hydrogen sorption into SWCNT and activated carbon samples (at 77 K and RT and up to 70 bar), mentioned

by Ahn et al., (Ahn, 2005), but this exercise has not been published yet. Furukawa et al., (Furukawa et al., 2007) have proposed MOF-177 as a useful benchmark for high pressure hydrogen sorption at 77 K, but these results have not been validated by interlaboratory study. As far as we know, there is only one publication reported in literature of an interlaboratory study in hydrogen physisorption, and it is the one reported by Zlotea and co-workers (Zlotea et al., 2009, Moretto, 2010). However, the reported results shown remarkable scatter in both 77 K and ambient temperature hydrogen sorption data obtained on the microporous Takeda (CMS 4A) carbon, over 14 labs (see Figure 2.13). The authors concluded that the disparity seen in the data could be very likely because of procedural errors (gas leakage, analysis conditions, thermodynamic equilibration and different equations of state), operator errors (hydrogen impurities, dry mass inaccuracy) and equipment calibration (buoyancy and sample volume) (Zlotea et al., 2009). These results clearly underscore the importance of more reliable procedures and standards to ensure hydrogen sorption data quality. In the public domain, standard materials and methodology for determining hydrogen sorption are not available, however we aim to address this in this work as a useful contribution to progress in study of materials and methods for hydrogen storage.

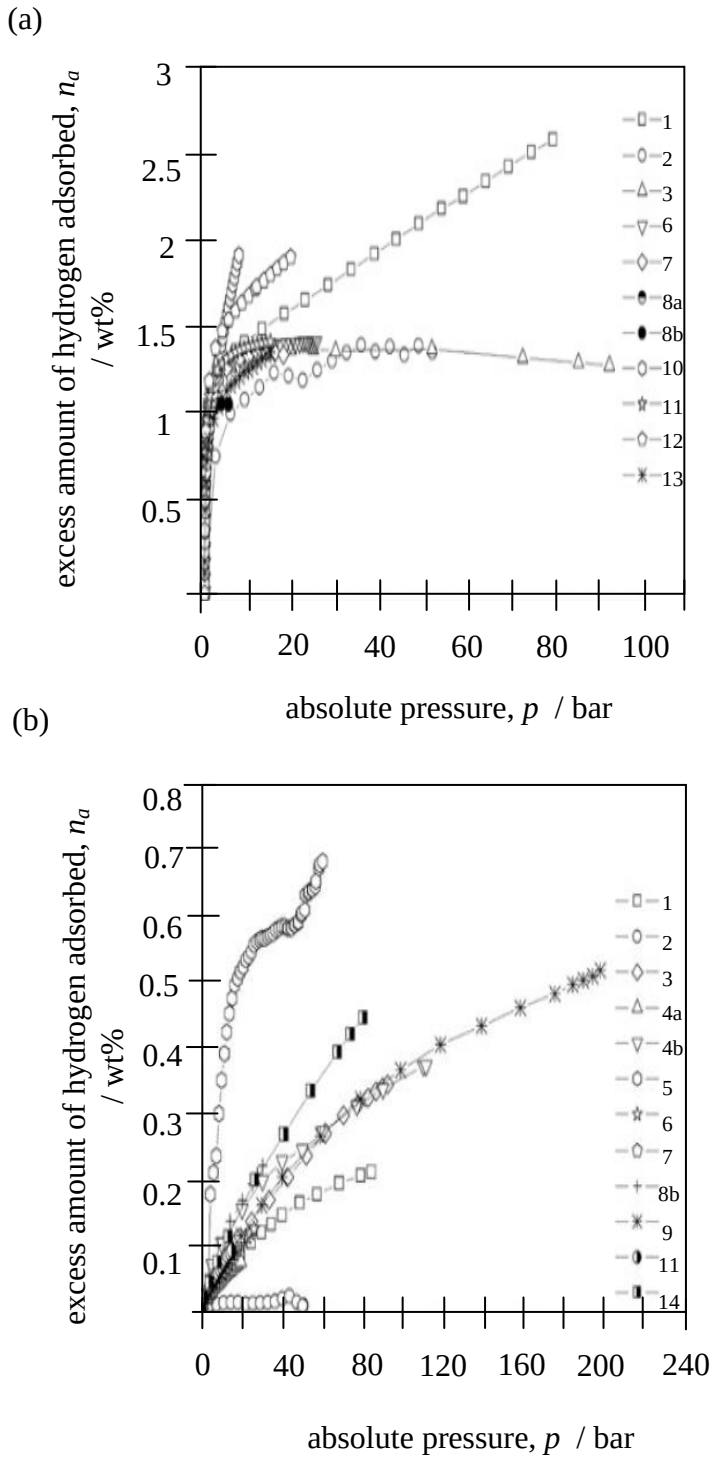

Figure 2.13: Excess hydrogen adsorption isotherms at 77 K (a) and ambient temperature (b) measured on Takeda (CMS 4A) carbon, while interlaboratory study reported by Zlotea et al. Adapted from (Zlotea et al., 2009) with kind permission from International Association of Hydrogen Energy.

2.8 Aims and Objectives of Research

The successful implementation of promising DOE hydrogen storage materials requires standards development based on accurate and validate measurements. To address this point the main aim of this thesis is to contribute to the development of new standards by providing relevant experimental procedures for analysis and validation of hydrogen storage measurements into nanoporous materials at 77 K. To achieve this aim the following objectives are set:

(1) Measurements comparison

In order to cover the issues related to qualitative measurements firstly we will undertake a series of standard experimental procedures to obtain key structure characteristic of potential benchmarking materials which later will be used as a subject of interlaboratory comparison. Secondly, we will improve data collection and analysis methods in order to provide the most accurate hydrogen storage capacities at 77 K. This mainly includes use of both volumetric and gravimetric procedures which allows us to discover and correct the main sources of experimental errors. Then we will analyse for reversibility and reproducibility on different gas sorption devices available in-house giving initial proof of the new methodology robustness.

(2) Measurements validation

As the hydrogen sorption methodology will be optimised we will intend to extend our work in the collaboration with external laboratories (including both academia and industrial organizations). This will be necessary to check method validity and analytical performance of our laboratory. Especially for this program we will set up the experimental protocols for reference sample preparation and analysis, which should be reproduced with extra care to yield small uncertainty in the collected data. The final results will be carefully inspected using statistical criteria to access reproducibility. Possible causes of variability will be identified and corrected.

Experiments planed under interlaboratory program include:

i) Low pressure (up to 1 bar) 77 K nitrogen sorption isotherms which will be analysed to yield the BET surface area and DR micropore volume.
ii) Low and high pressure (up to 200 bar) 77 K hydrogen sorption isotherms which will be analysed to yield hydrogen sorption capacities over the range of pressures.

(3) Measurements implementation

Based on the interlaboratory exercise we will make the final conclusion and recommendation for measurements improvement. A straightforward, universal procedure that allows routine hydrogen sorption checks on the similar materials type along different laboratories will be defined.

CHAPTER 3

EXPERIMENTAL DETAILS

3.1 Introduction

In this chapter all experimental techniques used to characterise the selection of nanoporous materials and to investigate their hydrogen storage properties are given. This refers to the instrumentation, methodology and calibration tests made to improve experimental data accuracy and quality. The chapter opens in Section 3.2 showing a range of the nanoporous materials, such as activated carbons, zeolites and metal organic framework judged to be suitable reference in future interlaboratory study. This is followed by description of the experimental techniques and procedures used to study materials structural properties (Section 3.3). These include the thermogravimetric analysis used mainly to determine materials stability and purity, but also to check the moisture content (Section 3.3.1). Then the chapter continues with a description of the helium pycnometry experiments used to obtain the skeletal density data necessary for free space and the buoyancy isotherms corrections (Section 3.3.2). The next stage of the research involves the scattering and transition electron microscopy study (Section 3.3.3) necessary to investigate materials morphology and to get first insights of present porosity. The energy dispersive X-ray spectroscopy (EDX) combined with the SEM equipment is also applied in this study to indentify materials elemental composition and support purity results. Several gas adsorption techniques including low/high pressure volumetry and high pressure gravimetry are employed to predict material hydrogen sorption capacities but also to examined porosity and accessible internal surface area (Section 3.4).

3.2 Materials Selection

A series of commercial nanoporous samples including activated carbons, zeolites and metal organic framework are selected and analysed in this study for the purpose of becoming a reference material as an important tool to validate hydrogen storage methodology. These materials are used because they represent a wide range of porosity, particle sizes, structural and surface characteristics, purity and composition. More information on each of the studied sample is described in the following Section 3.2.1, Section 3.2.2 and Section 3.2.3, summarised in the Table 3.1.

3.2.1 Activated Carbons

Four types of carbon based materials were acquired for this study. The first one represents the series of TE 7 (denoted as TE 7 I, TE 7 II and TE 7 III) activated carbon beads samples, supplied by MAST Carbon, UK. These carbons are derived from phenolic resin through a multistage process in which the resin is firstly carbonized and then activated at 750 ^{o}C in a steam atmosphere to produce microporous NOVACARB^{TM} structure. These carbons could be particularly interesting for this study because they have mechanical strength and high sorption capacities as well as high purities (eg., ash content of 0.67 ± 0.06 wt% for TE7 III sample, see Section 4.2.1.1). These materials are also been selected because they represent a wide range of structure characteristics, particularly interesting for hydrogen sorption applications. As specified by the manufacturer, TE 7 carbon beads are around 250–500 μm in diameter and have a BET surface area of 1100 (±100) m^2 g^{-1} with uniquely structured bimodal micropores of around 0.8 nm diameter and mesopores in the range of 15–300 nm. The beads have a typical bulk density of 0.4 g cm^{-3}, a typical pore volume of 1.23 cm^3 g^{-1} and are thought to be mainly amorphous in structure. The second carbon sample acquired for this study is Darco® activated carbon powder supplied from Sigma-Aldrich. This carbon is known to have a 100 mesh particle size (149 μm diameter), an ignition temperature of 450 °C, a bulk density of 0.25–0.60 g cm^{-1} and an ash content of around 3.5 wt%. Also this carbon is derived from a peat-bog source, is acid washed and is a commercial

product used to clean contaminants from air. The last two carbons, Respcarb-AR1 and Solcarb-607c are both granular activated carbons from the Chemviron Carbon Service. Respcarb is derived from coconut shells and is mainly applied for the removal of gases. Solcarb is used for catalytic purposes.

3.2.2 Zeolites

Two zeolites type were chosen for testing, both of the synthetic, 12-ring faujasite type (average particle size of 0.1-15 μm) (Zeolites, 2010). The first is a type of molecular sieve zeolite called 13X (type-X), made by Supelco. It is a pale-yellow powder with the chemical formula $Na_{86}[(AlO_2)_{86}(SiO_2)_{106}]\cdot 264H_2O$, is of 100/120 mesh size (125–149 μm) and has a thermal stability range of 600–800 °C (see Supplementary Information, S9) (Musyoka et al., 2013, Akbar et al., 2005, Steen et al., 2004). 13X's SiO_2/Al_2O_3 ratio is noted to be 2.0–3.0 and its pore sizes to be 0.74 nm (Zeolites, 2010). The second material is called Sodium-Y (type-Y) and is made by Sigma-Aldrich. Sodium-Y is a white powder in appearance. The general formula for this zeolite is noted as $Na_{56}[(AlO_2)_{56}(SiO_2)_{136}]\cdot 250H_2O$, its SiO_2/Al_2O_3 ratio is 3.0–6.0 and its pore aperture is 0.74 nm (Broach et al., 2000).

3.2.3 Metal Organic Framework

The metal organic framework (MOF) acquired for testing is called Basolite^{TM} C300, known as Cu-BTC (copper benzene-1,3,5-tricarboxylate), it is made by BASF and supplied by Sigma-Aldrich. It is a fine powder and is bright blue in appearance. Its chemical formula is $C_{18}H_6Cu_3O_{12}$, its molar mass is 604.87 g mol^{-1}, its claimed particle size is 15.96 μm, its bulk density is 0.35 g cm^{-3} and its BET surface area is in the range 1500–2100 m^3 g^{-1}. It has limited thermal stability up to 220 °C (Harvey, et al., 2011).

Table 3.1: Summary of physical property data for all tested nanoporous samples provided by materials suppliers.

material class	commercial name	supplier	precursor	activation conditions	particle diameter, x_d / μm	bulk density / g cm^{-3}	BET specific surface area, a_s / m^{2}g^{-1}	moisture m_{ad} / wt%	ash* a_{db} / wt%
TE 7	TE 7, Novacarb	Mast Carbon	phenolic resin	750 °C steam activated	250-500	0.3-0.4	1100	—	—
Respcarb	Respcarb™ AR grade product	Chemviron Carbon	coconut shell	N/A	1200	0.42	1420	4	3
Solcarb	Solcarb™ 607C 6X12	Chemviron Carbon	coconut shell	800 °C steam activated	2400	0.5	1100	3	1
Darco	Darco®G60	Sigma-Aldrich	charcoal	steam activated	100 mesh	0.25–0.6	600–900	—	3.5
Y-Zeolite	Molecular Sieves catalyst support, sodium Y Zeolite powder	Sigma-Aldrich	N/A	N/A	(7–94 mesh)	—	900	—	—
13X	Molecular Sieves 13X	Supelco	N/A	273–400 °C	125–149	—	600	—	—
Cu-BTC	Basolite®C300	Sigma-Aldrich	N/A	160 °C vacuum	16	0.35	1500–2100	—	—

*dry basis
N/A = not applicable

3.3 Materials Characterisation

3.3.1 Thermogravimetric Analysis

In this study, Thermogravimetric Analysis (TGA) was used to investigate weight loss, with the method involving the weight change as a function of temperature and time under a controlled atmosphere of flowing gas. Measurements are primarily used to determine the thermal decomposition of studied materials and predict their thermal stability at temperatures up to 1000 ^{o}C. Furthermore, the detailed analysis of the thermal profile is applied to calculate the ash and moisture content presented in its nanoporous structure. The apparatus used in this work is a Setaram TG-92 thermogravimetric analyser. The schematic cross-sectional diagram and design layout of the TGA rig is shown in Figure 3.1 and Figure 3.2 respectively.

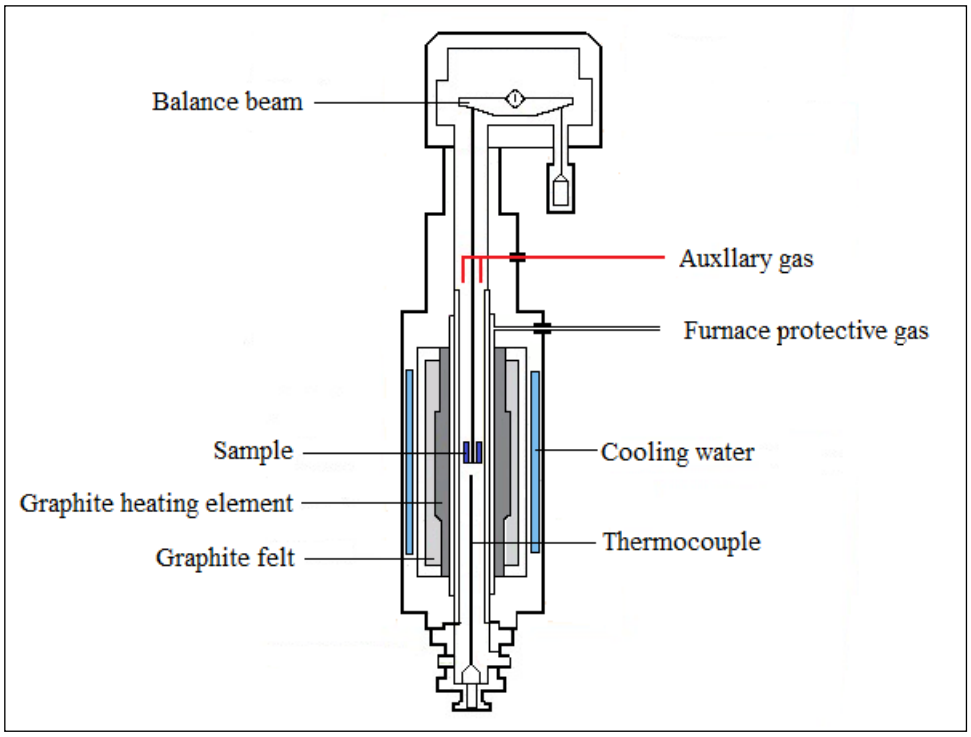

Figure 3.1: Schematic diagram of the Setaram TG-92 microbalance system.

The thermogravimetric analyser consists of a microbalance with hanged reference and sample pan, furnace, gas circuit and computer with Setsoft2000 software installed for data output and manipulation. The sensitive microbalance is a beam type and operates based on the null-balance principle. At the zero position, equal amounts of light shine on the two photodiodes. If the balance moves out of the null position an unequal amount of light shines on the two photodiodes. A certain amount of current is applied to the meter to return the balance to the zero position. The amount of the applied current is proportional to the weight loss. The cylindrical furnace is fitted with a graphite heating element operating from ambient to 1750 ^{o}C. Graphite felt sleeves insulate the heating element and the protective gas (argon) flowing in the heating area secures the graphite heating element. Moreover, the furnace is cooled by water circulation to prevent overheating. A matched platinum/platinum-rhodium thermocouple pair embedded in the ceramic beams provides direct sample, reference and differential temperature measurements and a dual balance mechanism gives accurate weight loss readings.

Figure 3.2: Design layout of the Setaram TG-92: A–microbalance housing, B–suspension, C–furnace, D–gas inputs, E–gas exhaust, F–suspension control lever, G–water flow-meter and H–control computer.

The operational procedure is initiated by purging the system for about one hour with air or inert gas to remove traces of other residual gases. The microbalance is then raised from the furnace and a clean, dry 100 µL alumina crucible (5 mm diameter, 9.9 mm height) is fitted on to the balance head. After lowering the balance back into the furnace, the system is tarred to negate the mass of the empty crucible and then removed from the furnace chamber again. A portion of sample weighing approximately 12 mg is loaded into the crucible and then carefully replaced on the balance. The balance arm is lowered back into the furnace once again where it is left to equilibrate. At this stage, the thermal program is set up with a furnace heating rate of 10 ^{o}C min^{-1} from 25 ^{o}C to 1000 ^{o}C. When the analysis is started, air is injected into the system at a flow rate of about 25 ml min^{-1} and the sample weight change is measured till the maximum temperature is reached. The results of these measurements are given in Section 4.2.1.1.

3.3.2 Helium Pycnometry

A Micromeritics AccuPyc1330 helium pycnometer (Figure 3.3) was used to determine the skeletal densities necessary to correct adsorption isotherms for the buoyancy or free space volume effects. This instrument operates by detecting the pressure change resulting from gas displacement by a solid sample. Helium is the displacement gas of choice because as a very small molecule it penetrates into very fine pores at ambient temperature and near ambient pressure (around 1.35 bar). It is generally accepted that helium will not adsorb under these conditions, but there is dispute among researchers whether this is reasonable assumption (Malbrunot et al., 1997), which is also the subject of the study presented in Section 4.2.2.6 of this thesis.

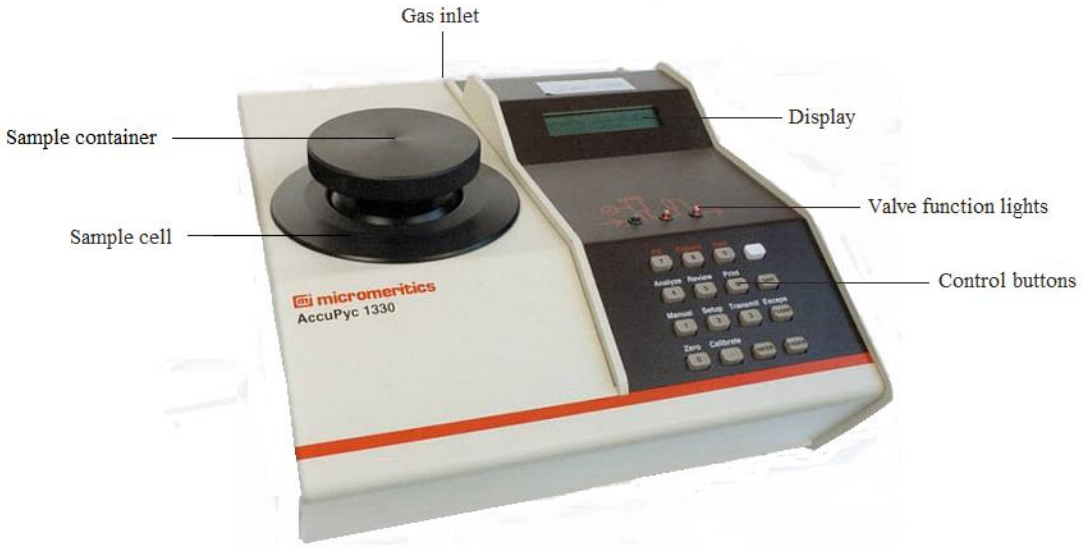

Figure 3.3: Design layout of the Micromeritics AccuPyc1330 helium pycnometer.

The helium pycnometry operational procedures used to test materials skeletal density are schematically illustrated in Figure 3.4. Where, the sample of unknown volume (V_s) is placed into a sealed sample cell of known volume (V_c). Then after sample cell sealing, the pressure inside the cell (P_c) is determined. An isolated reference cell of known volume (V_r) is charged to a pressure P_r, which is always higher than P_s. A value between two cells is opened and the pressure of the system (P_{sys}) is allowed to equilibrate. The ideal gas law, in the form of $PV = nRT$ is used to obtain of unknown V_s. The initial conditions can be described mathematically as follows:

$$P_c(V_c - V_s) + P_r V_r = nRT \tag{3.1}$$

where, P is the pressure of the gas, V is the volume of the gas, n is number of moles, T is temperature of the gas and R is the molar gas constant.

After the valve between the cells is opened, the conditions changed to:

$$P_{sys}(V_c + V_r - V_s) = nRT \tag{3.2}$$

This leads to following expression:

$$P_c(V_c - V_s) + P_r V_r = P_{sys}(V_c + V_r - V_s) \tag{3.3}$$

Where unknown sample volume is obtained from:

$$V_s = \frac{(P_{sys}V_c + P_{sys}V_r - P_c V_c - P_r V_r)}{(P_{sys} - P_c)} \tag{3.4}$$

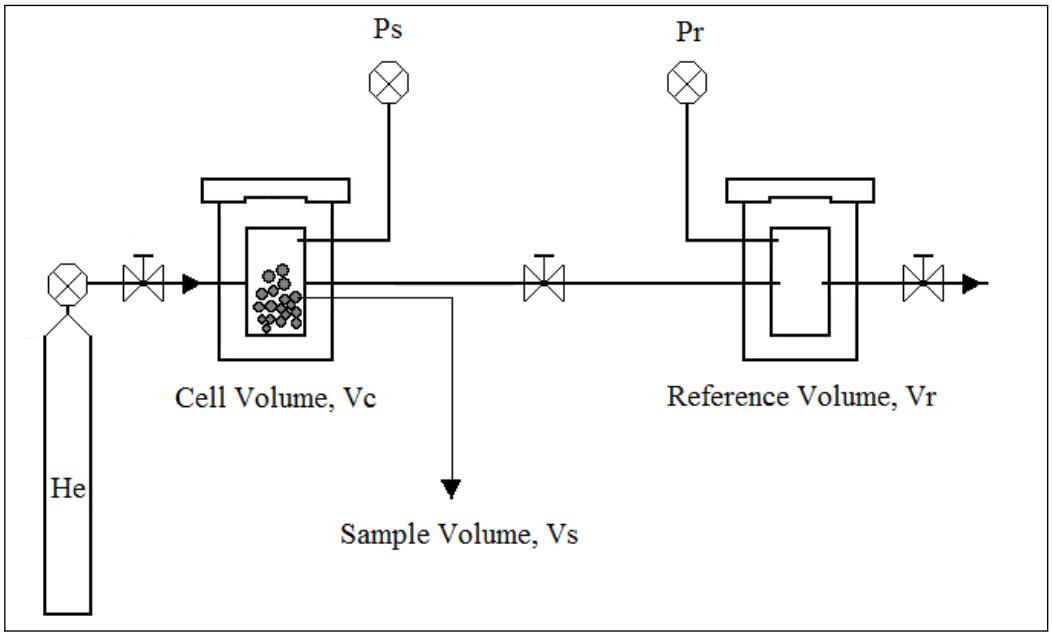

Figure 3.4: Schematic diagram illustrating the operational procedures used to determined skeletal density necessary to correct raw adsorption isotherms. Adapted from (Webb, 2001).

The transducer zero reset and the cell/expansion volumes calibration using reference steel balls having a total volume 6.3222 cm^3 are performed anytime pycnometer is restarted. Prior to the analysis, the tested material is pre-dried in a vacuum oven at 120 ^oC overnight and then left to cool in a dessicator. Then the sample is weighted on the external mass balance (to the nearest 0.0001 g) and

placed in the sample cell of the pycnometer to analyse. The sample volume is pressurised to 19.850 psig (1.35 bar) at 0.005 psig min^{-1} (0.7 bar min^{-1}) and the valve between the sample volume and reference volume is then opened. Using the pressure change between the sample and reference volume, the sample density is calculated. The measured density is the average value of 5 purge cycles followed by a 20 cycle run, which is calculated 20 times to obtain reliable results. A purge is used strictly for the sample and chamber clean up, resulting in elimination of water vapor and other contaminants. The obtained skeletal density data are essential for the buoyancy and dead volume corrections calculated for the data collected from the gravimetric and volumetric gas sorption measurements. These data are presented and discussed further in Section 4.2.1.2 of this thesis.

3.3.3 Electron Microscopy and Energy Dispersive X-Ray Spectroscopy

Both scattering and transmission electron microscopy analysis were performed to obtain more structure characterisation details of each studied sample. Scanning electron microscopy (SEM) is used to reveal information about the surface topology and morphology composition and was performed on a JEOL JSM-6480LV SEM apparatus. The schematic and basic diagram of the SEM operation is given in Figure 3.5. High energy electron beam emitted from an electron gun is focussed by one or two condenser lenses into a beam with a very fine focal spot. The electron beam passes through scanning coils in the objective lens that direct the beam into the area of sample surface. As the primary electrons strike the surface they are scattered by atoms in the sample. The electrons come from an electron gun filament targeted at the specimen inside a vacuum chamber. The beam is collimated by electromagnetic condenser lenses, focused by an objective lens and then swept across the specimen at high speed. The interaction between the electron beam and the sample generates secondary electrons. The electrons are processed and converted into electrical signal, but are only indicative of a single point on the sample. Then the signal is processed and displayed as an image. The intensity of the signal from the quality of secondary electrons is directly related to

the incident angle with the surface of the sample. The image observed reflects the topology of the sample.

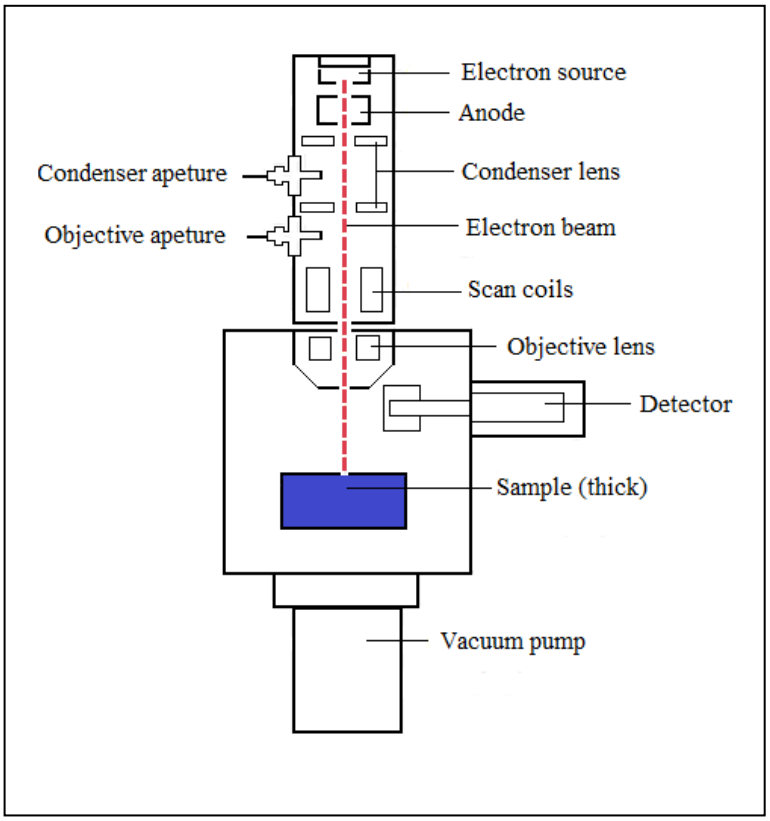

Figure 3.5: Basic schematic diagram of typical SEM system.

The SEM typically requires highly conductive samples, consequently the experiment is started with coating of non-conductive materials (like zeolites and metal organic framework) with gold to increase their conductivity. In the case of the activated carbon samples, which are very close to pure graphite (> 95 %) no gold coating is required and used. The sample is placed inside the microscope vacuum column through air-tight doors. The vacuum is necessary to minimalise interactions between the electrons and gaseous species, allowing for a focused beam of electrons. After the air is evacuated, an electron gun emits a beam of high energy electrons with the energy in the range of 100–50000 eV. This beam travels downward through a series of condenser lenses designed to focus the electrons to very fine spot size (1–5 nm). Near the bottom, a set of scattering coils moves the focused beam back and the forth across the surface of the sample. As electrons penetrate the surface, a number of interactions occur that result in the emission of electrons or photons from or through the surface. A detector counts these electrons

and sends the signal to an amplifier. The final image is built up from the number of electrons emitted from each spot on the sample. There are three principal images produced in SEM: secondary electron images, backscattered electrons images and elemental X-ray maps. Secondary and backscattered electrons are conventionally separated according to their energies. When the energy of the emitted electron is less than 50 eV, it is referred as a secondary electron and backscattered electrons are considered to be the electrons that exit the sample with the energy grater then 50 eV. Detectors of each type of the electrons are placed in the microscope in the proper position to collect them.

In order to optimise the picture quality at different magnifications, several variables are altered during the experimental study. The accelerating voltage and spot size are originally set at 15 and 25 kV respectively, but are optimised for each picture as well as the contrast, brightness and working distance.

Furthermore, energy dispersive X-ray spectroscopy (EDX) is used in conjunction with the SEM to determine the topography and chemical composition of the tested materials. When the electron beam bombards the sample, electrons are excited and ejected from their respective energy levels. This creates electron hole, which is then filled by an electron of a higher energy state, emitting an X-ray signal in the process. This X-ray signal (the energy difference between the higher and lower energy state) is specific to each element and the abundance of X-ray signals detected corresponds to the elemental composition of the sample (Materials Evolution and Engineering, 2010).

Additionally, to gain an even more refined picture of the tested samples, a Transmission Electron Microscope (TEM) is employed. The JEOL-JSM6480LV SEM can only achieve a maximum magnification of 300,000 times, where as a JEOL JEM-1200 EX II electron microscope can achieve a magnification of 500,000 times.

Prior to the TEM analysis, the tested samples were prepared by imbedding them in a resin and slicing into 100 nm thick sections. A TEM works on exactly the same principle as a light microscope but uses electrons instead of light. Like the

SEM, it too uses an electron gun and a series of electromagnetic lenses to focus a fine electron beam onto a specimen. But instead of electrons deflecting off the surface of the specimen, some of the electrons in a TEM can pass through the thin specimen. The transmitted electrons are then focused by an electromagnetic lens before hitting a phosphorous viewing surface at the bottom of the column. Electrons are invisible to the human eye, but when they strike the viewing screen they generate a visible photon, producing a 'shadow image' of the specimen with different areas displayed in different shades depending on their density. The TEM images can be then observed on a computer screen via a digital camera. The images obtained using these techniques are shown in Section 4.2.1.3.

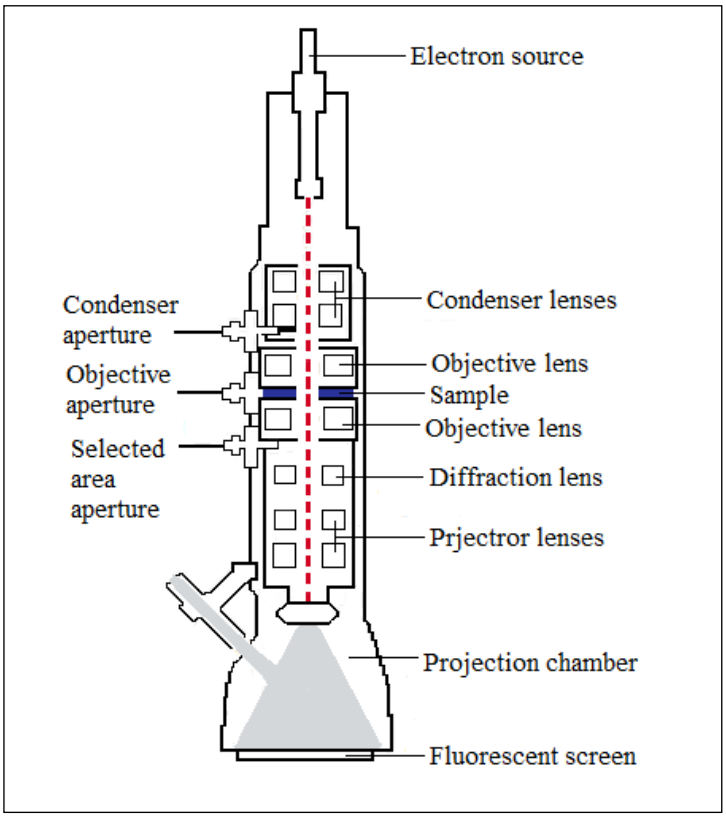

Figure 3.6: Basic schematic diagram of a typical TEM system.

3.4 Gas Sorption

The gas sorption characteristics of the investigated samples are measured gravimetrically and volumetrically using available in-house equipment. These different instruments are used firstly because this enables measurements to be made over different pressure ranges from very low vacuum (~ 10^{-6} mbar) up to 200 bar, and secondly this enables us to support and validate the findings from different apparatus and helps to predict data uncertainty.

3.4.1 Gravimetric Sorption

High pressure (up to 20 bar) gas adsorption measurements are performed using an Intelligent Gravimetric Analyser (IGA) supplied by Hiden Isochema Ltd., UK. The layout and a schematic representation of the IGA system are presented in Figure 3.7 and Figure 3.8 respectively. This instrument is an accurate microbalance system, which has a sample container hung against a counterbalance to monitor the sample weight change verses time at specific temperatures and pressures. The weight change is measured as a function of time and when the approach to equilibrium is established at the set pressure point, the pressure is increased to the next set pressure value and the subsequent uptake is measured until equilibrium is again established. It is important to note that in gravimetric sorption, the size of the sample determine the accuracy of the capacity measurement. In some cases accuracy can be improved by increasing the sample size (Gross, 2012). The IGA instrument used in this work has a microbalance calibrated for maximum capacity of 200 mg, with a resolution of around ± 0.1 μg, sufficient to perform accurate measurements on porous samples studied. However, if necessary the IGA microbalance can be easily set to run larger samples, by changing the counterweight configuration. Detailed, step by step recalibration procedure stated in the IGA user manual can be found in Supplementary Information, Section S11. Accurate control of gas pressure is achieved through the use of motorized inlet and outlet valves. A furnace or liquid dewar provides access to temperatures up to 500 ^{o}C (773 K) or as low as –196 ^{o}C (77 K). This

technique requires buoyancy corrections due to the sample and counterweight displacing different volumes of gas and sometimes being at different temperatures, which is discussed later in the Section 4.2.2 and Section 4.2.3 of this thesis.

Figure 3.7: Design layout of the Hiden IGA system: A–IGA main unit, B–thermostat, C–standard 500 ^{o}C furnace, D–liquid N_2 flask, E–analysis gas cylinder, F–liquid N_2 dewar, G–computer, H–purification system.

The operational procedure on the IGA begins with the loading of around 100 mg of tested material on the balance hangdown at ambient conditions. The reactor chamber is sealed and decontaminated overnight by evacuating the system to a very high vacuum. Then the reactor is purged with the analysis gas to ensure that no other gases or vapors remain in the system. The sample is outgassed using the combination of membrane and turbomolecular pumps at ramp rate of 30 mbar min^{-1} to about 10^{-6} mbar. The temperature is then increased to 350 ^{o}C with a ramp of 10 ^{o}C $min^{-1}$and any moisture and contaminants from the sample surface are removed. These conditions are maintained for 8 hours until the mass of the sample is established. The temperature and time duration were found to be reasonable based on the thermogravimetric analysis as described in Section 4.2.1.4. After the sample preparation is completed the sample is cooled to room

temperature and the dry mass is recorded. Measurements to produce a pressure composition isotherm are then performed, which consist of a series of adsorption/desorption pressure steps at the variable temperatures including 273 K, 87 K and 77 K. At each pressure steps the weight change is monitored a function of time and extrapolated to the asymptotic model using real-time analysis and allowed to reach equilibrium before moving onto the next pressure point. There are timing parameters that set a minimum and maximum equilibration time during the data collection at each pressure point. It should be kept in mind that no isotherm point can be collected until the minimum time which is set to 5 minutes elapsed. The maximum time out is set to 60 min for all collected isotherms ensuring true adsorption equilibrium as presented in Section 4.2.2.5. After all ad- and desorption pressure steps are completed, gas uptake is plotted against pressure. After each measurement is completed, the sample bucket was carefully flushed with air before loading the new portion of the sample. The buoyancy of the sample at each pressure is calculated by applying the Archimedes principle as given in Equation 3.5 below (Broom, 2011). The mass change due to buoyancy $f_{buoyancy}$ of the sample of density ρ_s and the mass m_s in a gas density ρ_g is given as:

$$f_{bouyancy} = m_s g\left(\frac{\rho_g}{\rho_s}\right) \tag{3.5}$$

where, g is the acceleration due to gravity.

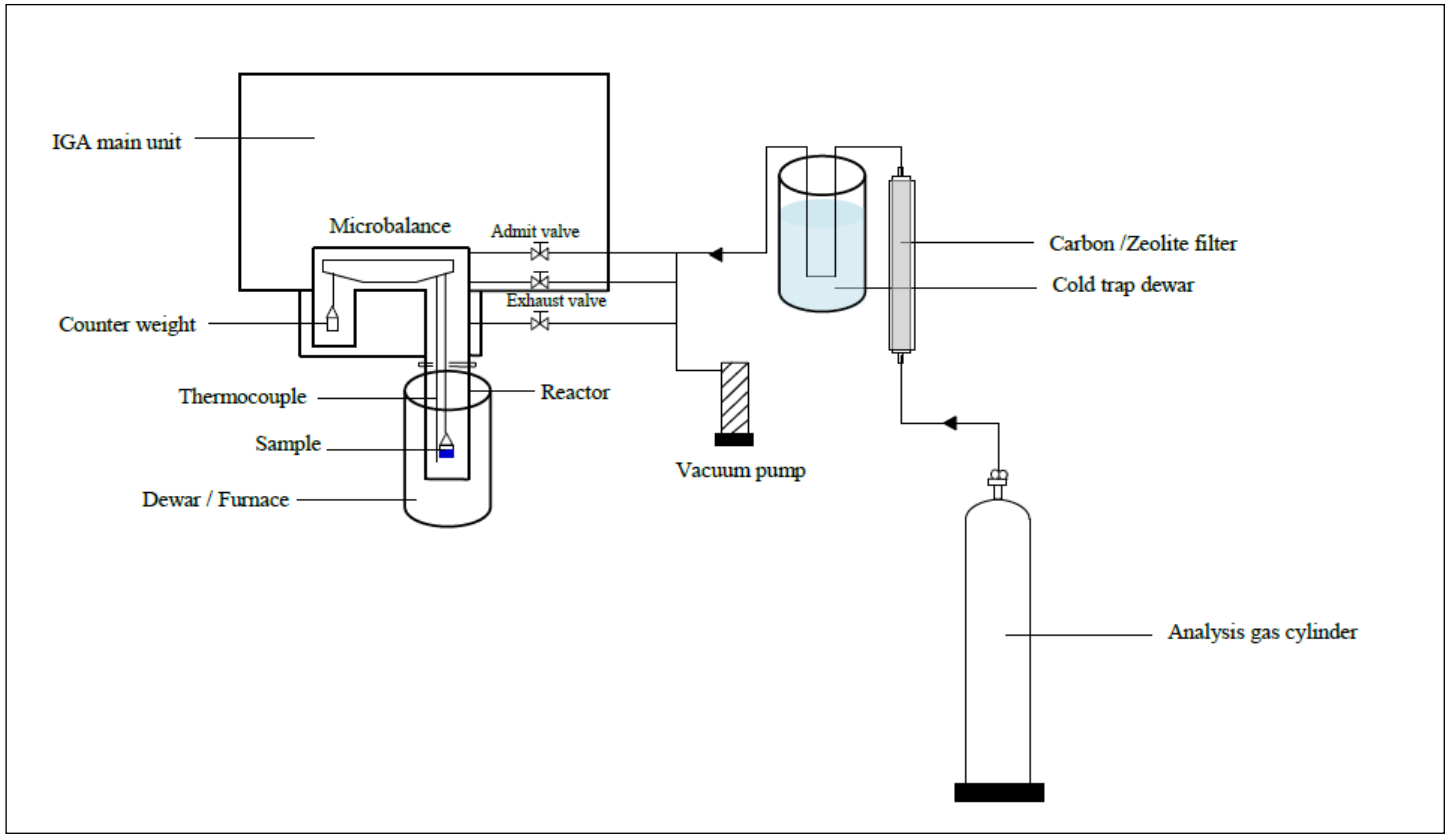

Figure 3.8: Schematic diagram of the Intelligent Gravimetric Analyser (IGA) system used in-house gas adsorption studies.

3.4.2 Low Pressure Volumetric Sorption

The low pressure (up to 1 bar) gas sorption isotherms were carried out using the Accelerated Surface Area and Porosimetry System (ASAP 2020) supplied by Micromeritics, Norcross, USA. The ASAP 2020 is an essential tool for providing very accurate surface area and porosity measurements on the wide variety of nanoporous samples. The system contains various data reduction methods to provide easy-to-interpret report options for each application and can be performed using physisorption and chemisorption analyses. It also allows an extended range of adsorptives, including vapors, to be used in adsorption/desorption analyses (ASAP 2020 Technical Information). It should be noted that only gaseous adsorptives and physisorption analyses will be performed in the context of this study.

The ASAP 2020 (see Figure 3.9) incorporates two independent vacuum systems, one for sample analysis and one for sample degassing. Having two separate systems, as well two degas ports, allows sample preparation and sample analysis to occur concurrently without interruption. Inline cold traps are located between the vacuum pump and the manifold in both the analysis and the degas systems. The sample saturation pressure tube is located next to the analysis port and allows to determine a saturation pressure and monitor the analysis temperature. Six gas inlet ports and cable connections are located conveniently on the side panel of the analyser for easy access.

Figure 3.9: Design layout of the Micromeritics ASAP 2020 system. Adapted from ASAP 2020 Technical Information, available at http://www.micromeritics.com/Repository/Files/ASAP_2020_Brochure_4.pdf as of April 2013.

A minimum of 100 mg of sample is weighed and loaded into the glass sample tube sealed with a Seal Frit stopper of known weight and connected to the sample degassing port for preliminary preparation. The sample is evacuated and degassed at 350 ^{o}C for 8 hours till vacuum (10^{-6} mbar) is reached. Any contaminant or moisture removed from the sample is condensed and collected in the cold trap which is filled with liquid nitrogen at –196 ^{o}C. After degassing is complete, the sample tube is backfilled with N_2 to return it to atmospheric pressure. The sample is then removed from the preparation port and weighed again to obtain its dry mass for subsequent data analysis. The sample is then moved to the analysis port where the adsorption process takes place. As the sample tube is initially under atmospheric pressure, the operator needs to manually control the valves to ensure that the pressure in the manifold is also under atmospheric pressure. Once equilibrated, the sample tube is evacuated and as before, the pressure is reduced to 10^{-6} mbar to obtain full vacuum conditions. During analysis the system will try to achieve a range of pressure points specified by the user by dosing known amounts of the adsorptive stepwise into the sample tube. When equilibrium is established at a

specified pressure point, the pressure is increased to the next set pressure value and the subsequent amount of gas adsorbed is measured until equilibrium is achieved again. The amount of adsorptive adsorbed is measured as a function of relative and absolute pressure for nitrogen and hydrogen respectively. Helium is used to measure the free space in the sample tubes needed for raw isotherm correction. The results from low pressure gas sorption experiments are presented in Section 4.2.2 and Section 4.2.3 of this thesis.

3.4.3 High Pressure Volumetric Sorption

The latest addition to the Hiden Isochema range of the gas sorption analysers is the High Temperature and Pressure (HTP-1) volumetric sorption system (Figure 3.10) specially designed for the measurement of hydrogen sorption in milligram quantities of the sample. The pressure/composition/temperature isotherms can be measured up to 200 bar at very wide ranges of sample temperature control from cryogenic –196 ^{o}C to 500 ^{o}C. Similar to the IGA system the equilibration kinetics are analysed by applying real-time analysis to ensure the best point by point accuracy of the collected data. The HTP-1 measures a pressure drop via a pressure transducer in a sealed volume. The apparatus comprises of two volumes, dosing and sample volume. During the experiment the dosing volume is filled to the programmed pressure and allowed to equilibrate. The valve between the dosing and the sample volumes is then opened and the pressure falls by approximately half due to the overall larger volume. Then the sample adsorbs the gas and the pressure continues to fall until reaching equilibrium. As the pressure, temperature and sample weight and volume are known, it is possible to determine the amount of gas adsorbed.

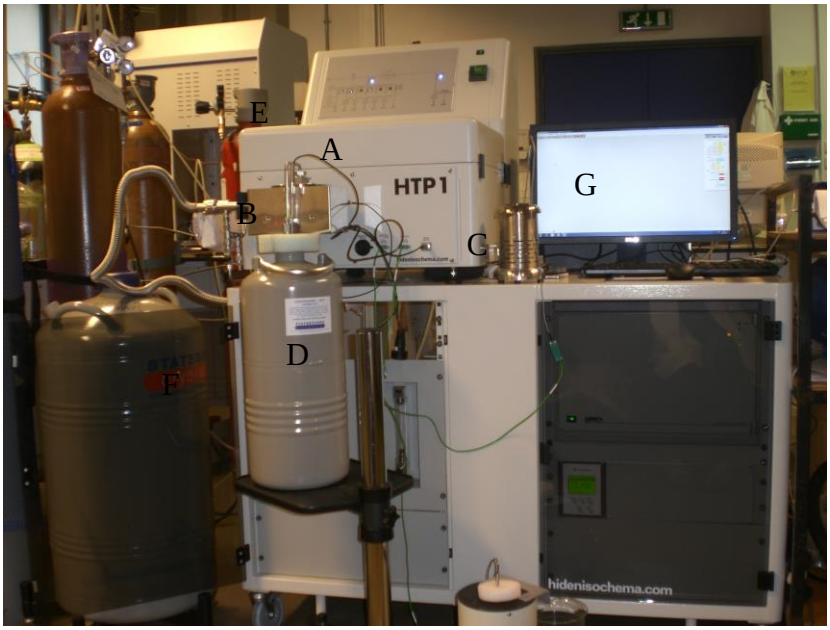

Figure 3.10: Design layout of the Hiden HTP-1 system: A–HTP-1 main unit, B–standard/immersion reactor, C–standard 500 ^{o}C furnace, D–liquid N_2 dewar, E–analysis gas cylinder, F–auto refiller, G–computer.

The typical experimental procedure is started with sample loading, where approximately 100 mg of the investigated sample is transferred into a previously tared sample container. A quartz wool plug (0.020 g) is placed above the sample in order to keep the material in place during the whole analysis. Then the fitted sample cell is placed in the reactor chamber and tightly sealed using a silver metal gasket face seal. High pressure (150 bar) helium is charged to the reactor volume and at least 100 min ambient temperature leak test is performed. After ensuring that there is no downward trend in the pressure response and the uptake does not change more than ± 50 µmol it is assumed that the system is leak free and ready to perform the analysis. Helium is then vented and the sample is outgassed at 10^{-6} mbar. The sample does not come in contact with the helium again, until all sorption isotherms are collected which prevents interference of residual helium. The furnace is placed in position around sample cell and temperature is raised to 350 ^{o}C (with a temperature ramp of 10 ^{o}C min^{-1}) and maintained for 8 hours. Afterward the furnace power is turned off, lowered from the sample cell and is allowed to cool to room temperature. In the case of the HTP-1 measurements all the corrections for the sample dry weight are input to the system at the end of analysis when the sample is unloaded. However it is an option to estimate outgassed weight from ex-situ

experiment and the preliminary dead volume by subtracting the sample volume from the empty system volume. All of these estimates must be verified and inputted with the direct values measured after the analysis is finished.

After the sample preparation is completed the sample volume is maintained under the vacuum and isolated from the reference volume. The furnace is changed to the liquid nitrogen dewar, ensuring that the level of the cryogenic liquid is always the same to ensure exactly the same thermal partition corrections. The HTP-1 handles this temperature gradient between the sample and pressure transducer through the fractional volume. The fractional volume calibration is determinate by analysing high pressure hydrogen isotherms performed on the empty calibration cell. The adsorption should be as close as possible to zero so dosing and sample cell volumes are modified using the fractional volumes. When the system is ready to perform the analysis the reference volume is filled with analysis gas to the pressure described for the first adsorption point. To ensure complete equilibration, the maximum time out is set up to 60 minutes for all collected isotherms. The procedure for desorption is similar, however the reference volume is vented and evacuated prior to each desorption step.

The final step of the analysis procedure is to confirm the estimated dead volume and the final degassed sample weight. When the analysis is completed, the sample is degassed again and the helium pycnometry at ambient temperature is performed. The reference volume is filled with 30 bar helium and after the pressure is stabilised the sample is exposed to the helium. Lastly, the sample is degassed again, the reactor chamber is disconnected under positive pressure, and the sample cell is removed and weighed to determine the accurate dry sample weight. The results obtained from high pressure HTP-1 gas sorption experiments are presented in Section 4.2.3 of this thesis.

CHAPTER 4

IN-HOUSE MATERIALS CHARACTERISATION: RESULTS AND DISCUSSION

4.1 Introduction

This chapter presents the results of in-house materials characterisation experiments carried out using methods described in Chapter 3. The results are organized into three main sections and illustrated using graphs and tables along with a detailed discussion on the most important findings. In the first part (Chapter 4.2) all important materials characterisation results with regards to purity, skeletal density, homogeneity, BET specific surface area and porosity are presented. The validity of the standard methods is discussed and some new approaches more suitable for the qualitative experimental data analysis are introduced. Secondly, in Chapter 4.2.3 the results of hydrogen adsorption properties in various nanoporous materials are analysed with a view to develop the most suitable adsorption system and experimental method for this application. This is followed by the results of testing main experimental variables such as equilibration time, data corrections, gas purity and sorption kinetics affecting adsorption process.

4.2 Investigation of Reference Material

In order to explore the potential methodology for hydrogen storage via physisorption a comprehensive in-house study based on structural and surface characteristics of the potential nanoporous material standards is undertaken. A full range of standard experimental procedures including thermogravimetry, helium pycnometry, SEM imaging and gas sorption analysis are applied. The particular focus is on the selection of the appropriate reference material, which will contribute to successful validation of hydrogen sorption methodology. In this approach various commercially available nanoporous materials including activate carbons, zeolites and metal organic framework systems are investigated. The most important aspects and challenges associated with their structure characteristics and hydrogen sorption performance are discussed. Please note that in these sections an appropriate selection of graphs in the text is provided. The full data sets are contained in Supplementary Information, Sections S1–S6.

4.2.1 Materials Characterization Results

4.2.1.1 Moisture and Ash Content

Thermogravimetric analysis (TGA) as described in Chapter 3.3.1 is used to determinate the moisture and ash content present in each investigated sample. The assessment of these components provide the initial direction for the degassing conditions necessary for sorption analysis and give a quantitative estimation of impurities which might be present in the particular sample. Please note that term ‘ash’ used here refers to the residual matter left behind after a specific thermal treatment.

In this work, the amount of moisture content is determined according to the British Standard method (BS), (BS, 2011) where essentially, a sample of known mass is dried at

105 ^{o}C over of period of 60 minutes under nitrogen atmosphere. For each determination, the moisture content, m_{ad} is calculated from the mass loss using Equation 4.1:

$$m_{ad} = \frac{(m_2 - m_3)}{(m_2 - m_1)} \times 100\% \tag{4.1}$$

where, m_1 is the mass of the empty crucible, m_2 is the mass of the crucible plus sample before drying and m_3 is the mass of the crucible plus sample after drying. Also of note, some materials are very hydrophobic and the moisture content may vary according to the sample conditioning and humidity of the surrounding atmosphere, so in this work we prefer to quote the moisture results as calculated on their wet basis.

Similarly, the ash content is determined using BS recommendation (BS, 2006), but in this case based on the material dry weight. In general analysis, the sample is firstly over-dried in a vacuum oven at 100 ^{o}C to remove remaining moisture and then cooled down in a dessicator to reach ambient temperature before the initial mass is estimated. Next, the sample of known mass is transferred to the TGA microbalance where it is dried at 550 ^{o}C over the isothermal period of 120 minutes in air atmosphere. For each determination, the ash content, a_{db} (on the dry basis) is calculated using the Equation 4.2:

$$a_{db} = \frac{(m_3 - m_1)}{(m_2 - m_1)} \times 100\% \times \frac{100}{100 - m_{ad}} \tag{4.2}$$

A summary of moisture and ash content results determined for each analysed sample is presented in Table 4.1. The results are reported as a mean ± standard deviation of measurements. From these data it can be observed that moisture and ash matter depend strongly of the type of material analysed. The results show that the highest level of moisture of around 6.50 ± 0.60 wt% was found for the TE 7 III activated carbon beads, where the 13X zeolite sample is almost dry (0.75 ± 0.92 wt%). Note that high moisture content can be particularly troublesome for achieving efficient gas sorption, since when

not fully removed can block the potential hydrogen sorption sides, as discussed in more detail in Section 4.2.1.4. Regardless of ash results, the percentage content was the highest for the Cu-BTC metal organic framework sample (35.78 ± 0.92 wt%) while the TE 7 III sample was almost pure (0.67 ± 0.06 wt%). Some of the authors showed that residual metal in carbon based adsorbents can play a significant role in the hydrogen adsorption properties, which take place via hydrogen spillover from the metal to the adjacent surface of a receptor enhancing hydrogen storage capacity (Lueking and Yang, 2004).

Table 4.1: Summary of moisture and ash content results for all investigated samples obtained by applying the British Standard method to thermogravimetry data. The reported results represent mean ± standard deviation of duplicate determination.

material	moisture content*, m_{ad} / wt%	ash content**, a_{db} / wt%
TE 7 I	6.25 ± 0.64	1.61 ± 0.10
TE 7 II	1.91 ± 0.38	5.10 ± 0.80
TE 7 III	6.50 ± 0.60	0.67 ± 0.06
Darco	2.44 ± 0.99	1.81 ± 0.42
Solcarb	1.24 ± 0.91	1.49 ± 0.20
Respcarb	2.90 ± 0.72	1.56 ± 0.41
13X	0.75 ± 0.92	8.35 ± 1.13
Y-Zeolite	1.20 ± 0.54	2.57 ± 0.80
Cu-BTC	1.70 ± 0.97	35.78 ± 0.92

*calculated on a wet basis
**calculated on a dry basis

While determining the moisture and ash content from BS method large uncertainty is introduced to the calculation due to the way in which the sample and crucible mass is estimated strongly relies on the operator precision. In this work, to ensure data accuracy, the moisture and ash matter obtained by standard BS analysis are compared to those predicted from the thermogramme profile, recorded directly by the TGA microbalance.

Figure 4.1 shows a representative TGA response curve which is used to calculate the amount of moisture present in the TE 7 III activated carbon sample. As can be seen the value of moisture matter determined in this way is around 6.75 wt%, similar to those in the Table 4.1 obtained via BS method. Statistical analysis of these two methods yielded

a moisture value of 6.62 ± 0.18 wt% which is in the range of acceptable error and supports the correctness of both methods. Furthermore, from visual verification of the TGA profile it can be seen that after around 18 minutes the long plateau is reached, which can confirm that the remaining moisture is fully lost at temperatures up to 105 ^{o}C.

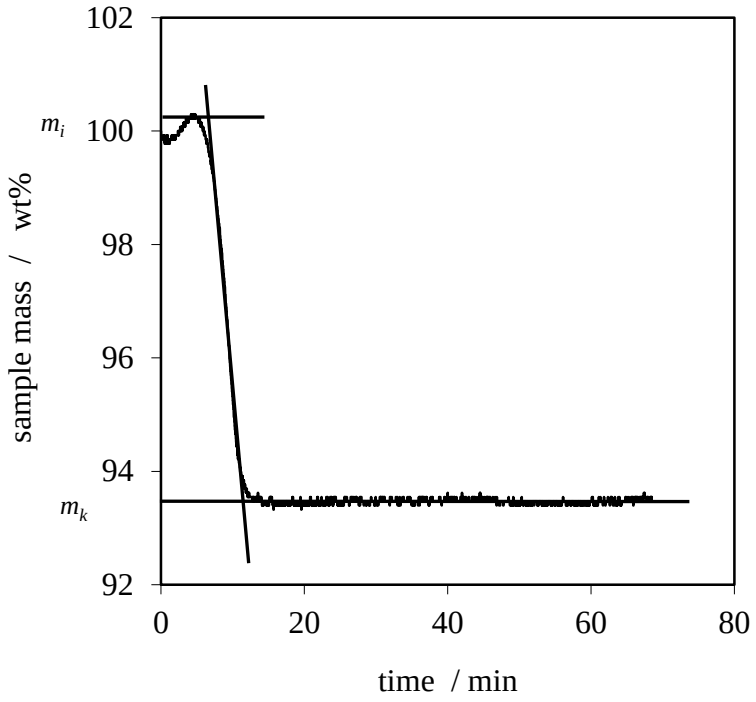

Figure 4.1: Representative TGA curve of thermal decomposition of TE 7 III carbon beads sample used for moisture content determination. Here, the analysis conditions follow the BS method: sample mass of around 13.5 mg, heating rate 10 ^{o}C min^{-1}, temperature profile from ambient to 105 ^{o}C, then isothermal heating at 105 ^{o}C for 60 min in nitrogen. Where, m_i is initial, m_k is a final mass of the sample recorded during first transformation.

In terms of ash content the same outcome is true when comparing results from both methods mentioned above. From the representative Figure 4.2 it can be seen that the predicted value of ash is around 0.70 wt% which is in very good agreement with results from the BS method (0.67 wt%). Furthermore, from the TGA profile it can be concluded that the first temperature plateau, where the sample mass remains constant is reached between 180–380 ^{o}C. Then the sample mass is decreasing dramatically up to approximately 550 ^{o}C reaching the second plateau after around 200 minutes where the

carbon is burned off completely leaving ash as a residue. These results show that the TE 7 III activated carbon is thermally stable up to around 380 ^{o}C which can provide insight for degassing conditions as discussed in Section 4.2.1.4.

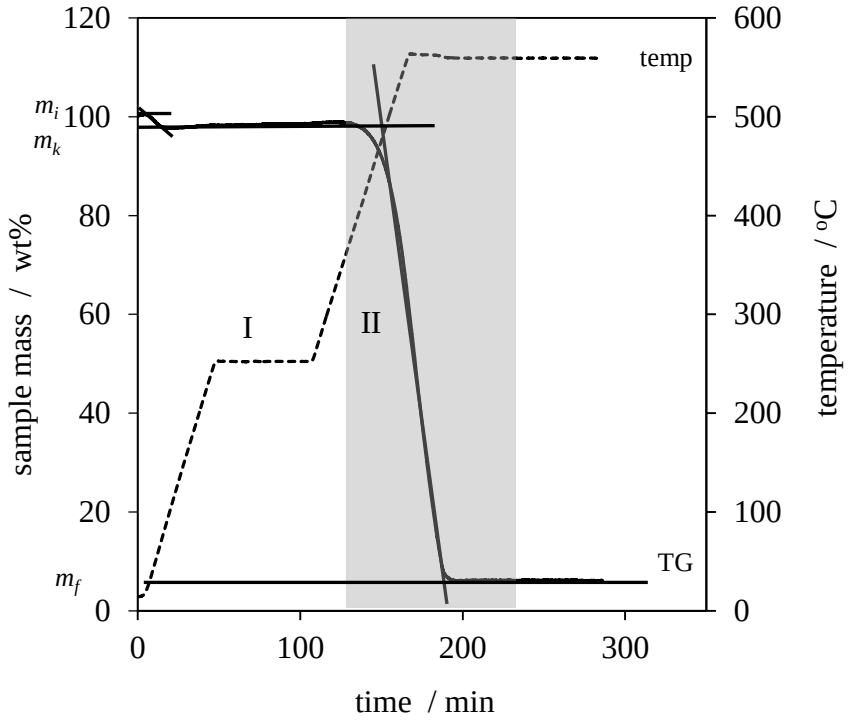

Figure 4.2: Representative TGA curve of thermal decomposition of TE 7 III carbon beads sample used for ash content determination. Here, the analysis conditions follows the BS method: sample mass of around 14.4 mg, heating rate 10 ^{o}C min^{-1}, temperature profile from ambient to 250 ^{o}C, then isothermal heating at 250 ^{o}C for 60 min, afterward temperature raised to 550 ^{o}C and maintained for 120 min in air atmosphere. Where, m_i is initial sample mass, m_k is the mass after first decomposition and m_f is a final mass after second decomposition. Here I, II indicate the first and the second decomposition stages, respectively.

4.2.1.2 Skeletal Density

In this work, ambient temperature (298 K) helium pycnometry as stated earlier in Chapter 3.3.2 was undertaken to obtain skeletal density (ρ_s) information necessary to correct raw sorption isotherms for buoyancy and dead volume effects. However, when performing these measurements it is necessary to make a few assumptions, for accessibility of helium molecules into all pores and no adsorption of helium at these operating conditions (298 K and around 1 bar), which can be misleading for some microporous samples. According to a recent study, significantly higher temperatures of around 400 ^{o}C (673 K) are recommended to avoid potential helium trapping in micropores (Malbrunot et al., 1997). It is also assumed that there are no contaminants in the helium stream, which potentially can mimic determined density values if the gas purity is not in the ppm level. Nevertheless, it is important to take great care when reporting the skeletal density data, as any inaccuracy can cause errors in the measured hydrogen capacities, particularly when possible helium adsorption in the micropores is taken into account, as discussed later in Section 4.2.2.6.

Here, the skeletal density is defined as the ratio of the degassed mass to the skeletal volume, which is the volume occupied by the sample (v_{solid}) including the volume of closed pores (v_c) and a simple illustration of this concept is shown in Figure 4.3 below.

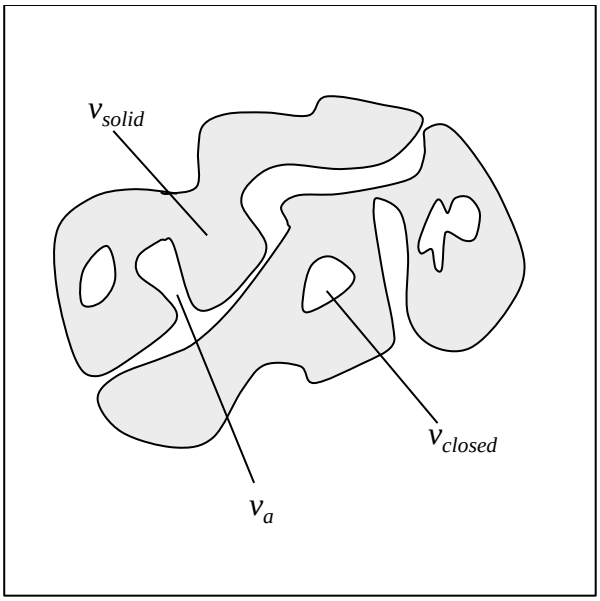

Figure 4.3: A schematic graph illustrating concept of skeletal volume which is the volume of the sample (v_{solid}) including volume of the closed pores (v_c). Here, for the illustration purpose the volume of open pores (v_a) is also shown.

Figure 4.4 illustrates the example of the skeletal density results plotted as a function of run number for the representative TE 7 II carbon sample. These results represent a mean ± standard deviation determined from three independent experiments. As can be seen the measured density creates a decreasing exponential trend, instead of remaining constant during the whole determination. It starts at a very high value of 4.9965 g cm^{-3} and then sharply deceases as the run number continue, reaching a plateau at around 1.9975 g cm^{-3}. This is general trend seen for almost all samples, with the exception of the Y-Zeolite where the skeletal density values are very consistent (all resulted skeletal density plots are provided in Supplementary Information, Section S1). The behavior presented here is due to sample drying in the inert helium atmosphere, which attribute that tested samples are not completely free of moisture, since as stated previously some materials can contaminate very easily when exposed to humid air.

Because of the nature of the data distribution, the skeletal density results presented here cannot be simply averaged to find the mean value from all 20 runs. Instead, to overcome this problem the following data can be treated in two ways. Firstly, equilibrium densities

may be determined by-eye from the pycnometry plot (see Figure 4.4). Optionally, a second order exponential decay function can be fitted to the experimental data using regression analysis and then the y_0 values at which the y-variable becomes constant is predicted (see Figure 4.5).

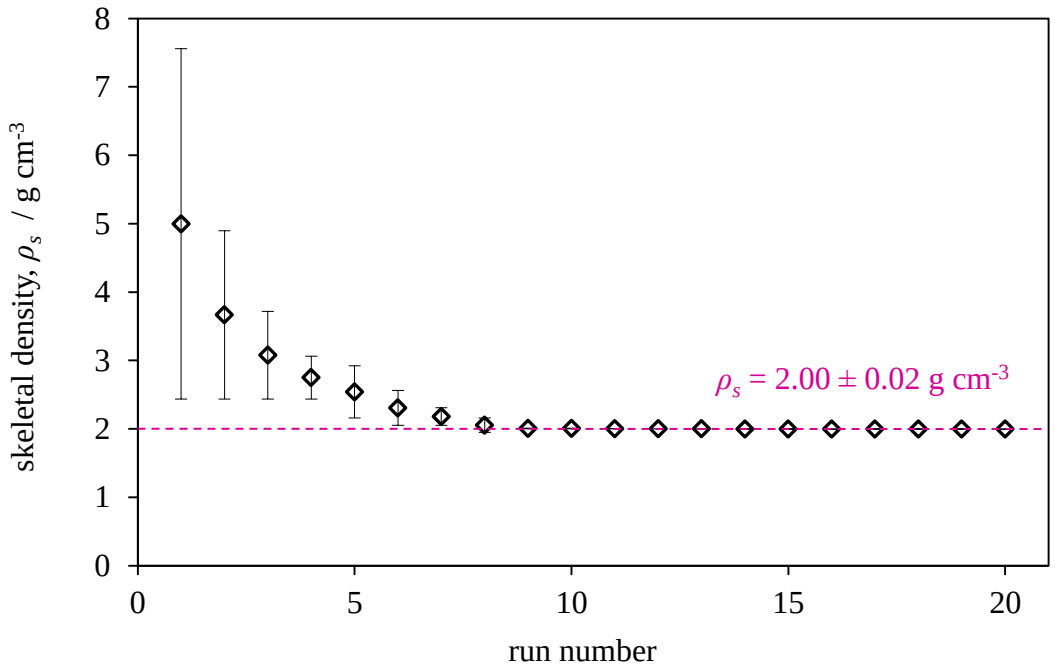

Figure 4.4: Skeletal density plotted against run number for a sample of TE 7 II activated carbon beads. The dotted line (---) represent the equilibrium reference value assigned as 2.00 ± 0.02 g cm^{-3}. The error bars represent the standard deviation of three independent measurements.

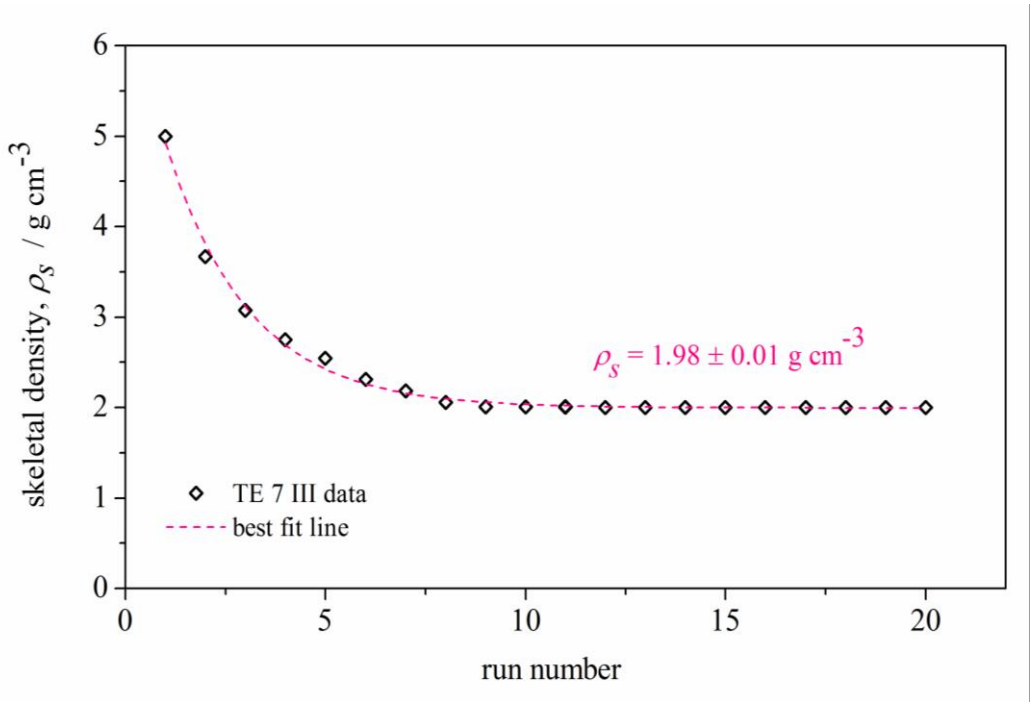

Figure 4.5: Skeletal density plotted against run number for a sample of TE 7 II activated carbon beads. The dotted line (---) represent an exponential decay curve ($y=A_1*exp(-x/t_1)+A_2*exp(-x/t_2)+y_0$) fitted to the experimental data. The predicted skeletal density value was assigned as 1.98 ± 0.01 g cm^{-3}.

Table 4.2 compares the skeletal density results obtained from by-eye with those estimated via fitting method. As can be seen both methods yield very close densities with a maximum deviation of around 3.5 % found for the Solcarb carbon. This good data agreement supports the reliability of the skeletal density results determined in our lab and implies that validity of both methods can be extended to moisture contaminated samples and where the drying pretreatment is not an option.

*Table 4.2: Summary of skeletal density results for all investigated samples obtained from He-pycnometry at ambient temperature (298 K). * The quoted results are equal to mean ± standard deviation of three independent measurements.*

material	skeletal density, ρ_s /cm^3 g^{-1}	
	by-eye results*	fitted results
TE 7 I	2.14 ± 0.09	2.12 ± 0.01
TE 7 II	2.00 ± 0.02	1.98 ± 0.01
TE 7 III	2.25 ± 0.11	2.21 ± 0.02
Darco	2.03 ± 0.04	2.02 ± 0.003
Respcarb	2.24 ± 0.07	2.20 ± 0.02
Solcarb	2.20 ± 0.02	2.15 ± 0.01
13X	2.21 ± 0.05	2.21 ± 0.02
Y-Zeolite	1.85 ± 0.002	1.87 ± 0.001
Cu-BTC	1.65 ± 0.02	1.65 ± 0.0003

Here, in order to compare the experimental densities tabulated above with theory and other studies, the analysed materials are classified into two categories: disordered carbons (marked grey) and crystalline structure (staying white). For activated carbons having disordered structure the limit for the matrix density is pure crystalline graphite and as expected all determined densities are below a maximum value of 2.26 cm^3 g^{-1}, due to possible imperfections and presence of closed pores or impurities in the structure (Pierson, 1993). From these results it can be concluded that TE 7 III and Respcarb samples are very crystalline, such that the densities are very close to maximum (2.25 cm^3 g^{-1} and 2.24 cm^3 g^{-1} respectively), while the TE 7 II and Darco carbons are slightly more amorphous (1.98 cm^3 g^{-1} and 2.03 cm^3 g^{-1}). Rey and co-workers (Rey et al., 2012) showed XRD patterns of micro- mesoporous Darco carbon studied in this work. The authors observed sharp peaks which they assumed due to silica type impurities in the carbon structure (SiO_2-quartz and SiO_2-cristoballite). This result could be related to low material density of 2.03 cm^3 g^{-1} (by-eye results) found for Darco carbon. Additionally, this result supports our EDX findings for Darco carbon, where the presence of silica was also observed (for more details see Section 4.2.1.3). Structural studies of others commercial disordered carbons such as AX-21, CXV and BP71 by

using high-energy XRD accompanied with computer simulations where carried out by Hawełek et al., (Hawełek et al., 2007). These authors also showed that disordered activated carbons have some defects in the crystal structure, which can result in lower material densities than pure graphite. In regards to crystalline materials, most skeletal densities reported in literature are based on the pure crystal values obtained from x-ray diffraction (XRD). However, we need to be careful with quoting this numbers because if we do not have experimental densities (which is very likely to be lower than XRD because of the differences in crystallinity degree, framework structure, nature of the cations, defects or impurities) it results in the possibility of underestimation of the skeletal volumes which could propagate into measurements of uptake as discussed in Section 4.2.2.6 of this thesis.

4.2.1.3 Particle Size and Morphology

In order to reveal morphology of the materials and their external structure qualitative SEM analysis was undertaken as detailed in Chapter 3.3.3. This can provide information about the particle size and geometry, but also give first insights of present porosity. Typical scanning electron micrographs of the regular geometry, such as TE7 III activated carbon sample are shown in Figure 4.6. In this case, the analysis is relatively easy as the particles are well separated and apparently all spherical in shape. The average particle diameter determined via a linear length measure was found to be 330 ± 20 μm (see Figure 4.6 (a)). From the SEM scans at higher magnification (see Figure 4.6 (b) and Figure 4.6 (c)) it is visible that sample texture is very complex, which could be indication of macroporosity, possibly leading to microporous structure that cannot be resolved at these magnifications. In order to verify these additional structural features, our carbon sample was examined with the TEM analysis and the examples of results are given in the Figure 4.7. Unfortunately, the resolution of the TEM available in our lab was unable us to see the micropores network as was hoped. However some TEM of carbon based materials have been reported in the literature (Yoshizawa et al., 1998, Oshida et al., 1995, Sharma et al., 1999, Rouzaud and Clinard, 2002).

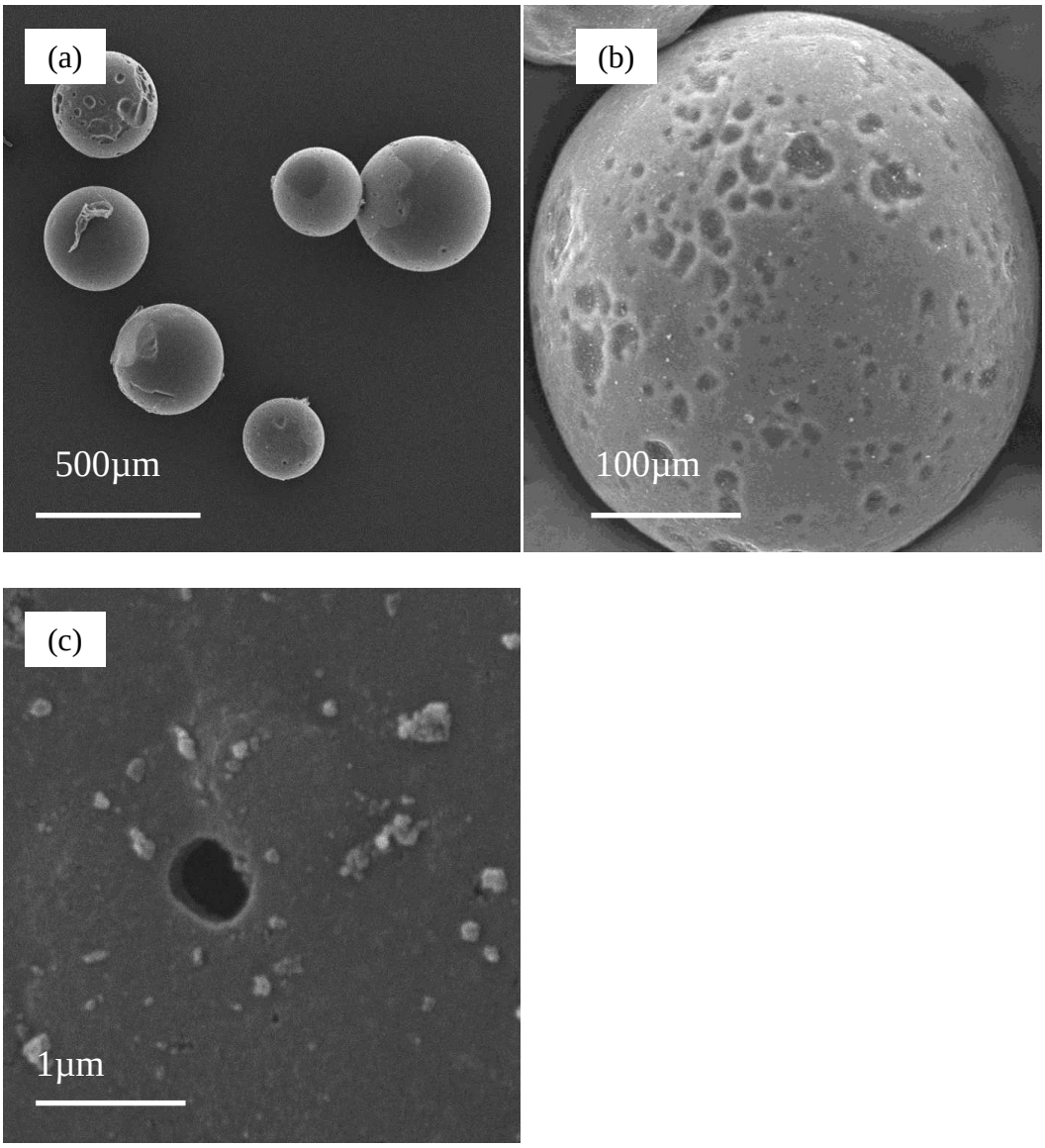

Figure 4.6: SEM secondary electron images (SEI) of TE 7 III activated carbon beads sample at increasing magnification from (a) to (c) with accelerating voltage of 15 kV.

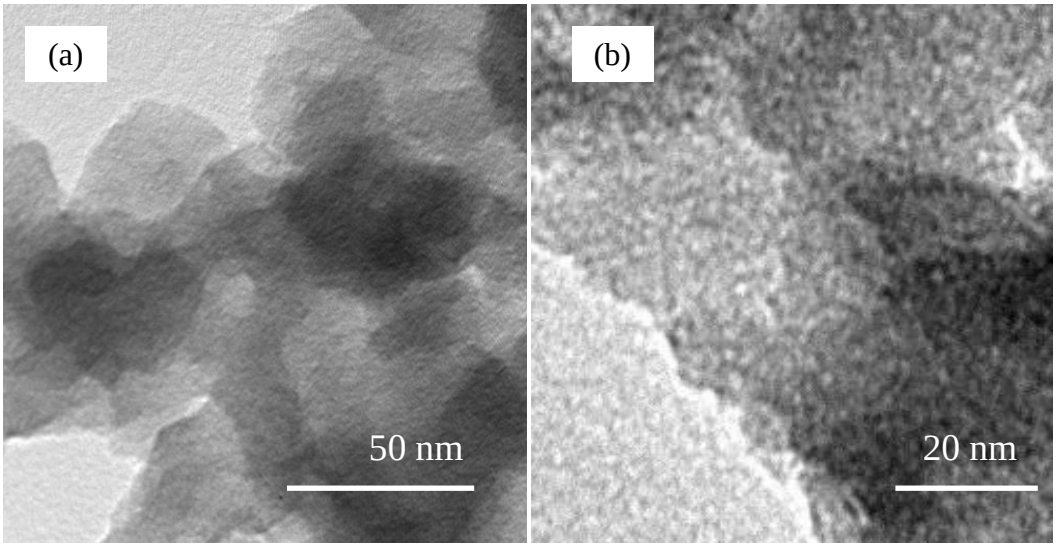

Figure 4.7: TEM electron images of TE 7 III carbon beads sample at increasing magnification from (a) to (b).

Accessing morphology becomes more difficult for the crystalline structures, like zeolites or MOFs which consist of non-uniform sizes, shapes or formation of large agglomerates where no single particle exists. Figures 4.8 and Figure 4.9 show an example of particles which vary in both size and shape, measured for the 13X, Y-Zeolite and Cu-BTC metal organic framework samples. Unlike the TE 7 III sample, these data cannot be simply treated via linear length measure, mainly because of lack of spherical geometry. However, they can be characterised using equivalent spherical diameter, which is a diameter of sphere with equivalent area as the projected particle. An example of analysis is displayed in Figure 4.8 (c), which shows one particle cut out from the measurement frame (Figure 4.8 (a)) and then fitted into a sphere to predict their diameter. However, for some irregular geometry like Cu-BTC sample, single sphere does not enough accurately describe the structure. In this case, method proposed by Hildebrand et al. and Remy et al. can be applied to predict the chamfer distance along its medial axis (Hildebrand and Ruegsegger, 1997, Remy and Thiel, 2002). The analysis starts with identifying the medial axis and then the individual spheres are fitted as shown in Figure 4.9 (b). The total diameter measured along a given axis is a diameter of maximal number of spheres fitted completely inside the investigated structure. Note that only

particles with their centroid point lying in the measured frame are accepted for counting. All particles outside the frame, or cut by the edges are excluded from further analysis.

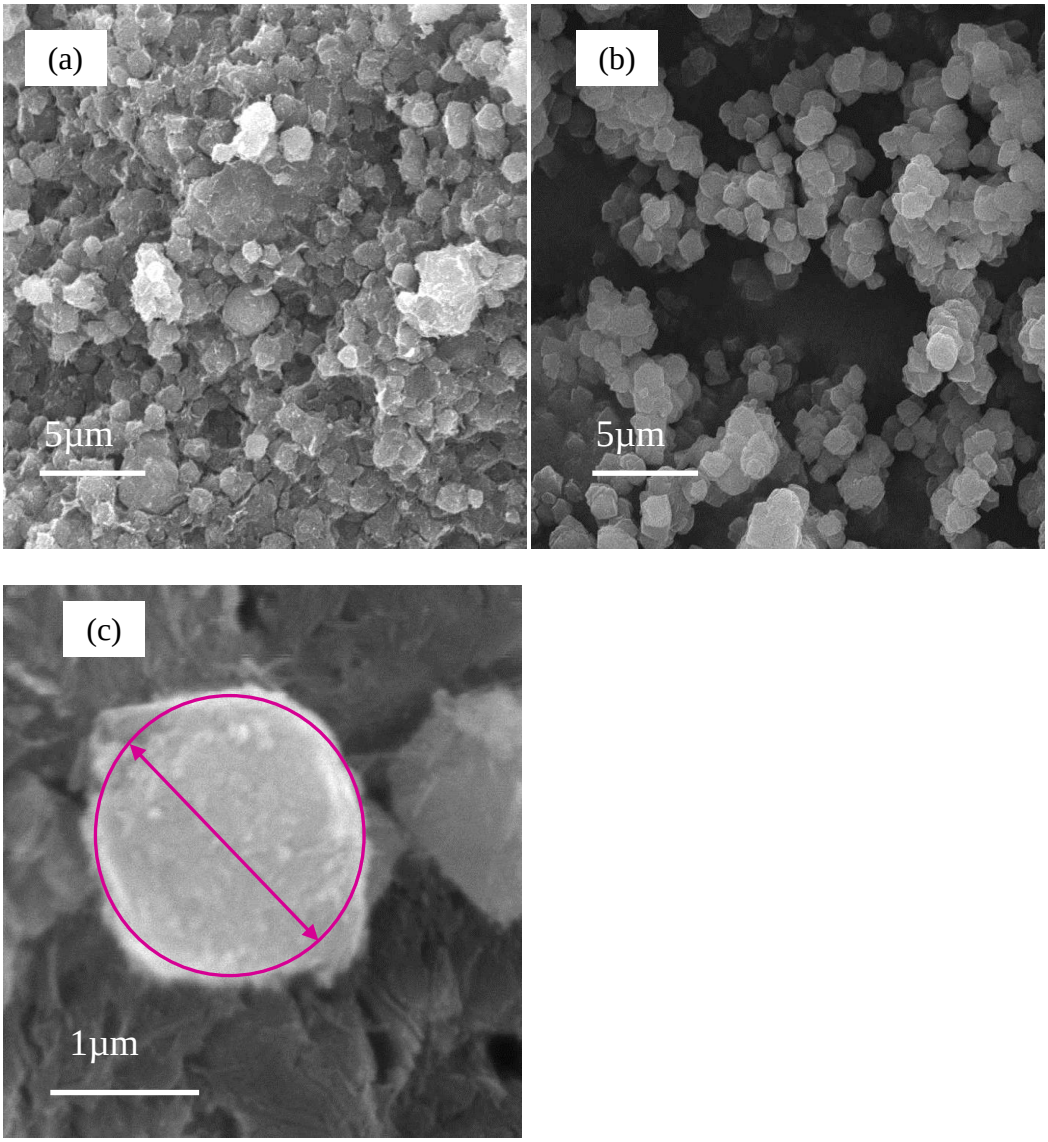

Figure 4.8: SEM secondary electron images (SEI) of (a) 13X, (b) Y-Zeolite sample characterised by the equivalent spherical diameters, showing (c) the enlarged view of individual particle fitted inside sphere in pink). Images accelerate voltage of 15 kV.

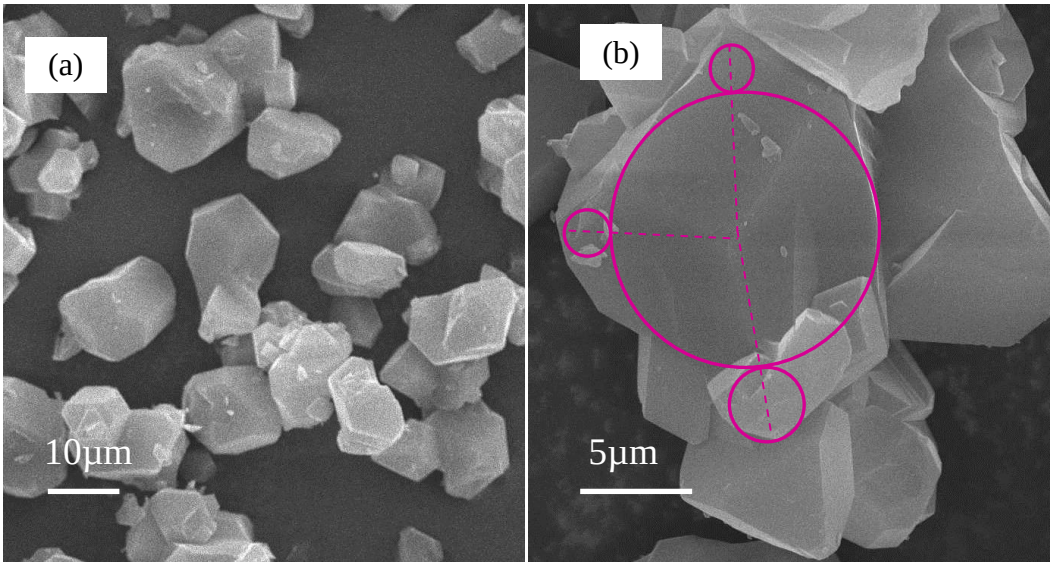

Figure 4.9: SEM secondary electron images (SEI) of Cu-BTC metal organic sample (a), showing the enlarged view of schematic representation of the particle diameters determination along the medial axes (---) (b). The total diameter of the particle is the diameter of the maximal spheres fitted within the structure. For illustration purpose only few shares are shown.

While performing the SEM analysis the elemental composition was also studied by energy dispersive X-ray (EDX) spectroscopy and the examples of obtained results are given in Figure 4.10. The EDX spectrum in Figure 4.10 (a) taken from the external surface suggest that TE 7 II carbon sample is very pure, as it is only composed of carbon and some oxygen. However, what is interesting for this sample that after a closer look at internal structure (see Figure 4.10 (b)) the presence of iron and silica was revealed. These small peaks might appear due to the synthesis route, where the micropore structure was created by phenolic resin activation in the iron and steel industrial furnace.

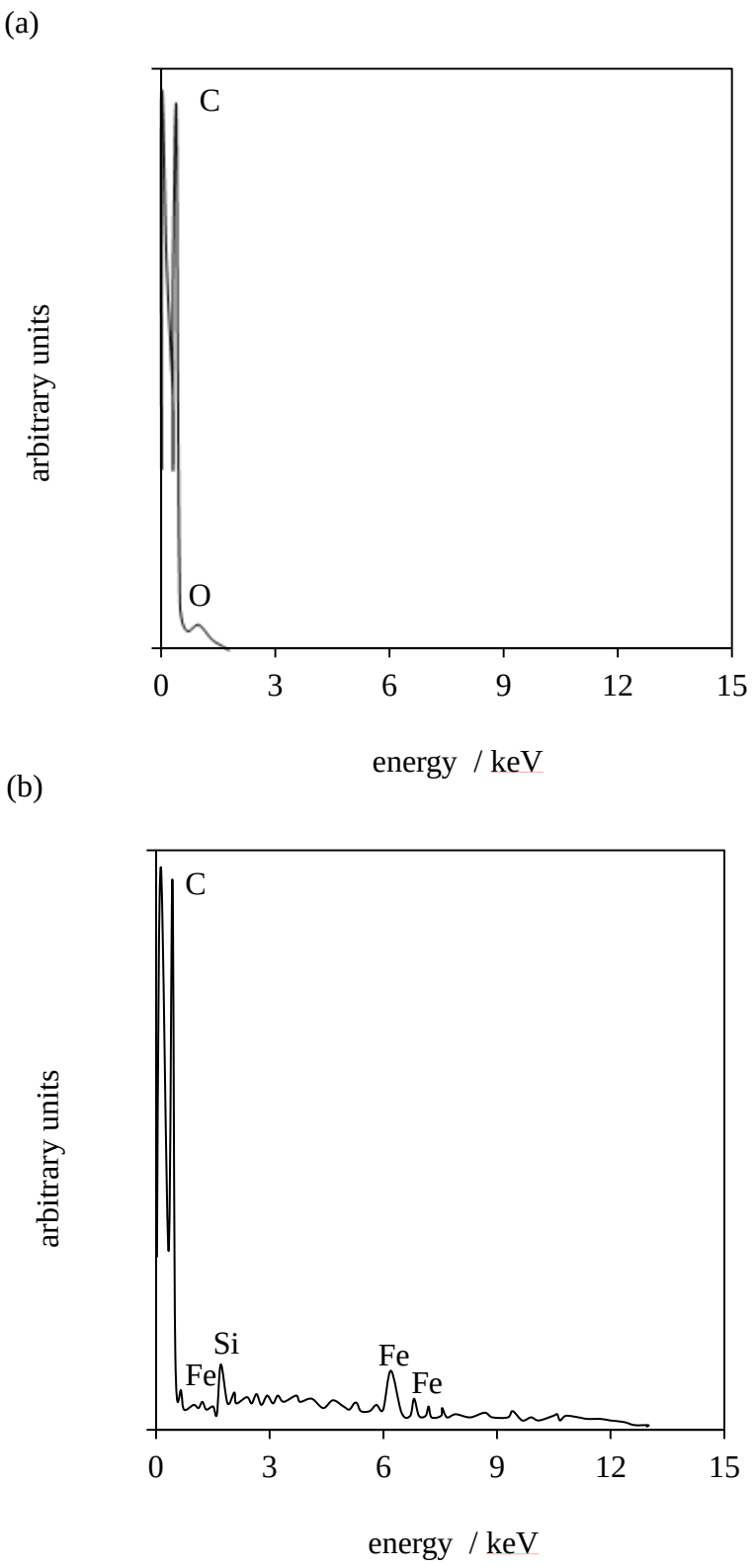

Figure 4.10: Representative EDX spectroscopy plots obtained for TE 7 II carbon beads sample showing composition of (a) the external and (b) internal surface.

A summary of obtained microanalysis results for each investigated sample are given in Table 4.3 below (all resulting SEM images are provided in Supplementary Information, Section S2). Standard deviation is included to indicate the uncertainties in the crystal size variation. For example, from looking at the elemental composition results it can be seen that the TE 7 III carbon beads has the highest purity along all examined carbons, supporting their low ash residue (0.67 ± 0.06 %) as determined by TGA method. EDX microanalysis also revealed the presents of chlorine (Cl) in both Darco and Solcarb carbons, which can be attributed to their purification method, since as stated previously in Chapter 3 acid washing was used to remove remanding metals from their structure.

*Table 4.3: Summary of the structural characterisation results for all investigated samples determined during SEM and EDX microanalysis. *The reported data represent mean ± standard deviation.*

material	particle diameter, x_d* / μm	composition
TE 7 I	460 ± 80	C, Si, Fe
TE 7 II	420 ± 70	C, Si, Fe
TE 7 III	330 ± 20	C, O
Darco	100 ± 8.0	C, Cl, Si
Respcarb	1460 ± 180	C, K
Solcarb	2790 ± 240	C, O, Cl
13X	1.70 ± 0.20	C, O, Ca, Fe, Na, Mg, Al, Si
Y-Zeolite	0.80 ± 0.10	C, O, Na, Al, Si
Cu-BTC	16.50 ± 1.50	C, O, H, Cu

4.2.1.4 Sample Degassing

"Accurate degassing procedure is crucial for obtaining a well-defined, reproducible surface prior to gas sorption analysis, where a clean surface is required and all physisorbed species that could block potential sorption sides need to be removed. This could be achieved by sample degassing at high vacuum (typically around 10^{-6} mbar) and elevated temperature. It should be keep in mind that degassing conditions such as time,

temperature and pressure are dictated by the nature of adsorbent, and must be carefully considered for individual systems analysed" (Hruzewicz-Kolodziejczyk et al., 2012).

According to sample type pre-treatment requirement of the sample may differ. Typical example of this is MOF where activation at high temperature and under vacuum may lead to loss of porosity due to framework collapse or presence of non-volatile substances, such as dimethyl or diethyl formamides (DMF or DEF) (Farha and Hupp, 2010). In such cases, alternative approaches such as solvent-exchange with a volatile substance or exchanging with liquid CO_2 and then removing it under supercritical conditions can be used for sample preparation (Farha and Hupp, 2010, Andrew et al., 2009, Furukawa).

Sensitivity to moisture is widely considered to be a major weakness of MOFs, which could affect the H_2 adsorption performance. Cu-BTC metal organic sample synthesized from a mixture of $Cu(NO_3)_2 \cdot 3H_2O$ and 1,3,5-benzenetricarboxylic acid (BTC) is one example of a MOF that shows strong affinity to water (Wang et al., 2002) and decomposition due to moisture (Kusgens et al., 2009). Kusgens et al. reported that the Cu-BTC structure breaks down after immersion in pure water (at 323 K, 24 h) with a significant decrease in BET surface area (48 %). A large variation into gas adsorption properties depending on materials preparation conditions have been also reported for MOF-5 sample by Kaye et al., (Kaye et al., 2007). Authors observed that depending on the degree of sample exposure to air the excess nitrogen and hydrogen capacities at 77 K can vary between 35.8 and 44.5 mmol g^{-1} (at 1 bar) and 5.1 to 7.1 wt% (at 40 bar), respectively.

Since some of the hydrogen storage nanoporous materials such as MOFs are sensitive to humid air it requires contamination free sample handling system to transfer between different instruments, to avoid structure decomposition or framework collapse. Some gravimetric and volumetric apparatus provide airless sample management systems, but the process is often as awkward and problematic as dealing with air or water sensitive samples (Gross, 2008). In order to avoid contamination it may be possible to incorporate

the entire instrument inside a 'glove box' where the sample can be transferred and loaded in an inert (argon or nitrogen) environment (Gross, 2008). An alternative to this method used in IGA instruments involves an inert atmosphere sample loader that can be temporarily attached to the instrument during the loading of the sample and then removing before starting the measurement (Broom, 2011).

"In this section the criterion that can be applied to determine optimal degassing conditions is demonstrated for the TE 7 III carbon beads sample as an example. Figure 4.11 shows the TGA plot which is used to determinate the material degradation temperature. As can be seen the sample degassing can be performed at any temperature from the range 110–380 ^{o}C, with the optimum temperature close to the top of that range. However, it should be kept in the mind that the kinetics of the mass loss observed from TGA measurements on the relatively small sample (~ 10 mg) under the carrier gas is not the same as degassing approximately 10 times larger sample under high vacuum conditions. For our carbon beads sample the TGA curve shows that all remaining moisture is removed after around 20 minutes, while from ASAP 2020 'stable weight' analysis (see Table 4.4) it was found that around 100 mg sample degassed at 350 ^{o}C under high vacuum required minimum 360 minutes to fully dehydrate" (Hruzewicz-Kolodziejczyk et al., 2012).

Table 4.4: Sample masses for a reference sample of TE 7 activated carbon beads, determined after different degassing times in vacuum (10^{-6} mbar) at 350 ^{o}C in the volumetric ASAP 2020 analyser. The sample mass was periodically checked on the external balance until stable.

degassing time / min	sample mass / g (± 0.0001 g)
0	0.1008
120	0.0937
240	0.0934
300	0.0933
360	0.0932
480	0.0932

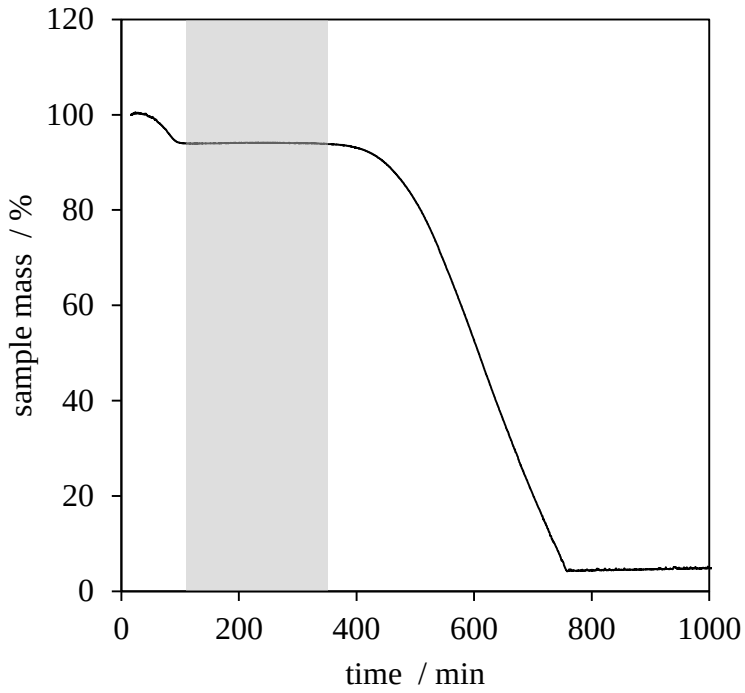

Figure 4.11: Representative TGA plot of the TE 7 III activated carbon beads showing the temperature range (marked grey) over which the sample should be degassed. Heating rate of 5 $^{o}C\ min^{-1}$ in air.

To ensure accurate measurements, the degassing procedure was also monitored using the IGA gravimetric microbalance, where the mass change is directly recorded via real-time analysis (see Figure 4.12). From comparison of these two methods it is clear that after around 360 minutes the sample mass is very stable, implying that remaining contaminants are fully removed. Based on above discussion, the optimal regeneration conditions for our reference sample of TE 7 III carbon beads used during gas sorption analysis discussed in Section 4.2.2 is selected to be: heating at 350 ^{o}C under 10^{-6} mbar vacuum for 480 minutes.

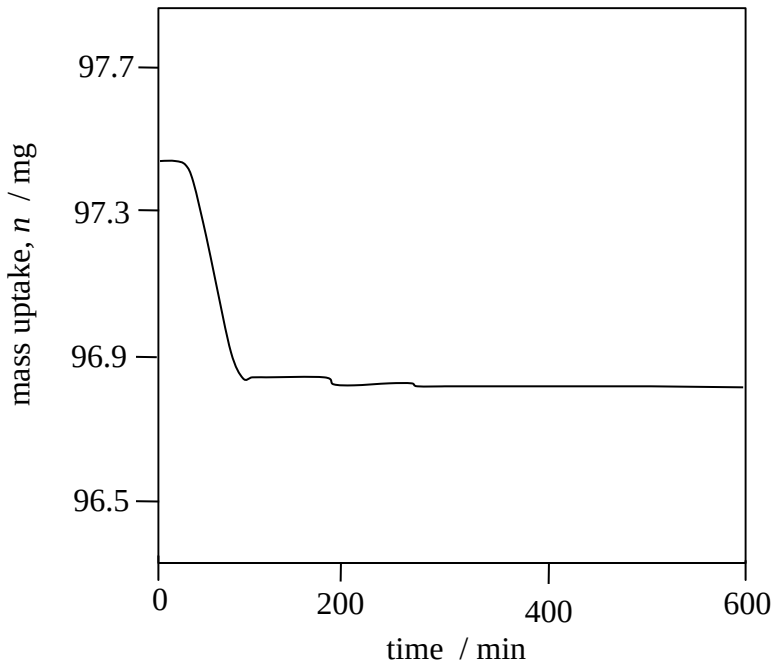

Figure 4.12: Representative mass uptake curve of the TE 7 III activated carbon beads recorded in real-time analysis by the IGA gravimetric microbalance while degassing at 350 ^{o}C.

The following criteria are applied for all investigated samples and the results of optimal degassing conditions are given in Table 4.5. As can be seen the different degassing approach is used just for the Cu-BTC metal organic framework sample where the lower degassing temperature of around 110 ^{o}C is chosen to prevent the framework degradation. Therefore, the much longer degassing time of 720 minutes is used to ensure that the solvent from the synthesis that can remain in the micropores is fully removed. Notably, the Cu-BTC sample changed its colour from light to cobalt blue after heat and vacuum activation. However, after exposure to moisture its colour reversibly turned back to light blue, indicating that water can be adsorbed/desorbed without structural changes, as confirmed later during the gas sorption analysis (see Section 4.2.2).

Table 4.5: Experimental degassing conditions used prior to gas sorption analysis for each investigated sample.

material	pressure, *p* / mbar	temperature, *T* / ^{o}C	time, *t* / min
TE 7 I	10^{-6}	350	480
TE 7 II	10^{-6}	350	480
TE 7 III	10^{-6}	350	480
Darco	10^{-6}	350	480
Respcarb	10^{-6}	350	480
Solcarb	10^{-6}	350	480
13 X	10^{-6}	350	480
Y-Zeolite	10^{-6}	350	480
Cu-BTC	10^{-6}	110	720

4.2.2 Developing the Gas Adsorption Method

The purpose here is to develop an accurate gas adsorption method which can be successfully applied to reliable characterisation of nanoporous materials. Having this in mind, we present here the results of systematic adsorption measurements with different types of gaseous probes having different molecular size, shape and polarity which help us to explore the accessible pore structure and available internal surface. The primary method involves 77 K nitrogen adsorption isotherms to yield the specific surface area and the micropore volume, but also to provide materials classification. However, we point out here the limitation of this standard routine for resolving porosity and surface areas as a consequence of diffusion limitations in the narrowest micropores. We present an alternative approach, which involves carbon dioxide at 273 K and argon at 87 K analysis, since increasing the operational temperature helps to overcome the energy barrier and allows to determinate microporosity not accessible to nitrogen at 77 K.

4.2.2.1 N_2, CO_2 and Ar Sorption Isotherms

Figure 4.13 to Figure 4.21 show the 77 K adsorption/desorption nitrogen isotherms recorded for each investigated sample on the Micromeritics ASAP 2020 volumetric analyser. As can be seen almost all determined isotherms exhibit Type I behavior according to the Brunauer, Deming, Deming and Teller (BDDT) classification (Sing et al., 1985), implying that the materials are microporous (pore sizes below 2 nm). These isotherms are characterised by a horizontal plateau when the saturation pressure is reached, which is a consequence of the complete micropores filling (Gregg, 1982). However, some isotherms show a slight upward turn at relative pressures close to 1, which corresponds to the filling of larger micropores or the presence of small amount of the mesoporosity (see Figure 4.13). A slightly different, Type IV behavior is found for the mesoporous Darco carbon and 13X zeolite (pore sizes between 2–50 nm) showing pore condensation with pronounced adsorption-desorption hysteresis loop as displayed in Figure 4.16 and Figure 4.19.

Also of note, some collected isotherms shown rounded knees around 10^{-7} of the relative pressure (see Figure 4.13 (b)), which we attributed to not complete sample degassing or problems with reaching adsorption equilibrium by a particular system, as very low pressures are considered here where the sensitivity of gas sorption equipment might be very limited.

The given isotherms represent the measurements of the repeatability determined from two independent experiments. Table 4.6 summarizes the overall repeatability results, showing the variation in the amount of nitrogen adsorbed at different relative pressures. The ratio Run1/Run2, their mean and the standard deviation values are also displayed. For example, from closer look at TE 7 III results, the ratio of 1.0259, 1.0124 and 1.1366 is found at 0.2, 0.6 and 1.0 p/p^o respectively. The standard deviation of these ratios is only approximately 2.06 %, which represents very small oscillation assuring well data repeatability.

(a)

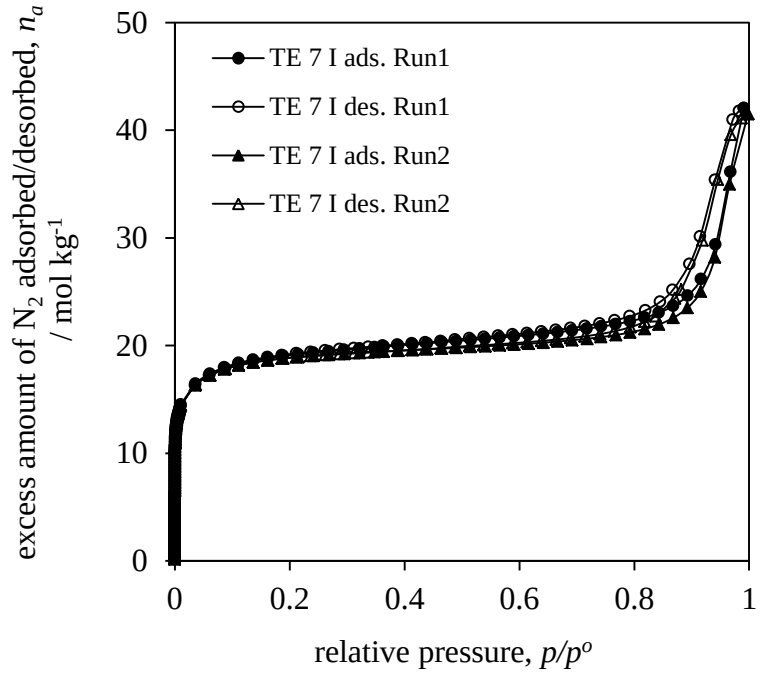

(b)

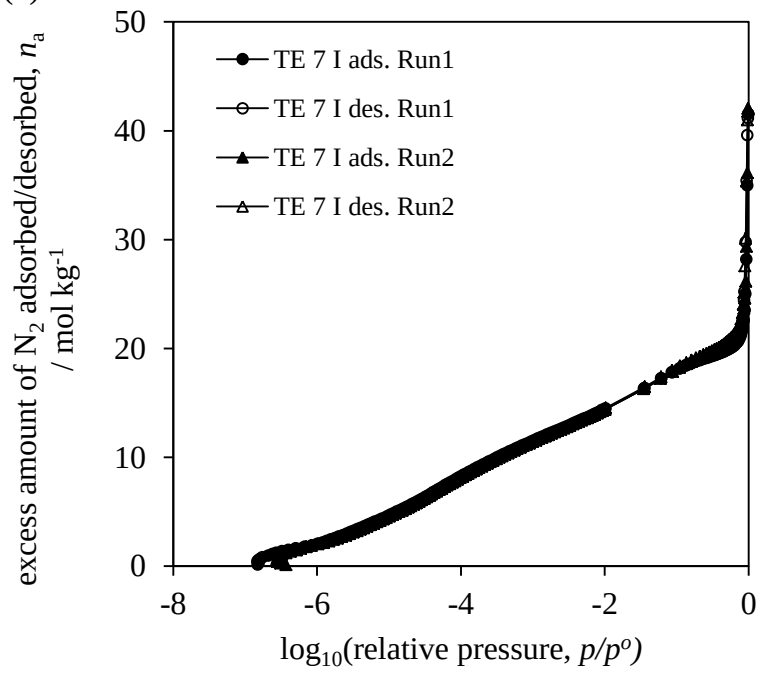

Figure 4.13: Experimental results of volumetric ASAP 2020 excess nitrogen sorption isotherms at 77 K for the TE 7 I activated carbon beads sample in (a) linear and (b) logarithmic scale of relative pressure. The lines on the plots join points to illustrate trends in the data. Filled and open symbols represent adsorption and desorption points respectively.

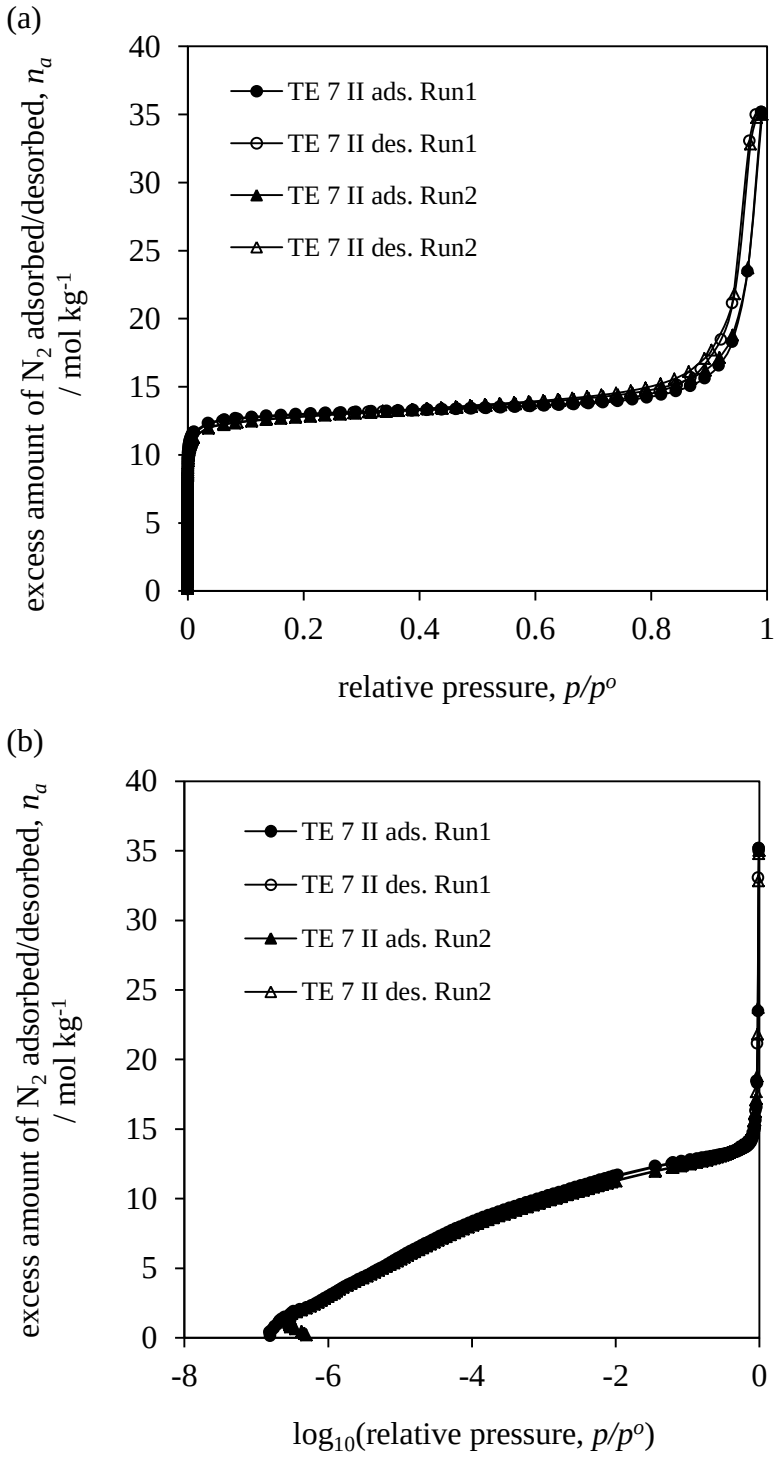

Figure 4.14: Experimental results of volumetric ASAP 2020 excess nitrogen sorption isotherms at 77 K for the TE 7 II activated carbon beads sample in (a) linear and (b) logarithmic scale of relative pressure. The lines on the plots join points to illustrate trends in the data. Filled and open symbols represent adsorption and desorption points respectively.

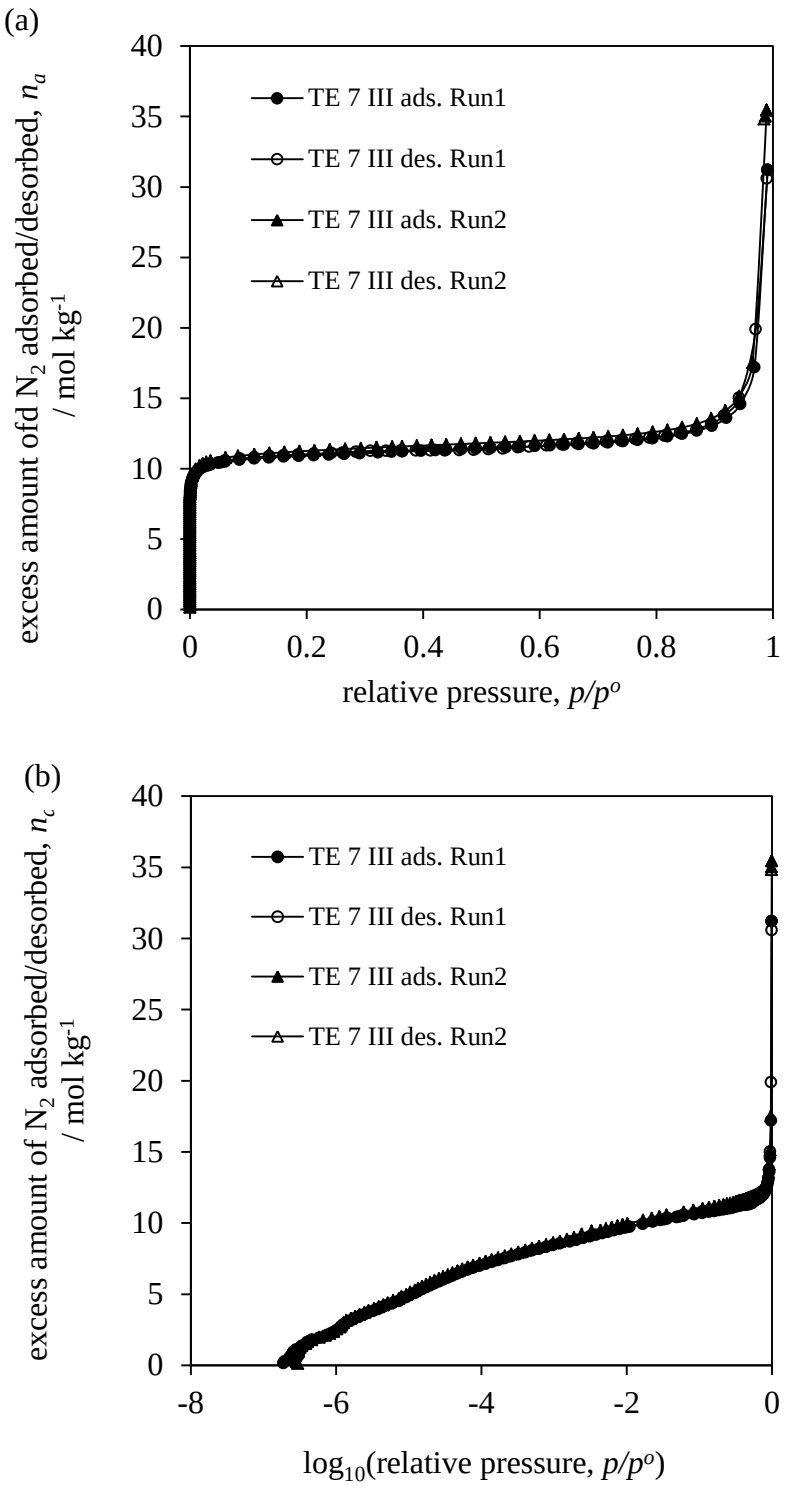

Figure 4.15: Experimental results of volumetric ASAP 2020 excess nitrogen sorption isotherms at 77 K for the TE 7 III activated carbon beads sample in (a) linear and (b) logarithmic scale of relative pressure. The lines on the plots join points to illustrate trends in the data. Filled and open symbols represent adsorption and desorption points respectively.

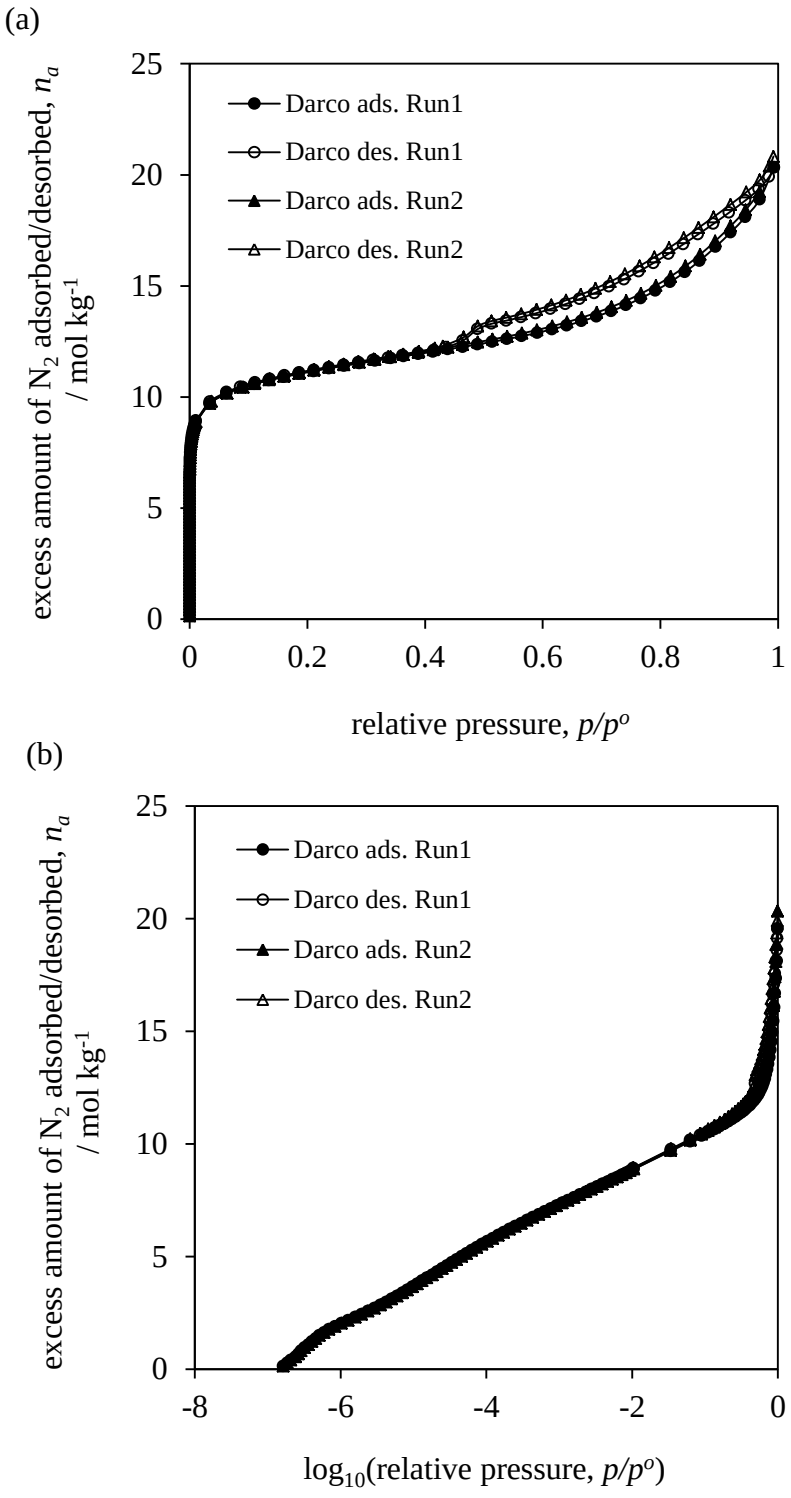

Figure 4.16: Experimental results of volumetric ASAP 2020 excess nitrogen sorption isotherms at 77 K for the Darco activated carbon sample in (a) linear and (b) logarithmic scale of relative pressure. The lines on the plots join points to illustrate trends in the data. Filled and open symbols represent adsorption and desorption points respectively.

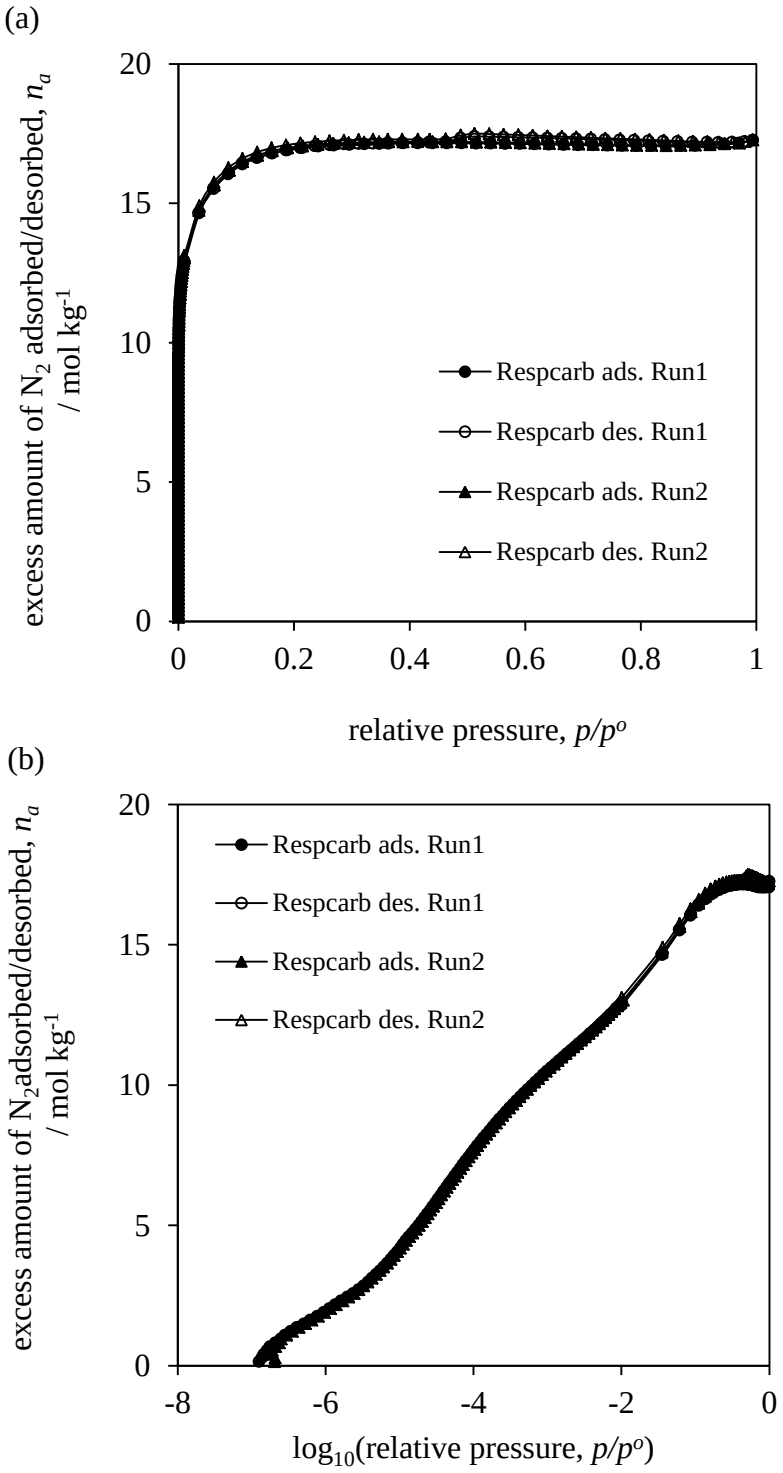

Figure 4.17: Experimental results of volumetric ASAP 2020 excess nitrogen sorption isotherms at 77 K for the Respcarb activated carbon sample in (a) linear and (b) logarithmic scale of relative pressure. The lines on the plots join points to illustrate trends in the data. Filled and open symbols represent adsorption and desorption points respectively.

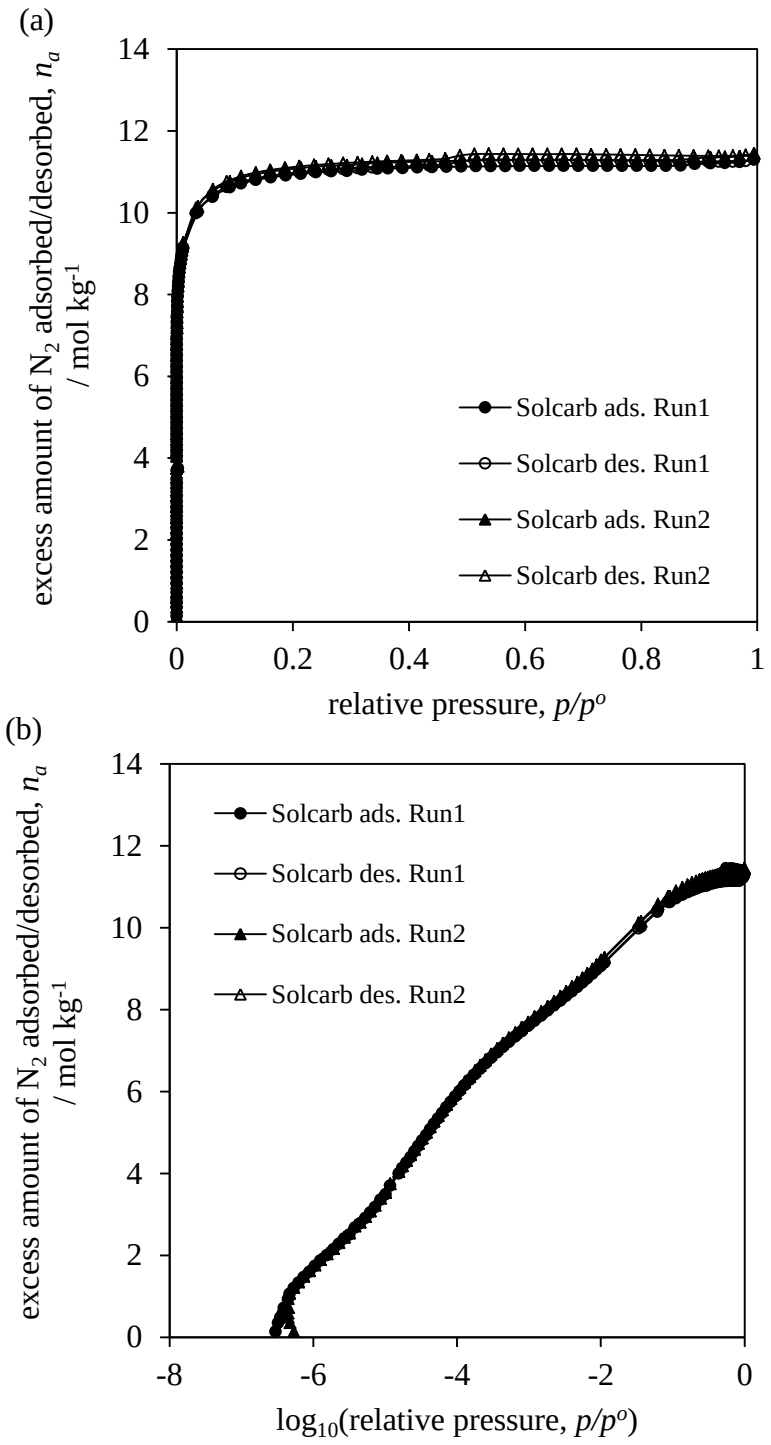

Figure 4.18: Experimental results of volumetric ASAP 2020 excess nitrogen sorption isotherms at 77 K for the Solcarb activated carbon sample in (a) linear and (b) logarithmic scale of relative pressure. The lines on the plots join points to illustrate trends in the data. Filled and open symbols represent adsorption and desorption points respectively.

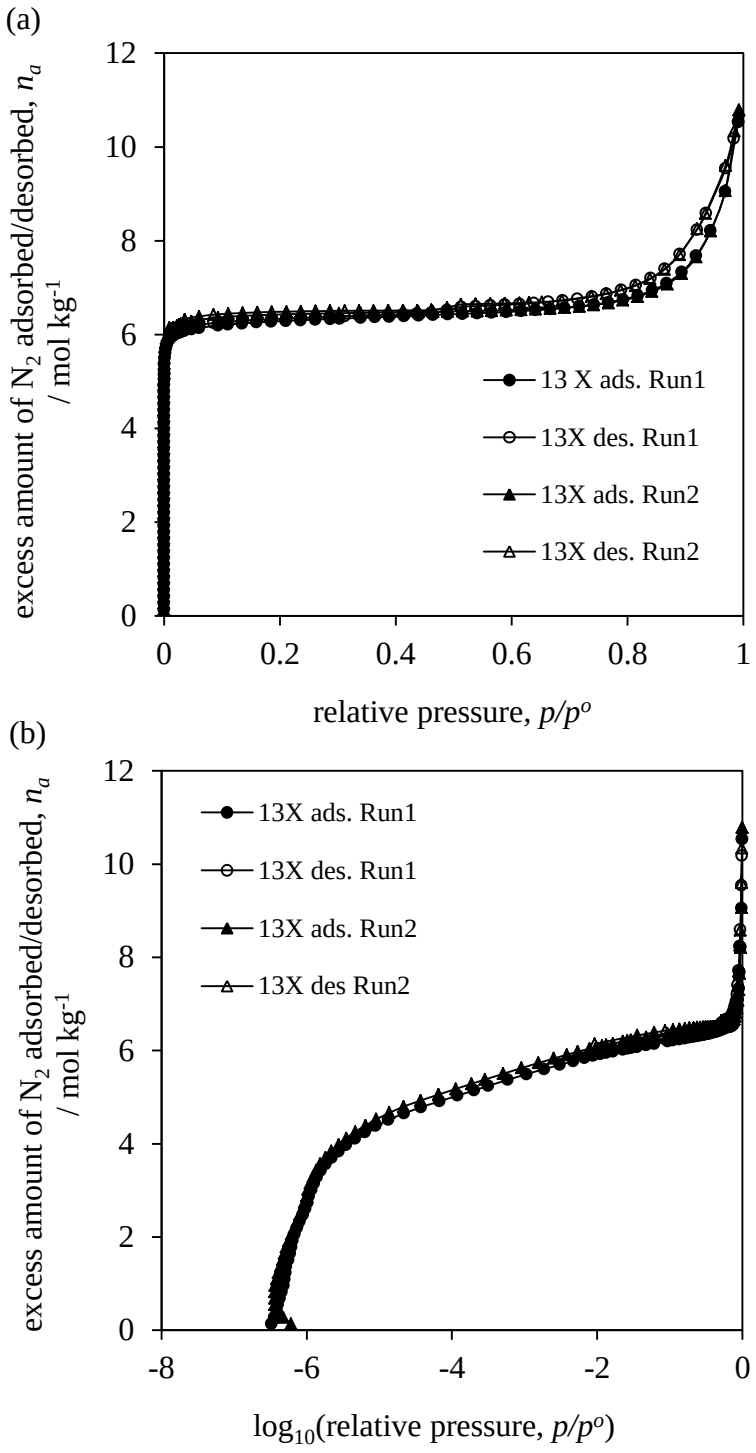

Figure 4.19: Experimental results of volumetric ASAP 2020 excess nitrogen sorption isotherms at 77 K for the 13X zeolite sample in (a) linear and (b) logarithmic scale of relative pressure. The lines on the plots join points to illustrate trends in the data. Filled and open symbols represent adsorption and desorption points respectively.

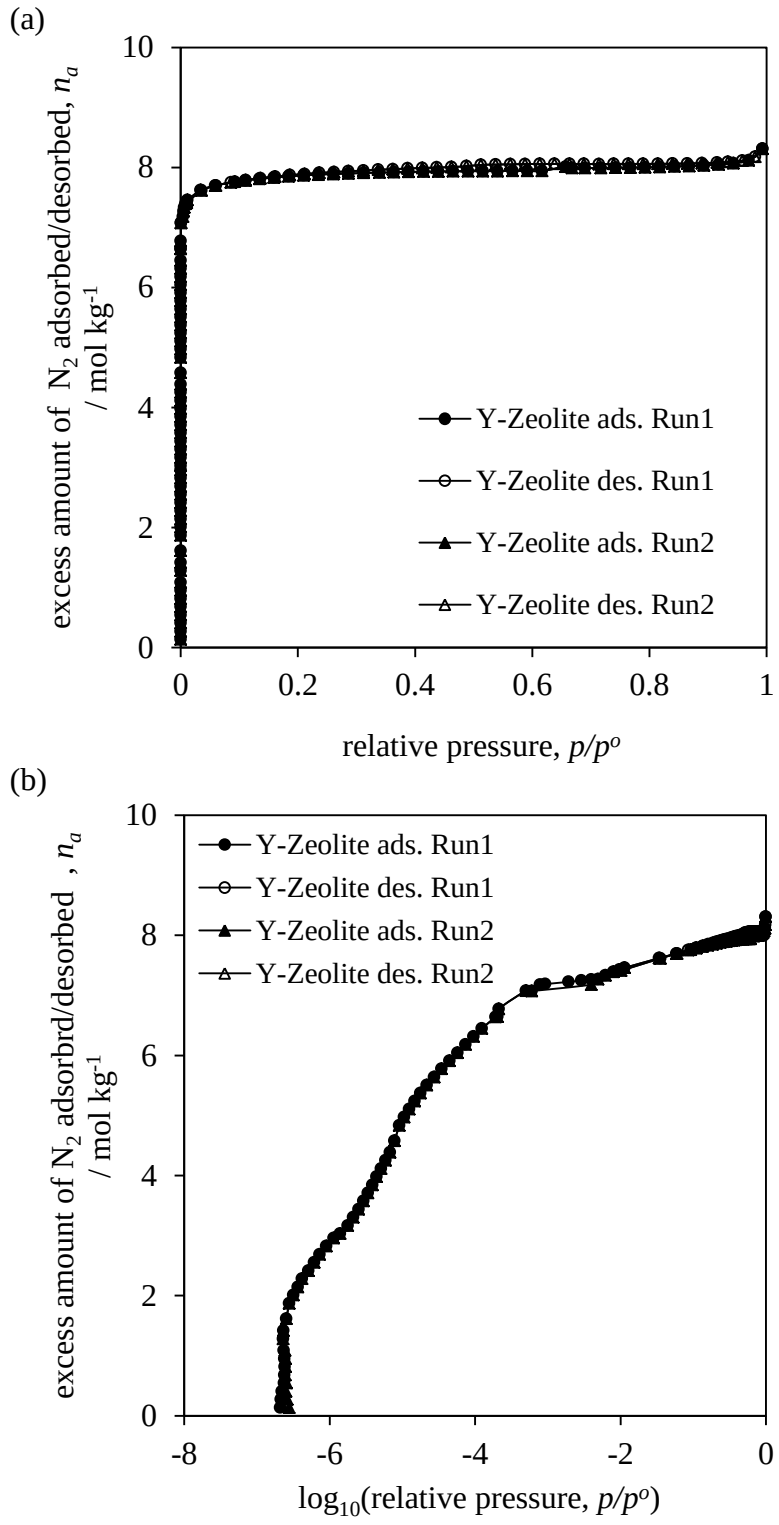

Figure 4.20: Experimental results of volumetric ASAP 2020 excess nitrogen sorption isotherms at 77 K for the Y-Zeolite sample in (a) linear and (b) logarithmic scale of relative pressure. The lines on the plots join points to illustrate trends in the data. Filled and open symbols represent adsorption and desorption points respectively.

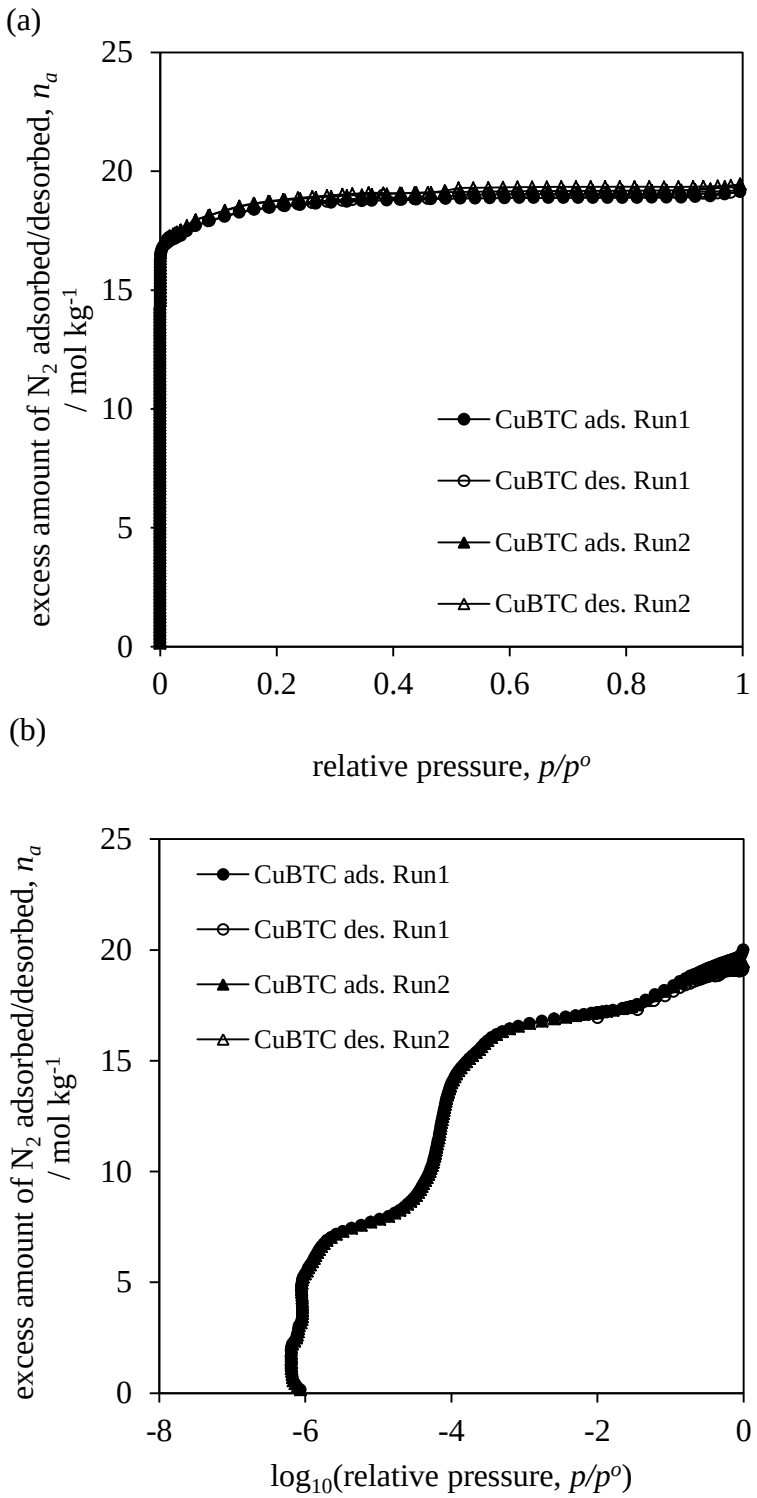

Figure 4.21: Experimental results of volumetric ASAP 2020 excess nitrogen sorption isotherms at 77 K for the Cu-BTC metal organic framework sample in (a) linear and (b) logarithmic scale of relative pressure. The lines on the plots join points to illustrate trends in the data. Filled and open symbols represent adsorption and desorption points respectively. Note, unusual shape of the isotherm seen in low relative pressures is attributed to problems with sample degassing.

Table 4.6: Comparison between excess amounts of nitrogen adsorbed obtained from two individual ASAP 2020 experiments at different relative pressures. Results are displayed as a ratio Run1/Run2 together with a mean and standard deviation obtained from two independent determinations.

material class	relative pressure, p/p^o	excess amount adsorbed, n_a / mol kg^{-1}		ratio	ratio mean ± standard deviation
		Run 1	Run 2		
TE 7 I	0.2	19.1904	18.9247	1.0140	1.0230 ± 0.0166
	0.6	20.8536	20.0090	1.0422	
	1.0	42.0521	41.5191	1.0128	
TE 7 II	0.2	13.0361	12.8368	1.0155	1.0006 ± 0.0192
	0.6	13.5727	13.8252	0.9817	
	1.0	35.1796	35.0191	1.0046	
TE 7 III	0.2	11.2260	10.9425	1.0259	1.0583± 0.0206
	0.6	11.9735	11.8273	1.0124	
	1.0	35.4598	31.1960	1.1366	
Darco	0.2	11.1635	11.1967	0.9970	0.9898 ± 0.0076
	0.6	12.8919	13.0157	0.9905	
	1.0	18.8884	19.2355	0.9819	
Respcarb	0.2	16.9765	17.0553	0.9954	0.9996 ± 0.0054
	0.6	17.1278	17.1684	0.9976	
	1.0	17.2556	17.1584	1.0057	
Solcarb	0.2	10.9515	11.0946	0.9871	0.9872 ± 0.0025
	0.6	11.1414	11.2856	0.9872	
	1.0	11.2990	11.4452	0.9872	
13X	0.2	6.2918	6.4331	0.9780	0.9836 ± 0.0106
	0.6	6.4835	6.5107	0.9958	
	1.0	10.5357	10.7849	0.9769	
Y-Zeolite	0.2	7.8674	7.8675	0.9999	0.9989 ± 0.0006
	0.6	7.9302	7.9418	0.9985	
	1.0	8.2974	8.3108	0.9984	
Cu-BTC	0.2	18.8946	18.7811	1.0060	1.0170 ± 0.0111
	0.6	19.4723	19.1521	1.0167	
	1.0	20.0029	19.4513	1.0283	

Figure 4.22 shows a comparison of 77 K nitrogen, 87 K argon and 273 K carbon dioxide sorption isotherms determined for the representative TE 7 III sample on the volumetric ASAP 2020 analyser. Note that these adsorptives have different molecular sizes and measurement temperatures, so we are not expecting them to yield the same isotherms. The 87 K argon isotherms were collected at relative pressures up to 1.00 p/p^o, with the 273 K carbon dioxide to 0.03 p/p^o, required to maintain the maximum pressure within limits of 1 bar sorption apparatus. It is observed that for nitrogen, adsorption in micropores begins at relative pressures close to 10^{-7}, so in order to measure the initial part of the isotherm very high vacuum conditions are necessary. For argon, adsorption begins at about 10^{-6} p/p^o. In the case of carbon dioxide, adsorption starts at about 10^{-4} p/p^o so the initial part of the isotherm can be more easily determined. This comparison clearly demonstrates that in order to analyse adsorption in micropores it is more convenient and beneficial to use CO_2 at 273 K rather than N_2 at 77 K or Ar at 87 K (Anson et al., 2004). Further information about materials characteristic, such as micropore volume and surface area yielded from the presented sorption isotherms are all important parameters for hydrogen storage capacities, and are discussed in following sections.

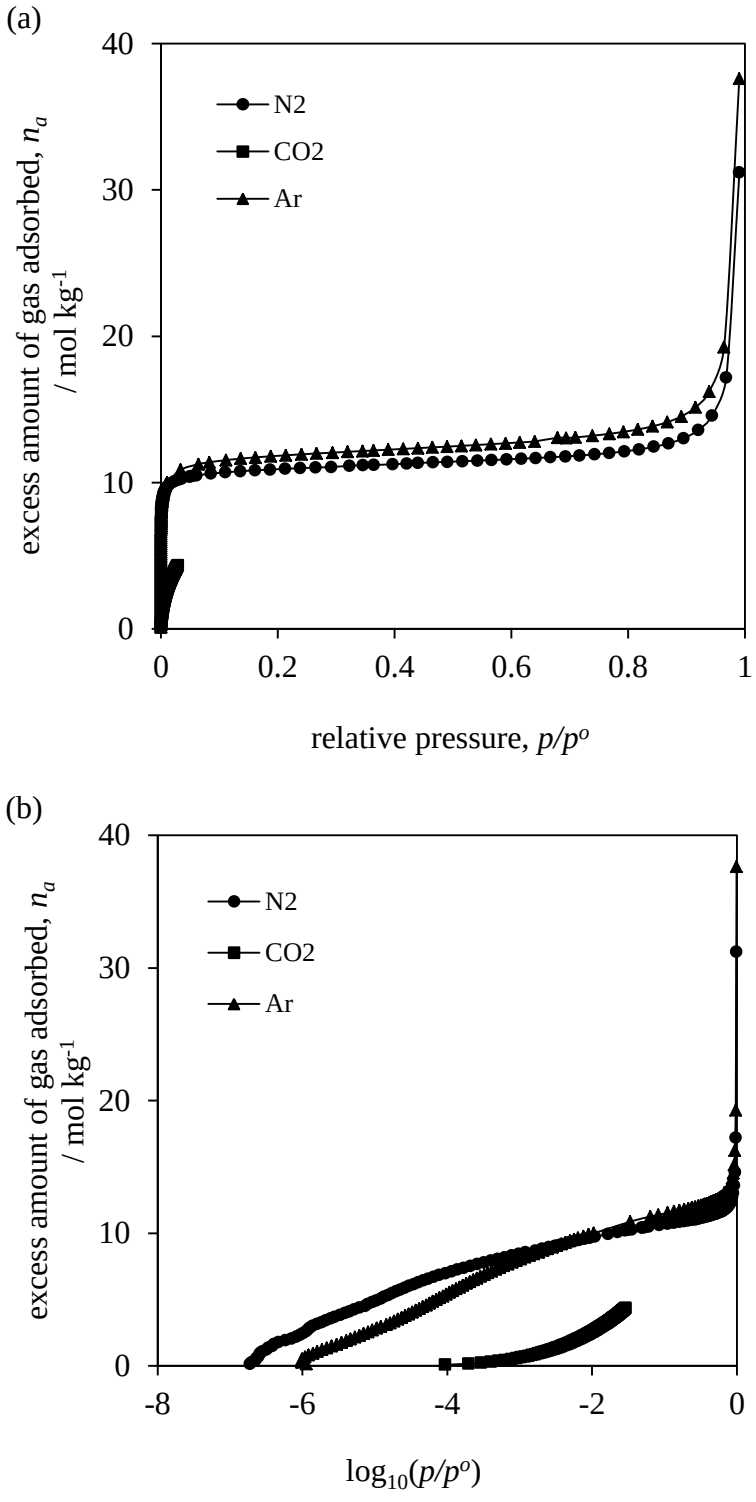

Figure 4.22: Experimental results of volumetric ASAP 2020 excess nitrogen (77 K), carbon dioxide (273 K) and argon (87 K) adsorption isotherms for the TE III carbon beads sample in (a) linear and (b) logarithmic scale of relative pressure. The lines on the plots join points to illustrate trends in the data.

So far, all adsorption isotherms presented here were obtained from volumetric experiments by using the ASAP 2020 analyser, which is one of the gas sorption devices available in our lab. Now we want to use the IGA gravimetric microbalance to analyse the same TE 7 III carbon bead sample and compare the results from both methods. As stated previously in Chapter 3, both setups have the same basic components such as reference volume, measuring sample cell, valves, high accuracy pressure transducers and the temperature control unit. In the volumetric measurements the amount of gas adsorbed is determined by measuring the change in pressure, while the gravimetric isotherm is determined by the weight change of the sample recorded during procedures. Both volumetric and gravimetric methods used helium as the reference gas to determinate the buoyancy (gravimetry) and dead volume of the sample cell (volumetry), assuming that helium is none adsorbing at these conditions (see Section 4.2.2.6 for more details).

Figure 4.23 to Figure 4.25 show a comparison of the ASAP 2020 adsorption isotherms with those obtained from the IGA experiments in the linear and logarithmic scale of the relative pressures for different adsorptive types. As can be seen all the volumetric isotherms are close to the gravimetric with an uncertainty (standard deviation) of around 2.50 %. The calculated volumetric/gravimetric ratios determined at different relative pressures are displayed in Table 4.7. This identity of the results validates the correctness of both methods applied in our lab to determine the gas sorption isotherms for different adsorptives.

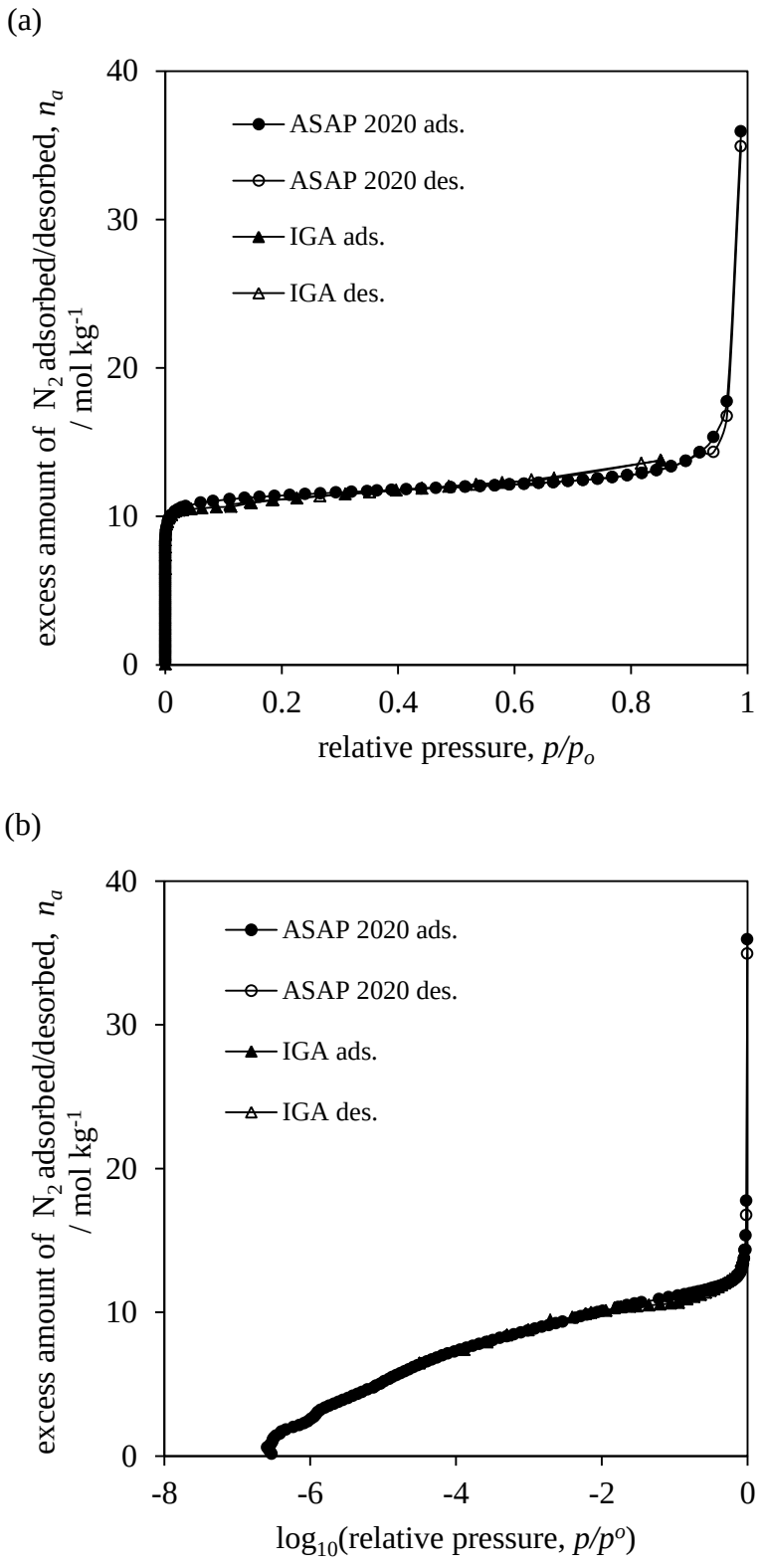

Figure 4.23: Experimental results for excess nitrogen sorption isotherms, at 77 K for a reference sample of TE 7 III activated carbon beads in (a) linear and (b) logarithmic scale of relative pressure, measured using different instrumental techniques available in-house.

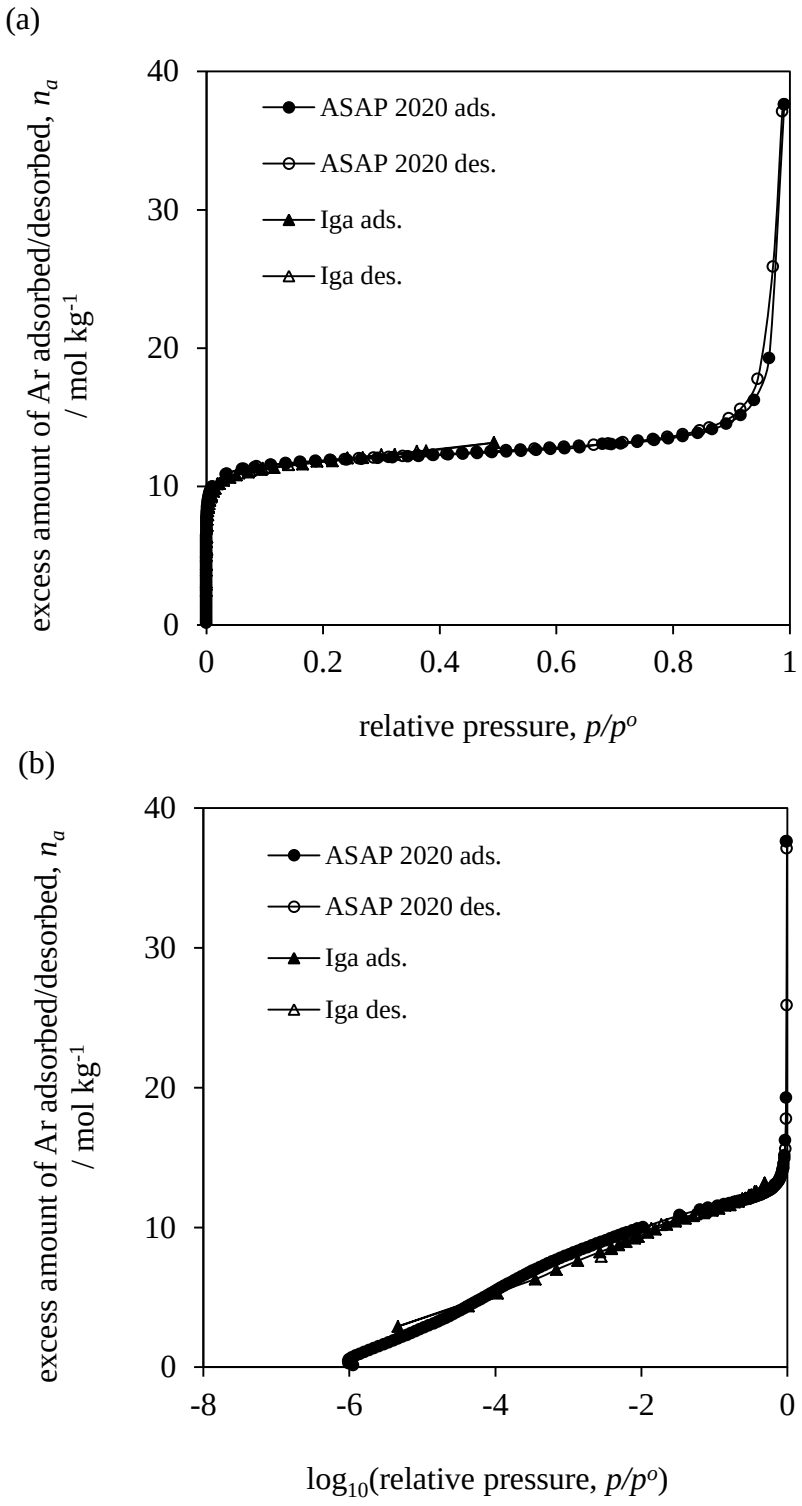

Figure 4.24: Experimental results for excess argon sorption isotherms, at 87 K for a reference sample of TE 7 III activated carbon beads in (a) linear and (b) logarithmic scale of relative pressure, measured using different instrumental techniques available in house.

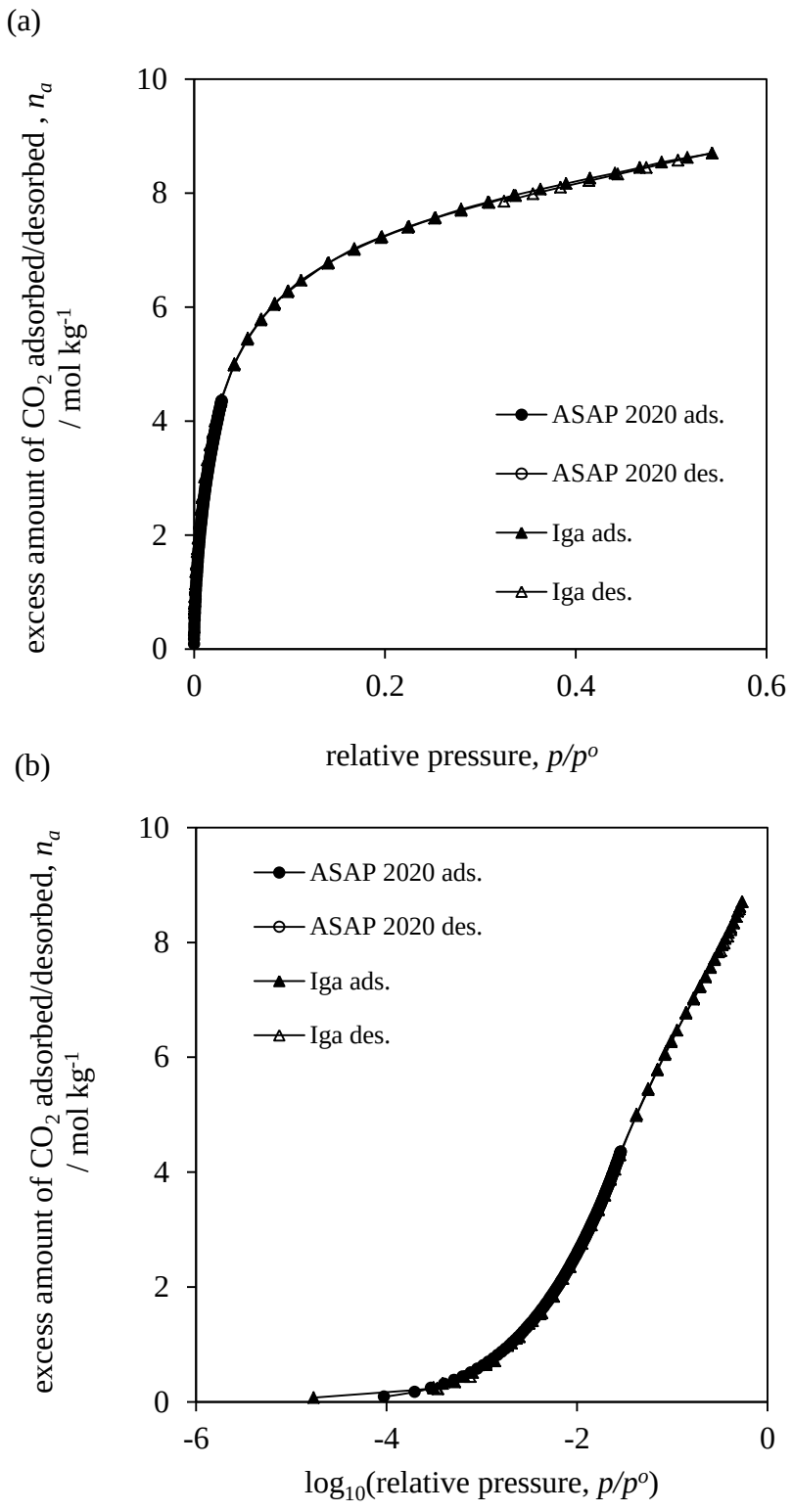

Figure 4.25: Experimental results for excess carbon dioxide sorption isotherms, at 273 K for a reference sample of TE 7III activated carbon beads in (a) linear and (b) logarithmic scale of relative pressure, measured using different instrumental techniques available in house.

Table 4.7: Comparison between amounts of gas adsorbed obtained from the volumetric and the gravimetric experiments. Results are displayed as a mean together with a standard deviation determined from the volumetric/gravimetric ratios for all three adsorptive types.

adsorptive	relative pressure, p/p^o	excess amount adsorbed, n_a / mol kg^{-1}		ratio
		volumetric	gravimetric	
N_2	0.2	11.3741	11.1022	1.0245
	0.6	12.0829	12.2726	0.9845
	0.8	12.7544	13.5682	0.9400
Ar	0.1	11.3551	11.3037	1.0045
	0.2	11.8306	11.8108	1.0017
	0.5	12.5442	13.1677	0.9526
CO_2	0.001	1.0218	1.0472	0.9757
	0.02	3.8103	3.8180	0.9979
	0.03	4.3544	4.3713	0.9961
			mean	0.9864
			stand. dev.	0.0250

Further method inspection, on the recently installed HTP-1 high pressure volumetric analyzer yield very good isotherms reproducibility, ensuring high measurement performance in our lab (see Figure 4.26).

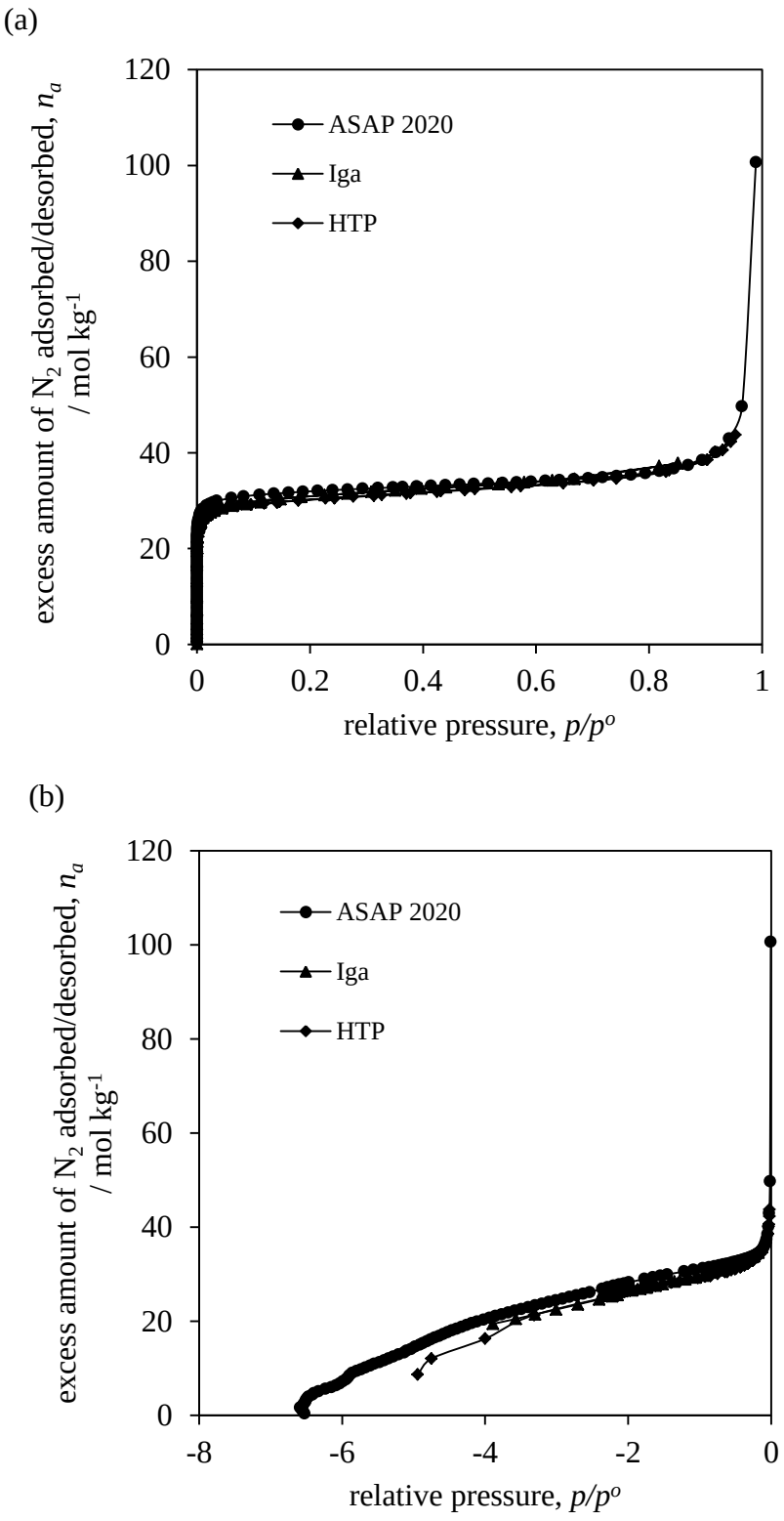

Figure 4.26: Experimental results for excess nitrogen sorption isotherms, at 77 K for a reference sample of TE 7 III activated carbon beads in (a) linear and (b) logarithmic scale of relative pressure, measured using three different gas sorption devices available in-house.

4.2.2.2 Surface Area Determination

In this section some important aspects and challenges associated with a qualitative assessment of the specific surface area for the microporous samples is discussed. The surface area is strictly a materials characterisation technique, although it is more frequently linked to the hydrogen storage capacity and is a very important factor in developing new materials and methods for this application. This is because of the fact that many nanoporous samples quoted in the literature show linear correlation between the amounts of hydrogen adsorbed and their surface area (Thomas, 2007, Bastos-Neto et al., 2012, Hirscher et al., 2010). However, note that this is only a general trend and there are some others influencing factors preferred in hydrogen sorption in different adsorbents, as reviewed later.

Currently, a benchmark for the specific surface area determination is by applying the Brunauer-Emmett and Teller (BET) theory (Brunauer, 1938) to the nitrogen adsorption isotherm measured up to 1 bar at 77 K. This is a standard routine which involves resolving of the BET equation, which in the linear form can expressed as:

$$\frac{p/p^o}{n_a(1-p/p^o)} = \frac{1}{n_m \times C} + \frac{(C-1)}{n_m \times C} \times p/p^o \tag{4.3}$$

where, p is the equilibrium pressure, p^o is the saturation vapor pressure of adsorptive, n_a is the specific amount of gas adsorbed at the relative pressure p/p^o, n_m is the monolayer capacity of adsorbate also known as the maximum capacity and C is the BET parameter describing the strength of interaction between the adsorbent and adsorbate, exponentially related to the heat of adsorption in the monolayer (Rouquerol et al., 1999):

$$C = \exp \times \left(\frac{E_1 - E_L}{RT} \right) \tag{4.4}$$

where, E_1 is the heat of adsorption for the first layer, and E_L is the heat of adsorption for the second and higher layers and is equal to the heat of liquefaction. According to the BS method (BS, 2010) the BET diagram, $\frac{p/p^o}{n_a(1-p/p^o)}$ plotted against p/p^o should give a straight line ($y=a+bx$) over limited range of pressure p/p^o=0.05–0.3, with a slope $b=\frac{\Delta y}{\Delta x}=\frac{(C-1)}{(n_m \times C)}$ and a positive intercept $a=\frac{1}{(n_m \times C)}$. The values of monolayer capacity can then be found by inputting the values of a and b into:

$$n_m = \frac{1}{(a+b)} \tag{4.5}$$

The C parameter used to indicate adsorbate-adsorptive interaction can be found from:

$$C = \frac{1}{(b/a)} \tag{4.6}$$

with a view of keeping quite sharp knee of the isotherm with the C parameter no less than 100, such values lower than 20 creates doubt for the BET method validity (Rouquerol et al., 1994, Sing et al., 1985).The BET specific surface area (a_s) per unit mass of the degassed sample can be calculated from monolayer capacity, n_m and the molecular cross-sectional area, σ, thus:

$$a_s = n_m \times L \times \sigma \tag{4.7}$$

where, L is the Avogadro constant.

It is often assumed that the BET nitrogen monolayer is closed packed giving, σ value equal to 0.162 nm^2 at 77 K and then Equation 4.7 becomes:

$$a_s = 9.76 \times 10^4 \times L \times \sigma \tag{4.8}$$

However, note that a constant value of σ is very unlikely and so caution should be exercised when quoting surface areas calculated in this way. Also, it must be realized that the BET theory can provide only an estimate of the specific surface area, thus it relies on some underlying assumptions for the uniform surface energy in all adsorption sides (*i.e.* $E_2=E_1=E_L$), for an infinite multilayer thickness at saturation pressure $p/p^o=1$ ($\rightarrow \infty$) and that no lateral interactions between molecules exist, which is not always the case for microporous sample (Rouquerol et al., 1999).

Based on the BS specifications the linear BET plots were created for each tested samples and the results summarized in Table 4.8 (all resulting BET plots for are provided in Supplementary Information, Section S3). It can be seen that all values of the BET parameter *C* are negative, which is unphysical and could imply that the BET equation does not correlate with the geometrical heterogeneity of the surface and is not suitable to adequately describe the particular experimental data. In this case, the BET surface area can provide only a semi-quantitative number which here will be used just for the materials comparison. In these context the highest BET specific surface area was the activated carbon TE 7 I (1332.8 ± 35.7 m^2 g^{-1}), with the 13X zeolite appearing to have the least (429.2 ± 11.7 m^2 g^{-1}).

Table 4.8: Summary of BET parameters obtained from volumetric ASAP 2020 nitrogen adsorption isotherms at 77 K based on the British Standard method. The quoted errors represent the standard deviation evaluated form error propagation analysis.

material	relative pressure range, p/p^o	monolayer capacity, n_m / mol kg^{-1}	BET parameter, *C*	BET specific surface area, a_s / m^2 g^{-1}
TE 7 I	0.0599 – 0.2947	13.6 ± 0.4	- 54.3 ±14.4	1332.8 ± 35.7
TE 7 II	0.0633 – 0.2907	9.1 ± 0.8	- 41.9 ± 8.9	887.8 ± 74.7
TE 7 III	0.0610 – 0.2933	8.0 ±0.2	- 43.9 ± 9.7	780.4 ± 19.5
Darco	0.0627 – 0.2885	8.1 ± 0.2	- 57.4 ± 13.3	786.5 ± 17.1
Respcarb	0.0610 – 0.2956	11.8 ± 0.1	- 44.4 ± 11.4	1157.0 ± 8.1
Solcarb	0.0617 – 0.2932	7.6 ± 0.5	- 41.0 ± 9.2	741.4 ± 9.2
13X	0.0607 – 0.2871	4.4 ± 0.1	- 40.1 ± 8.2	429.2 ± 11.7
Y-Zeolite	0.0588 – 0.2864	5.5 ± 0.1	- 40.0 ± 8.3	536.6 ± 9.7
Cu-BTC	0.0615 – 0.2939	12.9 ± 0.4	- 42.1 ± 9.5	1259.6 ± 39.0

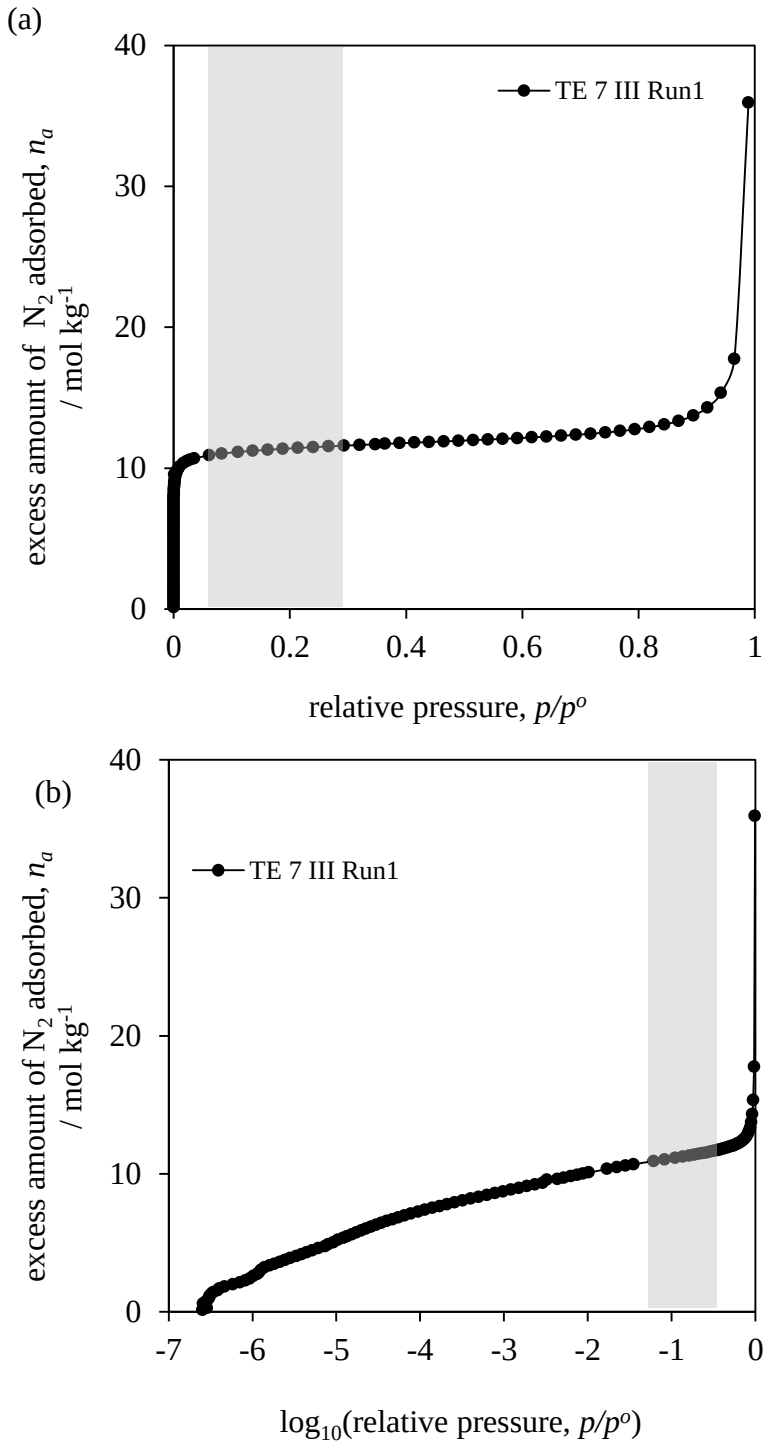

Figure 4.27: Excess nitrogen sorption isotherm for the TE 7III carbon beads sample in (a) linear and (b) logarithmic scale, showing the recommended British Standard pressure range 0.05–0.3 p/p^o (marked grey) used to calculate the BET specific surface area. The lines on the plots join points to illustrate trends in the data.

Therefore, it seems that several pressure ranges for plotting BET isotherms give roughly good linearity, which could create doubts for further surface area determination. In this respect some possible combinations of the BET plots are examined here, where the TE 7 III nitrogen isotherm shown in Figure 4.27 is used as an example of applied analysis.

Firstly, the primary results of nitrogen adsorption are transformed into a BET plot and then the monolayer capacity (n_m), the BET parameter C and the specific surface area (a_s) are calculated based on the best fitted line. In the case of standard analysis, restricted to the pressure range from 0.05 to 0.3, ten data points were used for fitting the linear regression as shown in the Figure 4.28. It is clear that these data points do not fall on a straight line but create bias (see Figure 4.29), with a maximum deviation of around 0.15 %.

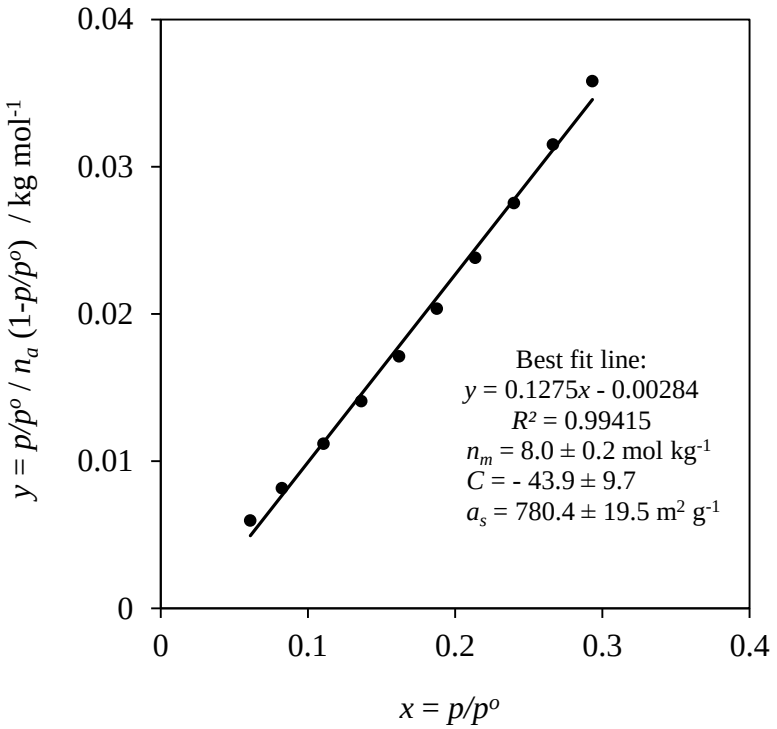

Figure 4.28: Linear fit to low pressure BET nitrogen sorption data for the TE 7 III activated carbon beads sample using the British Standard range (p/p^o=0.05–0.3).

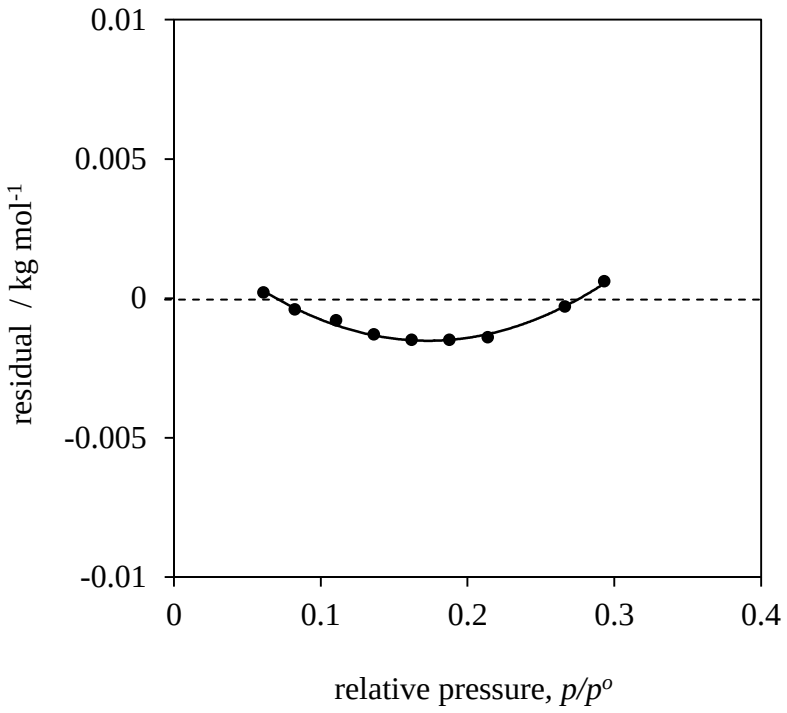

Figure 4.29: Residual plot of the linear BET fit on the TE 7 III activated carbon beads sample, recorded over the British Standard pressure range (p/p^o=0.05–0.3).

Also, it was found that different subsets of the pressure points give a different BET surface area result as is demonstrated in Figures 4.30 to 4.33 below. Figure 4.34 compares the BET surface areas determined from different data points within, above and below BS range. The dataset marked as a pink dotted line was considered to present the reference behavior, with the BET surface area value assigned as 780.4 m^2 g^{-1}. When considering 1st and 2nd datasets of five alternative points (see Figure 4.30) around 2.50 % deviation in relation to the reference value was found. Adding an extra point in fitting the BET plot underestimated a_s value around 10 % (see Figure 4.33). The difference became more significant when shifting the BET range to lower relative pressures, and this appears in the data presented in Figure 4.32. In this case the surface area is overestimated by around 12.50 %. These results clearly demonstrate a large variation in the determined surface areas due to the variety of linearity ranges applied for further BET calculations.

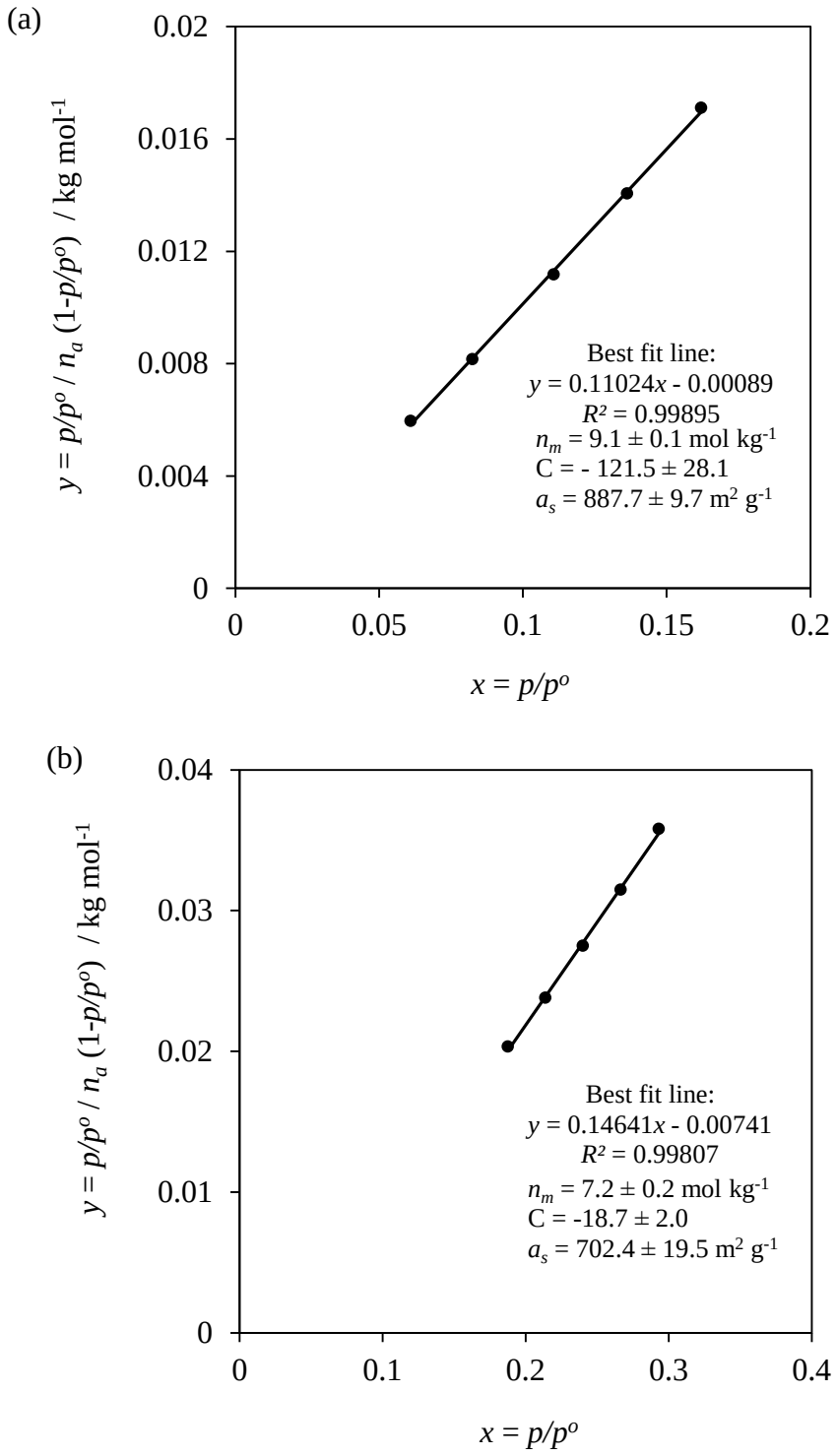

Figure 4.30: Linear fit to low pressure BET nitrogen sorption data using (a) 1st and (b) 2nd five data points in the British Standard range (p/p^o=0.05–0.3).

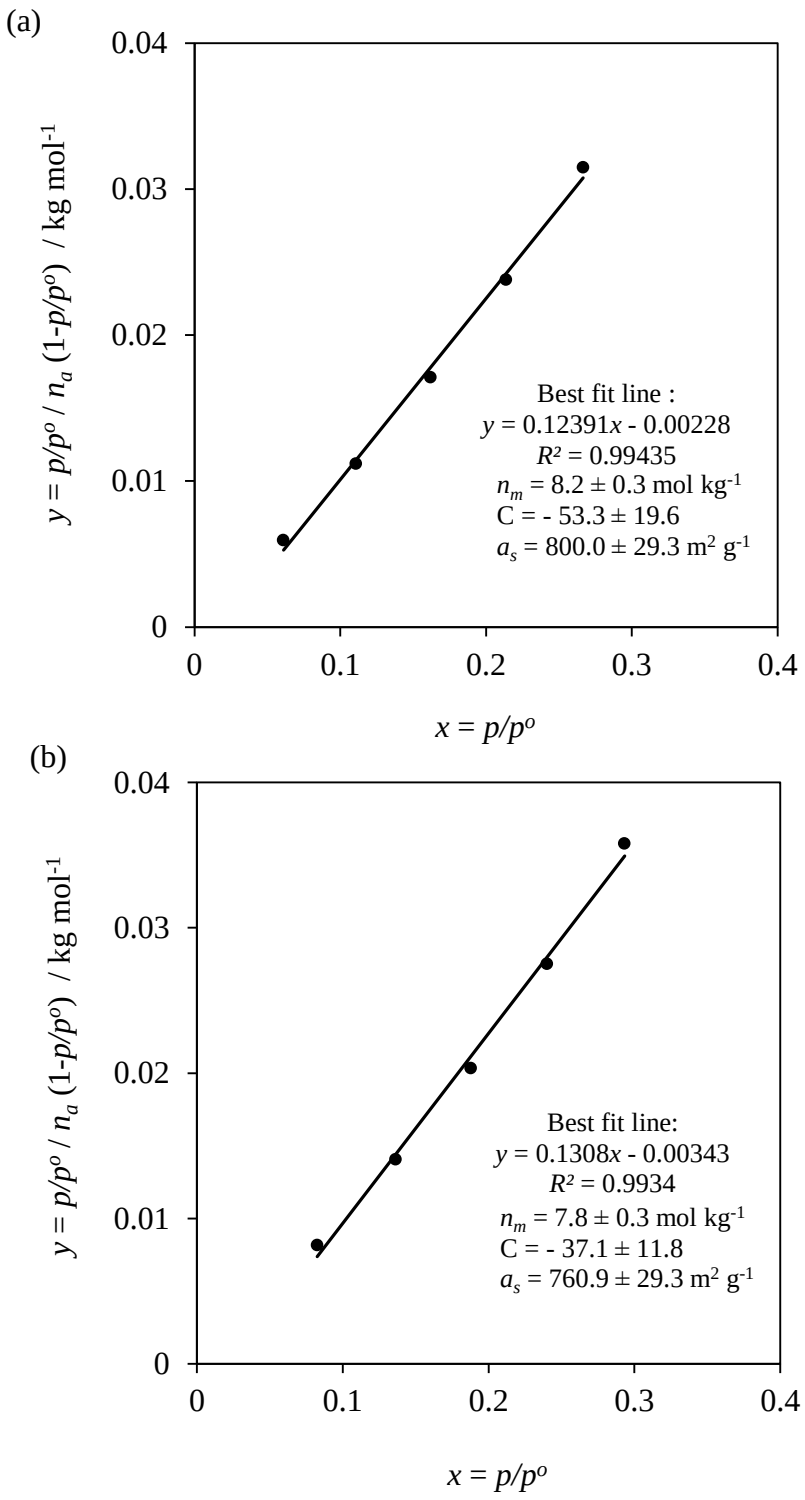

Figure 4.31: Linear fit to low pressure BET nitrogen sorption data using (a) 1st and (b) 2nd set of the alternative data points in the British Standard range (p/p^o=0.05–0.3).

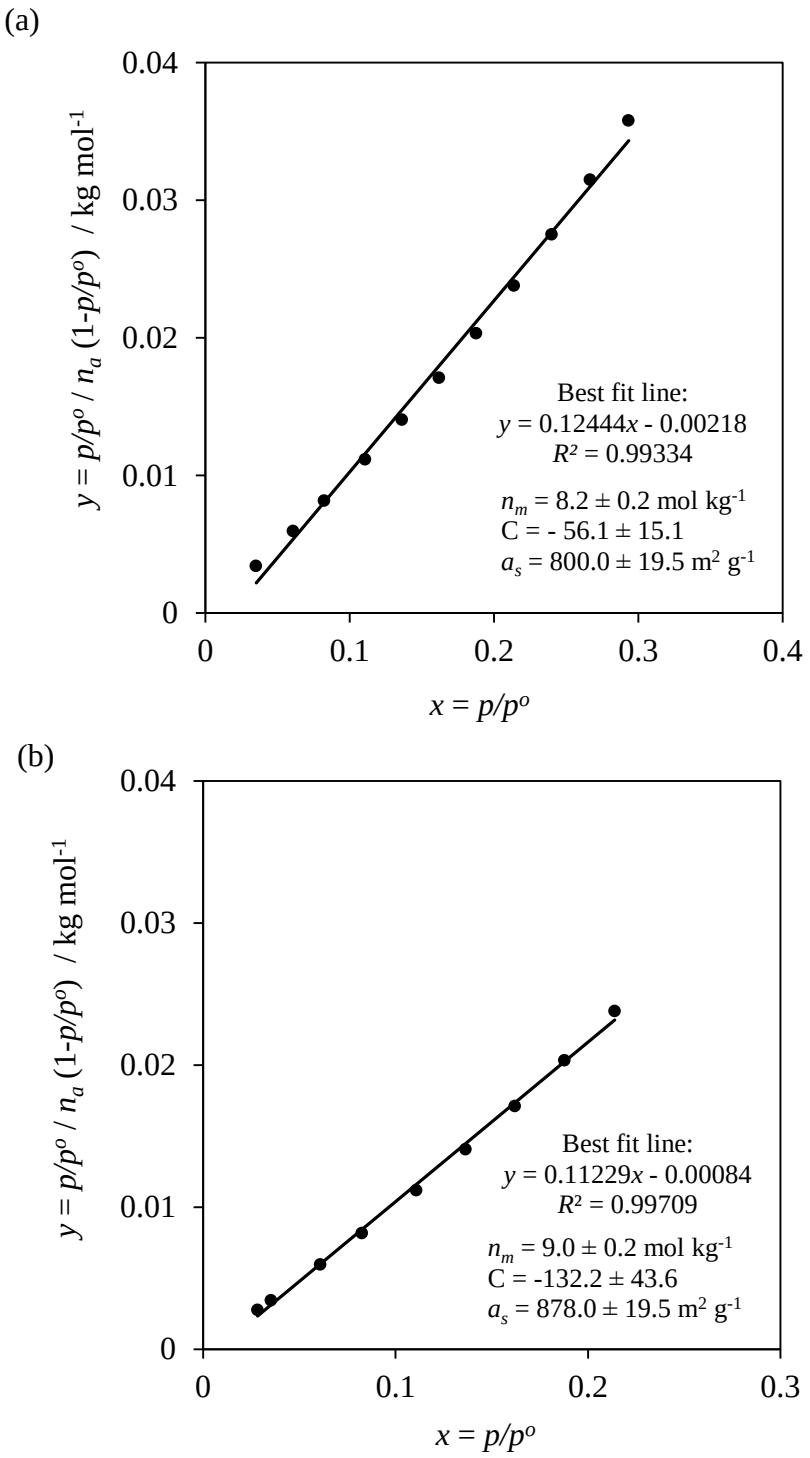

Figure 4.32: Linear fit to low pressure BET nitrogen sorption data recorded below the British Standard range (a) p/p^o=0.04–0.3 and (b) p/p^o=0.03–0.3.

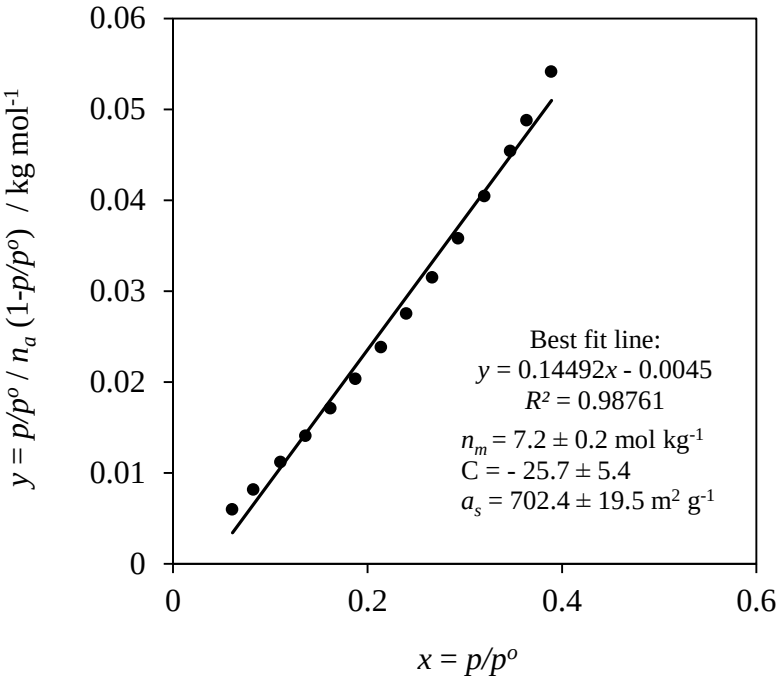

Figure 4.33: Linear fit to low pressure BET nitrogen sorption data recorded above the British Standard range (p/p^o=0.05–0.4).

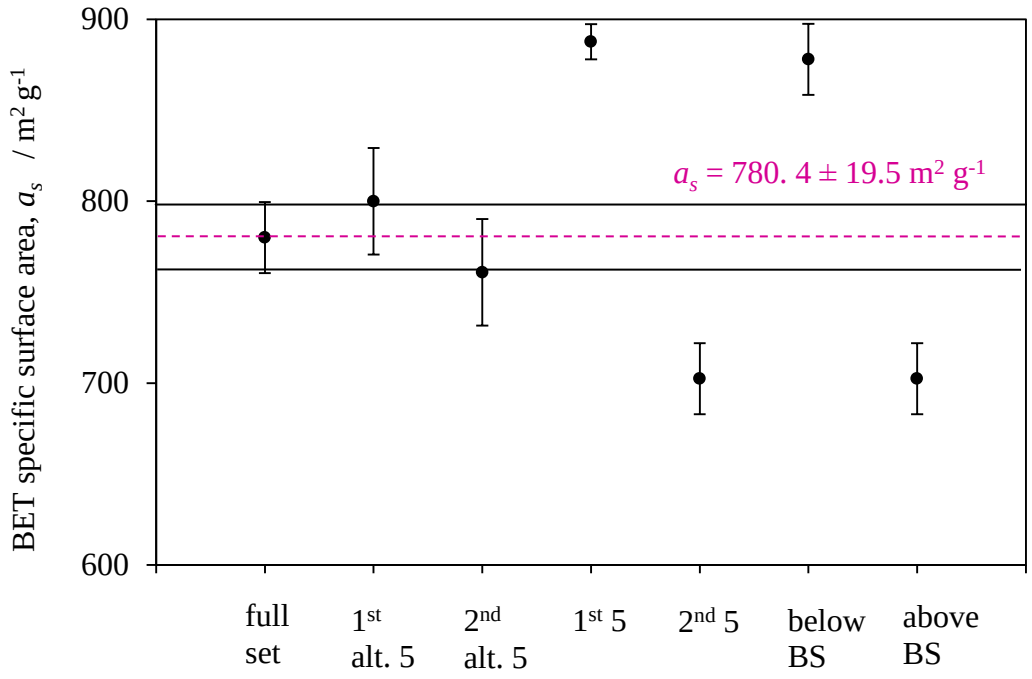

Figure 4.34: Variation of the BET specific surface area within, below and above the British Standard range. The dotted line (---) represent the reference value assigned as 780.4 m^2 g^{-1}, the solid line (—) indicate a ± 19.5 m^2 g^{-1} deviation. The error bars represent the standard deviation.

Table 4.9: Variation of BET parameters for different data subsets and pressure ranges for the TE 7 III activated carbon beads nitrogen isotherm at 77 K. The quoted errors represent the standard deviation valuated form error propagation analysis.

data set	monolayer capacity, n_m / mol kg^{-1}	BET parameter, C	BET specific surface area, a_s / m^2 g^{-1}
Full Set	**8.0 ± 0.2**	**- 43.9 ± 9.7**	**780.4 ± 19.5**
1st alternative 5	8.2 ± 0.3	- 53.3 ± 19.6	800.0 ± 29.3
2nd alternative 5	7.8 ± 0.3	- 37.1 ± 11.8	760.9 ± 29.3
1st 5	9.1 ± 0.1	- 121.5 ± 28.1	887.7 ± 9.7
2nd 5	7.2 ± 0.2	- 18.7 ± 2.0	702.4 ± 19.5
Below BS range	9.0 ± 0.2	- 132.2 ± 43.6	878.0 ± 19.5
Above BS range	7.2 ± 0.2	- 25.7 ± 5.4	702.4 ± 19.5

Until now all BET surface areas presented here are based on the universal nitrogen isotherms at 77 K determined via the British Standard method. However, it is more important in experimental practice to study other adsorptives, because the quadrupole moment of diatomic nitrogen causes an orientation problem on the heterogeneous surface and depending on the molecule layout the accessibility to the pores can be limited (Marsh and Wynnejones, 1964, Sweatman and Quirke, 2001). Here, as an alternative approach, argon sorption at 87 K is suggested, since it is composed of perfectly spherical monoatomic molecules and is chemically inert, which provides the possibility of more accurate surface area determination then nitrogen (Sing and Williams, 2004, Jagiello and Thommes, 2004).

Figure 4.35 shows the BET parameters obtained from Ar isotherm at 87 K. Similar like to nitrogen, biased linearity for the BET plot in the standard pressure range is observed, again concerning the applicability of the BS method for the characterisation of this microporous samples. Also, the a_s value is around 11 % lower compared to nitrogen, which can be attributed to a more dense packing of spherical argon molecules.

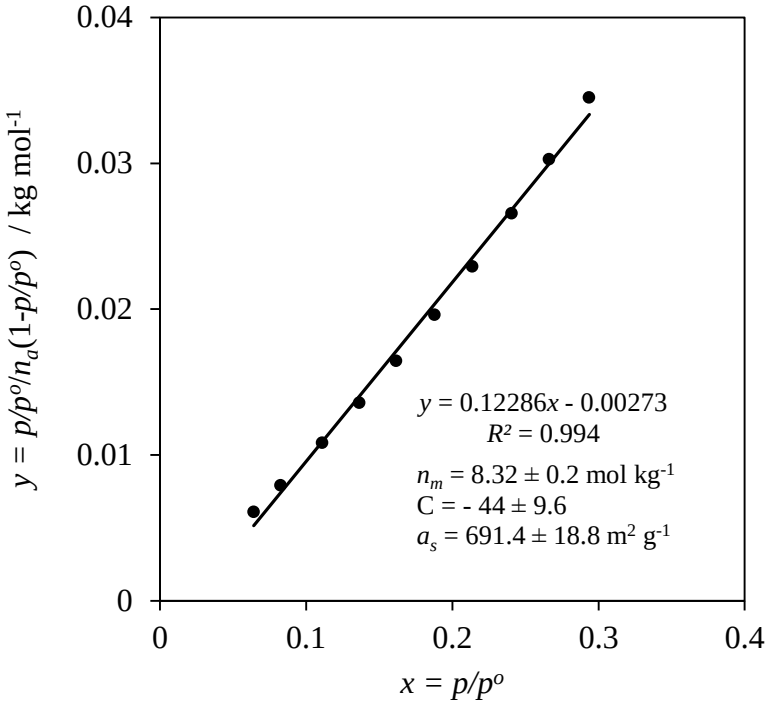

Figure 4.35: Linear fit to low pressure BET Ar at 87 K sorption data for the TE7 III activated carbon beads sample recorded in the British Standard range (p/p^o=0.05–0.3).

CO_2 sorption at 273 K is also considered here, as the most favorable in studies of narrow microporosity (ultramicropores smaller than 0.7 nm), as molecules diffusion and relaxation is much faster ensuring faster analysis and greater confidence that adsorption equilibrium is fully achieved (Thommes, 2010, Sing and Williams, 2004, Jagiello and Thommes, 2004). In fact the BET surface area yielded in this way is still in close agreements with those determined for Ar at 87 K (~ 0.80 % lower).

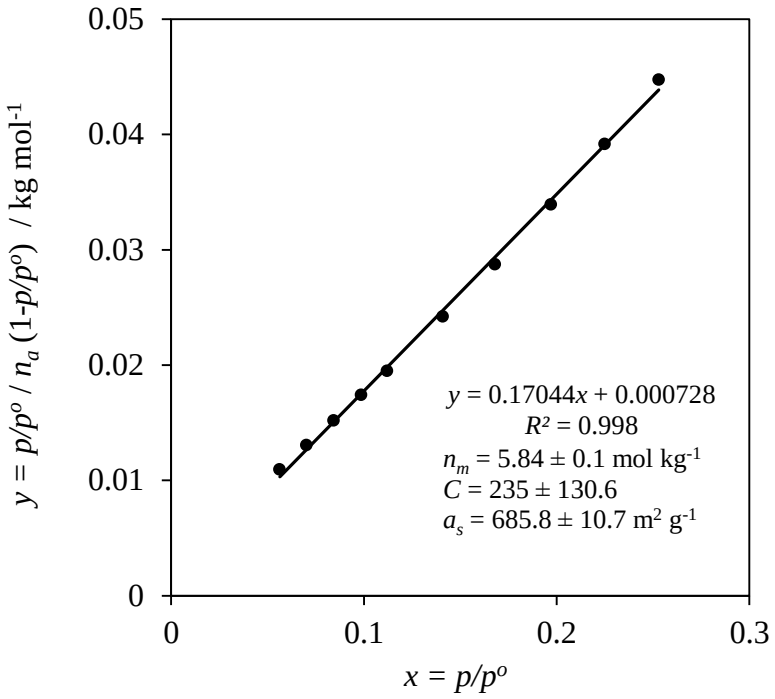

Figure 4.36: Linear fit to low pressure BET CO_2 at 273 K sorption data for the TE7 III activated carbon beads sample recorded in the British Standard range (p/p^o=0.05–0.3).

In our study, there are also some concerns about the molecular cross-sectional area, σ, which need to be known accurately for BET surface area determination. As can be seen from Table 4.10 below a very wide range of σ values can be found in the literature, depending on the adsorbent, adsorptive type and the calculation method. For example, for diatomic nitrogen, σ parameter calculated from the liquid density method ranges from 0.135 to 0.176 nm. For this non spherical molecule, having van der Waals diameters of 0.41 × 0.30 nm the maximum (most probable in adsorption) cross-sectional area is projected to be 0.101 nm^2 (Karnaukhov, 1985). However, for simplicity it is assumed that the nitrogen molecule is spherical, and that it is packed like a liquid on the adsorbent surface and that the σ value calculated from its density in a liquid state is equal to 0.162 nm^2, which strongly differs from values determined by other methods. Although, this value is still the most widely cited nitrogen cross-sectional area in a large number of papers even for microporous samples, which can lead potentially to large inaccuracy, as the more the molecule deviates from spherical the greater the error could be.

Table 4.10: Summary of adsorptive molecular cross-sectional areas and molecular diameters for nitrogen, argon and carbon dioxide molecules obtained from liquid density, Lennard-Jones and van der Waals methods.

adsorbate	molar mass, M / g mol^{-1}	molecular cross-sectional area, σ* / nm^2	molecular diameter, d / nm			references
			liquid density	Lennard-Jones	van der Waals	
H_2	2.0158	0.154[4] **0.142**[14] 0.083[4]	0.443 0.425 0.325	0.287[30] 0.289[1]	0.304[34]	[1](Sircar, 2006) [2](Rhodin, 1953) [3](Emmett, 1937) [4](Livingston, 1949)
N_2	28.02	0.176[20] **0.162**[3, 13,15,17)] 0.161[7,18)] 0.154[4] 0.152[19] 0.135[20] 0.166-0.175[21, 22)]	0.473 0.454 0.453 0.443 0.440 0.415 0.460-0.472	0.300[12] 0.331[6] 0.3549[33] 0.3572[10,32)] 0.3681[5] 0.370[11] 0.380[16] 0.364-0.380[1]	0.372[6] d_1=0.41, d_2=0.30[35)]	[5](Walton and Snurr, 2007) [6](Bae et al., 2010) [7](Gregg, 1982) [9](Gray et al., 1995) [10](Dombrowski et al., 2000) [11](Malbrunot et al., 1992) [12](Purewal et al., 2009) [13](Kaneko, 1994), [14](Streppel and Hirscher, 2011) [15](McClellan, 1967) [16](Reid, 1977) [17](Brunauer, 1938), [18](Jura, 1944), [19](Armbruster, 1944) [20](Jelinek and Kovats, 1994) [21],(Lowell, 2004) [22](Davis, 1947) [23](Singleton and Halsey, 1954) [24](Gardner et al., 2001) [25](Aristov and Kiselev, 1963) [26](Walker et al., 1953) [27](Berezkina, 1969) [28](Stermer et al., 1989) [30](Ben-Amotz and Herschbach, 1990) [31](Zhu, 2002) [32](Lastoskie et al., 1993) [33](Seaton et al., 1989) [34](Batsanov, 1999) [35](Karnaukhov, 1985)
Ar	39.95	0.111[23] 0.130[29] 0.1314[28)] **0.138**[7,9, 15, 24,25,26,27)] 0.140[29] 0.142[2,3] 0.146[4]	0.376 0.407 0.409 0.419 0.422 0.425 0.431	0.337[10] 0.340[30] 0.341[11] 0.342[6] 0.354[1] 0.370[30]	0.384[6]	
CO_2	44.11	**0.195**[4] 0.22[15] 0.142-0.244[13]	0.498 0.529 0.425-0.557	0.3644[31] 0.3648[30] 0.33-0.39[1]		

*determined from liquid density method

**bold numbers are the most commonly used values for specific surface area determination

The large sensitivity of the BET surface area with respect to the chosen σ value is also found for our TE 7 III carbon bead sample, as given in Table 4.11. Examples of σ and a_s values taken from liquid density method are displayed in columns 2 and 5. For comparison, the values calculated basing on the Lennard-Jones and van der Waals methods are also included in columns 3, 6 and 4, 7 respectively. For example, the estimated nitrogen surface area from liquid density and for Lennard-Jones method are respectively 782.4 $m^2 g^{-1}$ and 415.3 $m^2 g^{-1}$, in comparison with the corresponding value from van der Waals which is ranging from 654.0 $m^2 g^{-1}$ to 794.3 $m^2 g^{-1}$.

Table 4.11: Variation in the BET specific surface area with adsorptive molecular cross-sectional area calculated using liquid density, Lennard-Jones and van der Waals method for the reference TE 7 III activated carbon beads sample.

	cross-sectional area, σ / nm^2			BET surface area, a_s / $m^2 g^{-1}$		
adsorbate	liquid density	Lennard-Jones	van der Waals	liquid density	Lennard-Jones	van der Waals
N_2	0.176	0.071	0.1086	850.0	342.9	654.0
	0.162	0.086	0.1319	**782.4**	415.3	794.3
	0.161	0.099		777.6	478.1	
	0.154	0.100		743.8	483.0	
	0.152	0.106		734.1	511.9	
	0.135	0.107		652.0	516.8	
	0.166–	0.113		801.7–	545.7	
	0.175	0.104–		845.2	502.3–	
		0.113			545.7	
Ar	0.111	0.089	0.116	554.8	444.8	
	0.130	0.091		649.8	454.8	579.8
	0.1314	0.091		656.8	454.8	
	0.138	0.092		**689.8**	459.8	
	0.140	0.098		699.8	489.8	
	0.142	0.107		709.7	534.8	
	0.146			729.7		
CO_2	**0.195**	0.104		**681.1**	363.2	
	0.22	0.122		768.4	426.1	
	0.142–	0.085-		496.0–	296.8–	
	0.244	0.119		852.2	415.6	

*bold numbers are the most commonly used values for specific surface area calculations

Figure 4.37 to Figure 4.40 are plots of the BET specific surface area within varying adsorptive cross sectional areas for the respective adsorptive types. Obviously, this huge data scatter better visualizes the problem and makes a suitable approach for standard method revaluation.

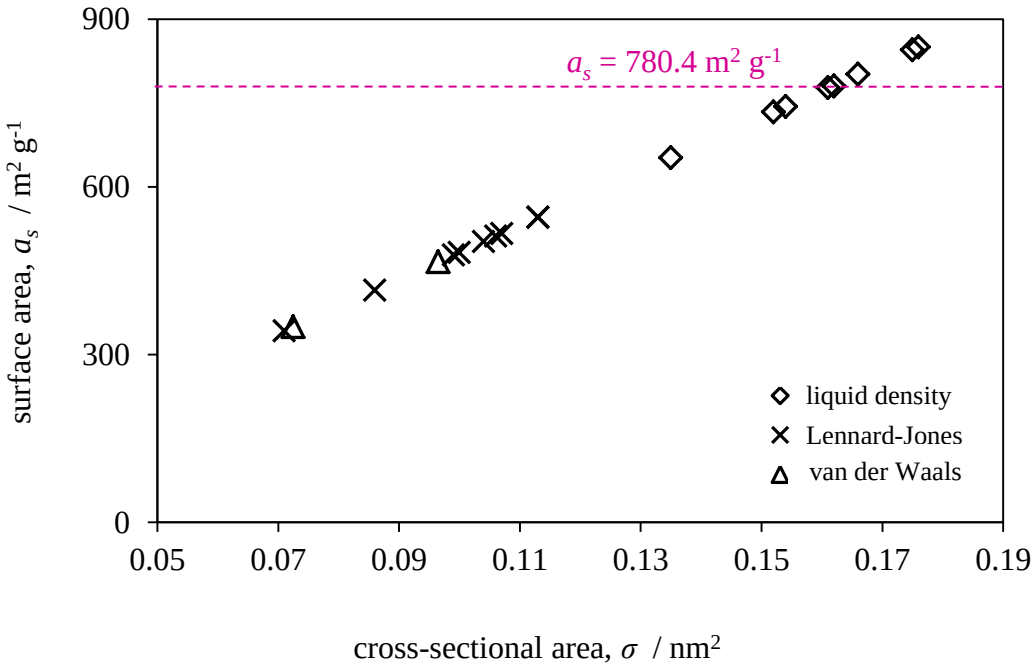

Figure 4.37: Variation of the nitrogen BET specific surface area with adsorptive molecular cross-sectional area for the TE 7 III activated carbon beads sample. The dotted line (---) represents the reference value assigned as 780.4 m^2 g^{-1} obtained by applying the recommended British Standard nitrogen cross-sectional area value of 0.162 nm^2.

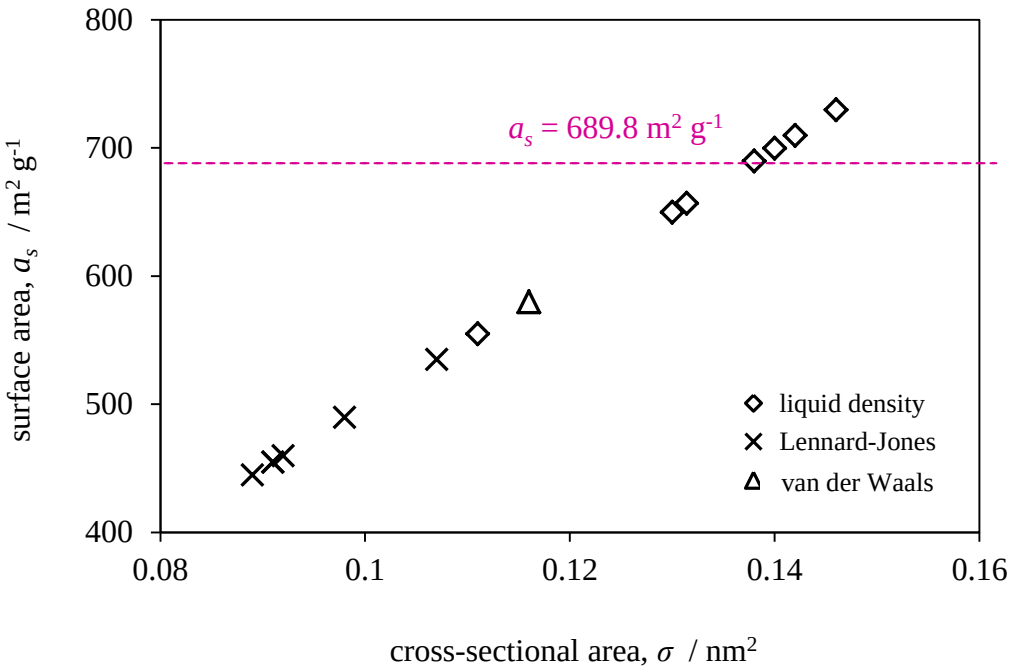

Figure 4.38: Variation of the argon BET specific surface area with adsorptive molecular cross-sectional area for the TE 7 III activated carbon beads sample. The dotted line (---) represents the reference value assigned as 689.8 m^2 g^{-1} obtained by applying the most commonly referred argon cross-sectional area value of 0.138 nm^2.

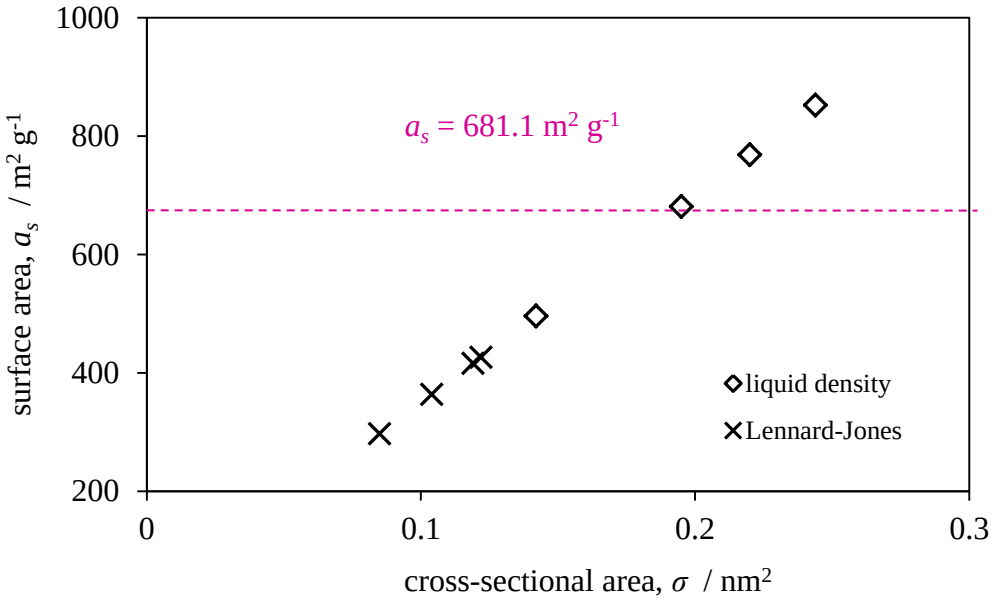

Figure 4.39: Variation of the carbon dioxide BET specific surface area with adsorptive molecular cross-sectional area for the TE 7 III activated carbon beads sample. The dotted line (---) represents the reference value assigned as 681.1 m^2 g^{-1} obtained by applying the most commonly referred carbon dioxide cross-sectional area value of 0.195 nm^2.

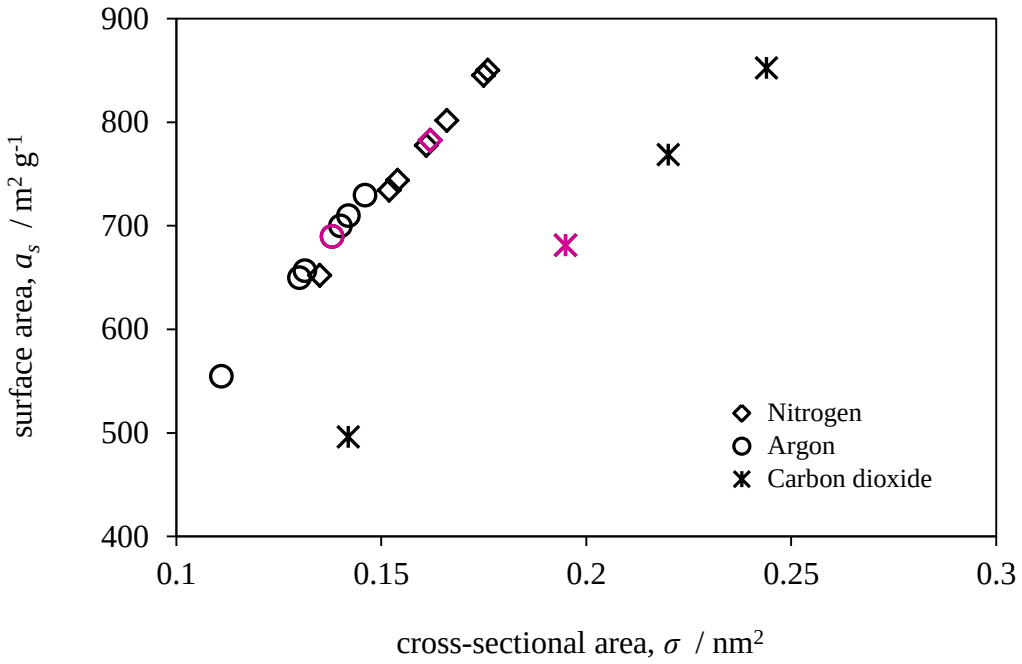

Figure 4.40: Variation of the BET specific surface area with adsorptive molecular cross-sectional areas of nitrogen, argon and carbon dioxide calculated from liquid density method. Marked pink points represent the most commonly referred molecular cross-sectional area values.

Another drawback for the BS method is the assumption that the monolayer is formed over restricted relative pressures range of 0.05–0.3. "However, in the case of microporous samples the pores are completely filled with nitrogen at relative pressures far below this standard range, so linear regression should also be performed on the data points at lower pressures than those recommended above. In order to choose an appropriate pressures two major criteria are proposed (Rouquerol et al., 2006). Firstly the values of $n_a(1–p/p^o)$ over the selected pressure range should increase monotonically with p/p^o and secondly, the chosen linear region must have a positive intercept a to yield a meaningful value of the BET parameter C. In this context, the BET specific surface areas calculated by the method based on the consistency criteria mentioned above is compared with the BS recommendation" (Hruzewicz-Kolodziejczyk et al., 2012).

"Figure 4.41 and Figure 4.42 show the results of applying the consistency criteria to the representative nitrogen isotherm for the TE 7 III activated carbon beads sample. Evidently, a plot $n_a(1\text{-}p/p^o)$ *vs* p/p^o (Figure 4.41) demonstrates that based on the first

criterion, only the pressures less than 0.035 should be used in the BET surface area calculations. The resulting plot in Figure 4.42 shows that after applying the relative pressure range 0.01–0.035 a much better linearity of the BET plot within correlation coefficient R^2 equal to 0.9999 is obtained. Moreover, the positive C parameter is found. The BET specific surface area obtained using the consistency criterion is much higher (a_s = 1019.5 ± 0.0014 m^2 g^{-1}) than when using the standard BET range (a_s = 780.4 ± 19.5 m^2 g^{-1}), which indicates the possibility of underestimation of the surface area when the BS range is applied. These results demonstrate that in order to calculate BET specific surface area of microporous materials such as our representative microporous TE 7 III sample, an appropriate pressure range should be used and that method based on the consistency criteria provides better metric in surface area estimation. Furthermore, it should be kept in mind that in order to compare the surface areas of identical materials the fitted BET pressure range must always be quoted" (Hruzewicz-Kolodziejczyk et al., 2012).

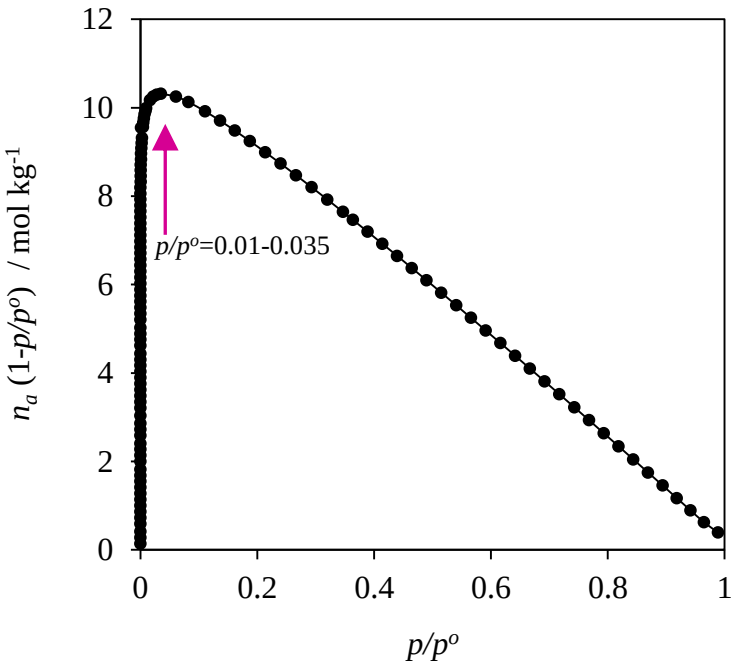

Figure 4.41: Plot of $n_a(1-p/p^o)$ vs p/p^o calculated from the TE 7 III nitrogen sorption isotherm showing the BET pressure range which should be used to calculate the BET specific surface area to satisfy the consistency criteria. The line on the plot joins points to illustrate trend in the data.

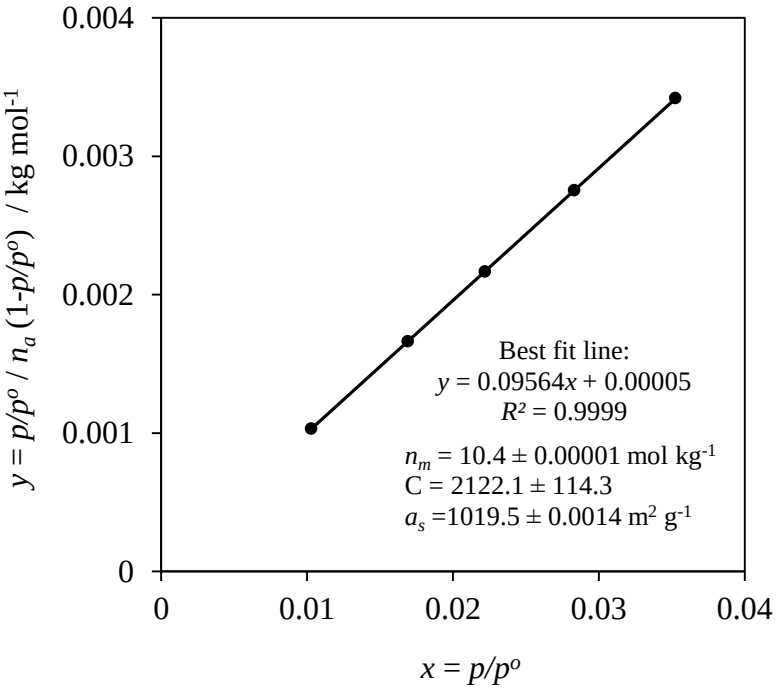

Figure 4.42: Linear fit to low pressure BET nitrogen sorption data using the consistency criteria range (p/p^o=0.01–0.035).

Based on the above discussion, we observe a large variation in the determined BET values in terms of linearity and cross-sectional area and we show that the results presented here could provide a first step to the revaluation of the British Standard method including going to different adsorptives types due to molecular sieving and different type of interaction with materials surface. However, we still accept the BS method, remembering about its geometrical problem because the BET model was developed for the flat surface. We picked the reference value of BET surface area (a^0_s) for the nitrogen at 77 K with σ value equal to 0.162 nm^2 and we call it the "BET number" instead of the BET surface area, because its distance from geometry. We suggest that instead of providing the BET value maybe an appropriate pressure range could be a better approach for the data comparison. Also of note, we need to be aware that some people link the BET surface area with hydrogen capacity and we must be very careful with this correlation since predicting exact surface area values continues to be a major challenge.

4.2.2.3 Micropore Volume Determination

The results given in this section are based on the Dubinin-Radushkevich (DR) method used to investigate the micropore volumes of the studied samples, an important parameter usually correlated to the hydrogen sorption capacity (Bastos-Neto et al., 2012). Originally, the DR equation was established to describe activated carbon adsorption based on Polanyi potential theory and the characteristic curve of adsorption for non-porous sorbents (Schüth, 2002, Rouquerol et al., 1999). One key feature of the DR model is an empirical relationship between the characteristic DR adsorption energy and pore size (Stoeckli, et al., 2001). According to these concepts the DR equation in the empirical form can be written as:

$$n = n_a^{\max} \times \exp\left[-\left[\left(\frac{RT}{\beta E_0} \right) \ln \frac{p_o}{p} \right]^2 \right] \tag{4.9}$$

where, n is the amount of gas adsorbed at p/p^o, n_a^{max} is the amount of gas adsorbed corresponding to the micropore volume, β is the affinity coefficient (in this work selected to be 0.33 for N_2, 0.35 for CO_2 and 0.31 for Ar) and E_0 is the characteristic energy of adsorption.

In the logarithmic form the DR isotherm can be given as follow:

$$\log_{10} n = \log_{10} n_a^{\max} - D\left(\log_{10} \frac{p_o}{p} \right)^2 \tag{4.10}$$

where, D is the empirical constant equal to:

$$D = 2.303\left(\frac{RT}{\beta E_0} \right)^2 \tag{4.11}$$

According to the British Standard method (BS, 2007), for the micro- and mesoporous materials Equation 4.10 should give a straight line between $\log_{10} n_a$ and $\log_{10}(p^o/p)^2$ with a slope D and intercept $\log_{10} n_a$ over a limited relative pressure range from 10^{-4} to 0.1.

Here, the Origin software was applied to compute the unknown DR parameters n_a and E_0, by extrapolating the linear portion of DR curve to the experimental adsorption data. Representative graphs of the nitrogen DR isotherm and a magnified view of the linear regression are shown in Figure 4.43 and Figure 4.44 respectively and this is an example of obtained results. The fitted range of linearity was chosen according to the BS recommendation to be from 10^{-4} to 0.1. The stepwise procedures of calculations and all resulting DR plots are provided in Supplementary Information, Section S4.

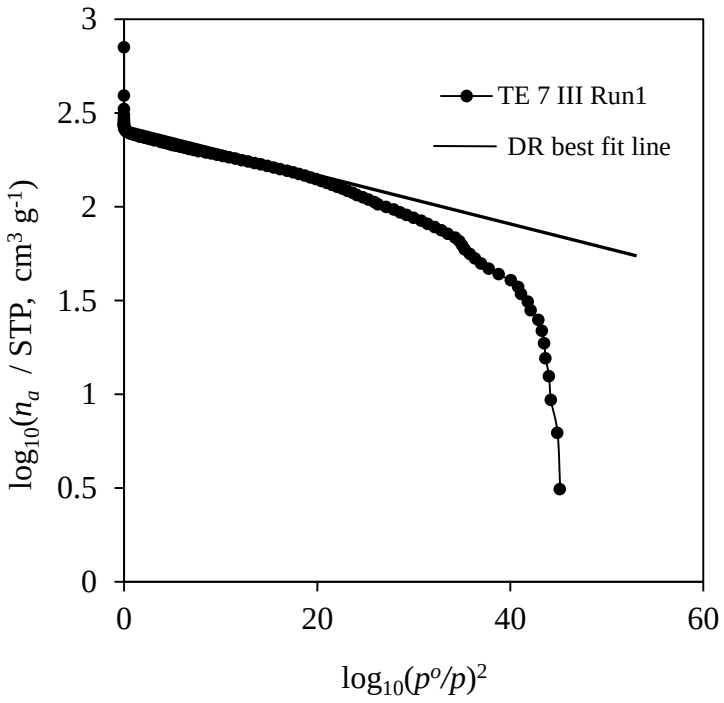

Figure 4.43: Dubinin-Radushkevich (DR) plot of the TE 7 III activated carbon beads sample obtained from the experimental nitrogen isotherm shown in Figure 4.15. The line on the plot joins points to illustrate trend in the data.

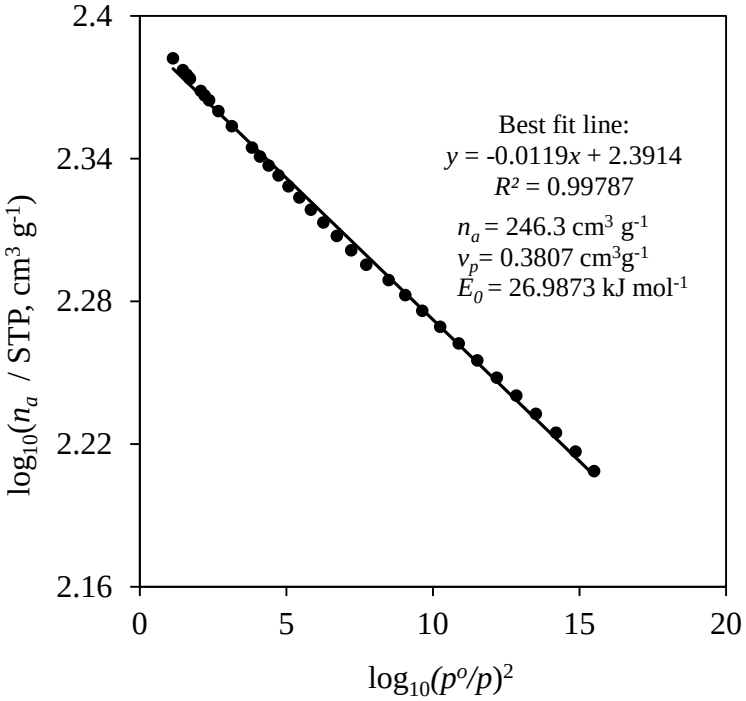

Figure 4.44: Magnified view on the fitted DR linear plot for the TE 7 III activated carbon beads sample obtained over the recommended British Standard relative pressure range (10^{-4}–0.1).

A summary of the DR parameters, such as limiting capacity (n_a), micropore volume (v_p) and characteristic energy (E_0) determined for each investigated sample are displayed in Table 4.12 below. From this results can be concluded that the 13X molecular sieve sample appears to have the lowest micropore volume, while the high BET surface area TE 7 I carbon sample has the highest value. Also noticeable is that the different values of respective characteristic energies (E_0) are obtained for different samples. The values appeared to be in the same magnitude for all activated carbons appear (E_0 ranging from 21 to 27 kJ mol^{-1}), while the much higher values are observed for the zeolites (E_0 from 37 to 39 kJ mol^{-1}) and MOFs (E_0 ~ 38 kJ mol^{-1}). This might be due to the different range of microporosity presented in the particular sample as seen from the nitrogen sorption isotherms in Section 4.2.2.1.

Table 4.12: Summary of DR parameters obtained from volumetric ASAP 2020 nitrogen adsorption isotherms at 77 K.

material	relative pressure range, p/p^o	limiting capacity, n_a / STP, $cm^3\ g^{-1}$	micropore volume, v_p / $cm^3\ g^{-1}$	characteristic energy, E_o / kJ mol^{-1}
TE 7 I	$1.02*10^{-4}$ – 0.0881	389.0	0.60	20.62
TE 7 II	$1.06*10^{-4}$ – 0.0822	295.5	0.45	26.78
TE 7 III	$1.15*10^{-4}$ – 0.0854	246.3	0.38	26.99
Darco	$1.03*10^{-4}$ – 0.0906	234.8	0.36	22.75
Respcarb	$1.04*10^{-4}$ – 0.0874	353.8	0.54	21.33
Solcarb	$1.10*10^{-4}$ – 0.0914	239.6	0.37	23.58
13X	$1.19*10^{-4}$ – 0.0929	142.2	0.22	37.15
Y-Zeolite	$1.24*10^{-4}$ –0.0924	175.8	0.27	39.17
Cu-BTC	$1.02*10^{-4}$ –0.0827	416.2	0.64	37.91

For comparison the DR experiment was repeated with CO_2 at 273 K and Ar at 87 K. The choice of these gases was made because they represent different probes sizes and different types of interactions with the surface. Table 4.13 below summarises the DR parameters determined for all adsorbates types. Complete DR isotherms are provided in supplementary information S2 and here just the magnified views on the fitted BS linearity range are given (see Figure 4.45 and Figure 4.46). As can be seen the DR micropore volumes for Ar and CO_2 are smaller than for N_2, which is apparently helpful in probing narrow microporosity not accessible for nitrogen at 77 K.

Table 4.13: Summary of DR parameters obtained for TE 7 III activated carbon beads sample from volumetric ASAP 2020 sorption isotherms using different adsorbate gases at different temperatures.

adsorbate	limiting capacity, n_a / STP, $cm^3\ g^{-1}$	micropore volume, v_p / $cm^3\ g^{-1}$	characteristic energy, E_o / kJ mol^{-1}
N_2 at 77 K	246.3	0.38	26.99
Ar at 87 K	278.6	0.35	28.38
CO_2 at 273 K	187.1	0.34	50.60

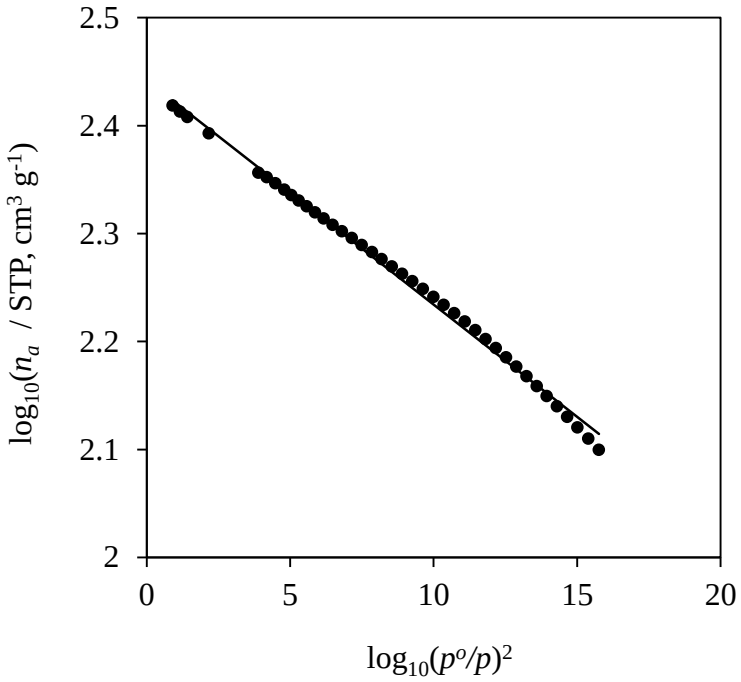

Figure 4.45: Magnified view on the fitted DR linear plot for Ar at 87 K on the TE 7 III activated carbon beads sample recorded over the recommended British Standard relative pressure range (10^{-4}–0.1). The line on the plot joins points to illustrate trend in the data.

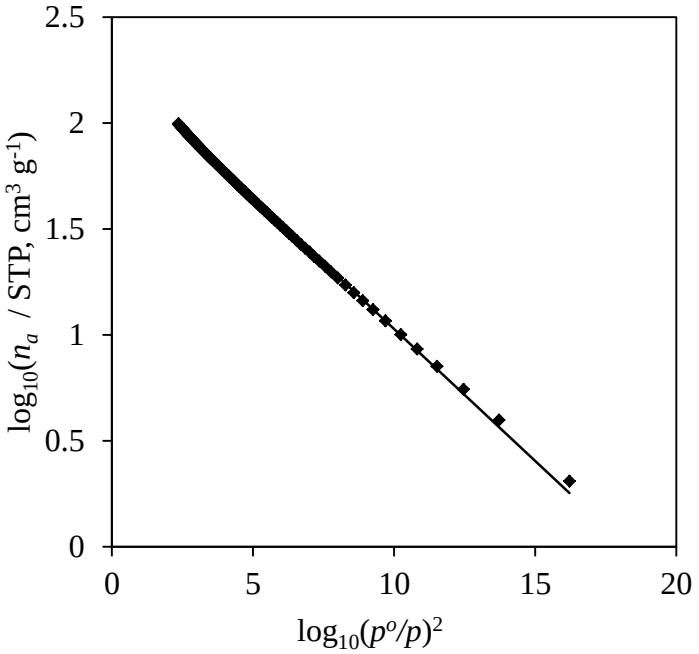

Figure 4.46: Magnified view on the fitted DR linear plot for CO_2 at 273 K on the TE 7 III activated carbon beads sample recorded over the recommended British Standard relative pressure range (10^{-4}–0.1).

4.2.2.4 Pore Size Distribution

In order to correlate the mechanism of hydrogen adsorption with particular sample properties, it is necessary to investigate their pore size distribution. Density functional theory (DFT), a method developed by Olivier (Olivier, 1995) is an effective way of studying the micropore filling and it also covers porosity over a wide range of pore sizes (Lastoskie et al., 1993, Tanaka et al., 2002). The calculation of the pore size distribution via the DFT method requires solving the integral adsorption equation using a common regularization method as shown below.

$$n(p/p^o) = \int_{h\min}^{h\max} f(h)v(h, p/p^o)dh \tag{4.12}$$

where, $n(p/p^o)$ is the experimentally determined excess amount of gas adsorbed in STP $cm^3\ g^{-1}$, $f(h)$ is the pore size distribution function and $v(h,p/p^o)$ is the kernel of theoretical isotherm in pores at different diameters. In order to find the solution of the $v(h,p/p^o)$ function the appropriate model of the pore geometry is required. Here, it is assumed that all samples are described by polydisperse slit-pore model as proposed by other authors (Do and Do, 2003, Scaife et al., 2000).

Typically, the pore size distribution is determined from the nitrogen adsorption isotherm measured at 77 K up to 1 bar. However, note that at this condition diffusion of nitrogen is very slow and can lead to time-consuming and none fully equilibrated results. Table 4.14 summarized the corresponding nitrogen pore size distributions determined via DFT method for each investigated sample (all resulting differential pore size distribution plots are provided in Supplementary Information, Section S5).

Table 4.14: Summary of differential pore size distribution results obtained by applying Density Functional Theory (DFT) to the volumetric ASAP 2020 nitrogen adsorption isotherms at 77 K.

material	range of pore diameters / nm	modal diameter / nm
TE 7 I	0.54 – 126.58	0.59
TE 7 II	0.39 – 136.68	0.39
TE 7 III	0.67 – 117.23	0.73
Darco	0.39 – 185.80	0.54
Respcarb	0.50 – 4.66	0.59
Solcarb	0.39 – 2.16	1.18
13X	0.39 – 136.68	0.39
Y-Zeolite	0.67 – 0.86	0.72
Cu-BTC	0.46 – 1.00	0.86

Figure 4.47 to Figure 4.49 show the pore size distribution plots determined for the representative TE 7 III activated carbon beads sample using N_2 at 77 K, CO_2 at 273 K and Ar 87 K as probe molecules. As can be seen for nitrogen the pore size distribution starts at 0.67 to 1.59 nm and then occurs in larger pores within 11.72 nm to 117.23 nm, and appears to peak at around 0.73 nm (see Figure 4.47). From Figure 4.48 it is evident that carbon dioxide at 273 K is able to easily access smaller pores than nitrogen at 77 K, as the distribution of pores starts at 0.40–0.87 nm, with a maximum peak at 0.62 nm. These confirm that CO_2 can be successfully used as an alternative probe to nitrogen, ensuring faster analysis and more importantly confirming that measured adsorption points are fully equilibrated. For Ar at 87 K the maximum peak appears at 0.47 nm, again extending the lower limit of pore size distribution, compared to nitrogen. Coincidently, our reference TE 7 III sample can be even more interesting, because as recently cited it has the optimal pores (0.6–0.7 nm) for high pressure hydrogen storage at 77 K (Gogotsi et al., 2009).

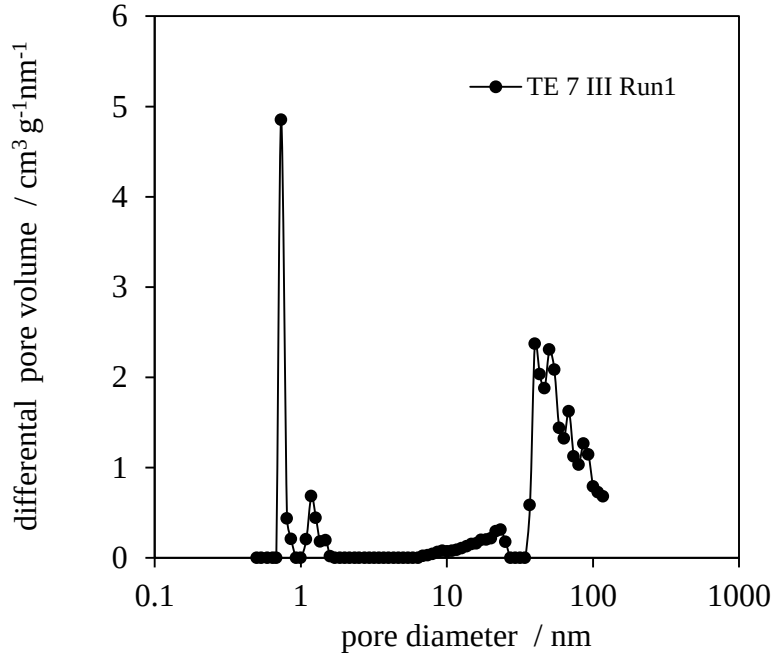

Figure 4.47: Differential pore size distribution for TE 7 III activated carbon beads sample obtained by applying Density Functional Theory (DFT) to the experimental nitrogen isotherm shown in Figure 4.15. The line on the plot joins points to illustrate trend in the data.

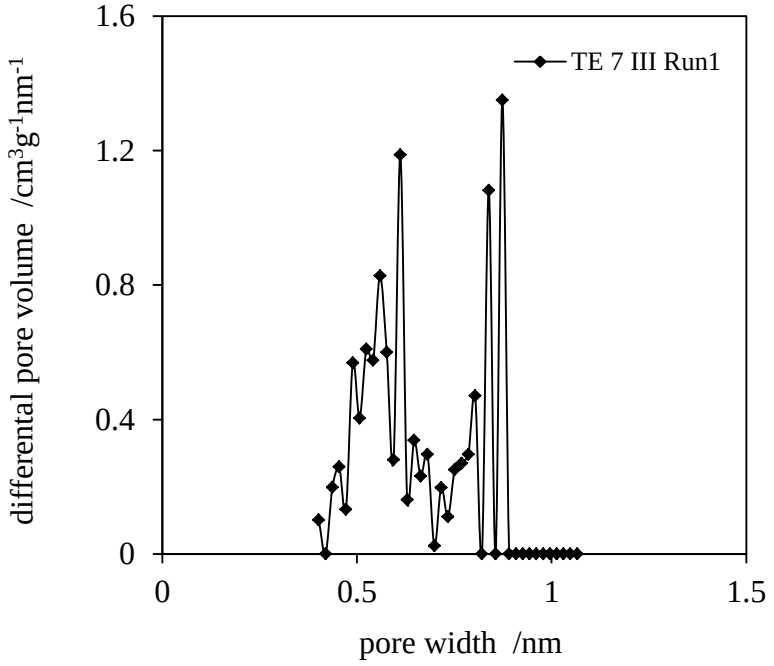

Figure 4.48: Differential pore size distribution for the TE 7 III activated carbon beads sample obtained by applying Density Functional Theory (DFT) to the experimental carbon dioxide isotherm shown in Figure 4.22. The line on the plot joins points to illustrate trend in the data.

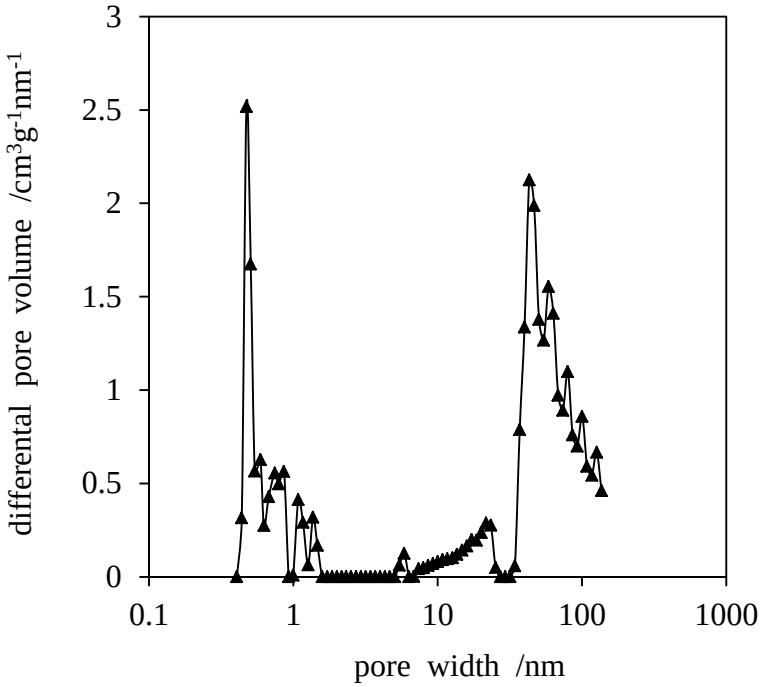

Figure 4.49: Differential pore size distribution for the TE 7 III activated carbon beads sample obtained by applying Density Functional Theory (DFT) to the experimental argon isotherm shown in Figure 4.22. The line on the plot joins points to illustrate trend in the data.

4.2.2.5 Investigation of Equilibration Time

The intention here is to investigate the appropriate equilibration time crucial for recording accurate hydrogen sorption isotherms. If each point on the adsorption isotherm is not truly equilibrated, the measured data are questionable and the recorded adsorption capacity could be artificially low. In this work, the time allowed for equilibration is defined as the delay between successive doses, and allows for a return to temperature after the expansion of the dosing gas and the exothermic adsorption event, as well as allowing the adsorptive to completely infiltrate the pores of the sorbent. "One has to be bear in mind that the equilibration times are expressed in adsorption software in different ways, but will almost certainly involve taking periodic readings after dosing and incorporate a threshold limit as a way of judging equilibration (i.e. if calculated

values of $\Delta wt\%$ per time (for gravimetric measurements) or $\Delta\%p$ (for volumetric) are above the set threshold, the analyser will not add the next dose). In the case of the ASAP 2020 volumetric analyser, the "equilibration time" that can be adjusted by the user refers to the time period between readings taken of the sample tube pressure. In addition, the $\Delta\%p < 0.01\%$ threshold for assessing equilibration is based on a "rolling average" of the last ten pressure readings. Thus, increasing the "equilibration time" has the effect of introducing a "soak time" of (10× the set "equilibration time") before the $\Delta\%p$ criterion can be applied" (Hruzewicz-Kolodziejczyk et al., 2012).

We recognize that recording data on a system that is not at equilibrium can lead to problems in the calculation of physical properties such as the nitrogen BET specific surface area, since equilibration time recommended by some manufacturers of gas sorption analysers for nitrogen 5-point BET analysis is very short (e.g. equivalent to a soak time of 2 min). Figure 4.50 shows BET result obtained over the recommended BS range (p/p^o=0.05–0.3) from nitrogen sorption isotherms collected using different equilibration times. Obviously, the amounts of nitrogen adsorbed at 2 min are not true adsorption capacities and the calculated BET surface area is artificially low. Table 4.15 shows raise in both the nitrogen monolayer capacity and the calculated BET specific surface area value as the equilibrium time is increased.

Table 4.15: BET specific surface area (over the p/p^o range according to the BS) calculated from nitrogen sorption isotherms at 77 K on the sample of TE 7 II activated carbon beads using different equilibration periods.

equilibration period / min	relative pressure range, p/p^o	monolayer capacity, n_m / mol kg^{-1}	BET specific surface area, a_s / m^{2}g^{-1}
2	0.0528 – 0.3030	8.8	858.5
9	0.0548 – 0.3038	9.4	917.0
12	0.0521 – 0.3029	9.5	926.0
60	0.0506 – 0.3031	9.6	936.5

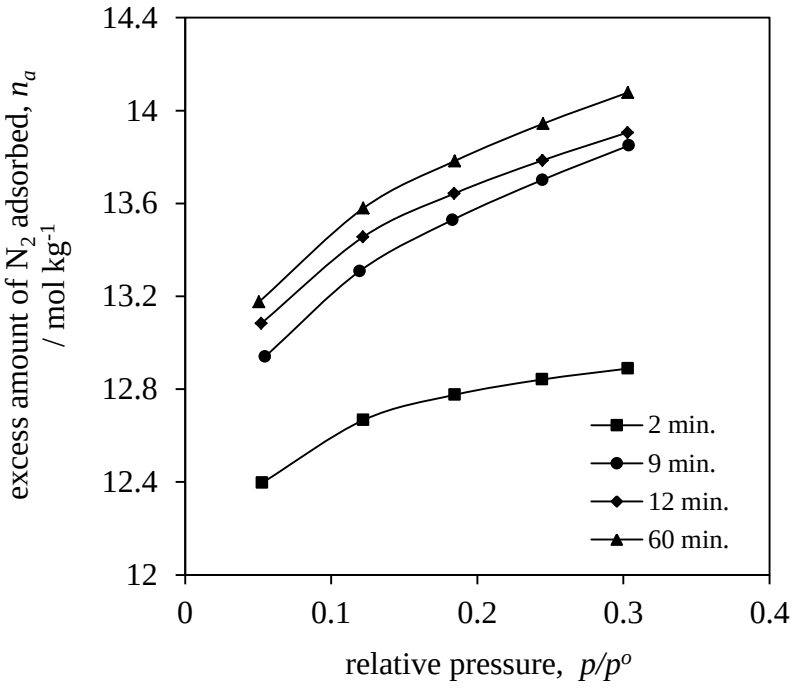

Figure 4.50: Comparison of the volumetric ASAP 2020 nitrogen sorption isotherms (recorded in BS range) on the TE7 II carbon beads sample, using several equilibration times from 2 to 60 min. The lines on the plots join points to illustrate trends in the data. Adapted from (Hruzewicz-Kolodziejczyk et al., 2012) with kind permission from International Association of Hydrogen Energy.

"A similar problem was found when the hydrogen sorption determined over recommended equilibration periods of 2 and 9 min was examined (Micromeritics, 2005). As can be seen from the representative hydrogen isotherms in Figure 4.51, despite having identical *Δ%p* thresholds, a soak time of 2 min leads to underestimation of the excess hydrogen sorption, and becomes more significant with increasing pressure. The difference between the maximum measured uptake at 1 bar using a 2 min and a 12 min equilibration period is over 13 % (1.80 wt% and 2.08 wt%, respectively see Table 4.16). Figure 4.51 also qualifies that the equilibrium uptake is effectively reached with a minimum equilibration period of approximately 12 min and there is no significant increase in excess adsorption using a much longer equilibration period of 60 min" (Hruzewicz-Kolodziejczyk et al., 2012).

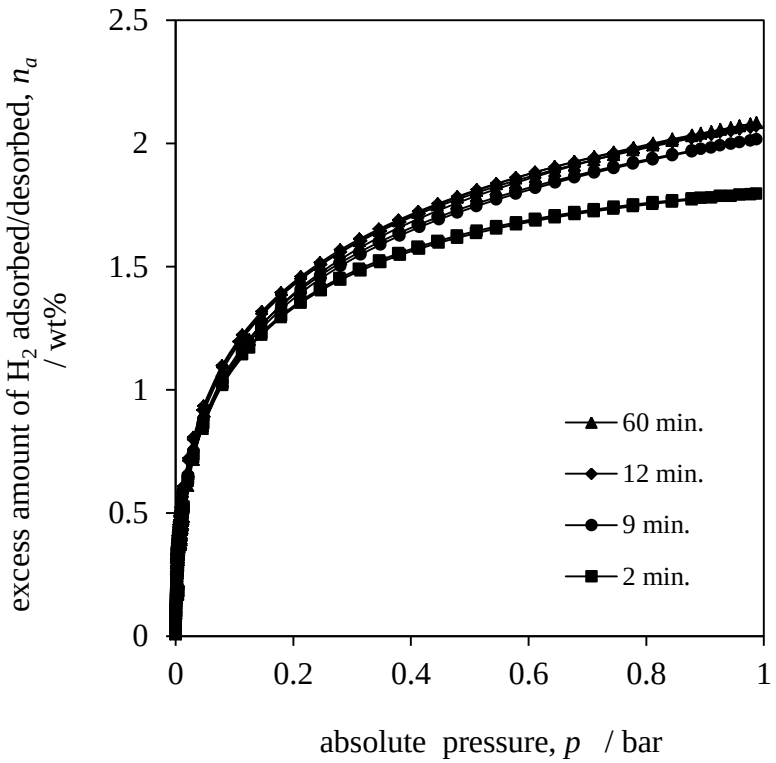

Figure 4.51: Comparison of the excess hydrogen uptakes on the TE 7 II carbon beads sample, using a range of equilibration periods from 2 to 60 min. per point. The lines on the plots join points to illustrate trends in the data. Adapted from (Hruzewicz-Kolodziejczyk et al., 2012) with kind permission from International Association of Hydrogen Energy.

Table 4.16: The measured excess amounts of hydrogen adsorbed at 1 bar and 77K for different equilibration periods from 2 to 60 min. Adapted from (Hruzewicz-Kolodziejczyk et al., 2012) with kind permission from International Association of Hydrogen Energy.

equilibration period / min	hydrogen uptake at 1 bar, n_a / wt %
2	1.80
9	2.01
12	2.07
60	2.08

"The differences between the uptake levels seen here could theoretically be rectified by changing the *Δ%p* criterion, but as this is not an option in many commercially-produced sorption systems. Other ways of confirming equilibration, for example, is by carefully monitoring the kinetic data for each individual pressure step (see Figure 4.52). However, if recording the kinetics during a sorption experiment is not an option, another way of ensuring that equilibrium is fully achieved is by measuring the adsorption isotherms with different equilibration times and establishing the shortest equilibrium time required for reaching a maximum excess uptake, bearing in mind that the data points in the low pressure (microporous) region of the isotherm will take the longest time to equilibrate" (Hruzewicz-Kolodziejczyk et al., 2012).

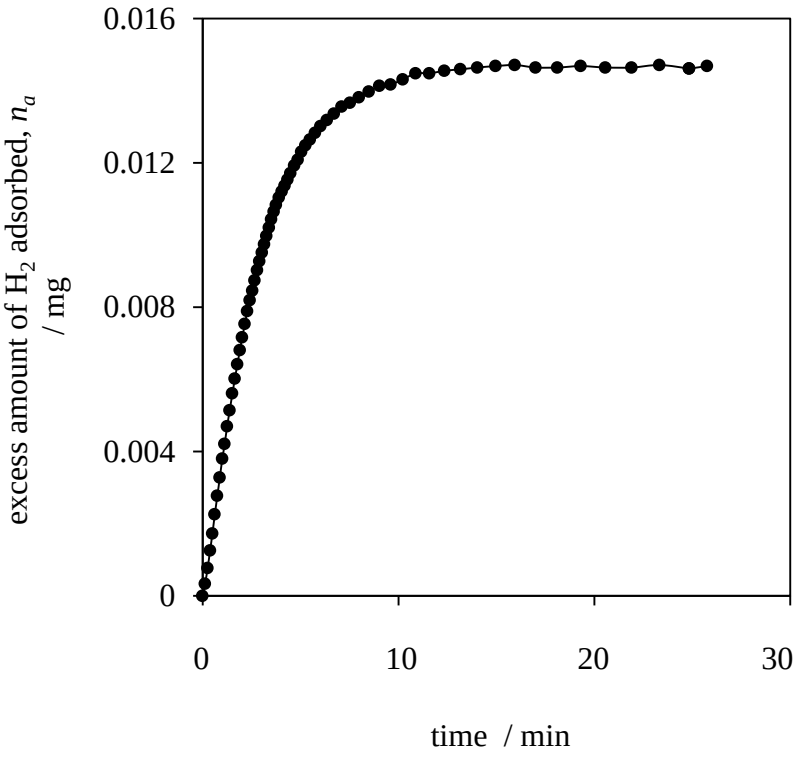

Figure 4.52: Representative kinetic data plot for the hydrogen adsorption at 77 K obtained on the TE 7 II carbon beads sample via real-time IGA gravimetric analysis. The lines on the plots join points to illustrate trends in the data.

4.2.2.6 Accurate Data Correction

The purpose here is to determine the accurate data correction method, crucial in reporting both volumetric and gravimetric isotherms, since any inaccuracy can drastically alter the shape of collected isotherm and change the apparent level of adsorption. In order to achieve this, a free space analysis (also known as dead volume) was undertaken as part of each volumetric measurement on the ASAP 2020 and HTP-1 analysers. "Typically, the free space measurements are performed by dosing a degassed sample with a non-interacting gas such as helium assuming that there is no significant adsorption. However, in some cases there is evidence of the presence of residual helium in the pores after free space measurement especially in the microporous samples. This can be seen from the nitrogen isotherms for a reference sample of TE 7 II carbon (Figure 4.53) before and after helium free space measurement. The triangular data points show the initial isotherm. Helium free space measurement was then performed on this sample, which was subsequently degassed for a second time and then a second nitrogen sorption isotherm was collected (circular data points). As can be seen the isotherm collected after the free space measurement has slightly lower nitrogen excess adsorption. A plot of uptake *vs* log (relative pressure, p/p^o) of the isotherms in Figure 4.53 (b) shows that the isotherm that was collected after the free space measurement has a curved tail at low pressures, which is indicative of incomplete degassing of the sample (Micromeritics, 1997). To avoid retention of helium, we propose here an alternative method of calculating the free space based on the volume of the empty sample bulb and an accurate independent measurement of the sample density (Rouquerol et al., 1999, Micromeritics, 2003). However, if the sample density cannot be easily determined (e.g. in the case of prohibitively small sample sizes), we advise to run the direct helium free space measurement after the sample analysis is completed, or at elevated (rather than cryogenic) temperatures to decrease the likelihood of helium interacting with the sample surface (Malbrunot et al., 1997)" (Hruzewicz-Kolodziejczyk et al., 2012).

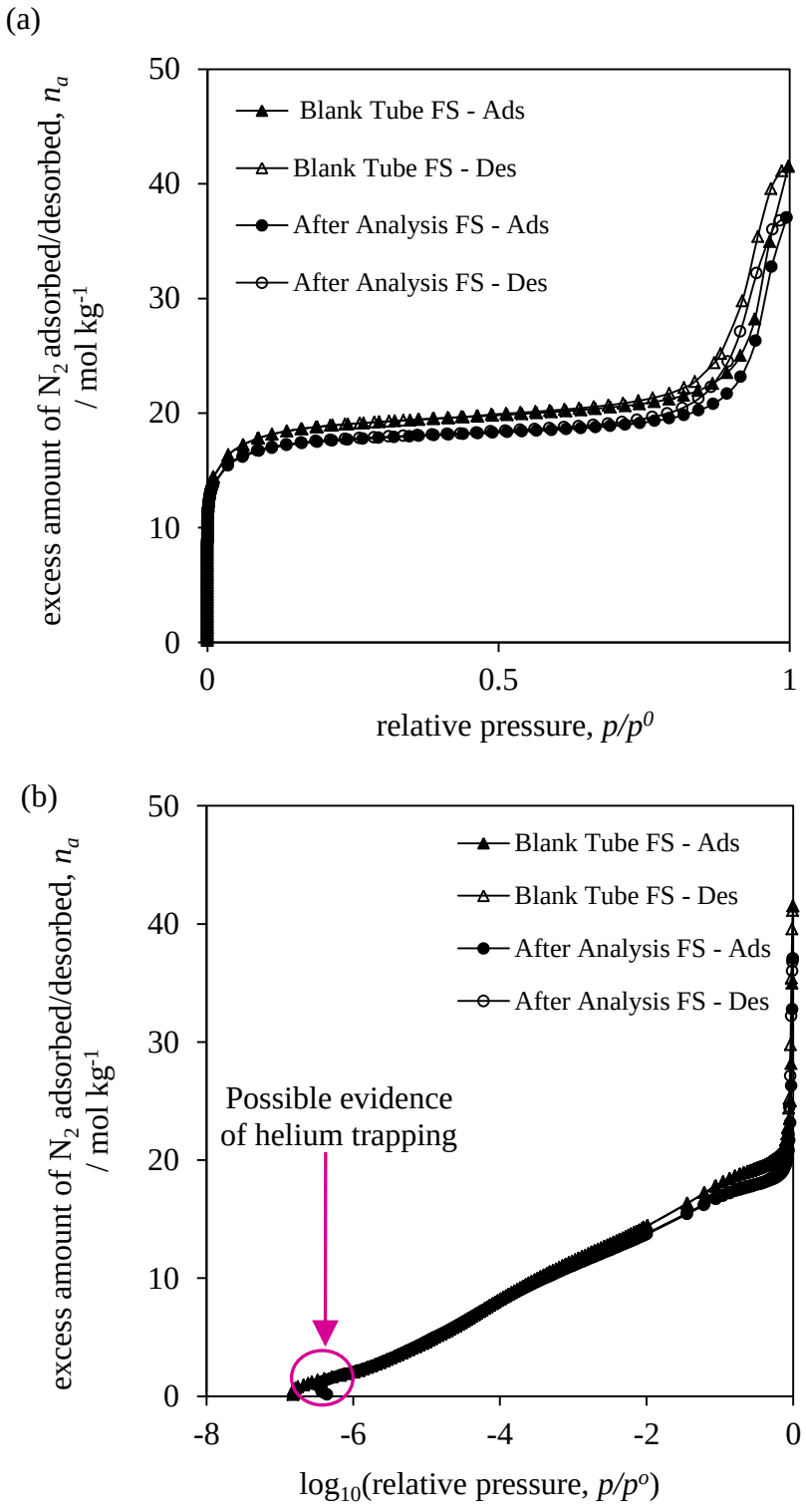

Figure 4.53: Volumetric ASAP 2020 excess nitrogen sorption isotherm for a sample of TE 7 II carbon beads at 77 K in (a) linear (b) logarithmic scale, on the freshly degassed sample (triangles) and the same sample degassed after helium free space analysis (circles).The lines on the plots join points to illustrate trends in the data. Adapted from (Hruzewicz-Kolodziejczyk et al., 2012) with kind permission from International Association of Hydrogen Energy.

Errors in both determined excess capacity and isotherm shape caused by inaccuracy in the helium pycnometry measurements can be also visible at higher hydrogen pressures. This is illustrated in Figure 4.54, showing the high pressure HTP-1 hydrogen adsorption isotherms determined at 77 K for the microporous TE 7 III sample, all corrected for room temperature pycnometry. In this example around 0.03 cm^3 g^{-1} increase in the sample volume causes around 7 % increase in the maximum hydrogen capacity, which could make helium calibration questionable.

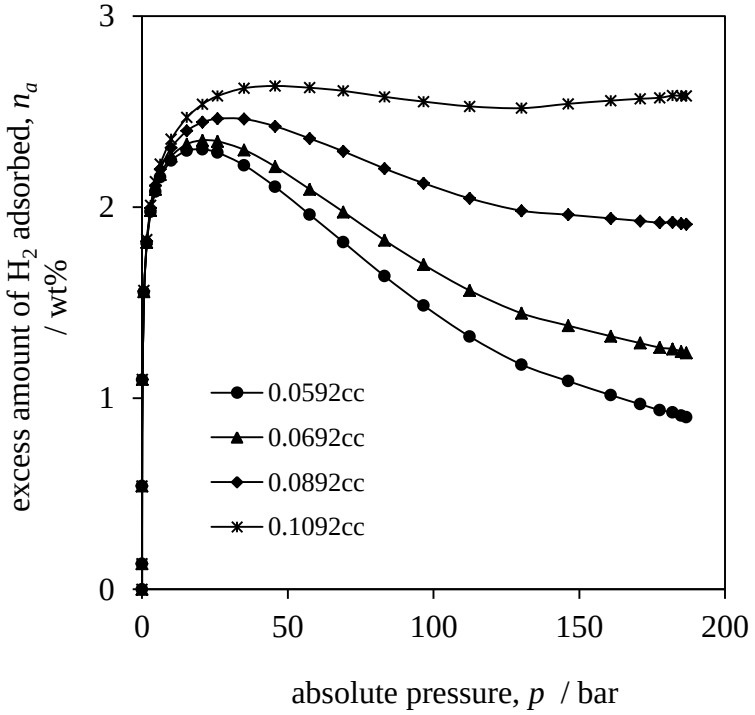

Figure 4.54: Volumetric HTP-1 excess hydrogen sorption isotherm for a sample of TE 7 III carbon beads at 77 K corrected for different sample volumes. The lines on the plots join points to illustrate trends in the data.

One simple way to test such effect is to perform direct helium sorption measurements on the same sample at several temperature ranges, from cryogenic up to limit of its thermal stability (623 K), as shown in Figure 4.55. As can be seen a significant increase in helium adsorption of around 44 times is observed at cryogenic temperatures. From these results it can also be concluded that ambient pycnometry is still questionable, as our microporous TE 7 III sample adsorbs around 0.006 wt% helium at these conditions (298 K and around 3 bars). Although, in order to obtain better accuracy in the

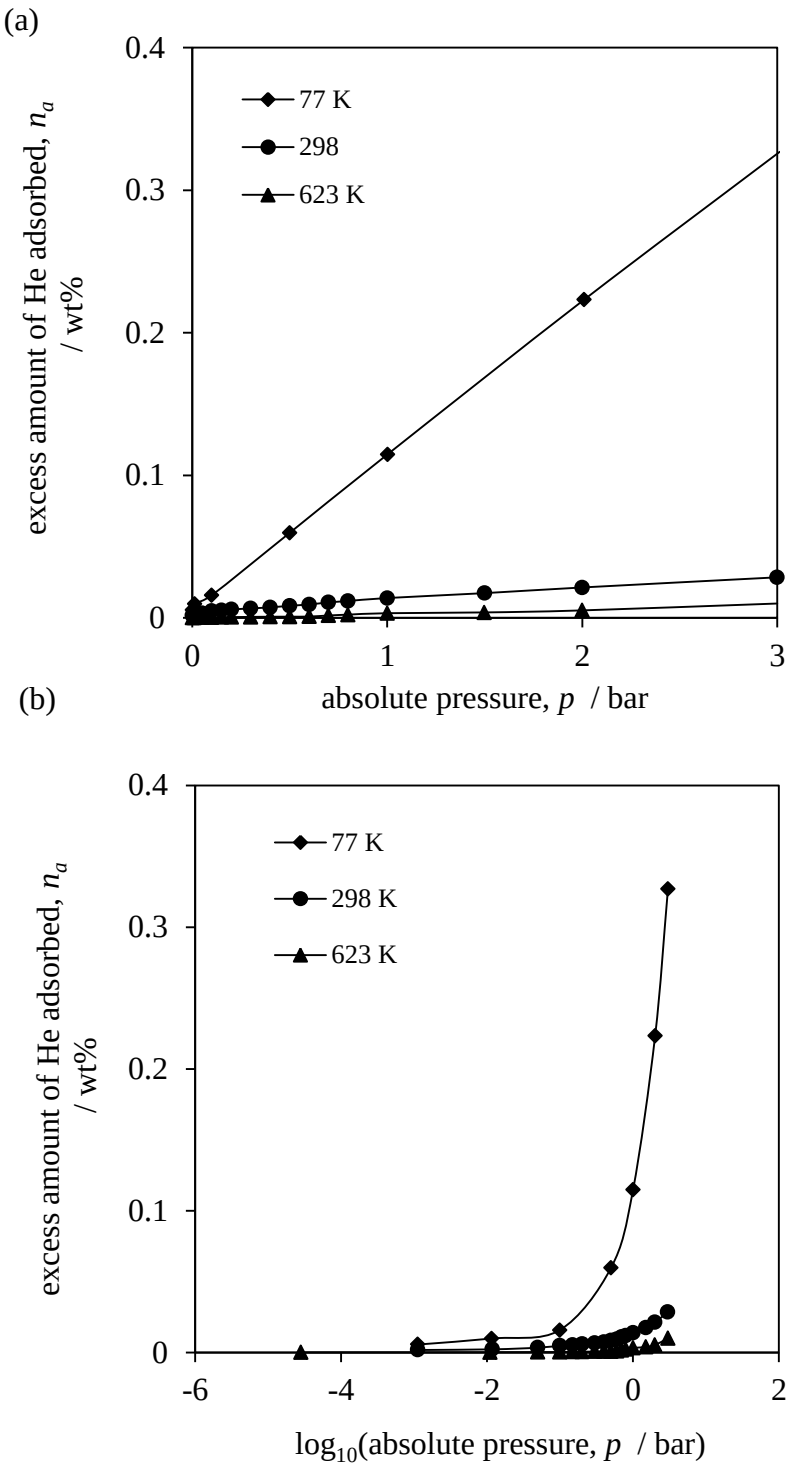

Figure 4.55: Gravimetric helium adsorption isotherm for a sample of TE 7 III activated carbon beads in (a) linear and (b) logarithmic scale of absolute pressure, measured at temperature ranging from 77 K to 623 K. The lines on the plots join points to illustrate trends in the data.

pycnometry calibration, we recommend measuring the sample volume as many times as possible, at least three and then using the average value to correct the final sorption isotherms results.

“Analogous to the free space correction in volumetric measurements, the data from the gravimetric technique must be corrected for the effects of buoyancy, which can be defined as an upward force on an object immersed in a fluid (liquid or gas), enabling it to float or appear lighter. In the case of buoyancy corrections, inaccurate measurements of density of the sample and/or sample holder (pan and hang-down) may lead to inexact measurements. Imprecise determination of the gas density will also lead to inaccuracies. In order to obtain the most accurate buoyancy correction possible, it is recommended the use of the best available equation of state to calculate the gas density (for hydrogen, it is Leachman’s 2009 equation of state (Leachman et al., 2009), available from the NIST website (NIST, 2012))” (Hruzewicz-Kolodziejczyk et al., 2012).

4.2.2.7 Sorption Kinetics

In this section adsorption kinetic uptakes of different adsorptives obtained from gravimetric experiment on the reference sample of TE 7 III activated carbon beads are analysed and discussed. Detailed examination of this data is used to assess true adsorption equilibrium and to estimate the mechanism of adsorption taking place in a particular adsorption system. Furthermore, the results are discussed with a reference to the relation of the geometry (size and shape) to the adsorption kinetic behavior of variety of adsorptive studied.

Numerous models can provide a satisfactory estimation of adsorption kinetics involved in the various nanoporous systems. In this work the approach follows the linear driving force (LDF) model, which is a multiplied form of much more complex Fickian diffusion equation (Reid and Thomas, 1999). Originally the LDF model was proposed by Glueckauf and Coates (Glueckauf and Coates, 1947) for adsorption chromatography and

isothermal adsorption of the pure gases in the single adsorbent particle can be written in the form as shown in Equation 4.13 (Sircar and Hufton, 2000, Sircar, 1983):

$$\frac{dn}{dt} = k(n_2 - n) \tag{4.13}$$

The LDF model assumed that the driving force for the mass uptake is proportional to the difference between the equilibrium adsorbate uptake and the actual uptake in the particle. With initial and boundary conditions ($t=t_1 \rightarrow n=n_1$ and $t\rightarrow\infty \rightarrow n\rightarrow n_2$), the solution to the Equation 4.13 can take the form:

$$n = n_1 + (n_2 - n_1)\left[1 - \exp\left(-k\left(t - t_1\right)\right)\right] \tag{4.14}$$

where, k is kinetic rate constant or mass transfer coefficient, n is the actual mass uptake at time t, n_2 is the equilibrium uptake at $t\rightarrow\infty$ and n_1 is the initial uptake at $t=t_1$. The kinetic rate constant, k is related to the diffusion coefficient, d_c and for a spherical particle with a radius, a can be written as (Glueckauf, 1955):

$$k = \frac{15 d_c}{a^2} \tag{4.15}$$

Figure 4.56 illustrates the typical asymptotic mass uptake curve versus time recorded in real-time during the IGA gravimetric experiment, which is used in the non-linear fitting procedure to determinate the unknown LDF model parameters k and n_2.

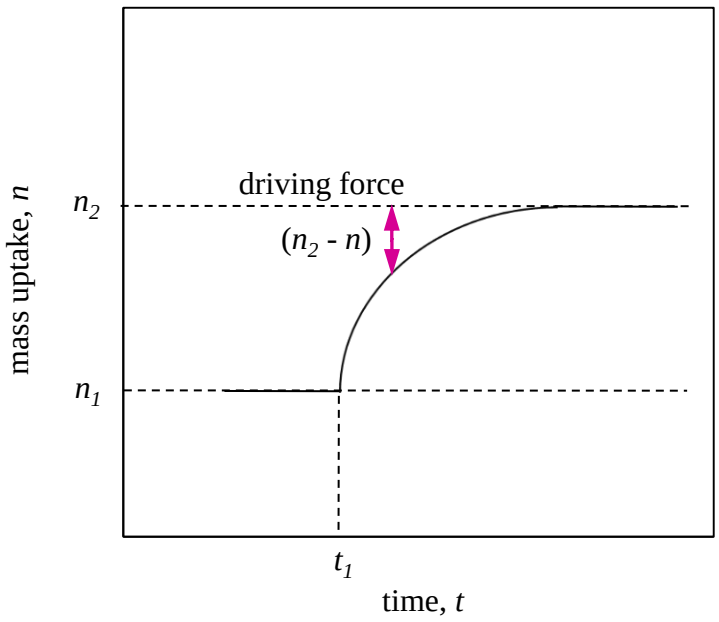

Figure 4.56: The individual asymptotic mass uptake versus time recorded in real-time by IGA gravimetric system while the sample is reaching adsorption equilibrium. Here, n is actual uptake, n_1 is the initial uptake at $t=t_1$, and n_2 is the equilibrium uptake at $t \rightarrow \infty$.

In this study, the LDF model in the form as given in Equation 4.14 is fitted to all kinetic data obtained from the experimental adsorption isotherms on the reference TE 7 III carbon sample. The examples of experimental and modeled in ORIGIN kinetic results for the adsorption of the various adsorptives are shown in Figure 4.58 and Figure 4.59 (all resulting plots are provided in Supplementary Information, Section S6). The solid lines on the plots represent the best fit relationship between the experimental data and the LDF model. As can be seen the modeled and experimental curves agree well for almost all adsorption steps and are valid in the wide range of operating pressures. However in some cases, fitting this equilibrium model to the experimental data would result in a mass uptake curve that deviates from ideal, as shown in Figure 4.59. For this data, resulting residual plots shown in the Figure 4.60 are evidently biased with the maximum deviation from the ideal curve of around 22.5 % for the hydrogen sorption (see 4.60 (b)). This deviation is not unexpected since these data were not obtained under fully isothermal and isobaric experimental conditions (as displayed in Figure 4.57), and so full equilibrium was not reached. It should be noted that these erroneous data are

excluded from further analysis to reduce the uncertainties of estimated kinetic parameters to minimum.

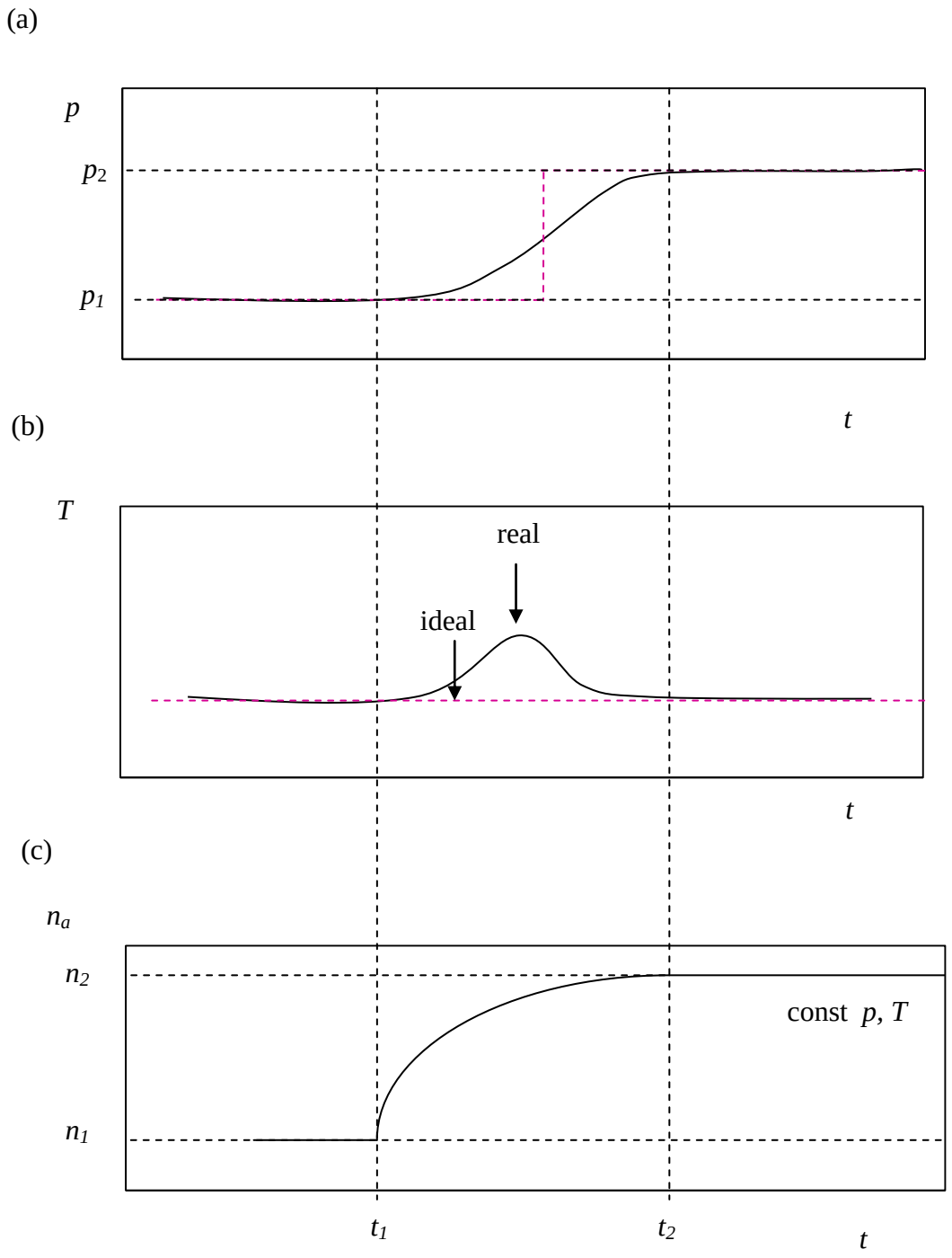

Figure 4.57: Schematic representation of the kinetic sorption step obtained during isothermal and isobaric experiment on the gravimetric (IGA) analyser. Solid black (—) and dotted pink (---) lines represent the real and ideal data, respectively.

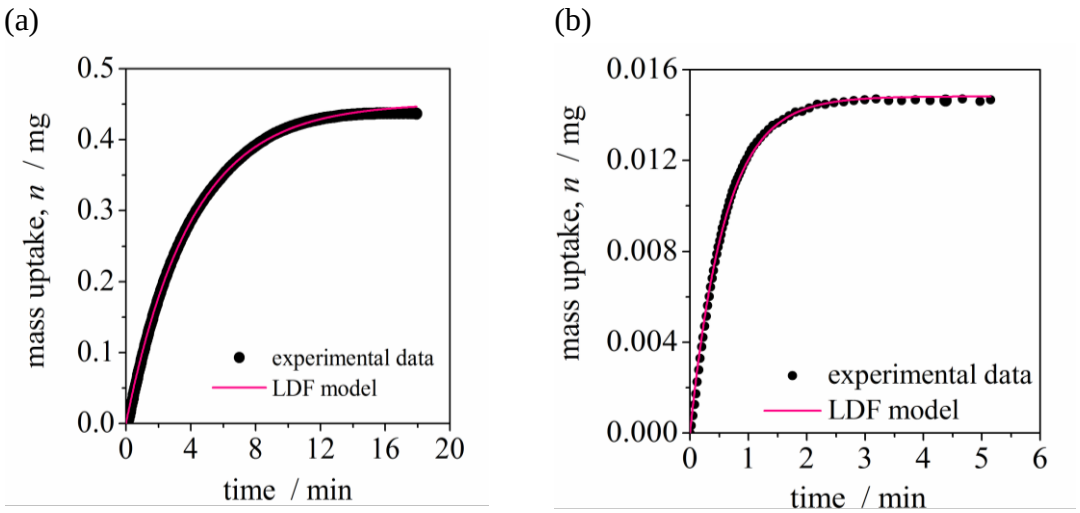

Figure 4.58: Representative plots showing the Linear Driving Force model fits to the (a) nitrogen and (b) hydrogen adsorption kinetic data on the reference sample of TE 7 III activated carbon beads measured under isothermal and isobaric conditions.

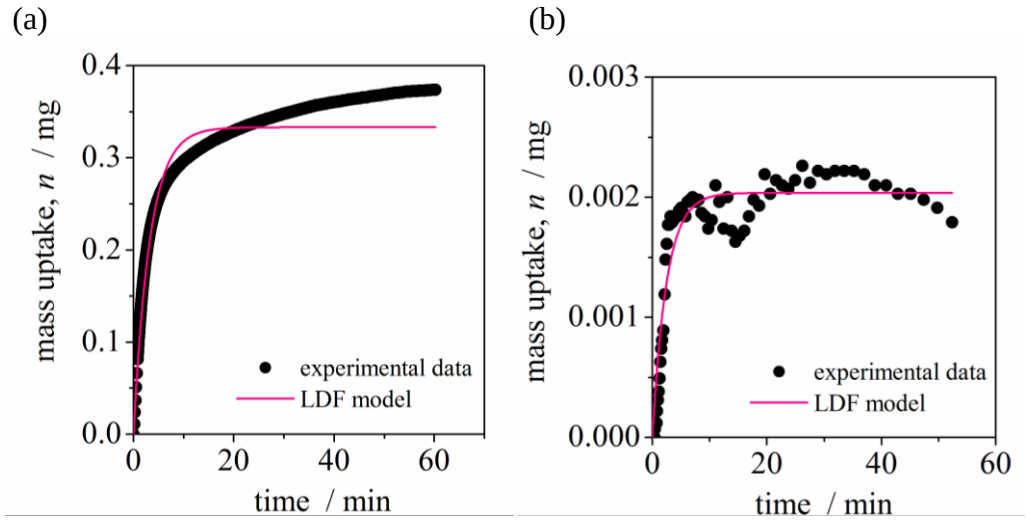

Figure 4.59: Representative plots showing the deviation of (a) nitrogen and (b) hydrogen experimental adsorption kinetic data from fitted Linear Driving Force model caused by non fully isothermal and isobaric conditions.

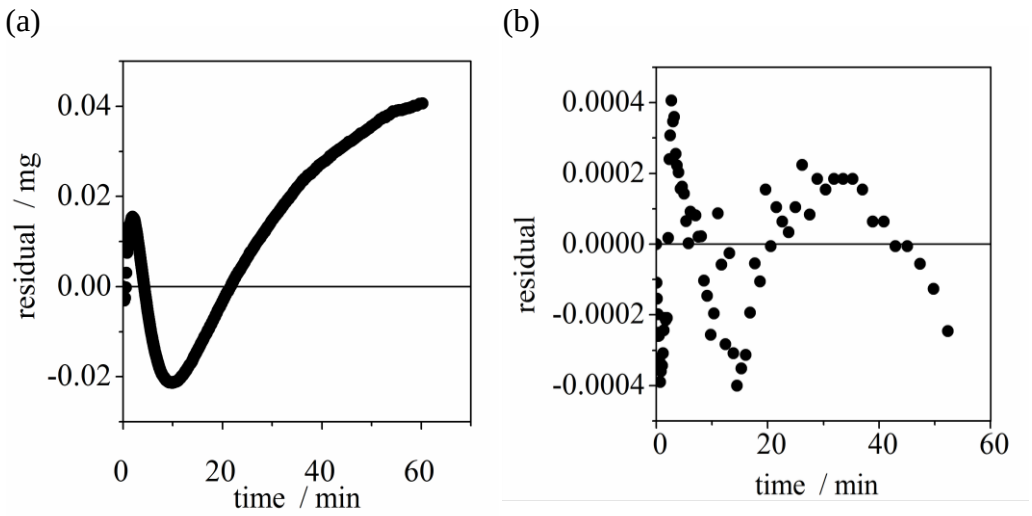

Figure 4.60: Representative residual plots of the Linear Driving Force model fits to the (a) nitrogen and (b) hydrogen adsorption kinetic data.

Figure 4.61 shows how the rate constant, k varies with pressure for the nitrogen, hydrogen isotherms all measured at 77 K. It can be seen that it is quite difficult to predict a proper trend because the scattering of the data is big and the corresponding results are slightly different for both adsorptives. For the nitrogen Figure 4.61 (a)), the rate constant appears to start at around 7×10^{-3} s^{-1} at low pressures (p=0.001 bar) and then slowing down in the pressure range from 0.012 to 0.05 bar reaching the plateau with k~8.5×10^{-3} $s^{-1}$and finally increase to around 4×10^{-2} s^{-1}at p=1 bar. In the case of hydrogen (Figure 4.61 (b)) it can be observed that initially the rate constant is lower compared to nitrogen and ranging from around 2-3×10^{-2} s^{-1} for p=0.02 bar and then clearly decreasing to 8×10^{-3} s^{-1} (around p=5 bar) before increasing to 3.3 $\times10^{-2}$ s^{-1} at p=19.5 bar.

Therefore, from comparison of adsorption rates at the same pressures (e.g. for p=0.03 bar) it can be seen that hydrogen exhibits around ten times faster uptake than nitrogen adsorption. In the case of hydrogen full equilibrium is achieved over of period of approximately 2–3 minutes. These results support the argument concerning the relationship between molecular diameter and adsorption kinetics which the comparison

clearly demonstrates that the following order is apparent: H_2>N_2, since the hydrogen has the smaller molecular diameter and represents the faster kinetic. Furthermore, the knowledge of the rate constant and particle radius can be used to calculate the diffusion coefficient for each adsorption system investigated. The calculations are made considering the Equation 4.15 with the assumption that the tested TE 7 III sample is spherical and homogeneous with individual particle radius equal to 210 µm. The graphs showing the variations of the diffusion coefficient within pressure for different adsorptives are given in Figure 4.62 below and the results are summarized in Table S1 Table S2 in the Supplementary Information, Section S6.

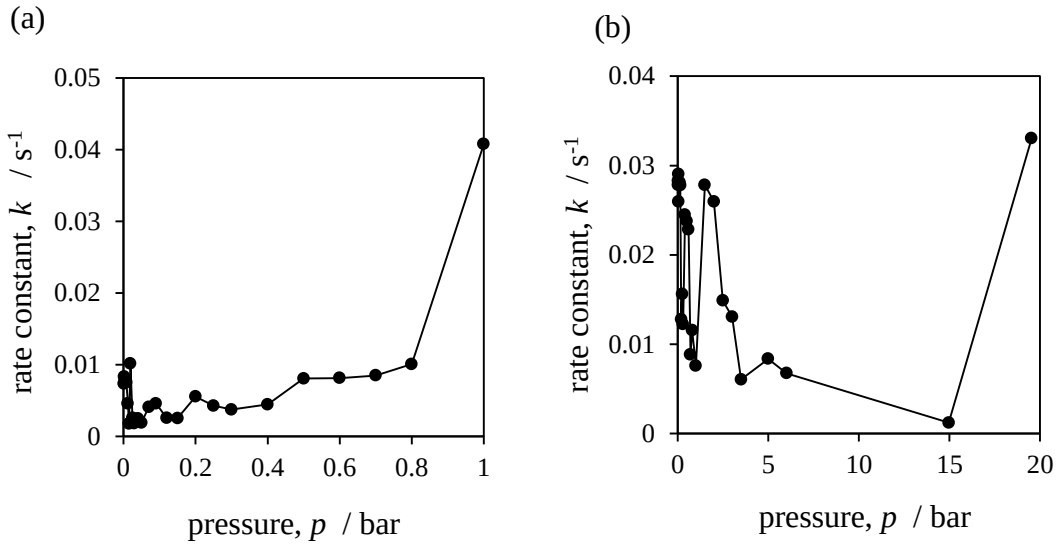

Figure 4.61: Variation of the adsorption rate constant within pressure for the reference sample of TE 7 III activated carbon beads with (a) nitrogen and (b) hydrogen as adsorptives. The lines on the plots join points to illustrate trends in the data.

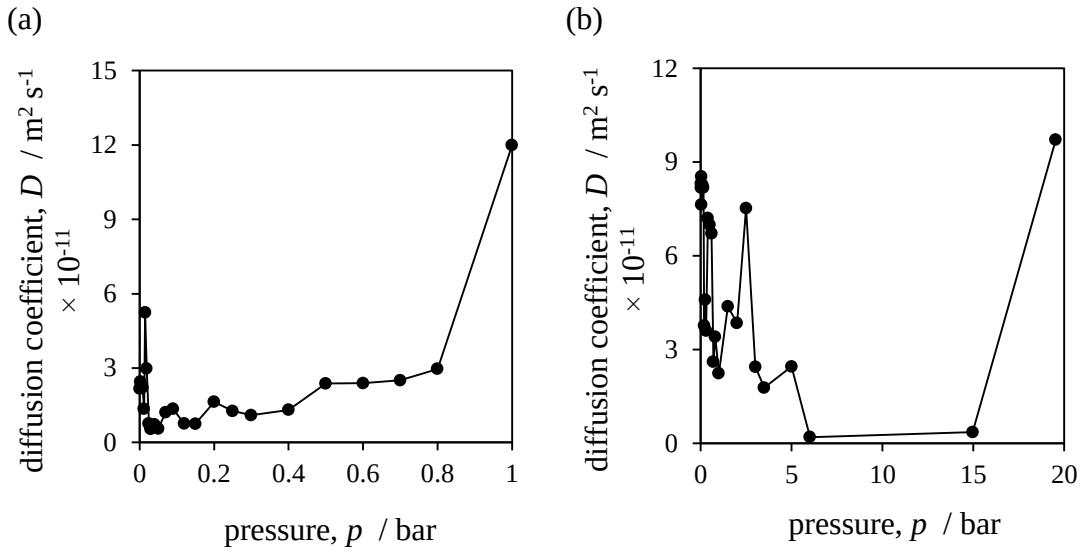

Figure 4.62: Variation of the diffusion coefficient within pressure for the reference sample of TE 7 III activated carbon beads with (a) nitrogen and (b) hydrogen as adsorptives. The lines on the plots join points to illustrate trends in the data.

4.2.3 Development of Hydrogen Adsorption Method

In the following section, the relevant results of hydrogen sorption measurements at 77 K using the experimental procedures detailed earlier in Chapter 3 are given. The most important aspects of the qualitative analysis in terms of reproducibility, reversibility and equivalents of hydrogen storage capacities achieved by different gas sorption apparatus available in–house are discussed. The section ends with critical assessment of hydrogen stream purity as the main contributor affecting the experimental gravimetric isotherms.

4.2.3.1 Hydrogen Sorption Isotherms

The volumetric ASAP 2020 adsorption/desorption isotherms of hydrogen at 77 K up to 1 bar for each investigated sample are displayed in Figure 4.63 to Figure 4.71 in a linear and logarithmic scale of the absolute pressure. All reported isotherms are corrected for

the free space volumes as described in Section 4.2.2-6 using helium pycnometry directly after hydrogen sorption analysis is finished. In the first step, we look at the isotherm shapes with view to determine the pressure range at which hydrogen uptake is reversible and to predict maximum hydrogen capacity. As can be seen, all collected isotherms show typical Type I behavior, where the amount of hydrogen adsorbed increase monotonically with the pressure and no excess is observed at this conditions. In all cases, is believed that hydrogen sorption take place via physisorption as reversible desorption at decreasing pressures and absence of the hysteresis in the resulting isotherms is presented. From these data it is also observed that the highest hydrogen capacity of around 2.46 wt% has been recorded for the Cu-BTC metal organic sample, which could be attributed to its high DR micropore volume (0.64 $cm^3\ g^{-1}$) and high BET surface area (1259.6 ± 39.0 $m^2\ g^{-1}$).

The given hydrogen isotherms represent the measurements of the repeatability determined from two independent ASAP 2020 experiments. Table 4.17 summarizes the overall repeatability results, showing the variation in the amount of hydrogen adsorbed at different relative pressures up to 1 bar. The ratio Run1/Run2, their mean and the standard deviation values are also displayed. For example for the TE 7 III results, the ratio of 0.9964, 0.962 and 0.9983 is found at 0.2, 0.6 and 1.0 bar respectively. The standard deviation of these ratios is only approximately 0.08 %, confirming a high level of isotherm reproducibility.

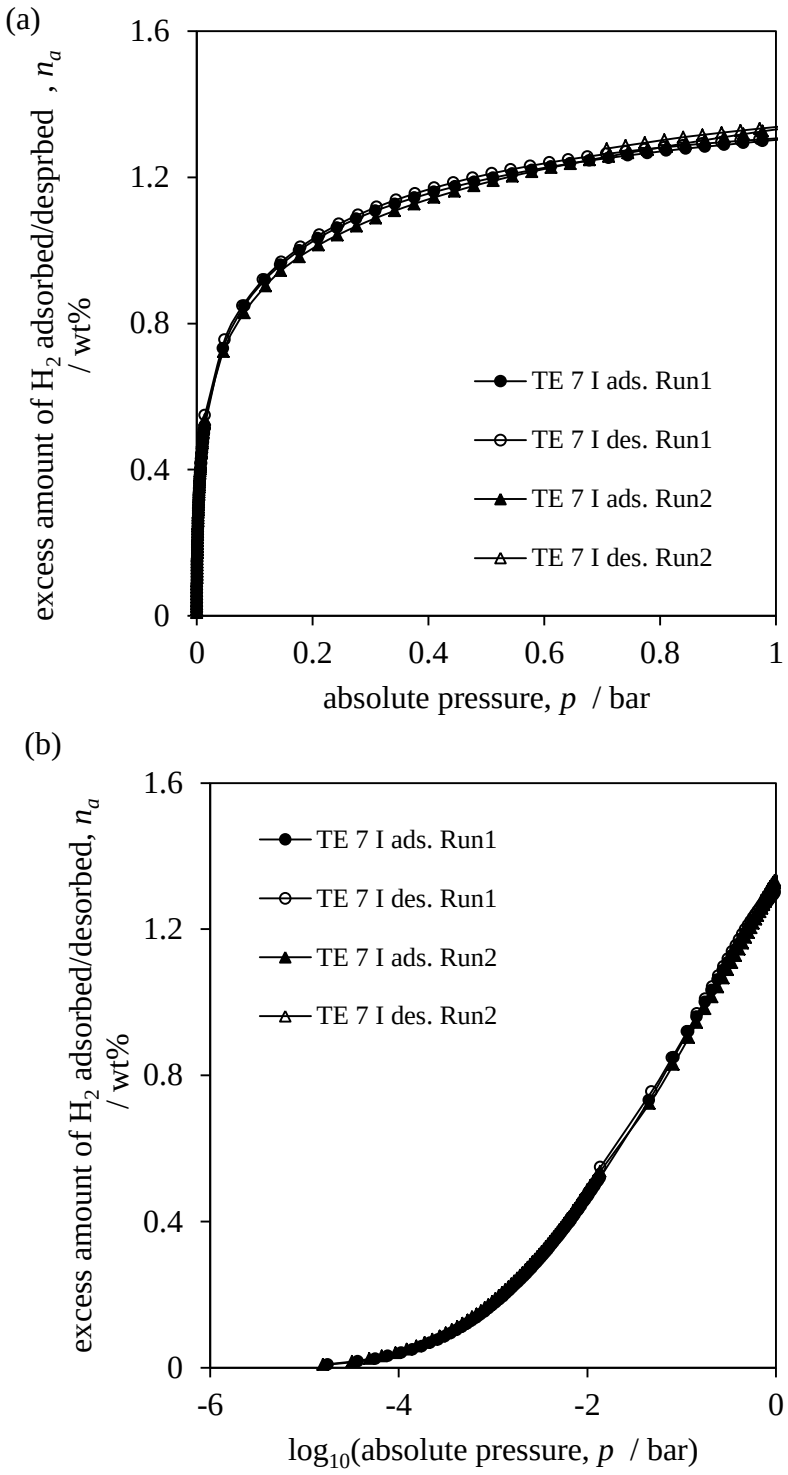

Figure 4.63: Experimental results of volumetric ASAP 2020 excess hydrogen sorption isotherms at 77 K for the TE 7 I activated carbon beads sample in (a) linear and (b) logarithmic scale of absolute pressure. The lines on the plots join points to illustrate trends in the data. Filled and open symbols represent adsorption and desorption points respectively.

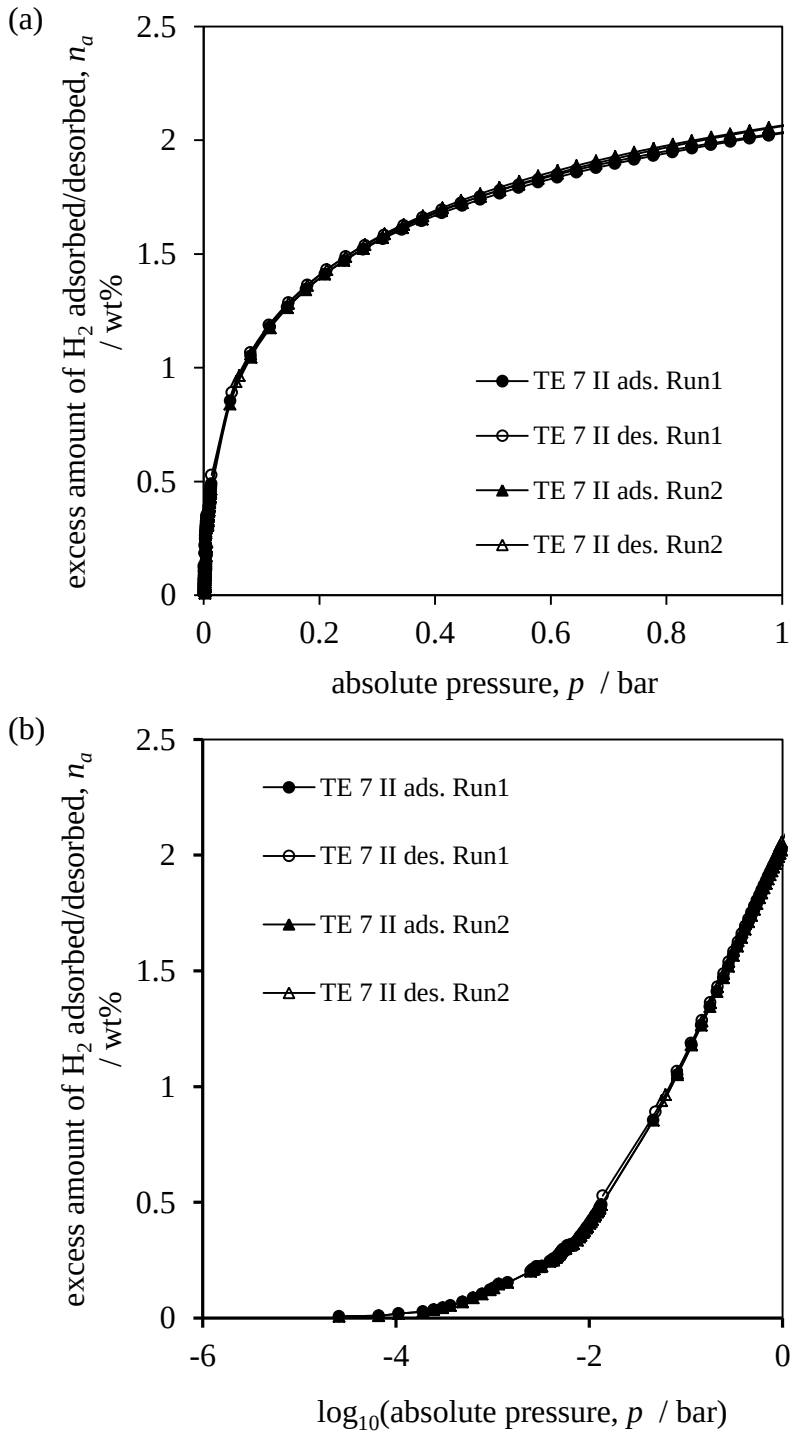

Figure 4.64: Experimental results of volumetric ASAP 2020 excess hydrogen sorption isotherms at 77 K for the TE 7 II activated carbon beads sample in (a) linear and (b) logarithmic scale of absolute pressure. The lines on the plots join points to illustrate trends in the data. Filled and open symbols represent adsorption and desorption points respectively.

(a)

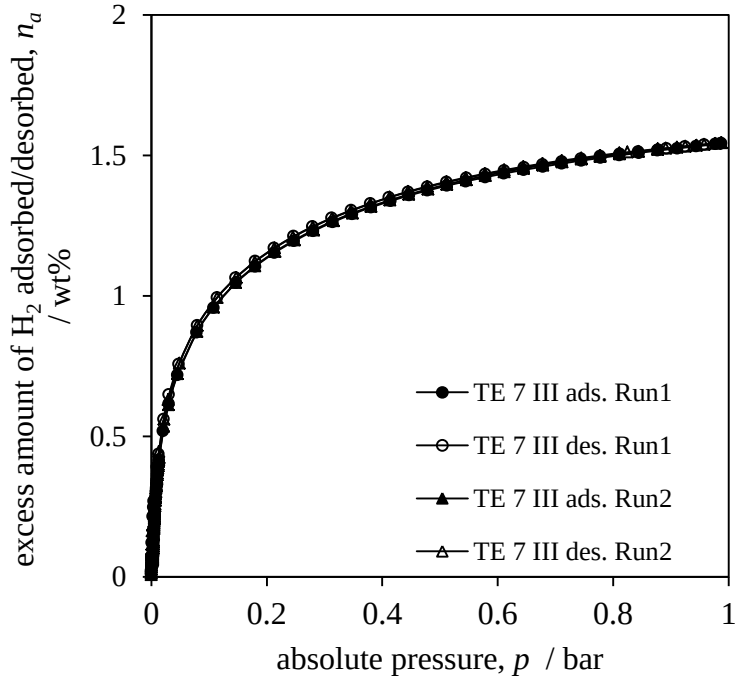

(b)

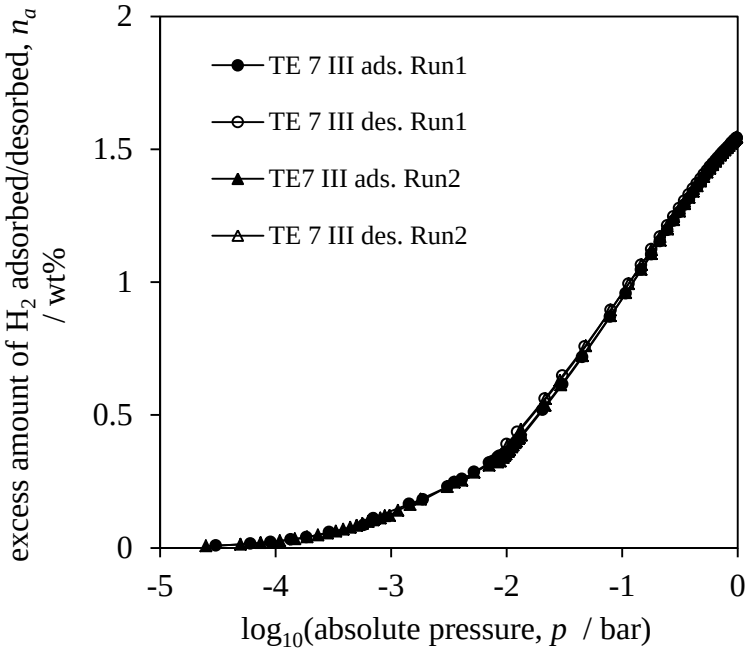

Figure 4.65: Experimental results of volumetric ASAP 2020 excess hydrogen sorption isotherms at 77 K for the TE 7 III activated carbon beads sample in (a) linear and (b) logarithmic scale of absolute pressure. The lines on the plots join points to illustrate trends in the data. Filled and open symbols represent adsorption and desorption points respectively.

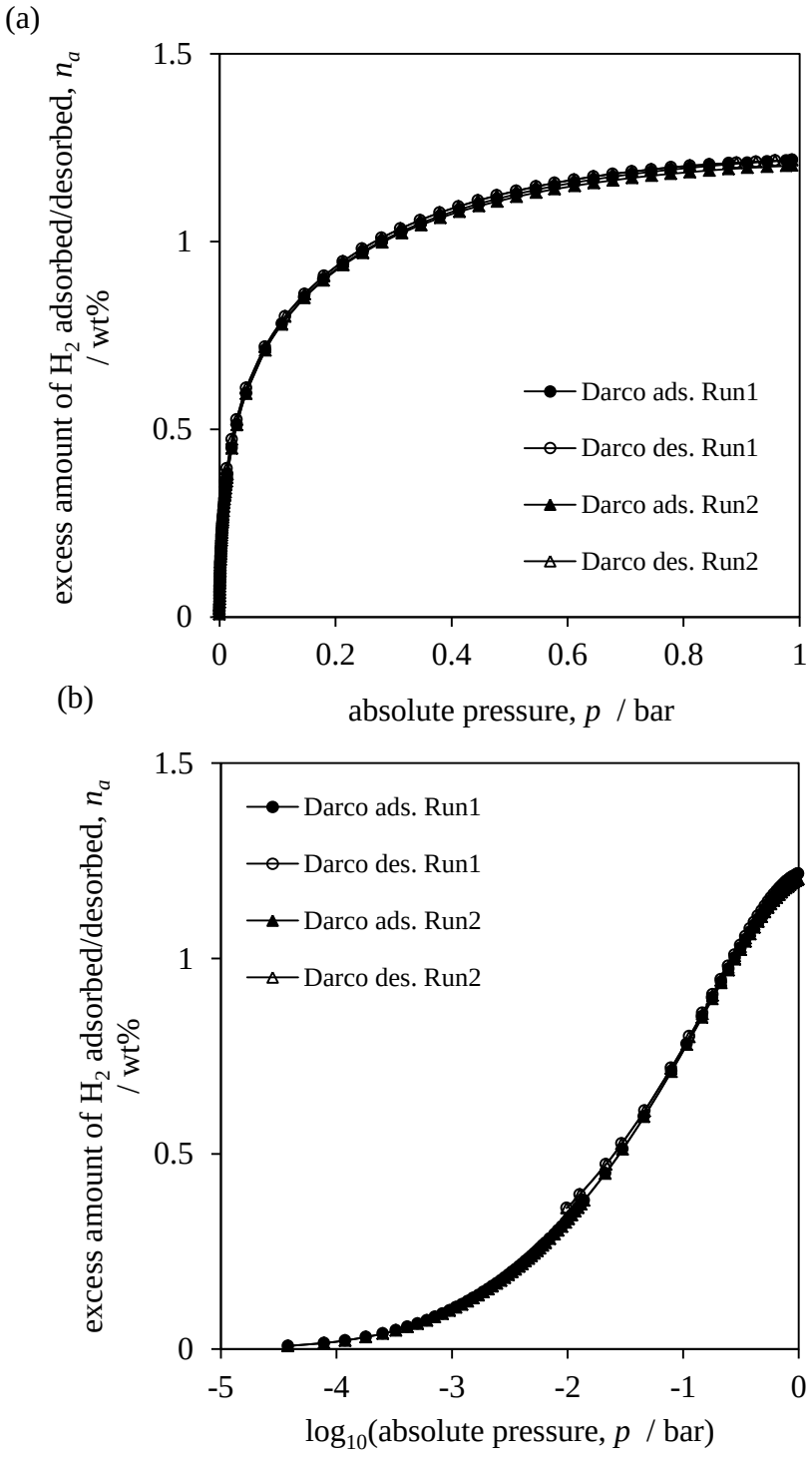

Figure 4.66: Experimental results of volumetric ASAP 2020 excess hydrogen sorption isotherms at 77 K for the Darco activated carbon sample in (a) linear and (b) logarithmic scale of absolute pressure. The lines on the plots join points to illustrate trends in the data. Filled and open symbols represent adsorption and desorption points respectively.

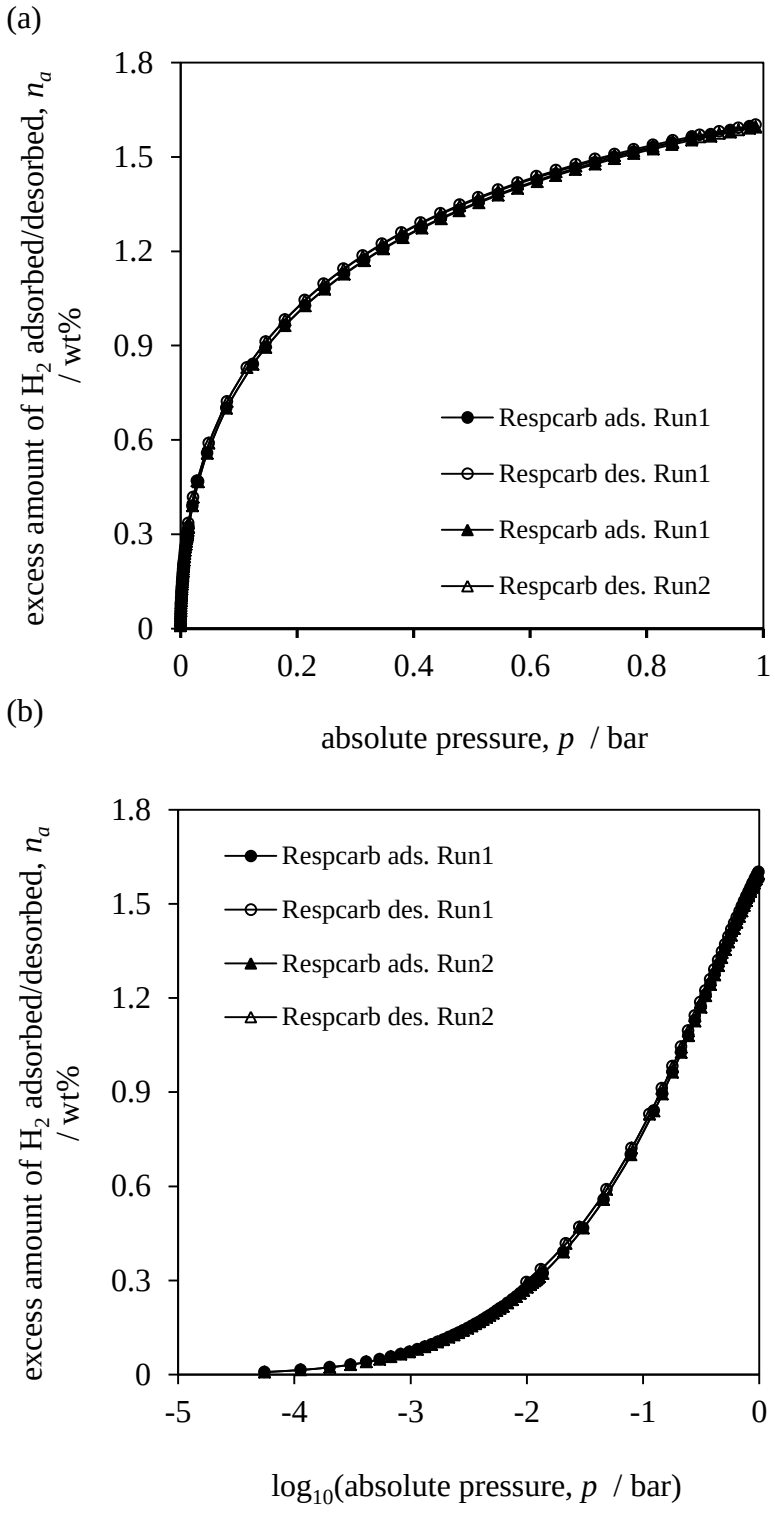

Figure 4.67: Experimental results of volumetric ASAP 2020 excess hydrogen sorption isotherms at 77 K for the Respcarb activated carbon sample in (a) linear and (b) logarithmic scale of absolute pressure. The lines on the plots join points to illustrate trends in the data. Filled and open symbols represent adsorption and desorption points respectively.

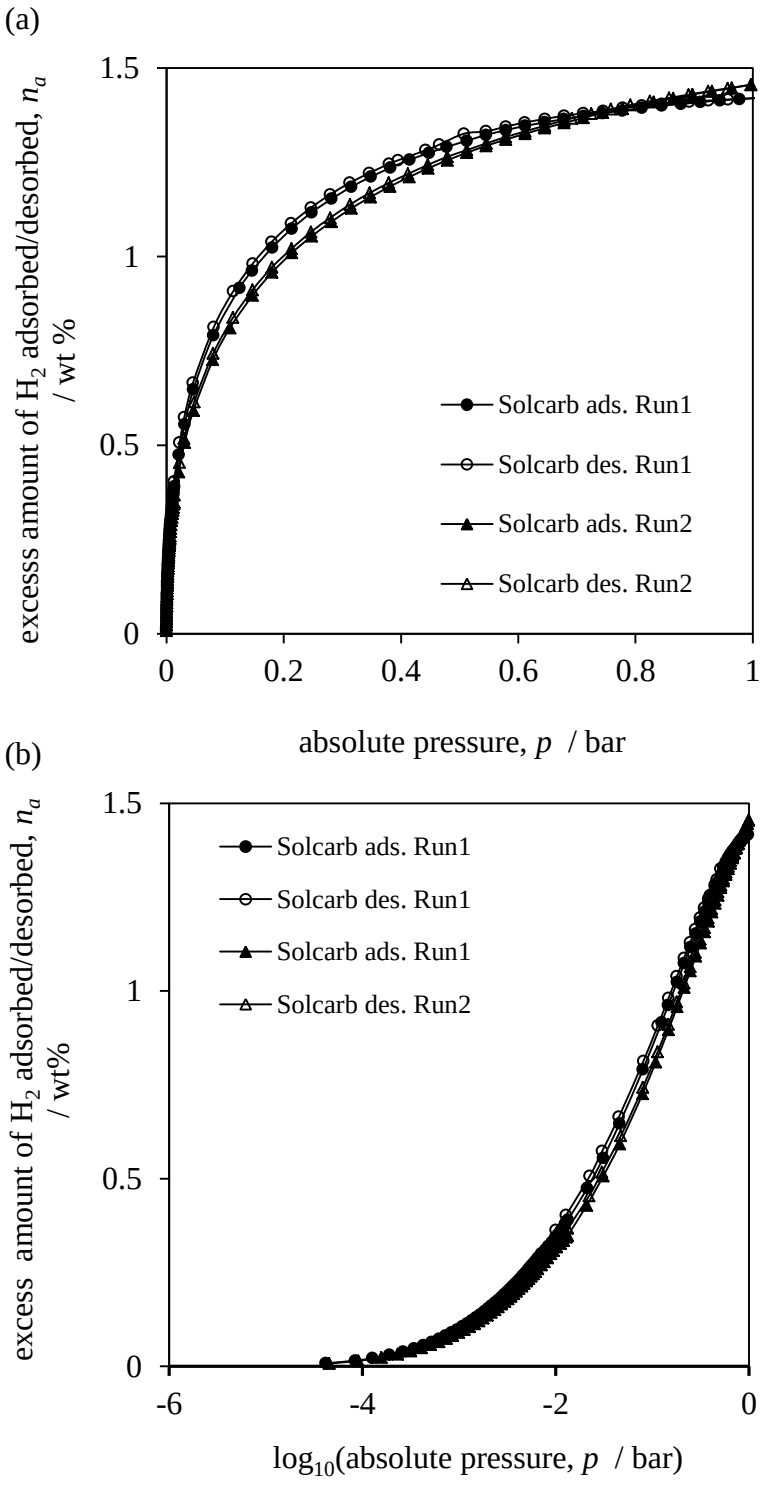

Figure 4.68: Experimental results of volumetric ASAP 2020 excess hydrogen sorption isotherms at 77 K for the Solcarb activated carbon sample in (a) linear and (b) logarithmic scale of absolute pressure. The lines on the plots join points to illustrate trends in the data. Filled and open symbols represent adsorption and desorption points respectively.

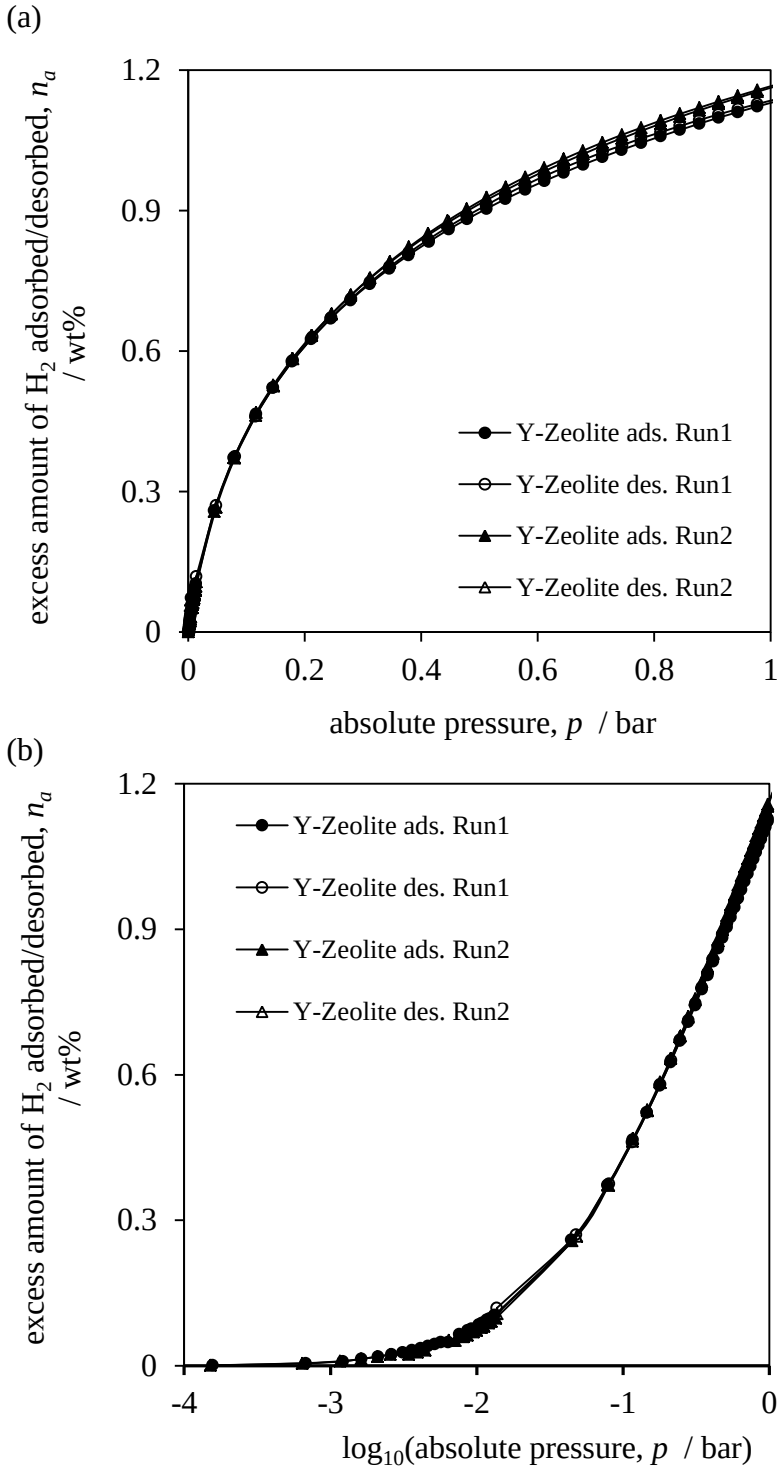

Figure 4.69: Experimental results of volumetric ASAP 2020 excess hydrogen sorption isotherms at 77 K for the Y-Zeolite sample in (a) linear and (b) logarithmic scale of absolute pressure. The lines on the plots join points to illustrate trends in the data. Filled and open symbols represent adsorption and desorption points respectively.

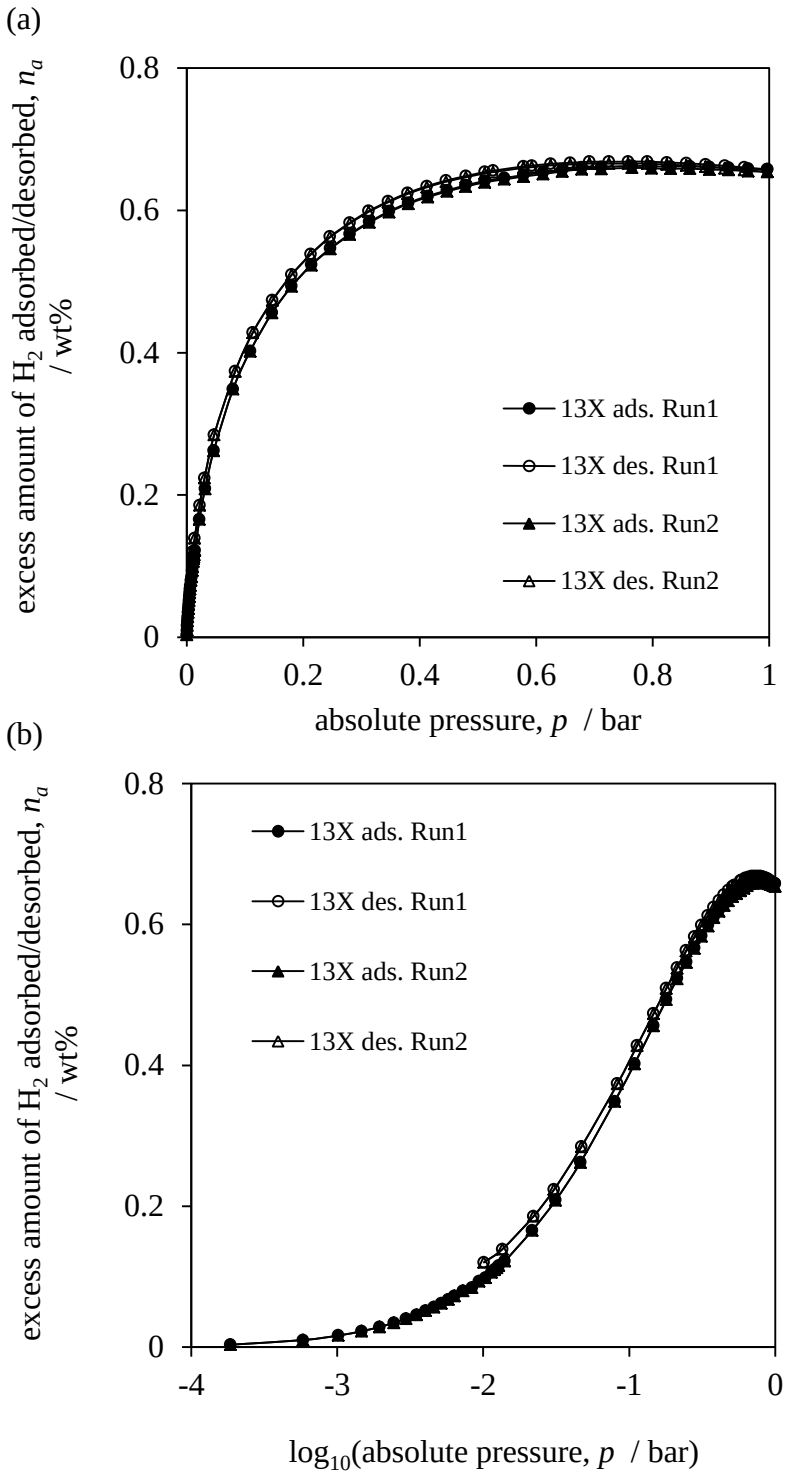

Figure 4.70: Experimental results of volumetric ASAP 2020 excess hydrogen sorption isotherms at 77 K for the 13X zeolite sample in (a) linear and (b) logarithmic scale of absolute pressure. The lines on the plots join points to illustrate trends in the data. Filled and open symbols represent adsorption and desorption points respectively.

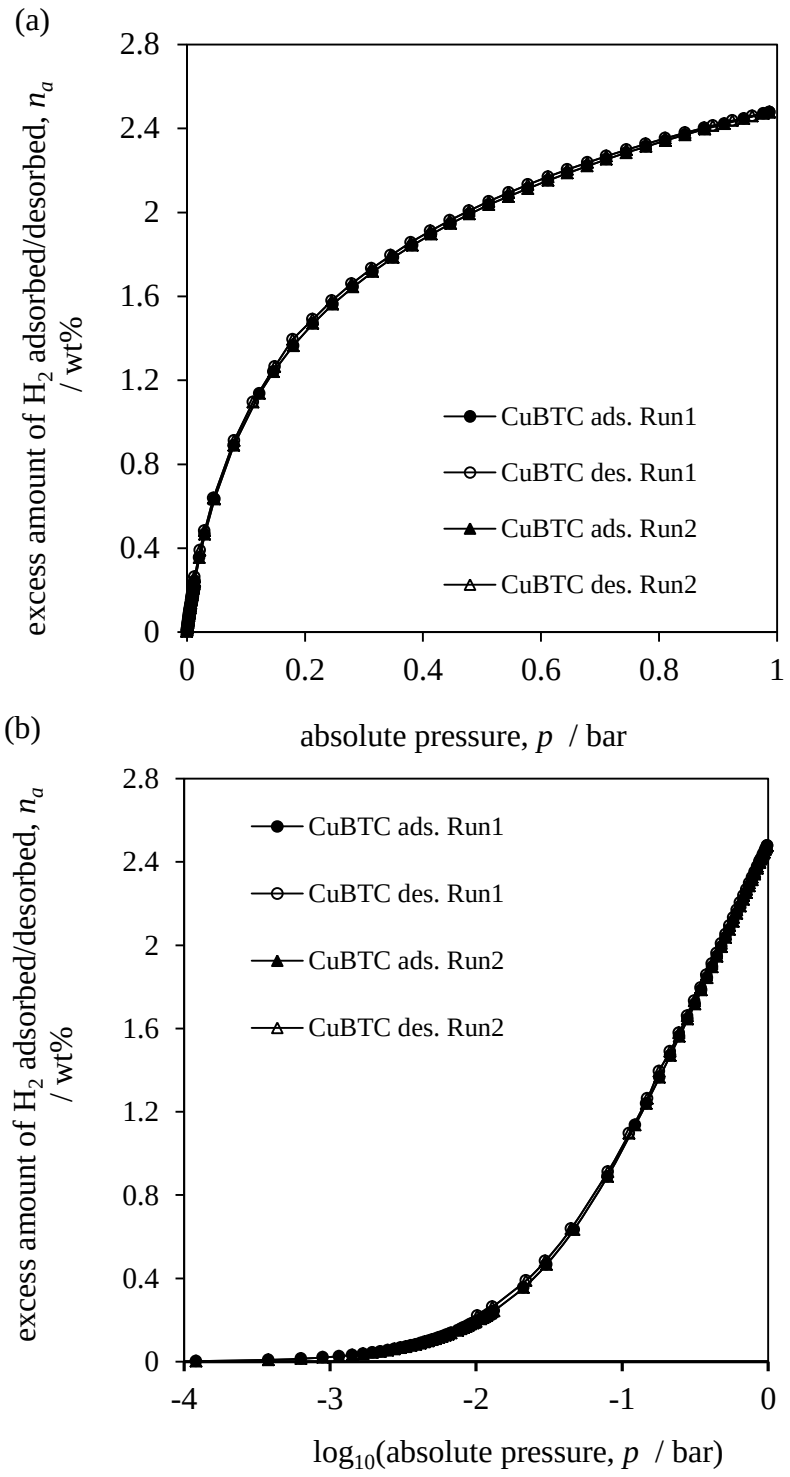

Figure 4.71: Experimental results of volumetric ASAP 2020 excess hydrogen sorption isotherms at 77 K for the Cu-BTC metal organic framework sample in (a) linear and (b) logarithmic scale of absolute pressure. The lines on the plots join points to illustrate trends in the data. Filled and open symbols represent adsorption and desorption points respectively.

Table 4.17: Comparison between excess amounts of hydrogen adsorbed obtained from two individual ASAP 2020 experiments at different absolute pressures. Results are displayed as a ratio Run1/Run2 together with a mean and standard deviation obtained from two independent determinations.

material class	absolute pressure, *p* / bar	excess amount adsorbed, n_a / wt%		ratio	ratio mean ± standard deviation
		Run 1	Run 2		
TE 7 I	0.2	1.0329	1.0144	0.9989	0.9930 ± 0.0130
	0.6	1.2292	1.2267	1.0020	
	1.0	1.3038	1.3331	0.9780	
TE 7 II	0.2	1.4115	1.3952	1.0117	1.0179 ± 0.0066
	0.6	1.8372	1.8065	1.0170	
	1.0	2.0345	1.9851	1.0249	
TE 7 III	0.2	1.1532	1.1574	0.9964	0.9970± 0.0011
	0.6	1.4359	1.4413	0.9962	
	1.0	1.5427	1.5453	0.9983	
Darco	0.2	0.9401	0.9371	1.0032	1.0075 ± 0.0042
	0.6	1.1569	1.1482	1.0076	
	1.0	1.2170	1.2030	1.0116	
Respcarb	0.2	1.0274	1.0259	1.0015	1.0019 ± 0.0008
	0.6	1.4253	1.4213	1.0028	
	1.0	1.5975	1.5953	1.0013	
Solcarb	0.2	1.0738	1.0094	1.0638	1.0184 ± 0.0441
	0.6	1.3461	1.3254	1.0156	
	1.0	1.4201	1.4554	0.9757	
13X	0.2	0.5236	0.5228	1.0015	0.9939 ± 0.0147
	0.6	0.6533	0.6511	1.0033	
	1.0	0.6578	0.6541	0.9769	
Y-Zeolite	0.2	0.6260	0.6330	0.9889	0.9800 ± 0.0084
	0.6	0.9636	0.9842	0.9790	
	1.0	1.1338	1.1663	0.9721	
Cu-BTC	0.2	1.4707	1.4708	0.9999	0.9999± 0.00007
	0.6	2.1519	2.1520	0.9999	
	1.0	2.4779	2.4778	1.0000	

4.2.3.2 Reproducible Hydrogen Sorption

During the course of the hydrogen sorption experiment, we are able to show good isotherm reproducibility obtained on different gas sorption apparatus available in-house. Figure 4.72 summarizes the results of hydrogen sorption experiments on the reference sample of TE 7 III carbon beads all measured at liquid nitrogen temperature (77 K). These include low/high pressure ASAP 2020, HTP-1 volumetric, and high pressure gravimetric IGA experiments. As can be seen remarkably good agreement in both isotherms shape and magnitude of hydrogen uptake is observed. When integrated over a similar pressure range, the adsorption capacity values determined with the three instruments agree, as shown in Table 4.18. From these results it can be concluded that the applied method yields the same hydrogen adsorption isotherms under the same experimental conditions. However, note that in order to obtain this equivalents it took a large number of calibration experiments, mainly influenced by the hydrogen purity as will be discussed in next section.

Table 4.18: Comparison between excess amounts of hydrogen adsorbed obtained for TE 7 III sample from three different apparatus available in-house at different absolute pressures. Results are displayed as a mean hydrogen uptake ± standard deviation.

absolute pressure, p / bar	excess amount of H_2 adsorbed, n_a / wt %			mean ± standard dev.
	ASAP 2020	IGA	HTP-1	
0.2	1.2072	1.1709	1.1003	1.1595 ± 0.0384
0.6	1.5289	1.4912	1.5531	1.5244 ± 0.0220
1.0	1.6614	1.6492	1.6679	1.6595 ± 0.0067
5.0	–	2.0597	2.0774	2.0685 ± 0.0124
10.0	–	2.2572	2.2362	2.2467 ± 0.0148
15.0	–	2.2788	2.2840	2.2814 ± 0.0037
20.0	–	2.2913	2.2916	2.2914 ± 0.0001

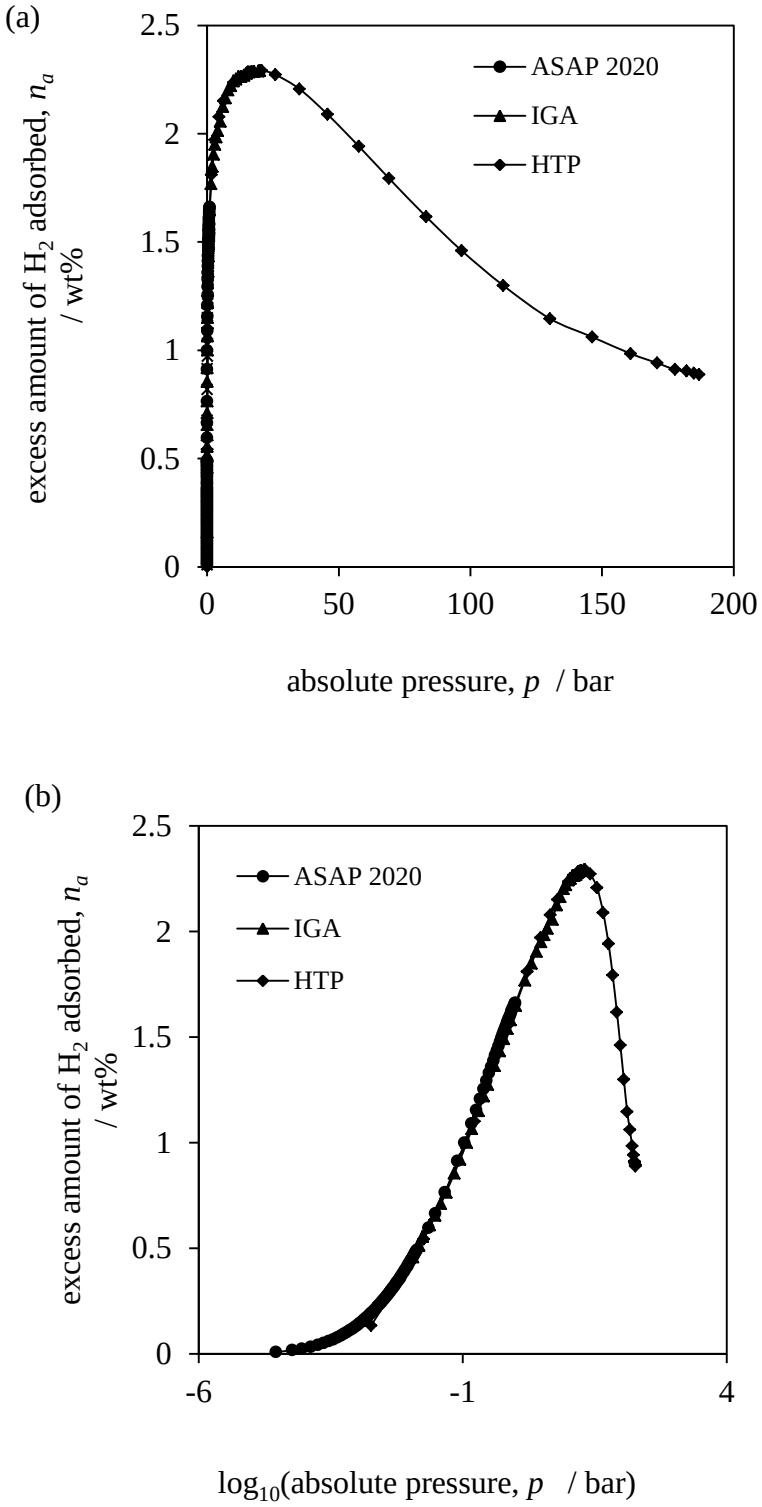

Figure 4.72: Experimental results of excess hydrogen sorption isotherms at 77 K for the TE 7 III activated carbon beads sample in (a) linear and (b) logarithmic scale of absolute pressure determined on different gas sorption devices available in-house. The lines on the plots join points to illustrate trends in the data. Filled and open symbols represent adsorption and desorption points respectively.

4.2.3.3 Influence of Hydrogen Purity

Generally, the hydrogen purity can be considered from two sides, firstly as a purity of hydrogen loaded into storage material and secondly as a purity of hydrogen desorbed from the storage material and delivered to the fuel cell (Yang et al., 2010). In the first case, gas impurities such as water, carbon dioxide and other organic species are introduced to the storage medium during initial loading and can either lead to artificially high levels of hydrogen stored due to uptake of much heavier molecules in preference or artificially low levels if the impurities block the pores or brake down the material structure (Strobel et al., 2006). In second situation, the impurities are desorbed from the storage material and can either dilute the hydrogen fuel (like nitrogen) or 'poison' the sensitive FC catalyst, causing its irreversible degradation (for example ammonia) (Yang et al., 2010). For these reasons the purity of hydrogen should always be tested carefully.

In this section the influence of hydrogen purity on the experimental hydrogen sorption at 77 K for the representative TE 7 III sample is discussed. Two types of commercial hydrogen were tested. These include, the standard grade hydrogen (SG-H_2) supplied by BOC, containing approximately 50 ppm impurities, and the ultra pure BIP-H_2,claimed to be the purest hydrogen gas available on the UK market from Air Products, having around 1 ppm impurities level (Air Products). However, it is important to realize that specified purities refer to initial loading not contained in the cylinders, so the out-put hydrogen stream can vary as discussed in the next pages of this section.

From the measurements side, the simplest way to identify the hydrogen stream contamination is by checking the gravimetric isotherm uptakes, since impurities such as moisture, carbon dioxide or other organics having much larger molecular masses and interactions energies then hydrogen would have a great effect on the collected data. Figure 4.73 shows the hydrogen sorption results determined gravimetrically (IGA) for the representative TE 7 III carbon beads sample using different hydrogen purity grades. It can be seen that for two isotherms on the top (denoted as the SG-H_2 and BIP-H_2) the excess hydrogen uptake is incredibly high. For example, for the isotherm collected using

standard grade hydrogen (SG-H_2) the determined maximum hydrogen capacity was approximately 41.80 wt%, where for ultra pure BIP-H_2 was slightly lower of around 33 wt%. Moreover, both isotherms show the appearance of hysteresis during desorption, implying that sorption cycles are irreversible. Please note that prior to hydrogen sorption measurements the outgas was run to bring the IGA system to very low vacuum conditions (10^{-6} mbar), ensuring that any potential contaminants from the tubing are removed.

In order to minimize hydrogen stream contamination, the filtration chamber was designed (see Figure 4.74) and located just after the BIP hydrogen cylinder next to the IGA (see schematic diagram in Figure 3.8, Chapter 3). As can be observed in Figure 4.74 a stainless steel filtration chamber incorporates two different sorbents sections with a 50/50 fill ratio. The first section contains microporous WSC 470 carbon (Chemviron Carbon) and is used to remove heavy organic species (such as carbon dioxide or methane), and the second section with 13X Zeolite bed (UOP) is selected for moisture trapping, which is believed to be the main pollutant present in the tested cylinder. As can be seen in Figure 4.73 (the third isotherm from the top, denoted as BIP-H_2 + filter) even with sorbent based filtration chamber the small quantities of impurities are still present in hydrogen stream, which is evident by a higher than expected uptake of 4.5 wt% (4 bar) and lack of reversibility in the adsorption/desorption cycle. Then, a liquid nitrogen trap was installed in-line, directly after the sorbents filtration chamber to ensure that the gas stream was moisture free. As can be seen (Figure 4.73 isotherm denoted as BIP-H_2+filter+cold trap) the accuracy of the hydrogen sorption measurements was improved to fully reversible level of around 2 wt% at 4 bars.

In order to determine accurate measurements it is important to replace or regenerate the sorbents in the filtration chamber before they are fully saturated. Regeneration can be performed in situ by wrapping the filtration chamber with a heating tape. However in practice this could introduce some errors into measurements, because of the difficulties in achieving uniform heating during the degassing stage or carbonisation of volatile on sorbents etc. For these reasons the recommendation is that replacing the sorbents with

new or regenerated the materials regularly, although this could also introduce some errors due to exposure to air or undetected leaks in the system.

Therefore, in our experimental practice a one step filtration system based on the LN_2 cold trap (without sorbent filter) could be an interesting alternative for moisture removal from the BIP-H_2 hydrogen stream, which entrains most of the gas contamination. This approach was successfully adopted by other groups (Abdul-Majeed et al., 2012, Phillips and Shivaram, 2007) and strongly recommended for reducing space requirements and cost of the system for on-board FC application.

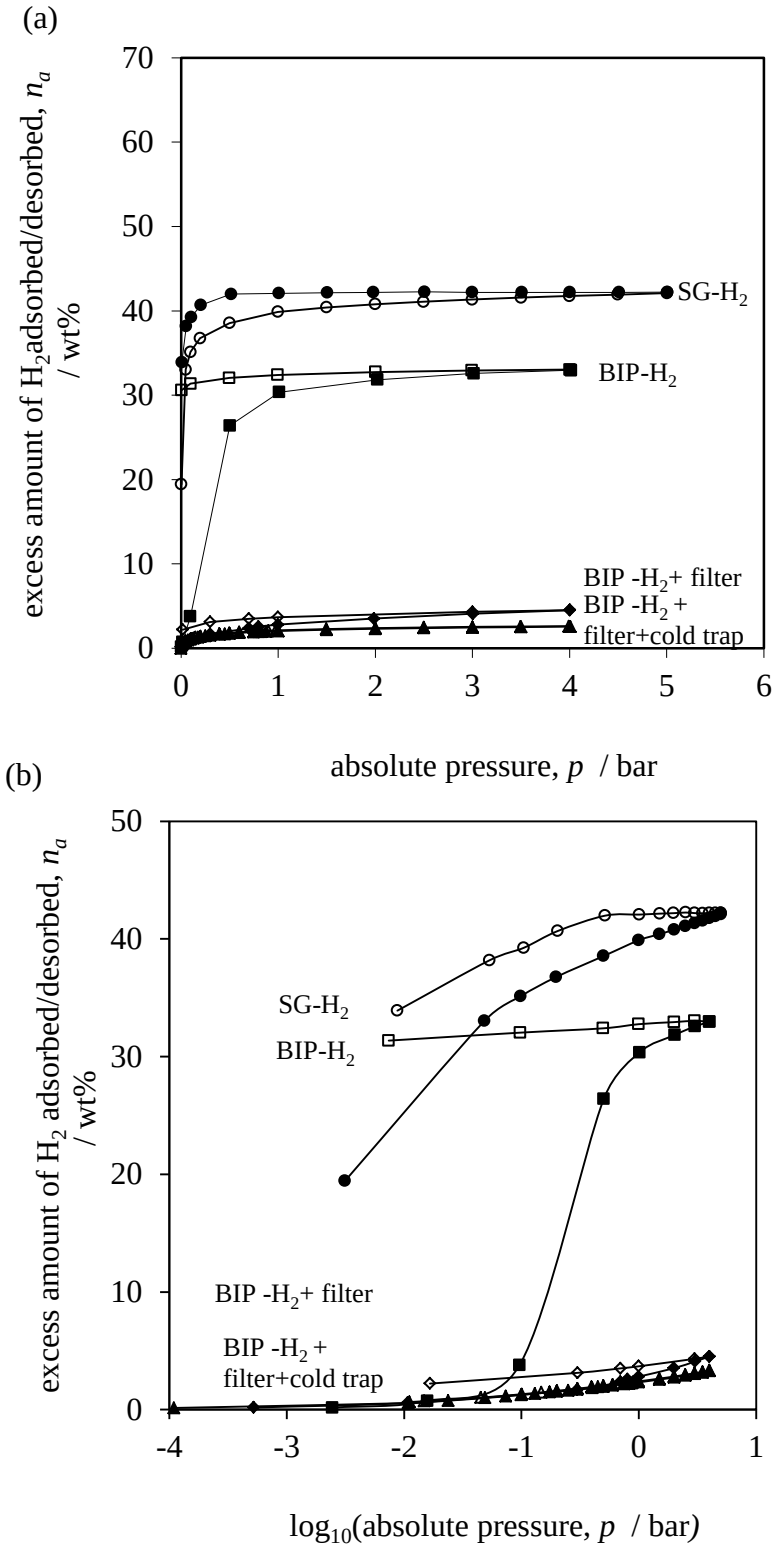

Figure 4.73: Effect of gas purity on the excess hydrogen sorption at 77 K recorded on the IGA gravimetric analayser for the representative sample of TE 7 III activated carbon beads (a) in linear and (b) logarithmic scale of absolute pressure. The lines on the plots join points to illustrate trends in the data.

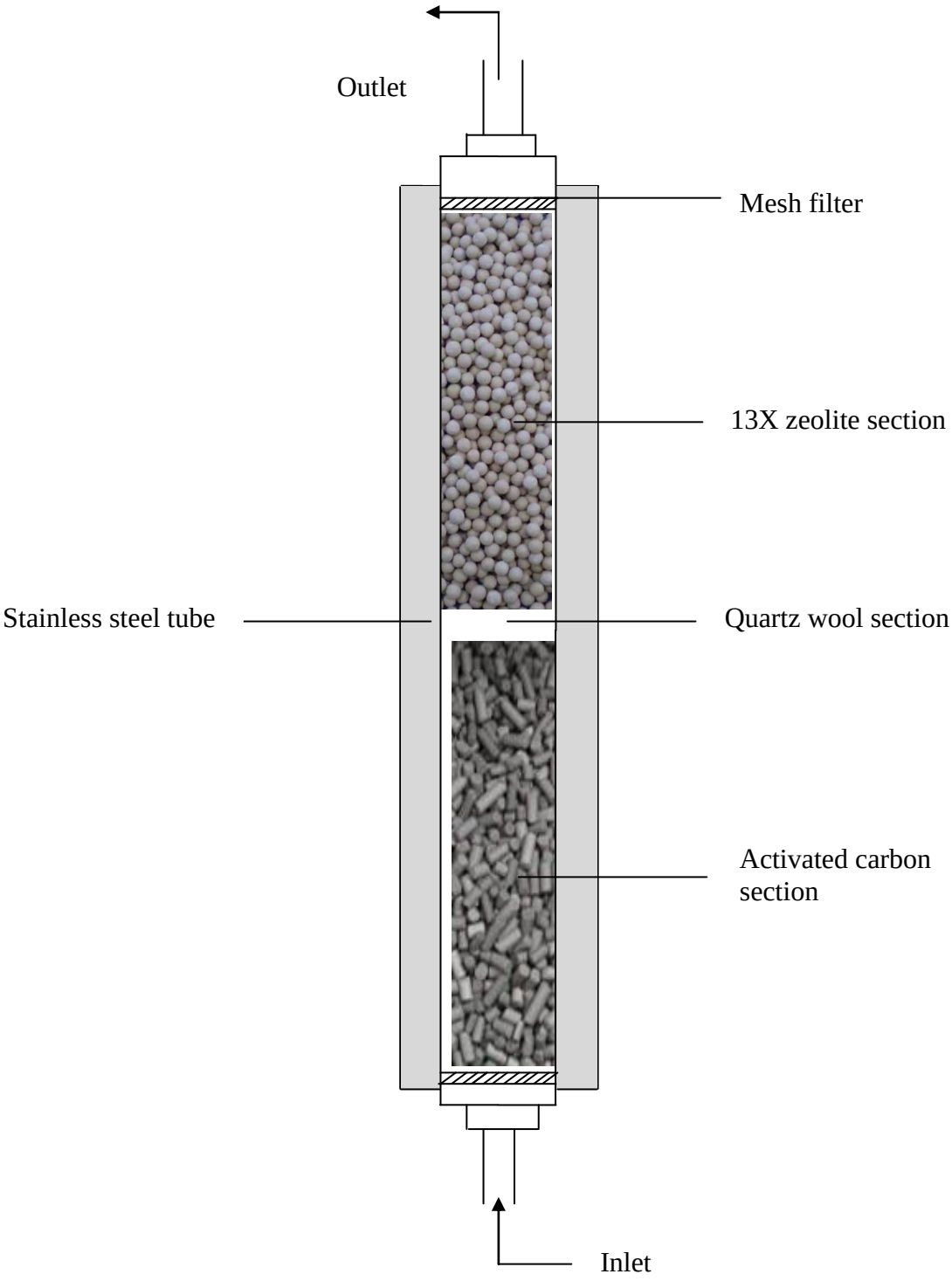

Figure 4.74: Schematic view of the scaled up hydrogen steam purification system designed for the IGA gravimetric system. Physical dimension: 6 cm×37 cm.

CHAPTER 5

INTERLABORATORY STUDY: RESULTS AND DISCUSSION

5.1 Introduction

This chapter is a report on an interlaboratory study for the low temperature (77 K) gas sorption measurements made on the reference TE 7 III nanoporous activated carbon bead sample by a number of different laboratories. The test method involved two individual procedures for determining low and high-pressure isotherms for both nitrogen and hydrogen adsorptives. The results presented below are organized into five main sections and illustrated using graphs and tables along with the discussion on the main findings of this comparison study. Firstly, a brief overview of the tested sample and on the proposed methodology along with the discussion how the experimental data were collected across different laboratories is presented (Section 5.2). Secondly, the results of the excess nitrogen sorption isotherms measured at 77 K are given with the view to determine the BET specific surface area (a_s) and micropore volume (v_p) (Section 5.3). The chapter continues with the third section (Section 5.4), where the selections of the low and high pressure excess hydrogen sorption isotherms collected by different groups are compared. This is followed by the section four (Section 5.5), where overall summary of this interlaboratory study together with a discussion on results variability and improvement are given. Finally, based on the collected results the most accurate testing methodology for the nitrogen and hydrogen sorption at 77 K in the nanoporous materials is proposed in Section 5.6.

5.2 General Observations

Because of lack of hydrogen sorption measurements standardisation, considerable problems in the data reproducibility become more significant, leading to conflicting reports on nanoporous materials in different labs. These problems have been addressed by recent interlaboratory study (Zlotea et al., 2009) where the hydrogen sorption of microporous Takeda carbon at 77 K and ambient temperature were determinate. The results clearly show remarkable scatter in the collected data among participating laboratories, particularly at the higher pressure ranges, emphasizing the need for the more rigorous and precise measurement techniques and procedures.

In this respect our research group at the University of Bath decided to design and conduct an interlaboratory study, in which the variability of the sorption results using both nitrogen and hydrogen gas were examined. In contrast to the previous work this interlaboratory test was set-up under tightly controlled experimental conditions in order to eliminate the sources of the possible errors to minimum. A well characterised sample of TE 7 III activated carbon beads, supplied from MAST Carbon, UK was used as a reference for this study. As stated previously, this carbon is a phenolic resin based, activated at high temperature in steam atmosphere. Detailed structural characterisation results of TE 7 III carbon beads using available 'in-house' standard experimental techniques are displayed in Figure 5.1 below. The reference value of the BET specific surface area (Figure 5.1 (d)) was assumed to be 780.4 ± 19.5 $m^2 g^{-1}$, obtained from low pressure nitrogen isotherm at 77 K, calculated over 10 data points in the relative pressure range between 0.05–0.3. The Dubinin-Radushkevich (DR) micropore volume was accepted as 0.38 ± 0.01 $cm^3 g^{-1}$, determinate in the relative pressure 3×10^{-5}–0.08

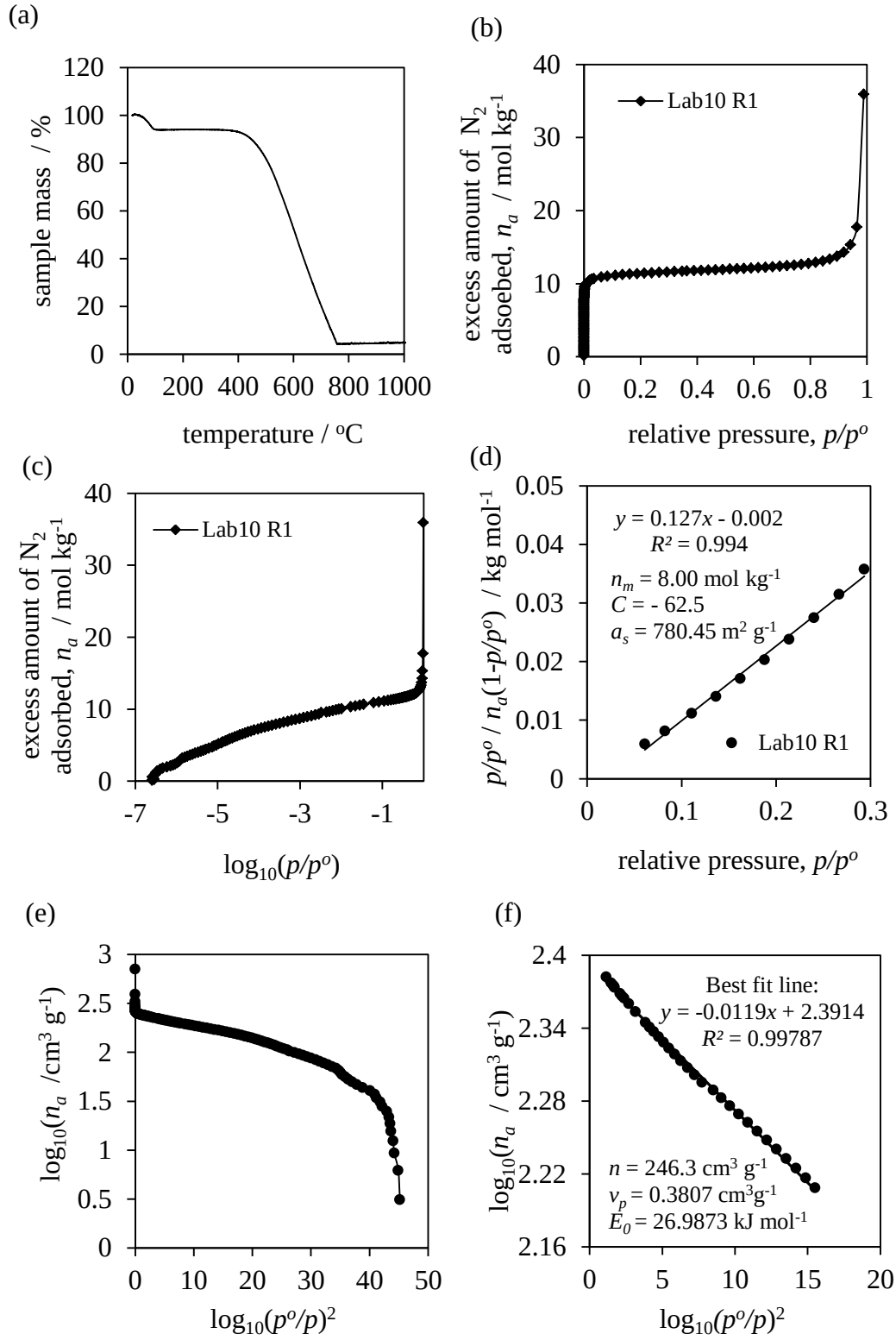

Figure 5.1: TE 7 III structure characterisation results: (a) TGA scan at 5 $^{o}C\ min^{-1}$ in air, nitrogen isotherm at 77 K (b) in a linear and (c) logarithmic scale of p/p^{o}, (d) BET surface area plot recorded in the BS range 0.05–0.3 p/p^{o}, (e) DR micropore volume over the whole pressures, and (f) enlarge view of the best fit line over the BS range 10^{-4}–0.1 p/p^{o}.

over 37 data points (Figure 5.1 (e), (f)). This material is highly homogeneous (see Figure 5.1 (g)) with the average particle diameters found as 330 ± 20 μm. Furthermore, TE 7 III sample is very stable at high temperature (up to 380 ^{o}C), which facilities the removal of the moisture and over contaminants from their surface without structure degradation (Figure 5.1 (a))

Prior to interlaboratory testing, the applicability of the new testing methodology based on the collected experience with a test sample were proven in-house study using different instrumental techniques as discussed in Chapter 4. Than best applicable set of criteria for sample preparation and analysis was chosen and presented as a part of the test protocol for this interlaboratory study (Supplementary Information, Section S7). The test method was titled: "Determination of nitrogen/hydrogen sorption isotherms using reference sample of nanoporous activated carbon beads", June 2011, and is also attached as part of S7. The first part of the testing method (Procedure 1) was conducted for the determination of low temperature and pressure nitrogen sorption isotherms which was used to evaluate the specific surface areas (a_s) and DR micropore volumes (v_p) of reference beads sample. The accuracy of the measurements was estimated by comparison of two replicate results. In the second part of the testing procedure (Procedure 2) which was used to determine low and high pressure hydrogen isotherms, the testing method was focused on the determination of the maximum hydrogen sorption capacities in different hydrogen pressures. Similar like for the Procedure 1, the accuracy and repeatability of the measurements was evaluated from two independent determinations. For the success of this study, all the participants were requested to slickly follow the procedures of sample degassing and analysis. A special Data Sheet forms were attached to the testing instructions, which were intended to obtain further information on the measurements conditions applied by the each laboratory. An example of the Data Sheet form is provided in S7.

For the first time this interlaboratory exercise was announced to the potential test participants on the UK-SHEC International Hydrogen Research Showcase in Birmingham on 13–15 April 2011. Invitation letters were sent to the 20 laboratories on

beginning of May 2011 and the appropriate notice, together with on-line registration form was published on the Dr Tim Mays research group web page (http://people.bath.ac.uk/anh22/round.htm) (shown in Supplementary Information, Section S8). Then, on the beginning of June a test samples were dispatched and the deadline for reporting of results was set to 31st July 2011. However, the deadline for submitting analysis results was extended on request of some participants twice to finally mid of February 2012.

Analysis results were received from six out of ten laboratories that were supplied with a test samples. The missing laboratories were repeatedly reminded to submit their data, but they either stated that they were not able to measure the test material due to problems with instruments calibrations or did not respond to the reminders. Therefore we decided to close the data submission mid of February 2012. As requested, the majority of laboratories sent complete sets of results for both type of sorption measurements. Only four of the participating laboratories fully performed their test as requested in the test protocol. The laboratories expressed their results in mol kg^{-1} for the nitrogen sorption and as wt% if the hydrogen sorption was taken into account. It should be noted, that in this study the identity or the sources of the results are not given. Each of laboratories is referred to by a test laboratory number (Lab Code). The results from individual laboratories are confidential and the origin of the results was not identified to other participants.

The sample degassing procedure was strictly defined amongst the participating laboratories, where about 100 mg of the tested sample were degassed at 350 ^{o}C using high vacuum (10^{-6} mbar) for 8 hours. Nearly all groups performed they sample degassing as requested, only one participating lab dried the sample at lower degassing temperature of the 300 ^{o}C.

Two different instrumental techniques were used in this comparison study to determinate nitrogen and hydrogen sorption isotherms, including volumetry and gravimetry. As stated in the Chapter 3, both setups have the same basic components

such as reference volume, measuring sample cell, valves, high accuracy pressure transducers and the temperature control unit. In the volumetric measurements the amount of gas adsorbed is determined by the measuring change in the pressure, while in the gravimetric isotherm is determined by the weight change of the sample recorded during procedure. Both volumetric and gravimetric methods used the helium as the reference gas to determinate the buoyancy (gravimetry) and dead volume of the sample cell (volumetry), assuming that as helium is non adsorbing gas at these conditions. But as previously recognized in Chapter 4 for our TE 7 III carbon beads sample even small degree of helium sorption will lead to an underestimation of the sample volume, and decrease the amount of gas adsorbed by the sample especially when the measurements are performed at 77 K.

5.3 Nitrogen Sorption Results

The 77 K excess sorption isotherms for nitrogen measured on the reference sample of the activated carbon beads by all the participating groups are plotted in Figure 5.2 on the linear (a) and the logarithmic scale of relative pressure (b). Moreover, a detailed information regarding micropore region (c) and capillary condensation (d) are accessed. It can be seen from these graphs that the collected isotherms show typical microporous Type I behavior, with plateau of around 10.80 mol kg^{-1} reached at 0.2 of relative pressure, p/p^o. Duplicate measurements results determinate by the individual laboratory show very good within-laboratory repeatability.

This interlaboratory comparison results shows that one sorption dataset reported by Lab 7 are slightly lower than those presented by the other participants, in the same pressure ranges with the maximum deviation of around 10 %. This is perhaps due to fact that not low enough degassing vacuum about 10^{-2} mbar was used and therefore that the sample size was too small in comparison to sample cell size. Generally the level of accuracy for these interlaboratory measurements is very good and the variability in the nitrogen sorption data between different laboratories is acceptable.

(a)

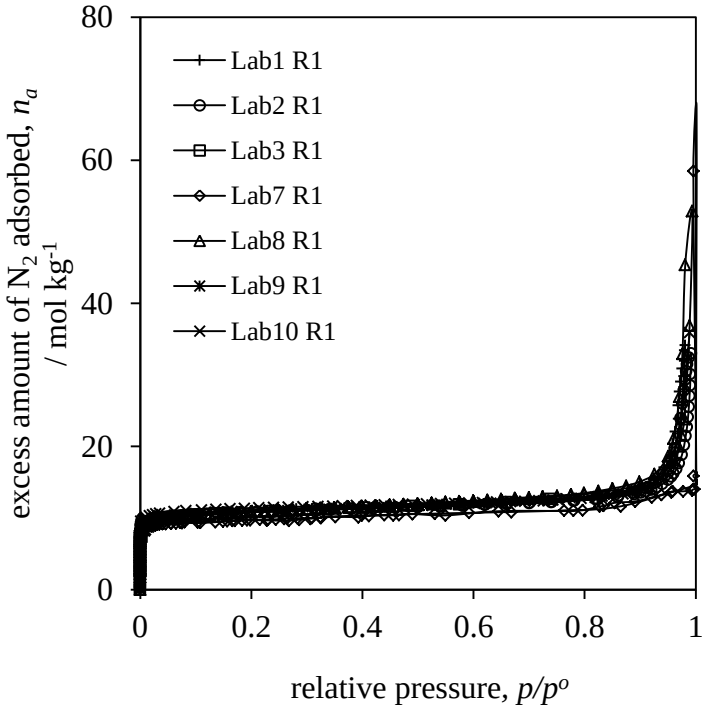
Lab1 R1
Lab2 R1
Lab3 R1
Lab7 R1
Lab8 R1
Lab9 R1
Lab10 R1
excess amount of N2 adsorbed, na / mol kg-1
relative pressure, p/po
0
20
40
60
80
0
0.2
0.4
0.6
0.8
1

(b)

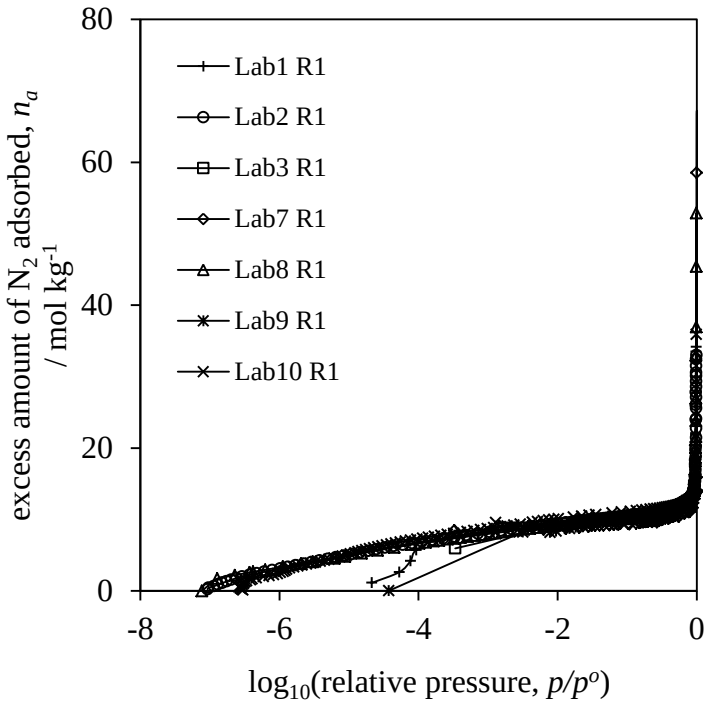
Lab1 R1
Lab2 R1
Lab3 R1
Lab7 R1
Lab8 R1
Lab9 R1
Lab10 R1
excess amount of N2 adsorbed, na / mol kg-1
log10(relative pressure, p/po)
0
20
40
60
80
-8
-6
-4
-2
0

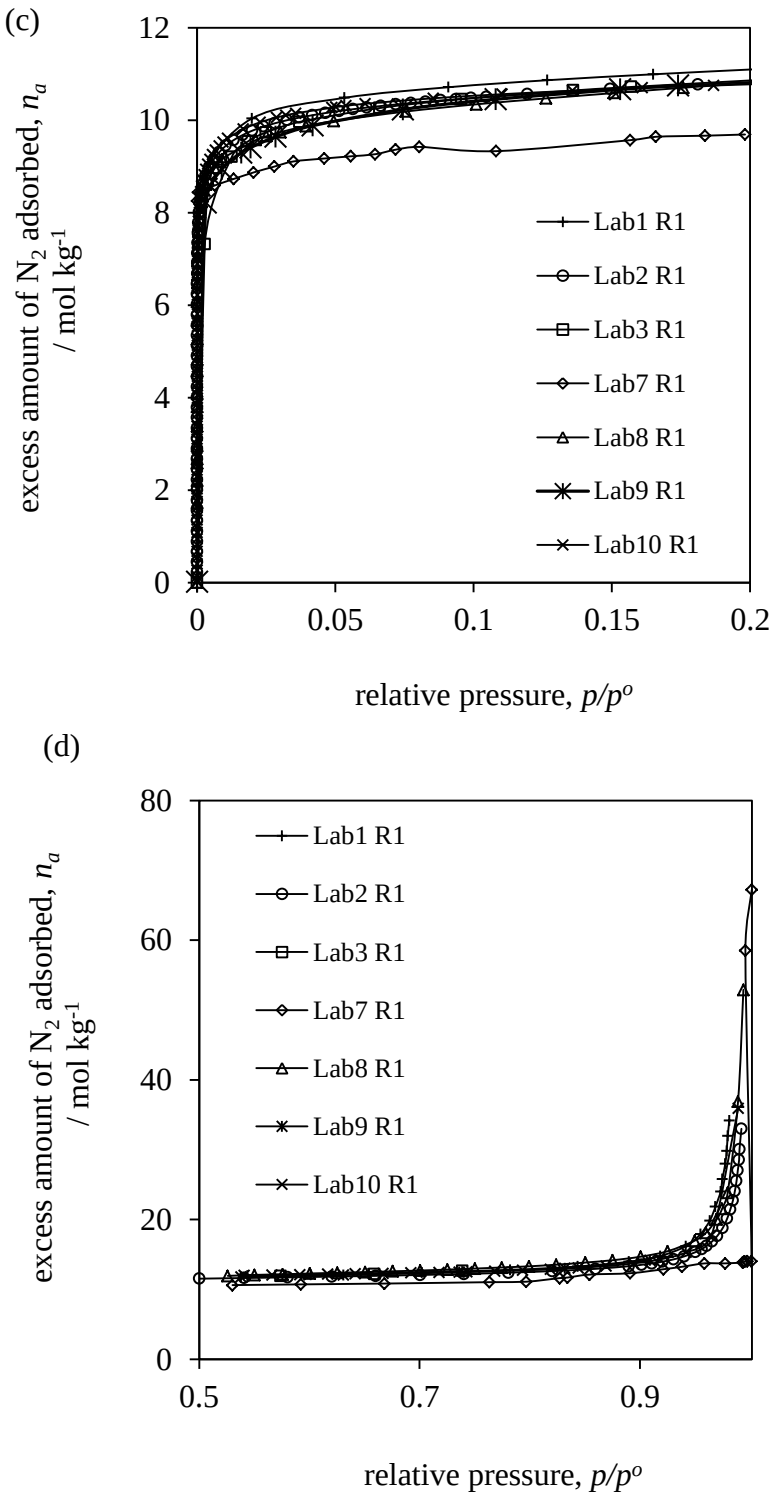

Figure 5.2: Comparsion of interlaboratory results for the nitrogen excess adsorption isotherms recorded at 77 K on reference TE 7 III activated carbon beads sample (a) in a linear and (b) logaritmic scale of relatve pressures, p/p^o, (c) showing enlarged view of the microporous and (d) across the capillary condensation range.

5.3.1 BET Specific Surface Area Results

In this section, the final results of the specific surface area determination within different participating laboratories are compared. For these purpose we applied well established BET analysis carried out in the British Standard linearity pressure range between 0.05–0.3 of p/p^o. The results for each replicate test are plotted as a function of relative pressure and displayed in the Figure 5.3 below.

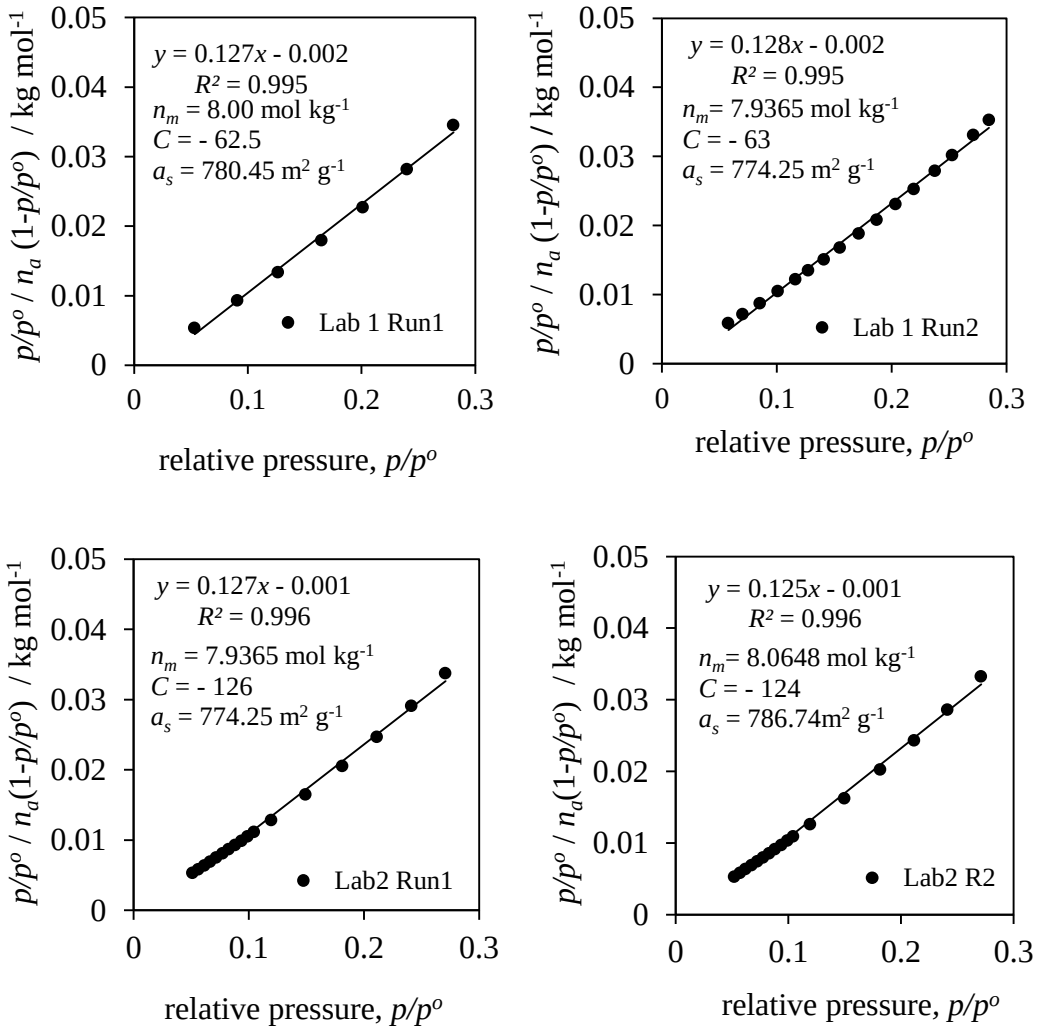

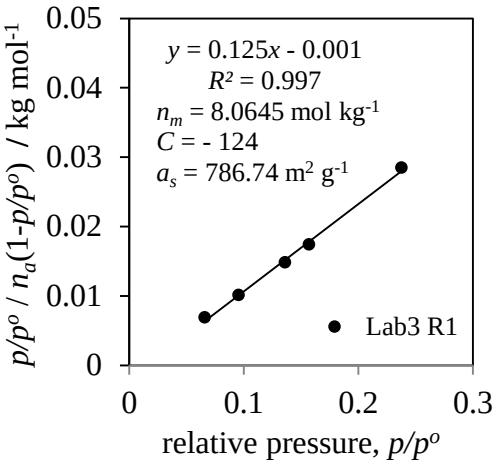
y = 0.125x - 0.001
R² = 0.997
n_m = 8.0645 mol kg-1
C = - 124
a_s = 786.74 m² g-1
Lab3 R1
p/p° / n_a(1-p/p°) / kg mol-1
relative pressure, p/p°

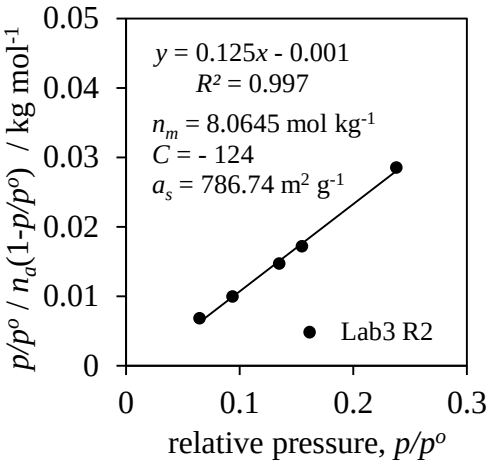
y = 0.125x - 0.001
R² = 0.997
n_m = 8.0645 mol kg-1
C = - 124
a_s = 786.74 m² g-1
Lab3 R2
p/p° / n_a(1-p/p°) / kg mol-1
relative pressure, p/p°

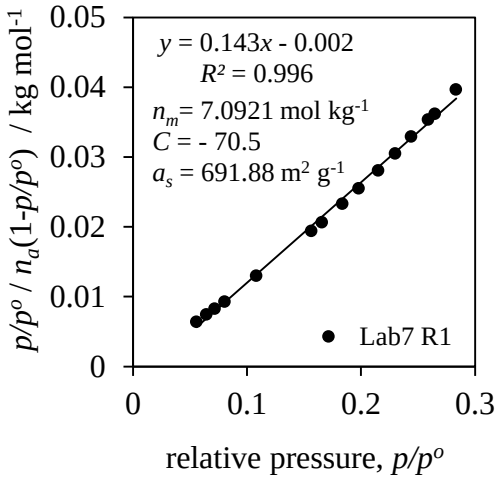
y = 0.143x - 0.002
R² = 0.996
n_m = 7.0921 mol kg-1
C = - 70.5
a_s = 691.88 m² g-1
Lab7 R1
p/p° / n_a(1-p/p°) / kg mol-1
relative pressure, p/p°

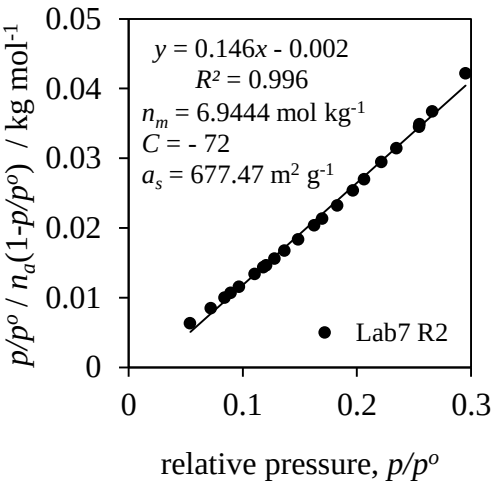
y = 0.146x - 0.002
R² = 0.996
n_m = 6.9444 mol kg-1
C = - 72
a_s = 677.47 m² g-1
Lab7 R2
p/p° / n_a(1-p/p°) / kg mol-1
relative pressure, p/p°

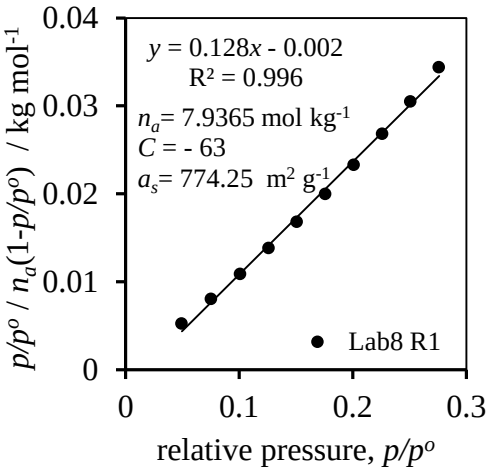
y = 0.128x - 0.002
R² = 0.996
n_a = 7.9365 mol kg-1
C = - 63
a_s = 774.25 m² g-1
Lab8 R1
p/p° / n_a(1-p/p°) / kg mol-1
relative pressure, p/p°

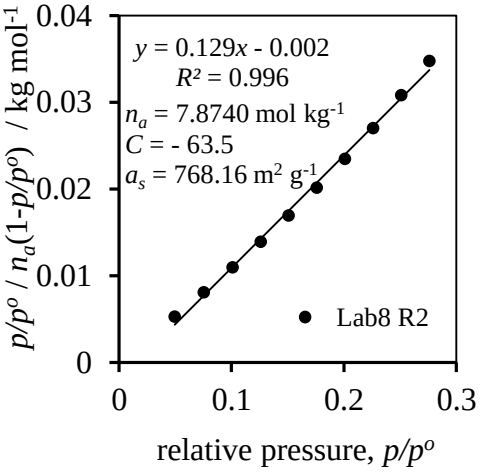
y = 0.129x - 0.002
R² = 0.996
n_a = 7.8740 mol kg-1
C = - 63.5
a_s = 768.16 m² g-1
Lab8 R2
p/p° / n_a(1-p/p°) / kg mol-1
relative pressure, p/p°

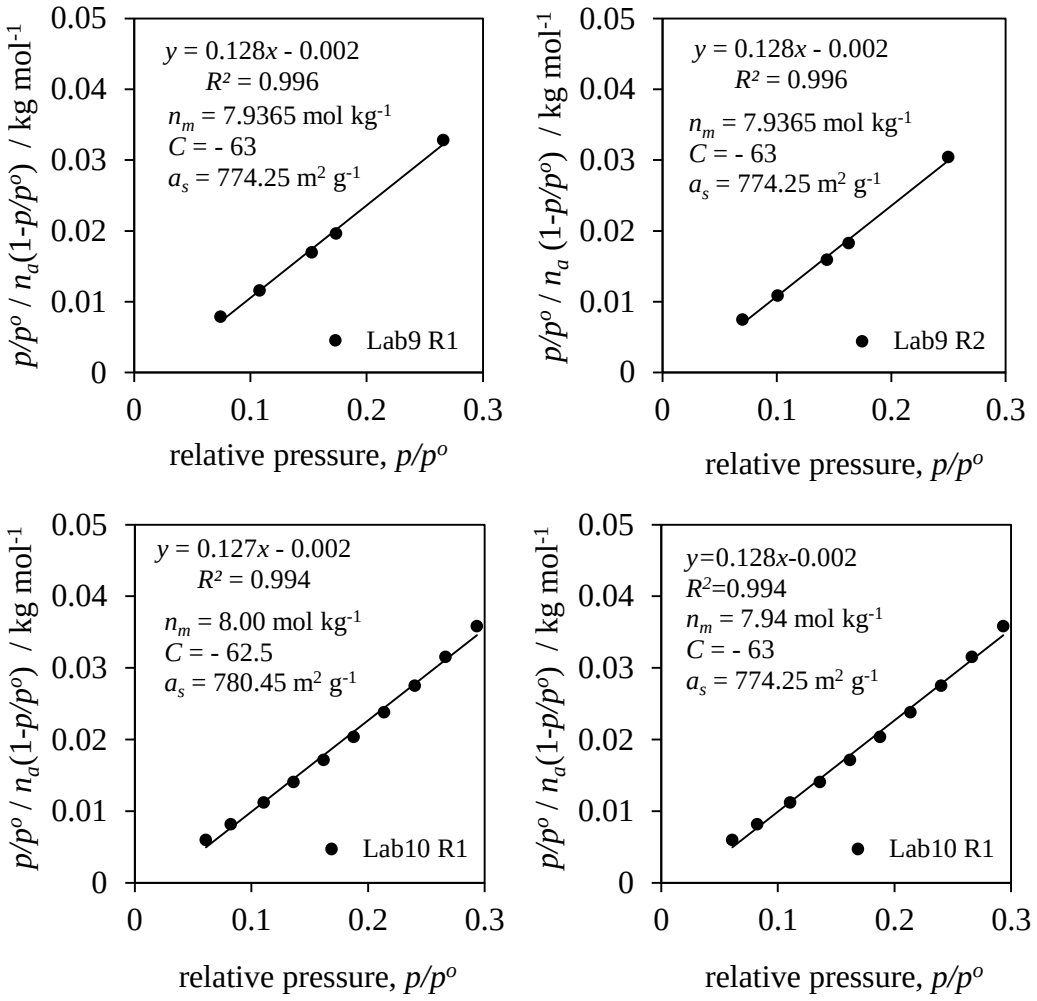

Figure 5.3: BET nitrogen plots measured on the reference TE 7 III carbon beads sample at 77 K by the interlaboratory study participants.

Firstly, we have calculated the BET surface area mean of two replicates for each laboratory seperately, including their standard deviation determination. We have also evaluated the total mean value for the whole set of measurements. The individual within laboratories mean values from two repeats are plotted and compared with total between laboratories mean (see Figure 5.4). Table 5.1 sumireses the overal results, showing the BET surface area variation within and between laboratories. The shaded cells in the table indicate data which were considered as an outlier and eliminated from further analysis.

Table 5.1: Individual results of replicate surface area measurements together with estimated mean and standard deviation values, hilighted cells represent the outling data.

code	a_s / m^2g^{-1}	within lab mean	standard dev.
Lab1	780.4 774.2	777.3	4.40
Lab2	774.2 786.7	780.4	8.80
Lab3	786.7 786.7	786.7	0.00
Lab7	691.9 677.5	684.7	10.20
Lab8	774.2 768.2	771.2	4.20
Lab9	774.2 774.2	774.2	0.00
Lab10	780.4 774.2	777.3	4.40

The total mean BET surface area determined was found as 777.8 m^2 g^{-1} with a standard deviation of around 6.2 m^2 g^{-1} and is shown as dashed line in the Figure 5.4. The deviation of the within laboratory mean from total between laboratory mean for the individual participant is display as a solid pink line. For each dataset the bottom bar represents the minimum and the top bar indicate the maximum value and the middle point represent the within labs BET surface area mean. After exclusion of outlier the corresponding within laboratory results are consistent and close to total mean value, indicating very good agreement in determinated BET surface area between diffren laboratories.

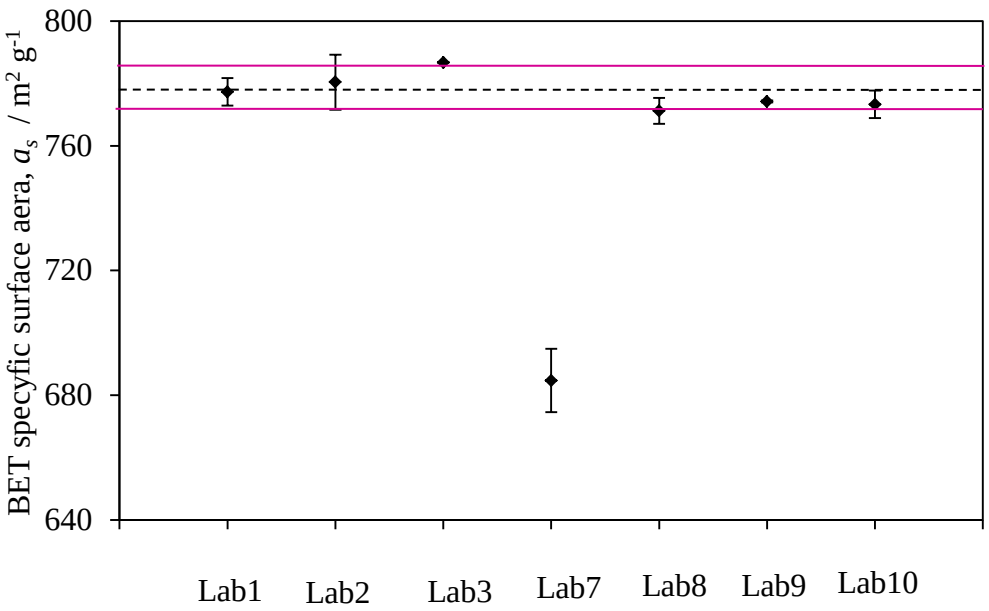

Figure 5.4: Plot of individual within laboratories surface area means calculated from two replicate measurements. The dotted line (---) represent the total between laboratory mean assigned as 777.8 m^2 g^{-1}, the solid line (—) indicate a ± 6.2 m^2 g^{-1} deviation from the mean value.

5.3.2 Micropore Volume Results

In this section validity of the micropore volume results reported basing on the collected excess nitrogen sorption isotherms at 77 K in different labs is examined. The micropore volume was calculated by applying the Dubinin-Radushkevich (DR) method where the intercept of the linear trend with the y-axis provides an estimate of the micropore capacity (see Figure 5.5 for details). The direct comparison of the individual results tabulated in Table 5.2 and Table 5.3 show that the lowest value of the DR micropore volume was 0.3326 cm^3 g^{-1}, determined from previously identified outlying dataset (Lab 7). The reference micropore volume value was considered as 0.3766 cm^3 g^{-1} within deviation of ± 7.8550 $\times 10^{-3}$ cm^3 g^{-1}. Figure 5.6 illustrates the individual within labs micropore volume mean values taken from the replicate tests. Comparisons of these data clearly show that after eliminating the outlying dataset agreement in determined individual micropore volumes by each lab is excellent.

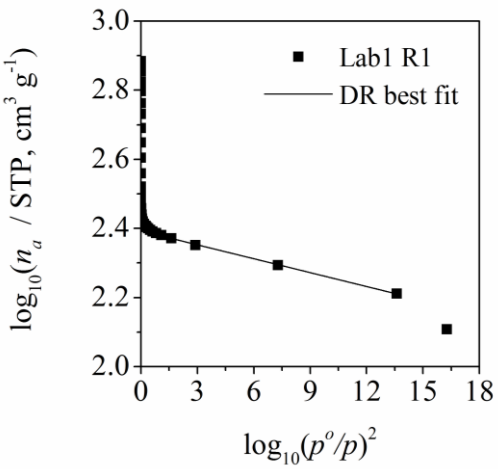
Lab1 R1
DR best fit
$\log_{10}(n_a$ / STP, cm^3 g^{-1})
$\log_{10}(p^o/p)^2$

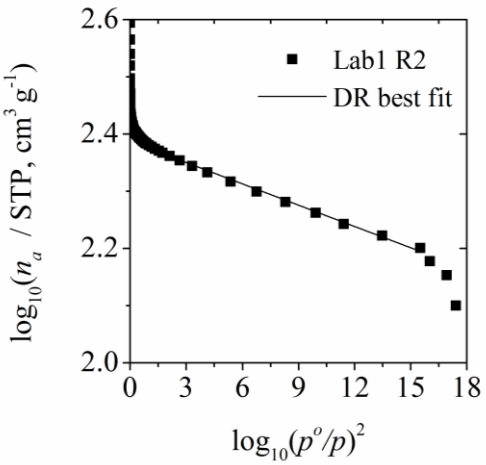
Lab1 R2
DR best fit
$\log_{10}(n_a$ / STP, cm^3 g^{-1})
$\log_{10}(p^o/p)^2$

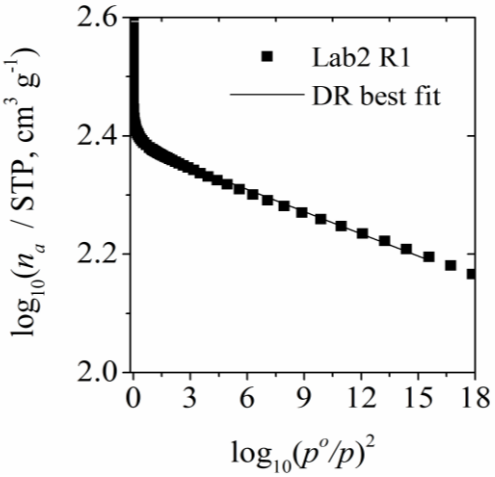
Lab2 R1
DR best fit
$\log_{10}(n_a$ / STP, cm^3 g^{-1})
$\log_{10}(p^o/p)^2$

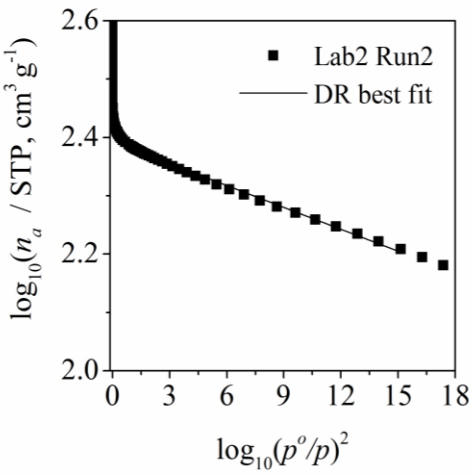
Lab2 Run2
DR best fit
$\log_{10}(n_a$ / STP, cm^3 g^{-1})
$\log_{10}(p^o/p)^2$

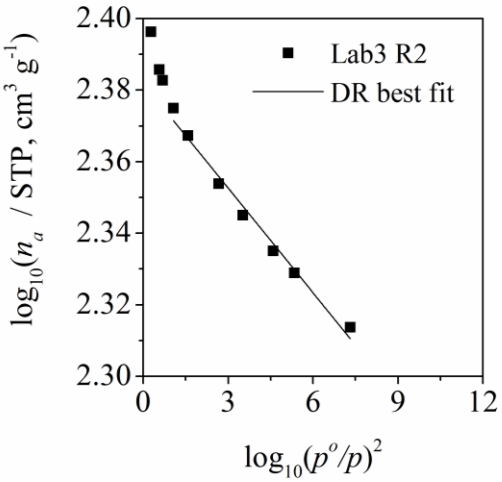
Lab3 R2
DR best fit
$\log_{10}(n_a$ / STP, cm^3 g^{-1})
$\log_{10}(p^o/p)^2$

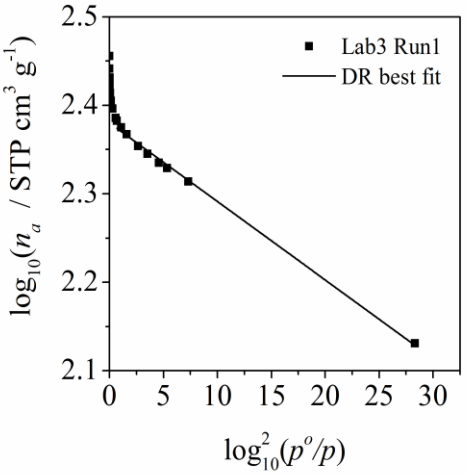
Lab3 Run1
DR best fit
$\log_{10}(n_a$ / STP cm^3 g^{-1})
$\log^2_{10}(p^o/p)$

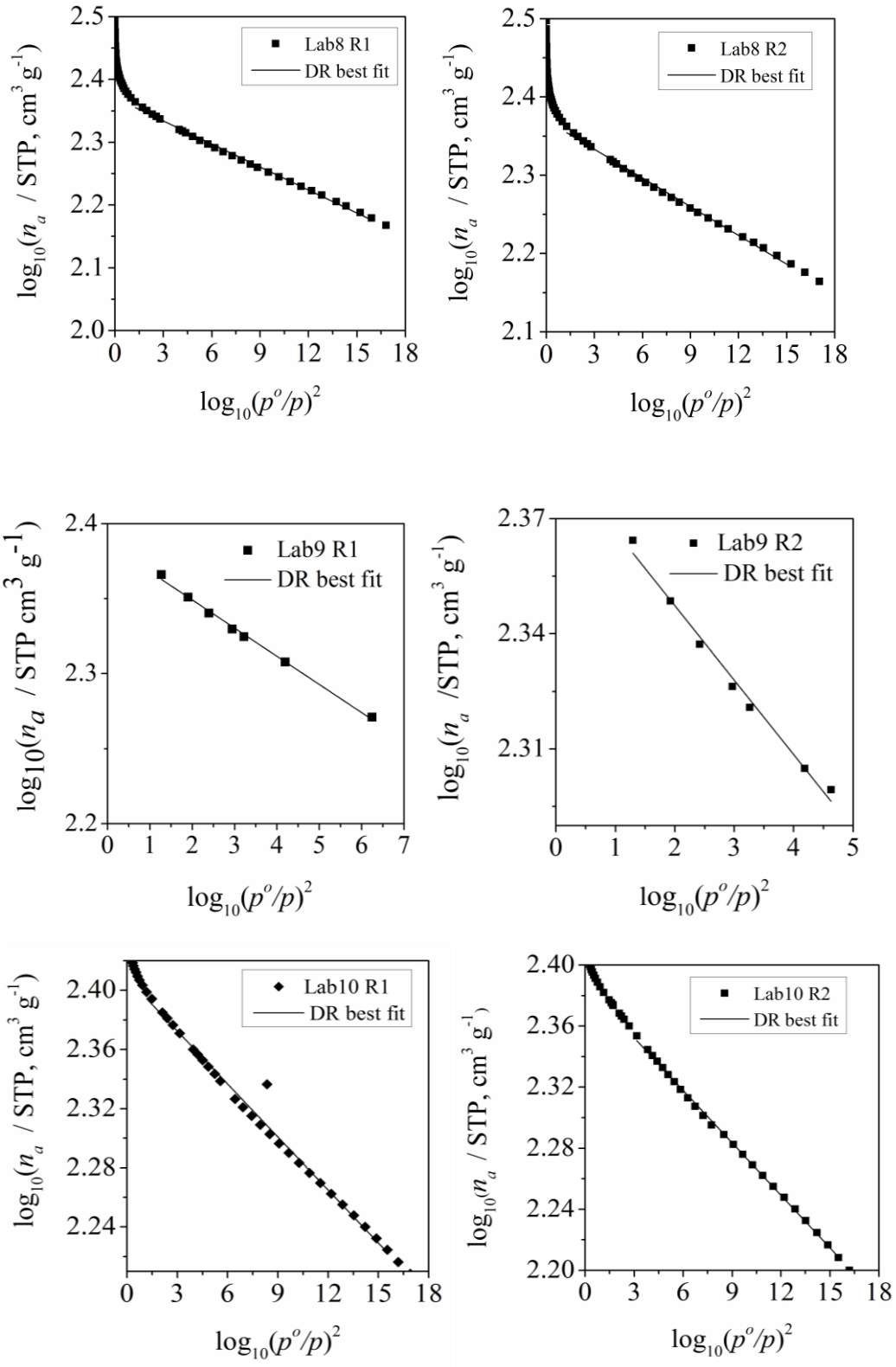

Figure 5.5: DR nitrogen plots for the reference TE 7 III activated carbon beads sample determined by a different laboratories participating in this interlaboratory study.

Table 5.2: Summary of Dubinin-Radushkevich (DR) parameters obtained from two replicates determined by individual laboratory participating in this round robin study. Hilighted cells represent the outling data.

code	fitted relative pressure range, p/p^o	limiting capacity, n_a / $cm^3\ g^{-1}$	micropore volume, v_p / $cm^3\ g^{-1}$	characteristic energy, E_o / kJ mol^{-1}
Lab1	$2.05*10^{-4}$ – 0.0909	246.8994	0.3817	25.4320
	$1.15*10^{-4}$ – 0.0853	243.9271	0.3771	26.4376
Lab2	$1.13*10^{-4}$ – 0.0991	242.2535	0.3745	26.3422
	$1.29*10^{-4}$ – 0.0991	246.8710	0.3817	26.3317
Lab3	$9.52*10^{-3}$ – 0.1000	250.0173	0.3865	22.5131
	$3.37*10^{-4}$ – 0.0940	240.9350	0.3725	29.7995
Lab7	$6.33*10^{-3}$ – 0.0803	218.5093	0.3378	27.8802
	$2.85*10^{-3}$ – 0.0969	211.7922	0.3274	34.4566
Lab8	$1.02*10^{-4}$ – 0.0754	234.7524	0.3629	26.6208
	$1.24*10^{-4}$ – 0.0755	234.3689	0.3623	26.6208
Lab9	$3.17*10^{-3}$ – 0.0744	243.6183	0.3766	21.4825
	$7.06*10^{-3}$ – 0.0728	243.3044	0.3761	21.1310
Lab10	$1.15*10^{-4}$ – 0.0854	246.2635	0.3807	26.9873
	$1.15*10^{-4}$ – 0.0888	250.0921	0.3866	27.3223

Table 5.3: Individual results of replicate micropore volume determination together with estimated mean and standard deviation values, hilighted cells represent the outling data.

code	DR, v_p / cm^3g^{-1}	within lab mean	standard dev.
Lab1	0.3817	0.3794	3.25×10^{-3}
	0.3771		
Lab2	0.3745	0.3781	5.09×10^{-3}
	0.3817		
Lab3	0.3865	0.3795	9.90×10^{-3}
	0.3725		
Lab7	0.3378	0.3326	7.35×10^{-3}
	0.3274		
Lab8	0.3629	0.3626	4.24×10^{-4}
	0.3623		
Lab9	0.3766	0.3763	3.53×10^{-4}
	0.3761		
Lab10	0.3807	0.3836	2.95×10^{-3}
	0.3866		

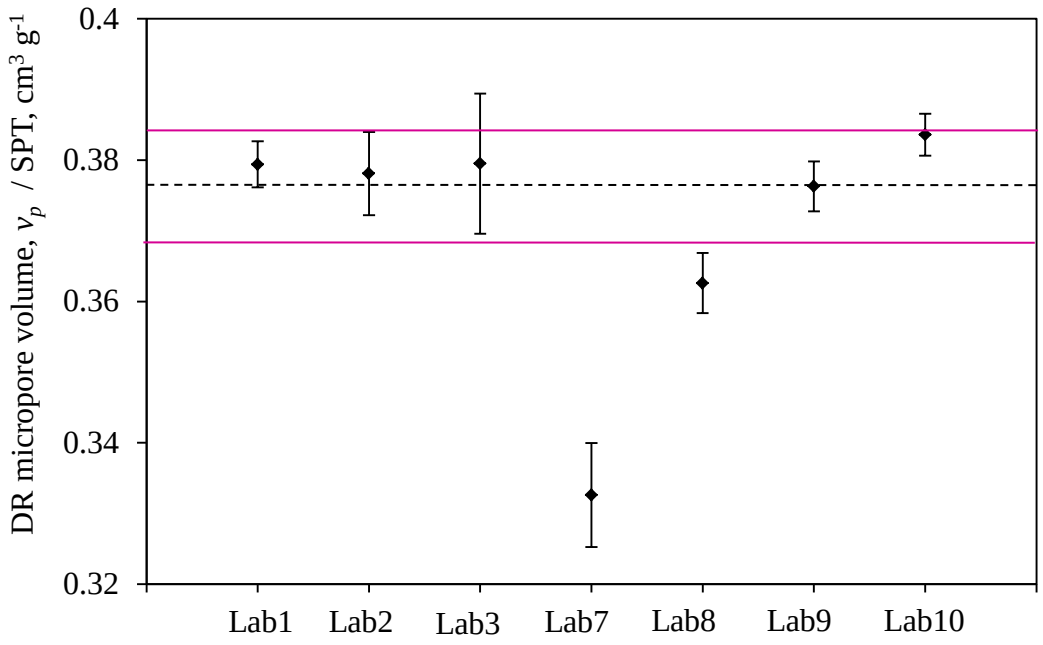

Figure 5.6: Plot of individual within laboratories DR micropore volume means calculated from replicate measurements. The dotted line (---) represent the total between laboratory mean assigned as 0.3766 $cm^3\ g^{-1}$, the solid line (—) indicate a ± 7.8550×10^{-3} $cm^3\ g^{-1}$ deviation from the mean value.

5.4 Hydrogen Sorption Results

The experimental low (up to 1 bar) and high pressure (20 bar and up to 200 bar) excess hydrogen isotherms at 77 K obtained in this interlaboratory study are presented in Figure 5.7, Figure 5.9 and Figure 5.11 respectively. The direct comparison of these results indicates very good agreement in the collected data between different laboratories. Selected issues concerned the accuracy of the experimental measurements was discussed in more detail in the sections below. The hydrogen purities used in the interlaboratory measurements can be found in Table S3 in Supplementary Information, Section S10.

5.4.1 Low Pressure Hydrogen Sorption

In Figure 5.7 the excess hydrogen sorption isotherms collected from all participating laboratories are plotted versus absolute pressure up to 1 bar. These isotherms exhibit the typical Type I Langmuir shape, with the maximum sorption capacity values of approximately 1.65 ± 0.04 wt%, which is similar almost for all collected isotherms. Only one dataset (Lab1) appears to show particularly low hydrogen uptake of 1.46 ± 0.01 wt% at around 1 bar, which underestimate hydrogen capacity by approximately 11.5 %. We attribute the lower uptake seen in this dataset, which was determined volumetrically, to incorrect dead volume calibration, which is consistent with increasing hydrogen pressure (see Chapter 5.4.2 below). This erroneous approach is reasonable, as a consequence of using 77 K helium pycnometry before isothermal hydrogen sorption measurements. As stated in Chapter 4.2.2.6 this correction method failed due to potential helium trapping in the micropores at 77 K, causing problems associated with the potential adsorption sides blocking, and produce an underestimation of hydrogen capacity. Other sources of error that could contribute to the deviation seen in Lab1 data are related to incomplete sample degassing (degassing temperature of around 300 ^{o}C instead as requested in the protocol 350 ^{o}C) and possible impurity contamination due to low purity of hydrogen used (99.999 %). The low hydrogen purity in this case is likely to affect the measurement accuracy as stated in Chapter 4.2.3.3. These suggest that the data sets reported by this participant can be erroneous and have been judged as an outlier and eliminated from further analysis.

From the Table 5.4 it appears that after excluded an outlier (Lab1) the hydrogen capacity measured at 77 K at 1 bar is in good between laboratories agreement with a mean value of 1.65 wt% and standard deviation of ± 0.04 wt%.

(a)

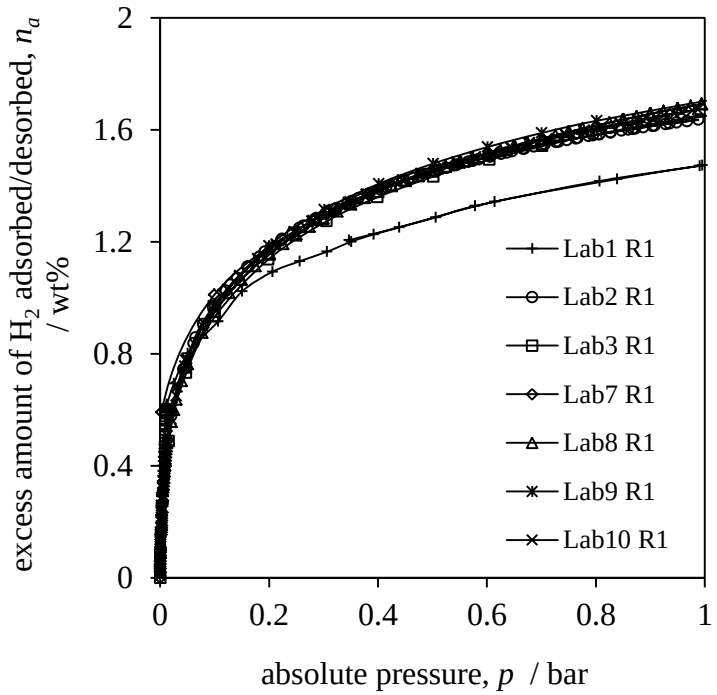

(b)

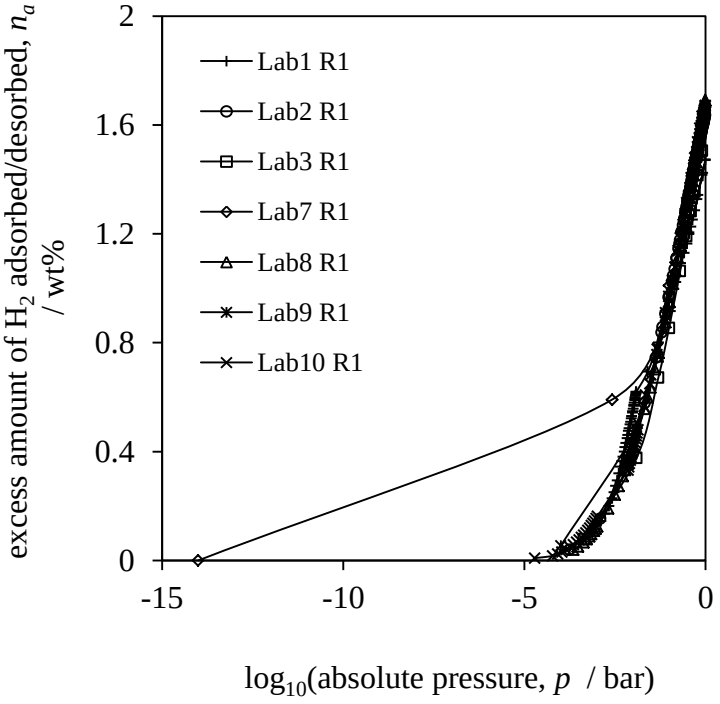

Figure 5.7: Comparsion of interlaboratory results for 77 K excess hydrogen sorption on reference TE 7 III activated carbon beads sample (a) over the whole pressure and (b) in a log plot ranging up to 1 bar.

Table 5.4: Individual results of hydrogen capacities replicate measurements together with estimated mean and standard deviation values, hilighted cells represent the outling data.

code	n_a / wt% (1 bar)	within lab mean	standard dev.
Lab1	1.47 1.45	1.46	0.01
Lab2	1.63 1.60	1.61	0.02
Lab3	1.57 1.58	1.57	0.07
Lab7	1.66 —	1.66	—
Lab8	1.69 1.67	1.68	0.01
Lab9	1.70 1.68	1.69	0.01
Lab10	1.67 1.66	1.66	0.07

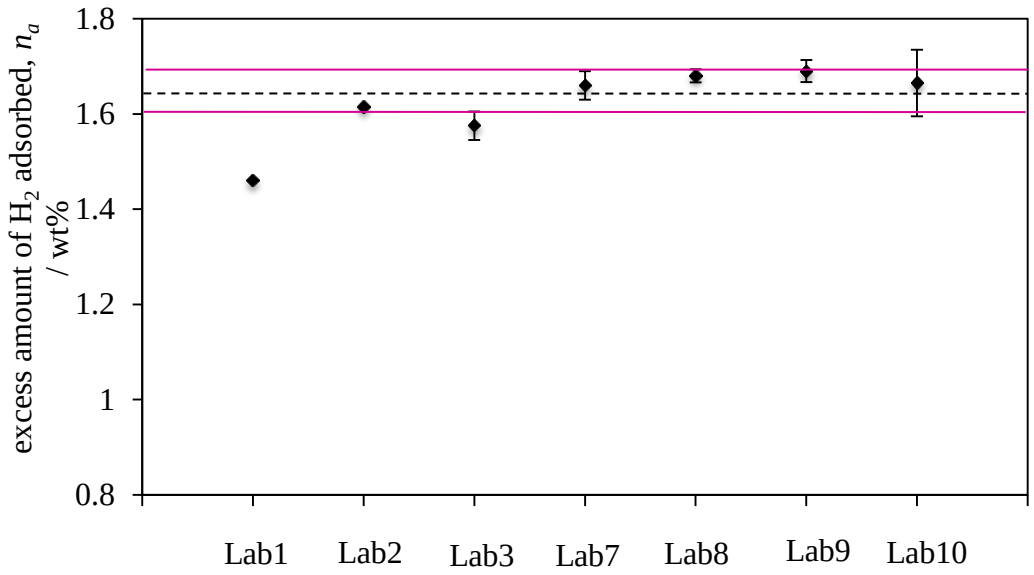

Figure 5.8: Plot of individual within laboratories hydrogen capacity means (up to 1 bar) calculated from replicate measurements. The dotted line (---) represents the interlaboratory mean assigned as 1.65 wt%, the solid line (—) indicates a ± 0.04 wt% deviation from the mean value.

5.4.2 High Pressure Hydrogen Sorption

With regards to the high-pressure hydrogen measurements, the results are displayed in the insets of Figure 5.9 and 5.11 and clearly demonstrated that the two datasets appear to show evident spread in the hydrogen capacity results. Selected issues concerned the accuracy of the experimental results of the dataset one (Lab1) as discussed in the previous section. Another data set (Lab7) which overestimate the hydrogen capacity by approximately 30 % (at 20 bar) in relation to the reference value. We suggest that the large uptake indicated by Lab7 could be the result of incorrect free space corrections. Such the isotherms measured in the volumetric system were calibrated for helium pycnometry on the blank silica sample at 77 K, rather than on the tested sample which clearly demonstrates different porosity. Furthermore, it is possible that sample cell volume was too large to accurately measure the adsorbed gas volume on the chosen sample size. In the final report the Lab7 strongly suggested that the minimum of 1 g sample for this system volume is recommended. Moreover, the participating Lab7 reported problems with the temperature control between manifolds and sample cell zones, which they concluded can results in the unusual shape of the high pressure hydrogen isotherm. If we exclude these two outlying datasets (Lab1 and Lab7) the spread in the reported data is significantly reduced.

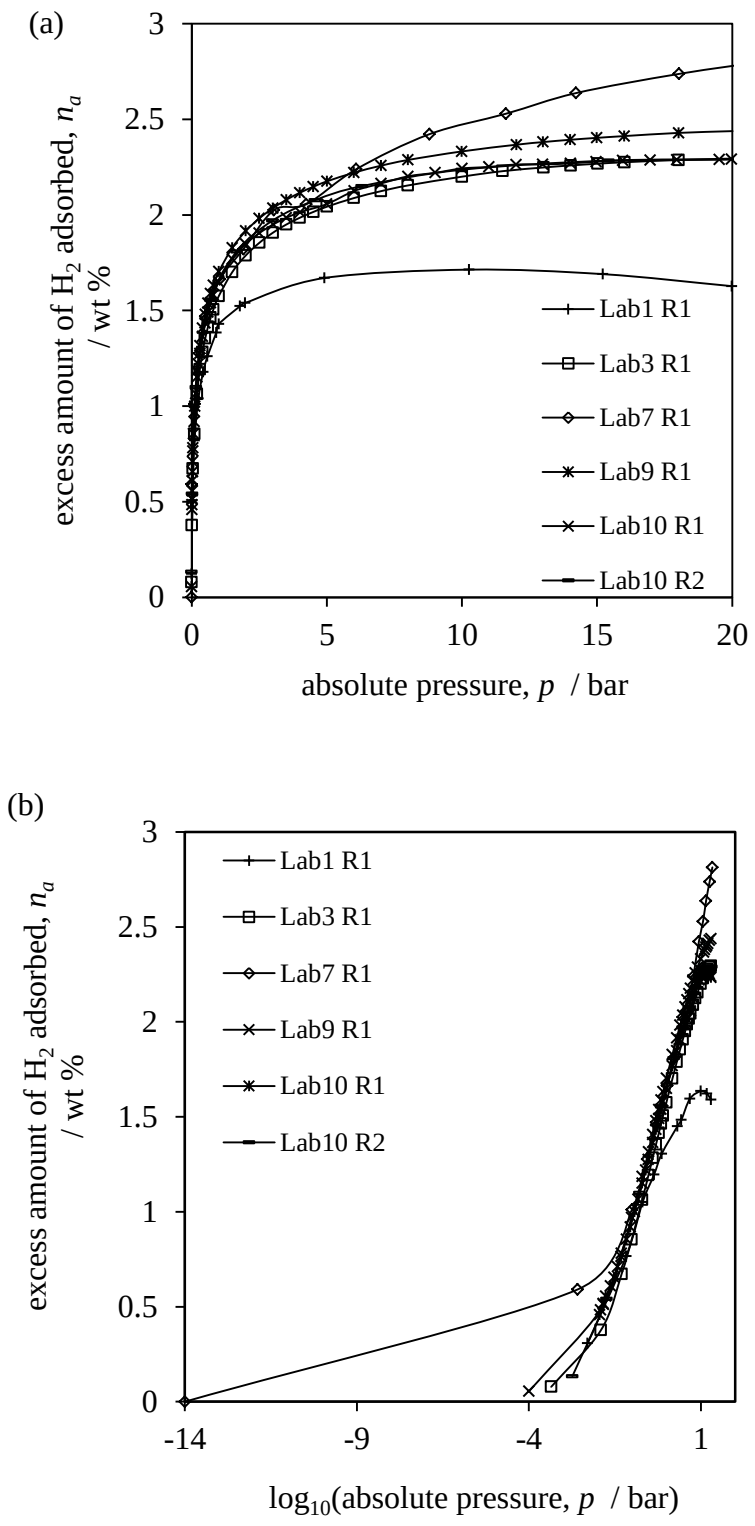

Figure 5.9: Comparsion of interlaboratory results for hydrogen excess sorption on reference TE 7 activated carbon beads sample over (a) the whole pressure and (b) in a log plot ranging up to 20 bar.

A summary of the maximum hydrogen sorption capacities (at 20 bar) determined for all participating labs together with the uncertainty estimation were presented in the Table 5.5. Combining all of these results (after outliers exclusion), the within labs mean hydrogen uptake at 20 bars was found as 2.33 wt%. The standard deviation of these measurements is only 0.07 wt%.

Table 5.5: Individual results of hydrogen capacities replicate measurements together with estimated mean and standard deviation values, hilighted cells represent the outling data.

code	n_a / wt% (20 bar)	within lab mean	standard dev.
Lab1	1.68 1.62	1.65	0.04
Lab2	— —	—	—
Lab3	2.29 2.29	2.29	0.00
Lab7	2.81 —	2.81	—
Lab8	— —	—	—
Lab9	2.44 2.41	2.42	0.02
Lab10	2.29 2.29	2.29	0.00

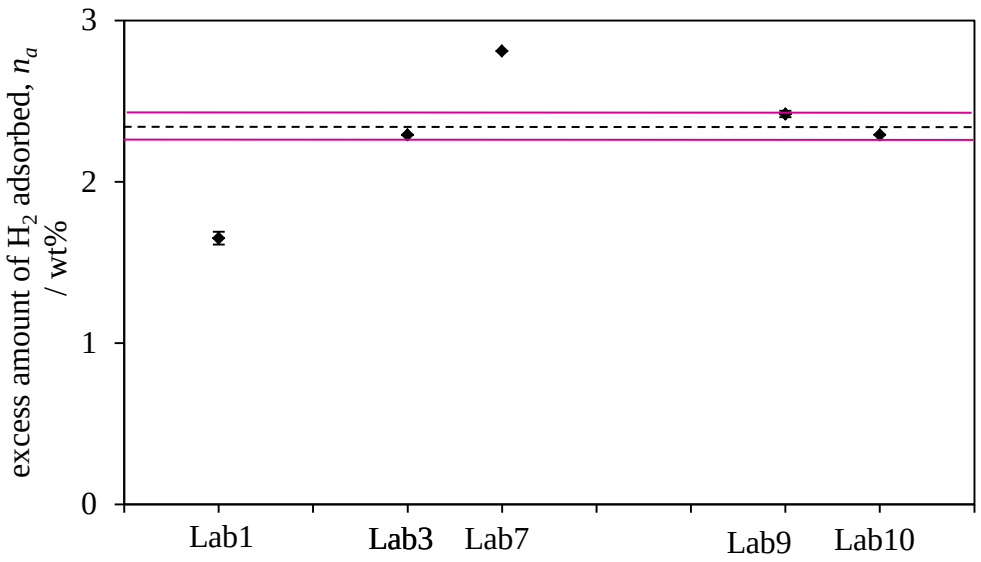

Figure 5.10: Plot of individual laboratories hydrogen capacity means (at 20 bar) calculated from replicate measurements. The dotted line (---) represents the intra laboratory mean assigned as 2.33 wt%, the solid line (—) indicate a ± 0.07 wt% deviation from the mean value.

The isotherms recorded above 20 bars show more significant scattering in the hydrogen sorption data compared to 20 bar results (Figure 5.11). However, a straightforward validation of these results is not possible since two of three presented datasets (Lab 1 and Lab 7) are already considered as erroneous. We believe that, the isotherm reported by Lab 9 show a reference trend with the hydrogen uptake of 2.07 ± 0.01 wt% at 40 bar (Table 5.6). We expect better results correlation if the high pressure isotherms will be reported by larger number of laboratories under better experimental conditions control.

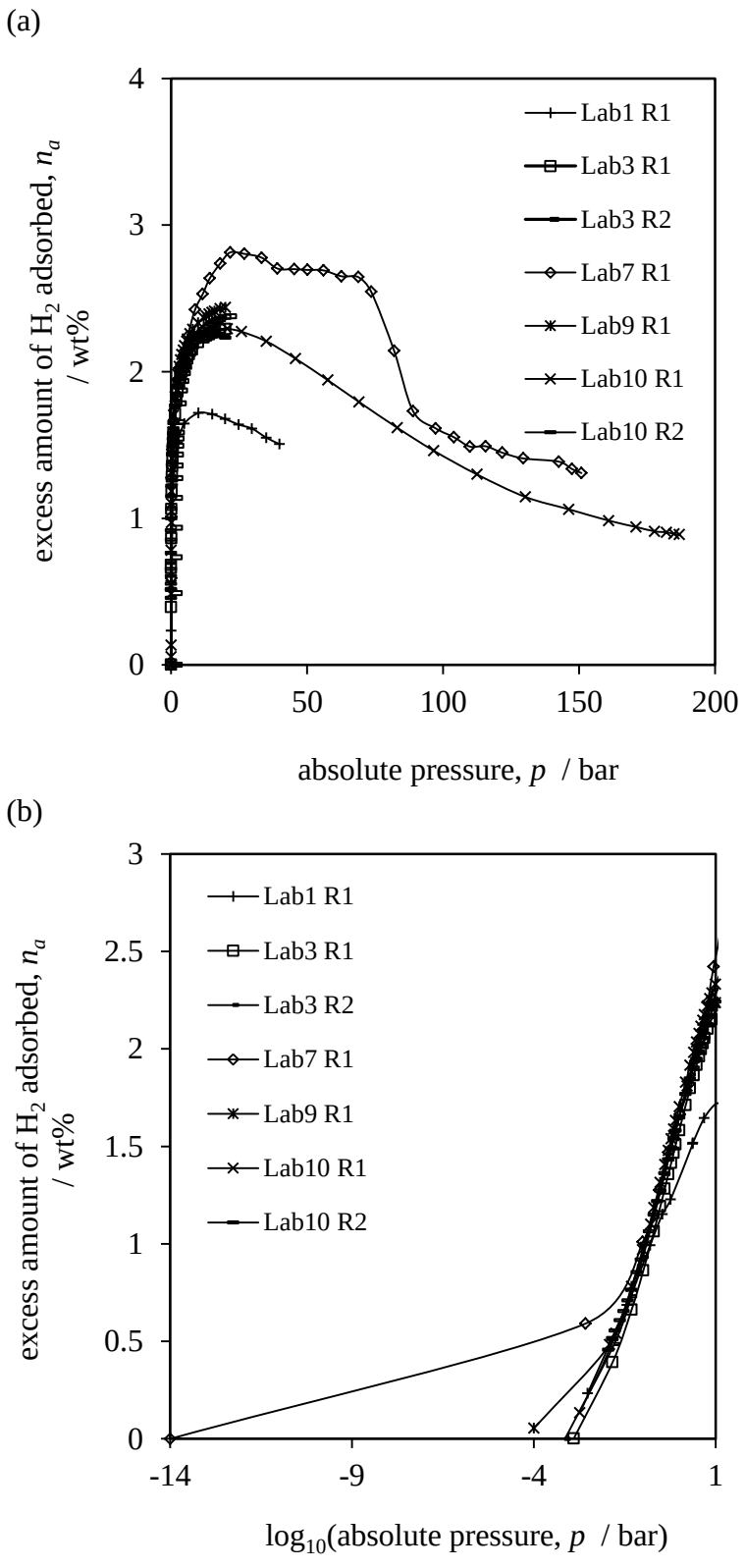

Figure 5.11: Comparsion of interlaboratory results for hydrogen excess sorption on reference TE 7 activated carbon beads sample over (a) the whole pressure and (b) in a log plot ranging up 200 bar.

Table 5.6: Individual results of hydrogen capacities replicate measurements together with estimated mean and standard deviation values, hilighted cells represent the outling data.

code	n_a / wt% (40 bar)	within lab mean	standard dev.
Lab1	1.50 1.40	1.46	0.04
Lab2	— —	—	—
Lab3	— —	—	—
Lab7	2.70 —	2.70	—
Lab8	— —	—	—
Lab9	— —	—	—
Lab10	2.07 2.08	2.07	0.01

5.5 Summary

A total of the seven laboratories, including academics and industrial organizations participated in this interlaboratory study. With two exceptions, all laboratories performed their measurements as stated originally in the testing protocol. The results of the nitrogen sorption isotherm at 77 K show an excellent agreement of the data obtained by almost all participating laboratories. The deviation in the nitrogen BET surface area is less than 0.8 % for each determination. The deviation in nitrogen DR micropore volume is around 2.0 %. Only one result is considered as an outlier and excluded from the comparison. Regardless hydrogen sorption isotherms, the results show reasonable agreement at low pressure but considerable spread at higher pressures. The deviation of the hydrogen uptake is equal to 2.4 % and 3.0 % respectively for the low (1 bar) and high pressure (20 bar) determination.

The main deviations from test protocol involved sample degassing and final isotherms corrections. As stated before variation in the degassing conditions may lead to incomplete contaminants removal causing pore blocking. Similarly, variations in free space corrections contribute to errors as a result of potential helium trapping in micropores leading to underestimation of hydrogen sorption capacity.

Basing on the interlaboratory results we can conclude that the accurate determination of the high pressure isotherm for the hydrogen at 77 K still represents a big challenge. We also reviewed a number of potential experimental problems, in particular related to instruments calibration and highlighted the importance of accurate data correction method and their impact on the final data quality. We stressed the importance of strictly following the defined procedures for the sample preparation and analysis as obligatory and necessary to determine the sorption capacities in the same experimental conditions.

5.6 Proposed Testing Methodology

We believe that the methodology outlined here will be helpful in resolving some of the uncertainties in experimental results collection and analysis, for materials similar to our reference TE 7 III carbon beads sample. This methodology is designed to test experimental excess nitrogen and hydrogen sorption data at the normal boiling point of nitrogen (77 K) and is based on results presented in Chapter 4 and the interlaboratory results.

Before outlining and justifying a methodology suitable for the experimental nitrogen/hydrogen sorption measurements, it would be important to mention the presentation of the final results. In all measurements stages it is recommended that the collected data should be repeated, a minimum of two times. As an indicator of the measurements results, the mean and the standard deviation should always be included. It is also important to include error bars in the graphs to improve on the results uncertainty visualization. Here, the standard deviation (*std*) is defined as positive squared root of variance given below:

$$std = \sqrt{\frac{1}{n-1}\sum_{i=1}^{n}(x_i - \bar{x})^2} \tag{5.1}$$

where, n is the number of data points and $\bar{x}$ is the mean of the values x:

$$\bar{x} = \frac{x_1 + x_2 + ... + x_n}{n} = \frac{1}{n}\sum_{i=1}^{n} x_i \tag{5.2}$$

where, $(x_i - \bar{x})$ is the deviation from the mean, and $(x_i - \bar{x})^2$ is the square of this deviation.

A very important procedure that should be always performed prior to sample analysis is equipment calibration. The calibration should be applied to thermocouples and pressure transducers. In addition, we recommended that the 'blank' or standard sample run should be carried out on a regular basis to ensure reliable measurements. Gas leakage tests should also be performed and the latest equations of state for the gases available from NIST (NIST, 2012) should be used.

The effect of sample degassing must always be studied. This is essential to ensure that material surface is appropriately activated and all contaminants such as moisture and other solvents from synthesis are fully removed, before the adsorption measurements start. This could be done for example by degassing a minimum of 100 mg of a test sample at 350 °C, under high vacuum of around 10^{-6} mbar for 8 hours (see Section 4.2.1.4 for more details). The dry/degassed mass of the material should be always accurately determined and recorded to the nearest 0.1 mg. The experiment should be initiated by inputting the sample dry/degassed mass into the apparatus before a proper analysis is started. Depending on the particular equipment type, this will involve measuring the sample mass on an external balance (volumetric system) or by recording and inputting the degassed weight directly from the microbalance (gravimetric system). Once the sample is loaded and the degassed mass is evaluated, the next step is to determine the nitrogen/hydrogen sorption isotherms, always with at least two duplicates.

The nitrogen sorption measurements must involve determination of both adsorption and desorption cycles, in repetition. The analysis should be performed at liquid nitrogen temperature (77 K) with temperature control better than 1 K, and the data should be collected in the pressure range 0−1 bar. The minimum sorption equilibration period should be set as 12 minutes, preferably as 60 minutes to ensure that true adsorption and thermal equilibration are reached (see Section 4.2.2.5). In order to obtain the BET surface areas (from both the BS and consistency criterion methods (BS, 2010, Rouquerol et al., 2006)) it would be useful to have the following relative pressure (p/p^o) points when the isotherms are collected: 0.01, 0.0125, 0.02, 0.025, 0.235, 0.05, 0.0875, 0.125, 0.175, 0.2, 0.3, since as discussed in Section 4.2.2.2 in order to compare the BET surface areas on the same materials the fitted pressure range should be always the same. For microporous samples similar to the TE 7 III beads, the method based on the consistency criteria is recommended as better method of surface area estimation (see Section 4.2.2.2).

The hydrogen sorption measurements must also incorporate both adsorption and desorption cycles, in repetition. We recommend always monitoring the hydrogen stream purity before testing the materials. If contamination is detected, a sorbent based filtration chamber with a liquid nitrogen cold trap should be used in order to improve gas purity (see Section 4.2.3.3). The hydrogen analysis should be performed at 77 K with the temperature control better than 1 K. The chosen minimum sorption equilibration period for hydrogen analysis should be set as being equivalent to minimum 12 minutes and, if applicable, the maximum time-out should be set as 60 minutes, for all the collected pressure points.

In all cases it is necessary to correct the final sorption isotherms. Depending of the type of sorption equipment (volumetric or gravimetric) all collected data should be corrected using the free space (dead volume) or buoyancy corrections, respectively. In the case of the volumetric method, the blank tube test is the preferred correction method, with the option of running the free space run after the analysis is finished. This ensures that the

sample is not exposed to helium before collection of adsorption/desorption hydrogen data, since possible helium trapping into micropores can occur (Section 4.2.2.6).

Finally, the essential step for checking measurement accuracy is to use complementary techniques to reproduce hydrogen sorption isotherms in a single laboratory (see Section 4.2.3.2). A high degree of isotherms agreement could be an indication of experimental measurements accuracy, which should also be approved with external groups during the course of the interlaboratory study.

CHAPTER 6

CONCLUDING REMARKS

6.1 Introduction

The purpose of this final chapter is to discuss the most interesting findings and conclusions revealed through this thesis. The presented results clearly contribute to better understanding of the accurate hydrogen sorption methodology, however this is only a beginning of the work that will be done for standardisation of methodology. The chapter begins with Section 6.2 where the overall summary of the work carried out in this investigation is presented. This is followed by the most relevant conclusions that can be drawn from this thesis in Section 6.3. Then chapter concludes with the suggestions for possible work that can be conducted in the future in Section 6.4.

6.2 Thesis Summary

This thesis focused on improving the experimental procedures and methods for determining hydrogen storage capacities in the selection of nanoporous materials at 77 K in order to resolve uncertainty of experimental results and to avoid measurements inaccuracy in the future. The motivation of such investigation was attributed to lack of clear protocols in collection and analysis of hydrogen sorption data that lead to results inconsistency between labs. To accomplish this, a theoretical framework was built up on the comprehensive literature study of hydrogen storage via physisorption in promising nanoporous materials in connection to the methods accuracy and validation

(Chapter 2). Then, all necessary experimental set-up and procedures for investigation structure properties linked to hydrogen storage capacities were tested (Chapter 3).The reference sample was chosen and used for in-house measurements qualification and validation. The main sources of possible experimental errors were identified and corrected (see Chapter 4). Standard sample and procedures were sent to external laboratories to ensure measurements robustness. Collected results were carefully examined using the statistical parameters such as mean and standard deviations and the final methodology for determining nitrogen/hydrogen isotherms at 77 K is proposed (Chapter 5).

6.3 Conclusions

When attempting to discuss the key thesis findings and conclusions, it is necessary to consider them in relation to the main research aims and objectives (see Section 2.8). The main goal of this thesis was to contribute to new standards development by providing relevant experimental procedures and methods for analysing and validation of hydrogen sorption measurements of nanoporous materials at 77 K. In order to achieve this, a number of objectives were successfully realised as outlined below.

In order to improve measurement quality we successfully adopted and tested some existing experimental procedures relevant for accessing materials purity, thermal stability, homogeneity, skeletal density and porosity. The results presented in Chapter 4 were essential in order to assess the efficiency of existing standards (such as British Standard methods) and to test new ways in which experimental data can be collected and analysed. As discussed in Section 4.2.1.2 the applicability of the skeletal density determination for the moisture contaminated samples was extended by introducing a second order exponential decay function which was successfully fitted to the experimental results with uncertainty (standard deviation) around 1.00 % for our reference carbon beads sample.

Progress was made in the assessment of accessible porosity and available surface by studying carefully selected probes of different molecular size, shape, and polarity. As identified in Section 4.2.2.2 it is extremely useful to have such comprehensive geometries as CO_2 at 273 K and Ar at 87 K to extend the lower limit of pore size distribution (~ 0.5–0.6 nm determined for reference TE 7 III sample) optimal for maximizing interactions with hydrogen at 77 K (Gogotsi et al., 2009).

A large fraction of the study was focused on improving the BS method for the BET surface area determination into microporous materials, such as the reference TE 7 III carbon beads. A wide range of BET values were observed ranging from 350 $m^2\ g^{-1}$ to 880 $m^2\ g^{-1}$ (determined from isotherm of N_2 at 77 K) depending on the linearity ranges, cross-sectional areas and geometries, as outlined in Section 4.2.2.2. Development of this study would be interesting, however at this research stage we need to accept the BS method for the surface area determination, but we still remember about its incorrect assumptions. The reference value of BET surface area $a_s = 780.4 \pm 19.5$ for N_2 at 77 K with molecular cross sectional $\sigma = 0.162$ nm^2 was selected, and referred to as the 'BET number' instead of BET surface area as it does not accurately represent the geometry of adsorbed species. One needs to be aware that it is common to see in the literature the BET surface area correlated against the hydrogen capacity: one should be very cautious using this approach due to the large potential variation in surface area estimation.

Significant findings were made while identifying the acceptable set of experimental conditions, critical for the accurate hydrogen storage measurements. As mentioned in Section 4.2.1.4 the preliminary experiments on the TGA, IGA and ASAP 2020 were run to find optimal sample degassing conditions necessary for efficient surface cleaning prior to hydrogen sorption measurements. Based on the weight loss profiles and stable weight criteria results, the optimal degassing settings for the TE 7 III reference sample carbon beads were selected to be: heating at 350 ^oC under 10^{-6} mbar vacuum for 480 minutes.

Another area that deserved attention was to ensure that the equilibration time at each isotherm point is long enough to ensure sufficient hydrogen adsorption and thermal equilibration. As discussed in Section 4.2.2.5 it is estimated that sorption measurements over recommended equilibration periods of 2 and 9 min lead to hydrogen capacity underestimation. These findings were critical because they involved a maximum 13 % hydrogen capacity difference between 2 min and 12 min equilibration periods measured at 1 bar. Furthermore we revealed that for TE 7 sample the equilibrium uptake is successfully reached with a minimum equilibration period of approximately 12 min and there is no significant increase in excess adsorption using a much longer equilibration period of 60 min.

The area that needs more serious attention is appropriate isotherms correction methods. This was addressed in Section 4.2.2.6 where the evaluation of the final gas sorption results indicated possible helium adsorption in the TE 7 beads microstructure. This was evident in the level of both nitrogen and hydrogen adsorption which was underestimated by around 17 % causing curved isotherm tails at lower pressures. A more accurate method for isotherm correction would be to use the volume of the empty sample tube and carry out an accurate independent measurement of the sample density, avoiding sample exposure to helium prior to hydrogen sorption measurements.

It is very important to consider hydrogen purity, such as presented in Section 4.2.3.3. The gas contaminants overestimated hydrogen capacity and promoted irreversible hydrogen sorption as well affecting the overall shape of the isotherms. System flushing, with an additional purification chamber packed with carbon/zeolite sorbents and an in-line liquid nitrogen cold trap, clearly improved the gravimetric sorption capacities of the reference sample. In all cases, experiments must always be performed with ultra high purity hydrogen (minimum 99.9999 %).

The last analytical study presented in Section 4.2.3.2 was a successful attempt in determining reversible and reproducible hydrogen sorption capacities. The preliminary experiment run on the ASAP 2020 and IGA and HTP-1 demonstrated high data

reproducibility with excess hydrogen capacities of 1.66 ± 0.007 wt% and 2.29 ± 0.0001 wt% for 1 bar and 20 bar hydrogen pressure, respectively.

Once in-house methodology was improved, the main focus of this study was turned to putting in place the interlaboratory collaboration. This will be important for the success of the new methodology implementation. Chapter 5 describes the interlaboratory exercise results successfully conducted with seven academic and industrial laboratories. Procedures for determining nitrogen and hydrogen isotherms at 77 K were compared. From the nitrogen sorption results it can be concluded that very good reproducibility of BET surface area and DR micropore volume was obtained, with individual laboratory repeatability of around 0.8 % and 2.0 %, respectively. Significant improvement in the reproducibility of the hydrogen capacities was made, with ratio of around 2.4 % at 1 bar and 3.0 % at 20 bar. The measurements show good consistency with the exception of outliers, where the variances were mainly caused by the differences in the sample degassing and the final isotherms correction methods. An improved agreement in the results may be expected if the measurements were performed under more strictly controlled experimental conditions.

The methodology described in this thesis provides useful information to illustrate the typical analysis which can be applied to characterise nanoporous structures for hydrogen storage applications. It is important to note that this work do not intend to develop the materials to meet the DOE's targets, rather the main interest is in improving methodology to make hydrogen sorption measurement results more comparable. The proposed methodology may help researchers to obtain better knowledge of how to minimize errors in their hydrogen sorption measurements. Finally, as a general conclusion author believe that this thesis will contribute towards pushing forward more accurate hydrogen sorption measurements. This study will be beneficial to hydrogen storage community in encouraging more rigorous data analysis and acquisition. I trust that this thesis contributes towards the hydrogen storage standards development programme, and that the ideas detailed in the following section are explored further.

6.4 Suggestions for Future Work

As addressed in the opening section there is clearly much work that could be done to explore more accurate and reproducible hydrogen physisorption measurements and clearly the results presented in this thesis contribute to the method standardisation. Developing the qualitative methodology, validated by in-house and interlaboratory performance is a good starting point to achieve these aims. The following suggestions are proposed as interesting future directions for this work:

1) A proposed methodology can setup the basic framework for certification of hydrogen storage measurements by international standards such as BS and ISO, which apparently is very complex and long-term process. Designing and conducting a series of protocols and interlaboratory testing under tightly controlled experimental conditions by a larger number of participants can apparently improve such a methodology and push it forward to certification.

2) Performing hydrogen sorption measurements on the 'reference' materials similar to those characterised here, for which hydrogen sorption is well known and well understood, is a key for the future routine measurements and instruments calibration.

3) More work needs to be done on improving high pressure hydrogen sorption capacity measurements. Gaining a better understanding of the various error and uncertainty sources at high hydrogen pressures should help reduce inaccurate data.

4) In addition, there are a wide variety of relevant methodologies for hydrogen storage purpose in the literature which need to be confirmed independently by number of individual laboratories. Regular round robin tests should improve their certification.

5) Possible revaluation of the British Standard methods in order to realise how the data should be selected and analysed is an interesting topic for future research. We originally wanted to contribute to this investigation but because of limitation of time we moved this work to the future directions. We suggest that maybe instead of providing for example the BET values in the BET surface area analyses more appropriate will be to quote accurate pressure range for linear BET fitting. Also introducing different probes due to molecular sieving and different types of interactions with a materials surface would be an interesting development for standardisation.

6) Continued efforts are needed for better understanding of hydrogen sorption properties on the molecular level, including both theory and simulations. Investigation of other complementary techniques such as solid state NMR and neutron diffraction methods will clearly help to reliably enhance additional information about promising DOE hydrogen storage materials. The interlaboratory validation and certification of such methods would have great impact on the future hydrogen storage programme.

7) In the future it will be necessary to expand the DOE targets by providing parameters on the system basis such as containment, piping and control systems. So far much emphasis has been placed on practical on-board hydrogen storage system for light duty vehicles, but research is also needed to develop other applications, such as stationary and portable where there is also much demand in stability and cost. On-board hydrogen storage targets are well established in the US, with other targets set in Japan and by the IEA (Riis, 2005). It would be useful in future for some consistency to be established in targets internationally with the understanding that they might be different for different specific end uses.

8) Furthermore, the research directed to the development of a methodology can further contribute to the design of novel storage system based containers which, can be used for the final on-board hydrogen storage and delivery applications.

9) The general methodology presented in this thesis can be made for other important transportation fuels such for example CO_2 and CH_4, which allow individual laboratories to compare their results.

REFERENCES

ABDUL-MAJEED., W.S., SERADAROGLU, G.M., ZIMMERMA, W.B. 2012. Application of Liquid Nitrogen Cold Trap for Purification of Hydrogen Gas Stream Generated from $NaBH_4$, *J. Chem. Chem. Eng.*, 6, 425-434.

ADAMSON, K. A. 2004. Hydrogen from renewable resources - the hundred year commitment. *Energy Policy,* 32**,** 1231-1242.

AHN, C., GRUBBS, R. H., AND BOWMAN, R. C., 2005. Enhanced Hydrogen Dipole Physisorpion, 2005 Annual Merit Review Proceedings of the US Department of Energy. California Institute of Technology with DOE Center of Excellence on Carbon-based Hydrogen Storage Materials. Avalable:http://www.hydrogen.energy.gov/pdfs/review05/stp_34_ahn.pdf.

AMENDOLA, S. C., SHARP-GOLDMAN, S. L., JANJUA, M. S., SPENCER, N. C., KELLY, M. T., PETILLO, P. J. & BINDER, M. 2000. A safe, portable, hydrogen gas generator using aqueous borohydride solution and Ru catalyst. *International Journal of Hydrogen Energy,* 25**,** 969-975.

ANDREW, P.N., OMAR, K.F., KAREN, L.M., JOSEPH, T.H. 2009. Supercritical Processing as a Route to High Internal Surface Areas and Permanent Microporosity in Metal Organic Framework Materials. *J. Am. Chem. Soc.*, 131(2), 458-460.

ANSON, A., JAGIELLO, J., PARRA, J. B., SANJUAN, M. L., BENITO, A. M., MASER, W. K. & MARTINEZ, M. T. 2004. Porosity, surface area, surface energy, and hydrogen adsorption in nanostructured carbons. *Journal of Physical Chemistry B,* 108**,** 15820-15826.

ANTON, D. & MOTYKA, T. 2011. Hydrogen Storage Engineering Center of Excellence. US Department of Energy Hydrogen and Fuel Cells Program 2011 Annual Merit Review, 2011.

ARISTOV, B. G. & KISELEV, A. V. 1963. Effect of dehydroxylation of the silica gel surface on the adsorption isoherms of nitrogen and argon vapors. *Zhurnal Fizicheskoi Khimii,* 37**,** 2520-2528.

ARMAROLI, N. & BALZANI, V. 2011. The Hydrogen Issue. *Chemsuschem,* 4**,** 21-36.

ARMBRUSTER, M. H. A. A., J. B., 1944. The Adsorption of Gases on Smooth Surfaces of Steel. *J. Am. Chem. Soc. ,* 66**,** 159-171

AWERBUCH, S., SAUTER, R. 2005. Exploiting the Oil-GDP Effect to Support Renewable.

AZARPOUR, A., SUHAIMI, S., ZAHEDI, G. & BAHADORI, A. 2013. A Review on the Drawbacks of Renewable Energy as a Promising Energy Source of the Future. *Arabian Journal for Science and Engineering,* 38**,** 317-328.

BAE, Y. S., YAZAYDIN, A. O. & SNURR, R. Q. 2010. Evaluation of the BET Method for Determining Surface Areas of MOFs and Zeolites that Contain Ultra-Micropores. *Langmuir,* 26**,** 5475-5483.

BALAT, M. 2007. Hydrogen in fueled systems and the significance of hydrogen in vehicular transportation. *Energy Sources Part B-Economics Planning and Policy,* 2**,** 49-61.

BALAT, M. 2008. Potential importance of hydrogen as a future solution to environmental and transportation problems. *International Journal of Hydrogen Energy,* 33**,** 4013-4029.

BASTOS-NETO, M., PATZSCHKE, C., LANGE, M., MOLLMER, J., MOLLER, A., FICHTNER, S., SCHRAGE, C., LASSIG, D., LINCKE, J., STAUDT, R., KRAUTSCHEID, H. & GLASER, R. 2012. Assessment of hydrogen storage by physisorption in porous materials. *Energy & Environmental Science,* 5**,** 8294-8303.

BATSANOV, S. S. 1999. Van der Waals radii of hydrogen in gas-phase and condensed molecules. *Structural Chemistry,* 10**,** 395-400.

BEN-AMOTZ, D. & HERSCHBACH, D. R. 1990. Estimation of effective diameters for molecular fluids. *The Journal of Physical Chemistry,* 94**,** 1038-1047.

BEN, T., REN, H., MA, S., CAO, D., LAN, J., JING, X., WANG, W., XU, J., DENG, F., SIMMONS, J. M., QIU, S. & ZHU, G. 2009. Targeted Synthesis of a Porous Aromatic Framework with High Stability and Exceptionally High Surface Area. *Angewandte Chemie International Edition,* 48**,** 9457-9460.

BEREZKINA, Y. F. D., M. M.; SARAKHOV, A. I. 1969. *Akad. Nauk SSSR, Ser. Khim. 1969, 2653; Bull. Akad. Sei. USSR, Diu. Chem. Sci. (Engl. Transl.) 1969, 2495.*

BERNDES, G. 2002. Bioenergy and water - the implications of large-scale bioenergy production for water use and supply. *Global Environmental Change-Human and Policy Dimensions,* 12**,** 253-271.

BICAKOVA, O. & STRAKA, P. 2012. Production of hydrogen from renewable resources and its effectiveness. *International Journal of Hydrogen Energy,* 37**,** 11563-11578.

BILEN, K., OZYURT, O., BAKIRCI, K., KARSLI, S., ERDOGAN, S., YIMAZ, M. & COMAKLI, O. 2008. Energy production, consumption, and environmental pollution for sustainable development: A case study in Turkey. *Renewable & Sustainable Energy Reviews,* 12**,** 1529-1561.

BLACKMAN, J. M., PATRICK, J. W. & SNAPE, C. E. 2006. An accurate volumetric differential pressure method for the determination of hydrogen storage capacity at high pressures in carbon materials. *Carbon,* 44**,** 918-927.

BOGDANOVIC, B., BRAND, R. A., MARJANOVIC, A., SCHWICKARDI, M. & TOLLE, J. 2000. Metal-doped sodium aluminium hydrides as potential new hydrogen storage materials. *Journal of Alloys and Compounds,* 302**,** 36-58.

BRITISH PETROLEUM COMPANY. 2012a. *BP Energy Outlook 2030*. Available: http://www.bp.com/liveassets/bp_internet/globalbp/STAGING/global_assets/downloads/O/2012_2030_energy_outlook_booklet.pdf.

BRITISH PERTOLUM COMPANY. 2012b. BP statistical review of world energy June 2012, London, British Petroleum Co. plc.

BROACH, R. W., JAN, D.-Y., LESCH, D. A., KULPRATHIPANJA, S., ROLAND, E. & KLEINSCHMIT, P. 2000. Zeolites. *Ullmann's Encyclopedia of Industrial Chemistry*. Wiley-VCH Verlag GmbH & Co. KGaA.

BROOM, D. P. 2007. The accuracy of hydrogen sorption measurements on potential storage materials. *International Journal of Hydrogen Energy,* 32**,** 4871-4888.

BROOM, D. P. 2011. Hydrogen storage materials : the characterisation of their storage properties, London ; New York, Springer.

BROOM, D. P. & MORETTO, P. 2007. Accuracy in hydrogen sorption measurements. *Journal of Alloys and Compounds,* 446**,** 687-691.

BROWNING, D. J., GERRARD, M. L., LAKEMAN, J. B., MELLOR, I. M., MORTIMER, R. J. & TURPIN, M. C. 2000. Investigation of the hydrogen storage capacities of carbon nanofibres prepared from an ethylene precursor, Coral Gables, Int Assoc Hydrogen Energy.

BRUNAUER, S., EMMETT, P.H., TELLER, E., 1938. Adsorption of Gases in Multimolecular Layers *J. Am. Chem Soc.,* 60**,** 309-319.

BRITISH STANDARD. 2007. Pore size distribution and porosity of solid materials by mercury porosimetry and gas adsorption. Analysis of micropores by gas adsorption. *BS ISO 15901-3:2007*.

BRITISH STANDARD. 2010. Determination of the specific surface area of solids by gas adsorption — BET method. *BS ISO 9277:2010.*

BRITISH STANDARD, 2006. Solid recovered fuels. Methods for the determination of ash content. *DD CEN/TS 15403:2006*.

BRITISH STANDARD, 2011. Solid recovered fuels. Determination of moisture content using the oven dry method, Moisture in general analysis sample. *BS EN 15414-3:2011*.

BUDD, P. M., BUTLER, A., SELBIE, J., MAHMOOD, K., MCKEOWN, N. B., GHANEM, B., MSAYIB, K., BOOK, D. & WALTON, A. 2007. The potential of organic polymer-based hydrogen storage materials. *Physical Chemistry Chemical Physics,* 9**,** 1802-1808.

CHAE, H. K., SIBERIO-PEREZ, D. Y., KIM, J., GO, Y., EDDAOUDI, M., MATZGER, A. J., O'KEEFFE, M. & YAGHI, O. M. 2004. A route to high surface area, porosity and inclusion of large molecules in crystals. *Nature,* 427**,** 523-527.

CHAHINE, R. & BOSE, T. K. 1994. LOW-PRESSURE ADSORPTION STORAGE OF HYDROGEN. *International Journal of Hydrogen Energy,* 19**,** 161-164.

CHAMBERS, A., PARK, C., BAKER, R. T. K. & RODRIGUEZ, N. M. 1998. Hydrogen storage in graphite nanofibers. *Journal of Physical Chemistry B,* 102**,** 4253-4256.

CHENG, H. S., CHEN, L., COOPER, A. C., SHA, X. W. & PEZ, G. P. 2008. Hydrogen spillover in the context of hydrogen storage using solid-state materials. *Energy & Environmental Science,* 1**,** 338-354.

CHUNG, T. C. M., JEONG, Y., CHEN, Q., KLEINHAMMES, A. & WU, Y. 2008. Synthesis of microporous boron-substituted carbon (B/C) materials using polymeric precursors for hydrogen physisorption. *Journal of the American Chemical Society,* 130**,** 6668-+.

COLLINS, D. J. & ZHOU, H. C. 2007. Hydrogen storage in metal-organic frameworks. *Journal of Materials Chemistry,* 17**,** 3154-3160.

COTE, A. P., BENIN, A. I., OCKWIG, N. W., O'KEEFFE, M., MATZGER, A. J. & YAGHI, O. M. 2005. Porous, crystalline, covalent organic frameworks. *Science,* 310**,** 1166-1170.

CRABTREE, G. W., DRESSELHAUS, M. S. & BUCHANAN, M. V. 2004. The hydrogen economy. *Physics Today,* 57**,** 39-44.

DARKRIM, F. L., MALBRUNOT, P. & TARTAGLIA, G. P. 2002. Review of hydrogen storage by adsorption in carbon nanotubes. *International Journal of Hydrogen Energy,* 27**,** 193-202.

DAS, D. & VEZIROGLU, T. N. 2008. Advances in biological hydrogen production processes. *International Journal of Hydrogen Energy,* 33**,** 6046-6057.

DAVIS, R. T., DEWITT, T.W, EMMETT, P.H, 1947. *J. Phys. Chem.,* 51**,** 1232.

DAWSON, R., COOPER, A. I. & ADAMS, D. J. 2012. Nanoporous organic polymer networks. *Progress in Polymer Science,* 37**,** 530-563.

DE LA CASA-LILLO, M. A., LAMARI-DARKRIM, F., CAZORLA-AMOROS, D. & LINARES-SOLANO, A. 2002. Hydrogen storage in activated carbons and activated carbon fibers. *Journal of Physical Chemistry B,* 106**,** 10930-10934.

DEMIRBAS, A. 2002. Fuel properties of hydrogen, liquefied petroleum gas (LPG), and compressed natural gas (CNG) for transportation. *Energy Sources,* 24**,** 601-610.

DILLON, A. C. & HEBEN, M. J. 2001. Hydrogen storage using carbon adsorbents: past, present and future. *Applied Physics a-Materials Science & Processing,* 72**,** 133-142.

DILLON, A. C., JONES, K. M., BEKKEDAHL, T. A., KIANG, C. H., BETHUNE, D. S. & HEBEN, M. J. 1997. Storage of hydrogen in single-walled carbon nanotubes. *Nature,* 386**,** 377-379.

DIMITRAKAKIS, G. K., TYLIANAKIS, E. & FROUDAKIS, G. E. 2008. Pillared Graphene: A New 3-D Network Nanostructure for Enhanced Hydrogen Storage. *Nano Letters,* 8**,** 3166-3170.

DINCER, I. 1998. Energy and environmental impacts: Present and future perspectives. *Energy Sources,* 20**,** 427-453.

DINCER, I. 1999. Environmental impacts of energy. *Energy Policy,* 27**,** 845-854.

DINCER, I. 2000. Renewable energy and sustainable development: a crucial review. *Renewable & Sustainable Energy Reviews,* 4**,** 157-175.

DINCER, I. 2008. Hydrogen and Fuel Cell Technologies for Sustainable Future. *Jordan Journal of Mechanical and Industrial Engineering* 2**,** 1-14.

DINCER, I. 2012. Green methods for hydrogen production. *International Journal of Hydrogen Energy,* 37**,** 1954-1971.

DINCER, I., ZAMFIRESCU, C., 2011. Sustainable Energy and Applications, New York: Springer, Verlag, 2011.

DO, D. D. & DO, H. D. 2003. Adsorption of supercritical fluids in non-porous and porous carbons: analysis of adsorbed phase volume and density. *Carbon,* 41**,** 1777-1791.

DOE. 2009. Targets for Onboard Hydrogen Storage System for Light-Duty Vehicles. Available: http://www1.eere.energy.gov/hydrogenandfuelcells/storage/pdfs/targets_onboard_hydro_storage_explanation.pdf.

DOE. 2008. Office of Efficiency and Renewable Energy's Fuel Cell Technologies Program, . FY 2008 Annual Progress Report , Hydrogen Program.Avaliable: www1.eere.energy.gov/hydrogenandfuelcells/storage/tech_status.html

DOMBROWSKI, R. J., HYDUKE, D. R. & LASTOSKIE, C. M. 2000. Pore size analysis of activated carbons from argon and nitrogen porosimetry using density functional theory. *Langmuir,* 16**,** 5041-5050.

DUFFIELD, W. A., AND SASS, J.H., 2003. Geothermal Energy—Clean Power From the Earth's Heat *In:* SERVICES, U. S. G. S. I. (ed.).

DYNE, B. 2013. Recent climate change research points to a growing global crisis. World Socialist Web Site. Available: http://www.wsws.org/en/articles/2013/01/12/warm-j12.html?view=print.

EBERLE, U., FELDERHOFF, M. & SCHUTH, F. 2009. Chemical and Physical Solutions for Hydrogen Storage. *Angewandte Chemie-International Edition,* 48**,** 6608-6630.

EDWARDS, P. P., KUZNETSOV, V. L., DAVID, W. I. F. & BRANDON, N. P. 2008. Hydrogen and fuel cells: Towards a sustainable energy future. *Energy Policy,* 36**,** 4356-4362.

EIA. 2011. International Energy Outlook 2011. Washington, DC: U.S. Energy Information Administration, 2011. Available: http://www.eia.gov/forecasts/ieo/pdf/0484%282011%29.pdf.

EMMETT, P. H., AND BRUNAUER, S., J. 1937. The Use of Low Temperature van der Waals Adsorption Isotherms in Determining the Surface Area of Iron Synthetic Ammonia Catalysts. *J. Am. Chem. Soc.* , 59 1553–1564.

EUBANK, J. F., WOJTAS, L., HIGHT, M. R., BOUSQUET, T., KRAVTSOV, V. C. & EDDAOUDI, M. 2011. The Next Chapter in MOF Pillaring Strategies: Trigonal Heterofunctional Ligands To Access Targeted High-Connected Three Dimensional Nets, Isoreticular Platforms. *Journal of the American Chemical Society,* 133**,** 17532-17535.

EUBANK, J. F., WOJTAS, L., HIGHT, M. R., BOUSQUET, T., KRAVTSOV, V. C., EDDAOUDI, M. 2011. The Next Chapter in MOF Pillaring Strategies: Trigonal Heterofunctional Ligands To Access Targeted High-Connected Three Dimensional Nets, Isoreticular Platforms. *Journal of the American Chemical Society,* 133**,** 17532-17535.

EWAN, B. C. R. & ALLEN, R. W. K. 2005. A figure of merit assessment of the routes to hydrogen. *International Journal of Hydrogen Energy,* 30**,** 809-819.

FARHA, O. K., YAZAYDIN, A. O., ERYAZICI, I., MALLIAKAS, C. D., HAUSER, B. G., KANATZIDIS, M. G., NGUYEN, S. T., SNURR, R. Q. & HUPP, J. T. 2010. De novo synthesis of a metal-organic framework material featuring ultrahigh surface area and gas storage capacities. *Nature Chemistry,* 2**,** 944-948.

FARHA, O.K., HUPP, J.T. 2010. Rational Design, Synthesis, Purification, and Activation of Metal Organic Framework Materials, *Acc. Chem. Res.*, 43(8),1166-1175.

FEREY, G., MELLOT-DRAZNIEKS, C., SERRE, C., MILLANGE, F., DUTOUR, J., SURBLE, S. & MARGIOLAKI, I. 2005. A chromium terephthalate-based solid with unusually large pore volumes and surface area. *Science,* 309**,** 2040-2042.

FURUKAWA, H., KO, N., GO, Y. B., ARATANI, N., CHOI, S. B., CHOI, E., YAZAYDIN, A. O., SNURR, R. Q., O'KEEFFE, M., KIM, J. & YAGHI, O. M. 2010. Ultrahigh Porosity in Metal-Organic Frameworks. *Science,* 329**,** 424-428.

FURUKAWA, H., MILLER, M. A. & YAGHI, O. M. 2007. Independent verification of the saturation hydrogen uptake in MOF-177 and establishment of a benchmark for hydrogen adsorption in metal-organic frameworks. *Journal of Materials Chemistry,* 17**,** 3197-3204.

FURUKAWA, H. & YAGHI, O. M. 2009. Storage of Hydrogen, Methane, and Carbon Dioxide in Highly Porous Covalent Organic Frameworks for Clean Energy Applications. *Journal of the American Chemical Society,* 131**,** 8875-8883.

GARDNER, L., KRUK, M. & JARONIEC, M. 2001. Reference Data for Argon Adsorption on Graphitized and Nongraphitized Carbon Blacks. *The Journal of Physical Chemistry B,* 105**,** 12516-12523.

GERBENS-LEENES, W., HOEKSTRA, A. Y. & VAN DER MEER, T. H. 2009. The water footprint of bioenergy. *Proceedings of the National Academy of Sciences of the United States of America,* 106**,** 10219-10223.

GLUECKAUF, E. 1955. Theory of chromatography .10. formulae for diffusion into spheres and their application to chromatography. *Transactions of the Faraday Society,* 51**,** 1540-1551.

GLUECKAUF, E. & COATES, J. I. 1947. Theory of chromatography .4. the influence of incomplete equilibrium on the front boundary of chromatograms and on the effectiveness of separation. *Journal of the Chemical Society,* 1315-1321.

GOGOTSI, Y., DASH, R. K., YUSHIN, G., YILDIRIM, T., LAUDISIO, G. & FISCHER, J. E. 2005. Tailoring of nanoscale porosity in carbide-derived carbons for hydrogen storage. *Journal of the American Chemical Society,* 127**,** 16006-16007.

GOGOTSI, Y., PORTET, C., OSSWALD, S., SIMMONS, J. M., YILDIRIM, T., LAUDISIO, G. & FISCHER, J. E. 2009. Importance of pore size in high-pressure hydrogen storage by porous carbons. *International Journal of Hydrogen Energy,* 34**,** 6314-6319.

GOSSELINK, J. W. 2002. Pathways to a more sustainable production of energy: sustainable hydrogen - a research objective for Shell. *International Journal of Hydrogen Energy,* 27**,** 1125-1129.

GOSWAMI, D. Y., MIRABAL, S. T., GOEL, N., INGLEY, H. A. & ASME 2003. *A review of hydrogen production technologies,* New York, Amer Soc Mechanical Engineers.

GRAY, M. J., MEBANE, R. C., WOMACK, H. N. & RYBOLT, T. R. 1995. Molecular mechanics and molecular cross-sectional areas - a comparison with molecules adsorbed on solid-surfaces. *Journal of Colloid and Interface Science,* 170**,** 98-101.

GREENWOOD, N. N. E., A. 1997. *Chemistry of Elements*, Elsevier, 1997.

GREGG, S. J., AND SING, K.S.W., 1982. *Adsorption Surface Area and Porosity,* London, Academic Press.

GROCHALA, W. & EDWARDS, P. P. 2004. Thermal decomposition of the non-interstitial hydrides for the storage and production of hydrogen. *Chemical Reviews,* 104**,** 1283-1315.

GROSS, K.J. 2008. Recommended Best Practices for the Characterization of Storage Properties of Hydrogen Storage Materials, National Renewable Energy Laboratory, Available Online: http://www1.eere.energy.gov/hydrogenandfuelcells/pdfs/bestpractices_h2_storage_materials.pdf

GROSS, K.J., CARRINGTON, K.R., BARCELO, S., KARKAMKAR, A., PUREWAL, J.,MA, S., ZHOU, H.C., DANTZER, P., OTT, K., PIVAK, Y., DAM, B., CHANDRA, D., 2012. Recommended Best Practices for the Characterization of Storage Properties of Hydrogen Storage Materials

GUPTA, B. K., AWASTHI, K. & SRIVASTAVA, O. N. 2000. New carbon variants: Graphitic nanofibres and nanotubules as hydrogen storage materials, Coral Gables, Int Assoc Hydrogen Energy.

HARRIS, I. R., BOOK, D., ANDERSON, P.A., AND EDWARDS, P.P., 2004. Hydrogen Storage: the Grand Challenge. *The Fuel Cell Review,* 1**,** 17-23.

HÄUSSINGER, P., LOHMÜLLER, R. & WATSON, A. M. 2000a. Hydrogen, 2. Production. *Ullmann's Encyclopedia of Industrial Chemistry*. Wiley-VCH Verlag GmbH & Co. KGaA.

HÄUSSINGER, P., LOHMÜLLER, R. & WATSON, A. M. 2000b. Hydrogen, 6. Uses. *Ullmann's Encyclopedia of Industrial Chemistry*. Wiley-VCH Verlag GmbH & Co. KGaA.

HÄUSSINGER, P., LOHMÜLLER, R. & WATSON, A.M. 2000c. Hydrogen, 1. Properties and Occurrence, *Ullmann's Encyclopedia of Industrial Chemistry*. Wiley- VCH Verlag GmbH & Co. KGaA.

HARVEY S.D., Eckberg, A.D., Thallapally P.K., 2011, Evaluation of copper–1,3,5-benzenetricarboxylate metal–organic framework (Cu MOF) as a selective sorbent for Lewis-base analytes, *Journal of Separation Science*, 34 (18), 2418–2426.

HENNENBERG, K. J., DRAGISIC, C., HAYE, S., HEWSON, J., SEMROC, B., SAVY, C., WIEGMANN, K., FEHRENBACH, H. & FRITSCHE, U. R. 2010. The Power of Bioenergy-Related Standards to Protect Biodiversity. *Conservation Biology,* 24**,** 412-423.

HIDY, G. M., CHOW, J. C., ENGLAND, G. C., LEGGE, A. H., LLOYD, A. C. & WATSON, J. G. 2012. Energy supplies and future engines for land, sea, and air. *Journal of the Air & Waste Management Association,* 62**,** 1233-1248.

HILDEBRAND, T. & RUEGSEGGER, P. 1997. A new method for the model-independent assessment of thickness in three-dimensional images. *Journal of Microscopy-Oxford,* 185**,** 67-75.

HIRSCHER, M., BECHER, M., HALUSKA, M., DETTLAFF-WEGLIKOWSKA, U., QUINTEL, A., DUESBERG, G. S., CHOI, Y. M., DOWNES, P., HULMAN, M., ROTH, S., STEPANEK, I. & BERNIER, P. 2001. Hydrogen storage in sonicated carbon materials. *Applied Physics a-Materials Science & Processing,* 72**,** 129-132.

HIRSCHER, M., PANELLA, B. & SCHMITZ, B. 2010. Metal-organic frameworks for hydrogen storage. *Microporous and Mesoporous Materials,* 129**,** 335-339.

HOLLADAY, J. D., HU, J., KING, D. L. & WANG, Y. 2009. An overview of hydrogen production technologies. *Catalysis Today,* 139**,** 244-260.

HONNERY, D. & MORIARTY, P. 2009. Estimating global hydrogen production from wind. *International Journal of Hydrogen Energy,* 34**,** 727-736.

HOSSEINI, M., DINCER, I., NATERER, G. F. & ROSEN, M. A. 2012. Thermodynamic analysis of filling compressed gaseous hydrogen storage tanks. *International Journal of Hydrogen Energy,* 37**,** 5063-5071.

HOU, P. X., YANG, Q. H., BAI, S., XU, S. T., LIU, M. & CHENG, H. M. 2002. Bulk storage capacity of hydrogen in purified multiwalled carbon nanotubes. *Journal of Physical Chemistry B,* 106**,** 963-966.

HRUZEWICZ-KOLODZIEJCZYK, A., TING, V. P., BIMBO, N. & MAYS, T. J. 2012. Improving comparability of hydrogen storage capacities of nanoporous materials. *International Journal of Hydrogen Energy,* 37**,** 2728-2736.

IAEA. 2009. Energy, electrocity and nuclar power estimates for the period up to 2030. *In:* VIENNA: IAEA (ed.).

INTERNATIONAL ENERGY AGENCY. 2010. World Energy Outlook 2010, OECD Publishing.

INTERNATIONAL ENERGY AGENCY. 2012. World Energy Outlook 2012, OECD Publishing.

INTERNATIONAL ENERGY AAGENCY, B. 2009. Bioenergy – The Impact of Indirect Land Use Change:Summary and Conclusions from the IEA Bioenergy ExCo63 Workshop.

INTERNATIONAL ENERGY AGENCY. 2008. World Energy Outlook 2008, OECD Publishing.

IOANNATOS, G. E. & VERYKIOS, X. E. 2010. H-2 storage on single- and multi-walled carbon nanotubes. *International Journal of Hydrogen Energy,* 35**,** 622-628.

IPCC. 2007. Climate Change 2007: The Physical Science Basis. *In:* PRESS, C. U. (ed.).

IPCC. 2011. Special Report on Renewable Energy Sources and Climate Change Mitigation, United Kingdom and New York, NY, USA, Cambridge University Press.

IRANI, R. S. 2002. Hydrogen storage: High-pressure gas containment. *Mrs Bulletin,* 27**,** 680-682.

JACOBSEN, R. T., LEACHMAN, J. W., PENONCELLO, S. G. & LEMMON, E. W. 2007. Current status of thermodynamic properties of hydrogen. *International Journal of Thermophysics,* 28**,** 758-772.

JAGIELLO, J. & THOMMES, M. 2004. Comparison of DFT characterization methods based on N2, Ar, CO2, and H2 adsorption applied to carbons with various pore size distributions. *Carbon,* 42**,** 1227-1232.

JELINEK, L. & KOVATS, E. S. 1994. TRUE SURFACE-AREAS FROM NITROGEN ADSORPTION EXPERIMENTS. *Langmuir,* 10**,** 4225-4231.

JENA, P. 2011. Materials for Hydrogen Storage: Past, Present, and Future. *Journal of Physical Chemistry Letters,* 2**,** 206-211.

JIN, H. G., XU, Y. J., LIN, R. M. & HAN, W. 2008. A proposal for a novel multi-functional energy system for the production of hydrogen and power. *International Journal of Hydrogen Energy,* 33**,** 9-19.

JOHNSTON, B., MAYO, M.C., KHARE, A., 2005. Hydrogen: the energy source for the 21st century. *Technovation,* 25**,** 569-585.

JORGENSEN, S. W. 2011. Hydrogen storage tanks for vehicles: Recent progress and current status. *Current Opinion in Solid State & Materials Science,* 15**,** 39-43.

JOSHI, A. S., DINCER, I. & REDDY, B. V. 2011. Solar hydrogen production: A comparative performance assessment. *International Journal of Hydrogen Energy,* 36**,** 11246-11257.

JURA, H. A. 1944. Absolute method of surface area determination. *J. Am. Chem. Soc.*, 66**,** 919.

KANEKO, K. 1994. Determination of pore-size and pore-size distribution .1. adsorbents and catalysts. *Journal of Membrane Science,* 96**,** 59-89.

KARNAUKHOV, A. P. 1985. Improvement of methods for surface-area determinations. *Journal of Colloid and Interface Science,* 103**,** 311-320.

KAYE, S. S., DAILLY, A., YAGHI, O. M. & LONG, J. R. 2007. Impact of preparation and handling on the hydrogen storage properties of Zn4O(1,4-benzenedicarboxylate)(3) (MOF-5). *Journal of the American Chemical Society,* 129**,** 14176-+.

KAYIRAN, S. B. & DARKRIM, F. L. 2002. Synthesis and ionic exchanges of zeolites for gas adsorption. *Surface and Interface Analysis,* 34**,** 100-104.

KING, D. A. 2004. Environment - Climate change science: Adapt, mitigate, or ignore? *Science,* 303**,** 176-177.

KIYOBAYASHI, T., TAKESHITA, H. T., TANAKA, H., TAKEICHI, N., ZUTTEL, A., SCHLAPBACH, L. & KURIYAMA, N. 2002. Hydrogen adsorption in carbonaceous materials - How to determine the storage capacity accurately. *Journal of Alloys and Compounds,* 330**,** 666-669.

KOJIMA, Y., KAWAI, Y., NAKANISHI, H. & MATSUMOTO, S. 2004. Compressed hydrogen generation using chemical hydride. *Journal of Power Sources,* 135**,** 36-41.

KOTHARI, R., · BUDDHI, D., · SAWHNEY, R.L., 2004. Sources and technology for hydrogen production: a review. *International Journal of Global Energy Issues,* 21**,** 154.

KUBAS, G. J. 1988. Molecular-hydrogen complexes - coordination of a sigma-bond to transition-metals. *Accounts of Chemical Research,* 21**,** 120-128.

KUSGENS, P., ROSE, M., SENKOVSKA, I., FRODE, H., HENSCHEL, A., SIEGLE, S., KASKEL, S. 2009. Characterization of Metal-Organic Frameworks by Water Adsorption, *Microporous Mesoporous Mat.,* 120, 325.

LACHAWIEC, A. J., QI, G. S. & YANG, R. T. 2005. Hydrogen storage in nanostructured carbons by spillover: Bridge-building enhancement. *Langmuir,* 21**,** 11418-11424.

LANGMI, H. W., BOOK, D., WALTON, A., JOHNSON, S. R., AL-MAMOURI, M. M., SPEIGHT, J. D., EDWARDS, P. P., HARRIS, I. R. & ANDERSON, P. A. 2005. Hydrogen storage in ion-exchanged zeolites. *Journal of Alloys and Compounds,* 404**,** 637-642.

LASTOSKIE, C., GUBBINS, K. E. & QUIRKE, N. 1993. Pore size distribution analysis of microporous carbons: a density functional theory approach. *The Journal of Physical Chemistry,* 97**,** 4786-4796.

LATROCHE, M., SURBLE, S., SERRE, C., MELLOT-DRAZNIEKS, C., LLEWELLYN, P. L., LEE, J. H., CHANG, J. S., JHUNG, S. H. & FEREY, G. 2006. Hydrogen storage in the giant-pore metal-organic frameworks MIL-100 and MIL-101. *Angewandte Chemie-International Edition,* 45**,** 8227-8231.

LEACHMAN, J. W., JACOBSEN, R. T., PENONCELLO, S. G. & LEMMON, E. W. 2009. Fundamental Equations of State for Parahydrogen, Normal Hydrogen, and Orthohydrogen. *Journal of Physical and Chemical Reference Data,* 38.

LEE, J.-Y., WOOD, C. D., BRADSHAW, D., ROSSEINSKY, M. J. & COOPER, A. I. 2006. Hydrogen adsorption in microporous hypercrosslinked polymers. *Chemical Communications,* 0**,** 2670-2672.

LEUNG, W. B., MARCH, N. H. & MOTZ, H. 1976. PRIMITIVE PHASE-DIAGRAM FOR HYDROGEN. *Physics Letters A,* 56**,** 425-426.

LI, Y. & YANG, R. T. 2007. Gas adsorption and storage in metal-organic framework MOF-177. *Langmuir,* 23**,** 12937-12944.

LI, Y. W. & YANG, R. T. 2008. Hydrogen storage in metal-organic and covalent-organic frameworks by spillover. *Aiche Journal,* 54**,** 269-279.

LIN, X., TELEPENI, I., BLAKE, A. J., DAILLY, A., BROWN, C. M., SIMMONS, J. M., ZOPPI, M., WALKER, G. S., THOMAS, K. M., MAYS, T. J., HUBBERSTEY, P., CHAMPNESS, N. R. & SCHRÖDER, M. 2009. High Capacity Hydrogen Adsorption in Cu(II) Tetracarboxylate Framework Materials: The Role of Pore Size, Ligand Functionalization, and Exposed Metal Sites. *Journal of the American Chemical Society,* 131**,** 2159-2171.

LIU, C., FAN, Y. Y., LIU, M., CONG, H. T., CHENG, H. M. & DRESSELHAUS, M. S. 1999. Hydrogen storage in single-walled carbon nanotubes at room temperature. *Science,* 286**,** 1127-1129.

LIVINGSTON, H. K. 1949. The cross-sectional areas of molecules adsorbed on solid surfaces. *Journal of Colloid Science,* 4**,** 447-458.

LLEWELLYN, P. L., BOURRELLY, S., SERRE, C., VIMONT, A., DATURI, M., HAMON, L., DE WEIRELD, G., CHANG, J.-S., HONG, D.-Y., KYU HWANG, Y., HWA JHUNG, S. & FÉREY, G. R. 2008. High Uptakes of CO2 and CH4 in Mesoporous Metal琅Organic Frameworks MIL-100 and MIL-101. *Langmuir,* 24**,** 7245-7250.

LOWELL, S. 2004. Characterization of porous solids and powders: surface area, pore size and density, Kluwer Academic, 2004.

LUEKING, A. D. & YANG, R. T. 2004. Hydrogen spillover to enhance hydrogen storage - study of the effect of carbon physicochemical properties. *Applied Catalysis a-General,* 265**,** 259-268.

MALBRUNOT, P., VIDAL, D., VERMESSE, J., CHAHINE, R. & BOSE, T. K. 1992. Adsorption measurements of argon, neon, krypton, nitrogen, and methane on activated carbon up to 650MPa. *Langmuir,* 8**,** 577-580.

MALBRUNOT, P., VIDAL, D., VERMESSE, J., CHAHINE, R. & BOSE, T. K. 1997. Adsorbent helium density measurement and its effect on adsorption isotherms at high pressure. *Langmuir,* 13**,** 539-544.

MARSH, H. & WYNNEJONES, W. F. K. 1964. The surface properties of carbon .1. the effect of activated diffusion in the determination of surface area. *Carbon,* 1**,** 269-279.

MARTINOT, E., CHAUREY, A., LEW, D., MOREIRA, J. R. & WAMUKONYA, N. 2002. Renewable energy markets in developing countries. *Annual Review of Energy and the Environment,* 27**,** 309-348.

MAYS, T. J. 2007. A new classification of pore sizes. *In:* RODRIGUEZ-REINOSO, F., ROUQEROL, J., LLEWELLYN, P.L., SEATON, N., (ed.) *Stud surf sci catal.*: Elsevier.

MCHUGH, K. 2005. Hydrogen Production Methods. Virginia: MPR Associates Inc February.
MCCLELLAN, A. L., AND HARNSBERGER , H.F. 1967. Cross-sectional Areas of Molecules Adsorbed on Solid Surfaces. *J Colloid and Interface Sci,* 23**,** 577-599.
MCKEOWN, N. B. & BUDD, P. M. 2006. Polymers of intrinsic microporosity (PIMs): organic materials for membrane separations, heterogeneous catalysis and hydrogen storage. *Chemical Society Reviews,* 35**,** 675-683.
MCNICOL, B. D., RAND, D. A. J. & WILLIAMS, K. R. 2001. Fuel cells for road transportation purposes - yes or no? *Journal of Power Sources,* 100**,** 47-59.
MONIBA ENERGY DEVELOPMENT INITIATIVE. 2003. Preliminary Hydrogen Opportunities Report. In: DEPARTMENT OF ENERGY, S. A. T. Avalable from: (http://www.manitoba.ca/iem/energy/hydrogen/index.html.
MEE, I., MATERIALS EVALUATION AND ENGINEERING, INC 2010. Handbook Of Analytical Methods For Materials. Avaliable from: http://mee-inc.com/hamm72d.pdf.
MICROMERITICS. 1997. Application note no. 105: helium effects on ASAP series micropore analyses, available from micromeritics application notes and technical tips. Avaliable:http://www.micromeritics.com/Library/Application-Notes.aspx.
MICROMERITICS. 2003. Application note no. 104: determining free-space values for ASAP series micropore analyses. Available: http://www.micromeritics.com/Repository/Files/apnote104.pdf.
MICROMERITICS. 2005. Application note no. 136: using the ASAP 2020 for determining the hydrogen adsorption capacity of powders and porous materials. Available: http://www.micromeritics.com/Repository/Files/ap136.pdf. .
MIDILLI, A., AY, M., DINCER, I. & ROSEN, M. A. 2005. On hydrogen and hydrogen energy strategies I: current status and needs. *Renewable & Sustainable Energy Reviews,* 9**,** 255-271.
MILTNER, A., WUKOVITS, W., PROLL, T. & FRIEDL, A. 2010. Renewable hydrogen production: a technical evaluation based on process simulation. *Journal of Cleaner Production,* 18**,** S51-S62.
MINISTRY OF THE ENVIRONMENT GOVERNMENT OF JAPAN. 2011. Available: http://www.env.go.jp/en/focus/docs/files/20120801-02_05.pdf.
MIRANDA, C. R. & CEDER, G. 2007. Ab initio investigation of ammonia-borane complexes for hydrogen storage. *The Journal of chemical physics,* 126**,** 184703.
MOMIRLAN, M. & VEZIROGLU, T. N. 2002. Current status of hydrogen energy. *Renewable & Sustainable Energy Reviews,* 6**,** 141-179.
MOMIRLAN, M., VEZIROGLU, T., 1999. Recent directions of world hydrogen production *Renewable & Sustainable Energy Reviews,* 3**,** 219-231.
MORETTO, P., ZLOTEA, C., WEIDNER, E., INSTITUTE FOR ENERGY, JOINT RESEARCH CENTRE OF THE EUROPEAN COMMISSION 2010. *Round Robin Hydrogen Sorption Performance Characterisation of Carbon Adsorbants, Complex and Metal Hydrides,* Forschungszentrum Jülich GmbH, Zentralbibliothek, Verlag, 2010.
MORIARTY, P. & HONNERY, D. 2012. What is the global potential for renewable energy? *Renewable & Sustainable Energy Reviews,* 16**,** 244-252.

MORRIS, J. R., CONTESCU, C. I., CHISHOLM, M. F., COOPER, V. R., GUO, J., HE, L., IHM, Y., MAMONTOV, E., MELNICHENKO, Y. B., OLSEN, R. J., PENNYCOOK, S. J., STONE, M. B.,. ZHANG H., GALLEGO N. C. 2013. Modern approaches to studying gas adsorption in nanoporous carbons, *J. Mater. Chem. A.*, Feature Article.

MOURATO, S., SAYNOR, B. & HART, D. 2004. Greening London's black cabs: a study of driver's preferences for fuel cell taxis. *Energy Policy,* 32**,** 685-695.

MULLER-STEINHAGEN, H. & NITSCH, J. 2005. The contribution of renewable energies to a sustainable energy economy. *Process Safety and Environmental Protection,* 83**,** 285-297.

MUSYOKA N.M., PETRIK L.F., HUMS E., KUHNT A., SCHWIEGE W. 2013. Thermal stability studies of zeolites A and X synthesized from South African coal fly ash, *Res Chem Intermed*, Published online 10th May 2013: http://link.springer.com/content/pdf/10.1007/s11164-013-1211-3.pdf

NAS, National Academy of Science. 2004. The Hydrogen Economy: Opportunities, Costs, Barrires, and R&D Needs, National Academies Press, Washington, DC, 2004.

NEWELL. 2004. Low Cost, High Efficiency, High Pressure Hydrogen Storage [Online]. DOE Hydrogen, Fuel Cells & Infrastructure Technologies Program Review. Available: http://www.hydrogen.energy.gov/pdfs/review04/st_2_newell.pdf.

NI, M., LEUNG, M. K. H., SUMATHY, K. & LEUNG, D. Y. C. 2006. Potential of renewable hydrogen production for energy supply in Hong Kong. *International Journal of Hydrogen Energy*, 31**,** 1401-1412.

NIST 2012. NIST Chemistry WebBook. National Institute of Standards and Technology.

NRC, N. R. C. 2008. Transitions to Alternative Transportation Technologies-A Focus on Hydrogen, The National Academies Press.

OLIVIER, J. P. 1995. Modeling Physical Adsorption on Porous and Nonporous Solids Using Density Functional Theory. *Journal of Porous Materials,* 2**,** 9-17.

ORHAN, M. F., DINCER, I. & ROSEN, M. A. 2012. Investigation of an integrated hydrogen production system based on nuclear and renewable energy sources: a new approach for sustainable hydrogen production via copper-chlorine thermochemical cycles. *International Journal of Energy Research,* 36**,** 1388-1394.

ORIMO, S. I., NAKAMORI, Y., ELISEO, J. R., ZUTTEL, A. & JENSEN, C. M. 2007. Complex hydrides for hydrogen storage. *Chemical Reviews*, 107**,** 4111-4132.

OSHIDA, K., KOGISO, K., MATSUBAYASHI, K., TAKEUCHI, K., KOBAYASH, S. 1995. Analysis of pore structure of activated carbon fibers using high resolution transmission electron microscopy and image processing, *J. Mater. Res.*, 10 (10), 2507- 2517.

PAINULY, J. P. 2001. Barriers to renewable energy penetration; a framework for analysis. *Renewable Energy,* 24**,** 73-89.

PANELLA, B. & HIRSCHER, M. 2005. Hydrogen physisorption in metal-organic porous crystals. *Advanced Materials*, 17**,** 538.

PANELLA, B., HIRSCHER M., ROTH, S. 2005. Hydrogen adsorption in different carbon nanostructures, *Carbon*, 43, 2209-2214.

PARILLA, P. 2012. Hydrogen Sorbants Measurements Qualification and Chatracterization, 2012 Annual Progress Report for the DOE Hydrogen and Fuel Cells program

PETTERSSON, J., RAMSEY, B. & HARRISON, D. 2006. A review of the latest developments in electrodes for unitised regenerative polymer electrolyte fuel cells. *Journal of Power Sources,* 157**,** 28-34.

PHILLIPS, A.B., SHIVARAM, B.S. 2007. Hydrogen Absorption Studies in Transition Metal Ethylene complexes, International Symposium on Materials Issues in a Hydrogen Economy, Novemeber 12-15, 2007, Richmond, Virginia, USA.

POIRIER, E., CHAHINE, R., BENARD, P., LAFI, L., DORVAL-DOUVILLE, G. & CHANDONIA, P. A. 2006. Hydrogen adsorption measurements and modeling on metal-organic frameworks and single-walled carbon nanotubes. *Langmuir,* 22**,** 8784-8789.

POIRIER, E., CHAHINE, R., BENARD, P., COSSEMENT, D., LAFI, L., MELANCON, E., BOSE, T.K., DESILETS, S. 2004. Storage of hydrogen on single-walled carbon nanotubes and other carbon structures, *Appl. Phys. A,* 78, 961-967.

PRESS, R. J. 2009. Introduction to hydrogen technology, Hoboken, N.J., Wiley ; Chichester : John Wiley [distributor].

PRODUCTS, A. Available: http://www.airproducts.co.uk/speciality_gases/BIPGases/.

PUREWAL, J. J., KABBOUR, H., VAJO, J. J., AHN, C. C. & FULTZ, B. 2009. Pore size distribution and supercritical hydrogen adsorption in activated carbon fibers. *Nanotechnology,* 20.

REGLI, L., ZECCHINA, A., VITILLO, J. G., COCINA, D., SPOTO, G., LAMBERTI, C., LILLERUD, K. P., OLSBYE, U. & BORDIGA, S. 2005. Hydrogen storage in chabazite zeolite frameworks. *Physical Chemistry Chemical Physics,* 7**,** 3197-3203.

REID, C. R. & THOMAS, K. M. 1999. Adsorption of gases on a carbon molecular sieve used for air separation: Linear adsorptives as probes for kinetic selectivity. *Langmuir,* 15**,** 3206-3218.

REID, R. C., . PRAUSNITZ, J.M AND SHERWOOD, T.K. 1977. The Properties of Liquids and Gases, McGraw-Hill, New York, 1977.

REMY, E. & THIEL, E. 2002. Medial axis for chamfer distances: Computing look-up tables and neighbourhoods in 2D or 3D. *Pattern Recognition Letters,* 23**,** 649-661.

RESCH, G., HELD, A., FABER, T., PANZER, C., TORO, F. & HAAS, R. 2008. Potentials and prospects for renewable energies at global scale. *Energy Policy,* 36**,** 4048-4056.

RHODIN, T. N. 1953. PHYSICAL ADSORPTION ON SINGLE CRYSTAL ZINC SURFACES. *Journal of Physical Chemistry,* 57**,** 143-148.

RICHARDS, M. E., LISS, W.,. Natural Gas Reformer-Based Hydrogen Fueling Station Modeling. NGV International Conference 2002, 2002.

RIIS, T., SANDROCK, G., ULLEBERG, O., VIE, P.J.S. 2005. Hydrogen Storage–Gaps and Priorities, *HIA HCG Storage paper,* 1-13.

ROSEN, M. A. & SCOTT, D. S. 1998. Comparative efficiency assessments for a range of hydrogen production processes. *International Journal of Hydrogen Energy,* 23**,** 653-659.

ROSI, N. L; KIM, J.; EDDAOUDDI, M.; CHEN, B.; O'KEEFFE, M.; YAGHI, O.M. 2005. Rod Packings and Metal−Organic Frameworks Constructed from Rod-Shaped Secondary Building Units, J. Am. Chem. Soc., 127, 1504-1518.

ROSSEINSKY, M. J. 2004. Recent developments in metal-organic framework chemistry: design, discovery, permanent porosity and flexibility. *Microporous and Mesoporous Materials,* 73**,** 15-30.

ROUQUEROL, F., ROUQUEROL, J. & SING, K. S. W. 1999. Adsorption by powders and porous solids : principles, methodology, and applications, San Diego, Academic Press.

ROUQUEROL, J., AVNIR, D., FAIRBRIDGE, C. W., EVERETT, D. H., HAYNES, J. H., PERNICONE, N., RAMSAY, J. D. F., SING, K. S. W. & UNGER, K. K. 1994. Recommendations for the characterization of porous solids. *Pure and Applied Chemistry,* 66**,** 1739-1758.

ROUQUEROL, J., LLEWELLYN, P. & ROUQUEROL, F. 2006. Is the BET equation applicable to microporous adsorbents? *Characterization of Porous Solids Vii - Proceedings of the 7th International Symposium on the Characterization of Porous Solids (Cops-Vii), Aix-En-Provence, France, 26-28 May 2005,* 160**,** 49-56.

ROUZAUD J.N., CLINARD C. 2002. Quantitative high-resolution transmission electron microscopy: a promising tool for carbon materials characterization, *Fue*l *Processing Technology* , 77–78, 229–235.

ROWSELL, J. L. C. & YAGHI, O. M. 2004. Metal-organic frameworks: a new class of porous materials. *Microporous and Mesoporous Materials,* 73**,** 3-14.

ROWSELL, J. L. C. & YAGHI, O. M. 2005. Strategies for hydrogen storage in metal-organic frameworks. *Angewandte Chemie-International Edition,* 44**,** 4670-4679.

SAKINTUNA, B., LAMARI-DARKRIM, F. & HIRSCHER, M. 2007. Metal hydride materials for solid hydrogen storage: A review. *International Journal of Hydrogen Energy,* 32**,** 1121-1140.

SAKINTUNA, B. & YURUM, Y. 2005. Templated porous carbons: A review article. *Industrial & Engineering Chemistry Research,* 44**,** 2893-2902.

SANDROCK, G. 1999. A panoramic overview of hydrogen storage alloys from a gas reaction point of view. *Journal of Alloys and Compounds,* 293–295**,** 877-888.

SATYAPAL, S., PETROVIC, J., READ, C., THOMAS, G. & ORDAZ, G. 2007a. The US Department of Energy's National Hydrogen Storage Project: Progress towards meeting hydrogen-powered vehicle requirements. *Catalysis Today,* 120**,** 246-256.

SATYAPAL, S., PETROVIC, J. & THOMAS, G. 2007b. Gassing up with hydrogen. *Scientific American,* 296**,** 80-87.

SCAIFE, S., KLUSON, P. & QUIRKE, N. 2000. Characterization of porous materials by gas adsorption: Do different molecular probes give different pore structures? *Journal of Physical Chemistry B,* 104**,** 313-318.

SCHIFFER, H. W. 2008. WEC energy policy scenarios to 2050. *Energy Policy,* 36**,** 2464-2470.

SCHÜTH, F., SING, K.S.W., WEITKAMP, J., 2002. *Handbook of Porous Solids*, Weinheim: WILEY-VCH Verlag GmbH

SEATON, N. A., WALTON, J. P. R. B. & QUIRKE, N. 1989. A new analysis method for the determination of the pore size distribution of porous carbons from nitrogen adsorption measurements. *Carbon,* 27**,** 853-861.

SEVILLA, M., FOULSTON, R. & MOKAYA, R. 2010. Superactivated carbide-derived carbons with high hydrogen storage capacity. *Energy & Environmental Science,* 3**,** 223-227.

SEVILLA, M., MOKAYA, R. & FUERTES, A. B. 2011. Ultrahigh surface area polypyrrole-based carbons with superior performance for hydrogen storage. *Energy & Environmental Science,* 4**,** 2930-2936.

SHARMA, A., KYOTANI, T., TOMITA, A. 1999. A new quantitative approach for microstructural analysis of coal char using HRTEM images, *Fuel*, 78 (10), 1203–1212.

SHELL INTERNATIONAL BV. 2008. *Shell energy scenarios to 2050* [Online]. Available: http://www.manicore.com/fichiers/Shell_scenarii_to_2050.pdf.

SHERIF, S. A., BARBIR, F., VEZIROGLU, T.N. 2005. Towards a Hydrogen Economy. *The Electricity Journal,* 18**,** 62-76.

SCHOENECKER, P.M., CARSON, C.G., JASUJA, H., FLEMMING, C.J.J., WALTON, K.S. 2012. Effect of Water Adsorption on Retention of Structure and Surface Area of Metal-Organic Frameworks, I*nd. Eng. Chem. Res*., 51, 6513-6519.

SIEGEL, D. J., WOLVERTON, C. & OZOLINS, V. 2007. Thermodynamic guidelines for the prediction of hydrogen storage reactions and their application to destabilized hydride mixtures. *Physical Review B,* 76.

SING, K. S. W., EVERETT, D. H., HAUL, R. A. W., MOSCOU, L., PIEROTTI, R. A., ROUQUEROL, J. & SIEMIENIEWSKA, T. 1985. Reporting Physisorption Data for Gas Solid Systems with Special Reference to the Determination of Surface-Area and Porosity (Recommendations 1984). *Pure and Applied Chemistry,* 57**,** 603-619.

SING, K. S. W. & WILLIAMS, R. T. 2004. Review: The use of molecular probes for the characterization of nanoporous adsorbents. *Particle & Particle Systems Characterization,* 21**,** 71-79.

SINGLETON, J. H. & HALSEY, G. D. 1954. THE ADSORPTION OF ARGON ON XENON LAYERS. *Journal of Physical Chemistry,* 58**,** 330-335.

SIRCAR, S. 1983. LINEAR-DRIVING-FORCE MODEL FOR NON-ISOTHERMAL GAS-ADSORPTION KINETICS. *Journal of the Chemical Society-Faraday Transactions I,* 79**,** 785-796.

SIRCAR, S. 2006. Basic research needs for design of adsorptive gas separation processes. *Industrial & Engineering Chemistry Research,* 45**,** 5435-5448.

SIRCAR, S. & HUFTON, J. R. 2000. Why does the Linear Driving Force model for adsorption kinetics work ? *Adsorption-Journal of the International Adsorption Society,* 6**,** 137-147.

STEEN E., CALLANAN L.H. 2004. Recent Advances in the Science and Technology of Zeolites and Related Materials: Proceedings of the 14th International Zeolite

Conference, Cape Town, SouthAfrica, 25-30th April 2004, Part 2, Gulf Professional Publishing.
Available Online: http://books.google.co.uk/books?id=DmPr4R38lBUC&printsec=frontcover&source=gbs_ge_summary_r&cad=0#v=onepage&q&f=false

STEFFEN 2009. Climate change 2009—Faster change & more serious risks (Part 1). *In:* 2009, C. O. A. (ed.).

STERMER, D. L., SMITH, D. M. & HURD, A. J. 1989. Adsorbate shape effects on surface-roughness determination. *Journal of Colloid and Interface Science,* 131**,** 592-595.

STOECKLI, F., LOPEZ-RAMON, M.V., HUGI-CLEARY, D. 2001. Micropore sizes in activated carbons determined from the Dubinin-Radushkevich equation, *Carbon,* 39, 1115–1116.

STREPPEL, B. & HIRSCHER, M. 2011. BET specific surface area and pore structure of MOFs determined by hydrogen adsorption at 20 K. *Physical Chemistry Chemical Physics,* 13**,** 3220-3222.

STROBEL, R., GARCHE, J., MOSELEY, P. T., JORISSEN, L. & WOLF, G. 2006. Hydrogen storage by carbon materials. *Journal of Power Sources,* 159**,** 781-801.

SUMIDA, K., HILL, M. R., HORIKE, S., DAILLY, A. & LONG, J. R. 2009. Synthesis and Hydrogen Storage Properties of Be-12(OH)(12)(1,3,5-benzenetribenzoate)(4). *Journal of the American Chemical Society,* 131**,** 15120.

SWEATMAN, M. B. & QUIRKE, N. 2001. Characterization of porous materials by gas adsorption: Comparison of nitrogen at 77 K and carbon dioxide at 298 K for activated carbon. *Langmuir,* 17**,** 5011-5020.

TANAKA, H., EL-MERRAOUI, M., STEELE, W. A. & KANEKO, K. 2002. Methane adsorption on single-walled carbon nanotube: a density functional theory model. *Chemical Physics Letters,* 352**,** 334-341.

TEDDS, S., WALTON, A., BROOM, D.P., BOOK, D. 2011. Characterisation of porous hydrogen storage materials: carbons, zeolites, MOFs and PIMs, *Faraday Discussions,* 151, 75-94.

THOMAS, K. M. 2007a. Hydrogen adsorption and storage on porous materials. *Catalysis Today,* 120**,** 389-398.

THOMMES, M. 2010. Physical Adsorption Characterization of Nanoporous Materials. *Chemie Ingenieur Technik,* 82**,** 1059-1073.

TOZZINI, V. & PELLEGRINI, V. 2013. Prospects for hydrogen storage in graphene. *Physical Chemistry Chemical Physics,* 15**,** 80-89.

TURNER, J., SVERDRUP, G., MANN, M. K., MANESS, P. C., KROPOSKI, B., GHIRARDI, M., EVANS, R. J. & BLAKE, D. 2008. Renewable hydrogen production. *International Journal of Energy Research,* 32**,** 379-407.

TURNER, J. A. 2004. Sustainable hydrogen production. *Science,* 305**,** 972-974.

VAJO, J. J., SKEITH, S. L. & MERTENS, F. 2005. Reversible storage of hydrogen in destabilized LiBH4. *Journal of Physical Chemistry B,* 109**,** 3719-3722.

VAN DEN BERG, A. W. C. & AREAN, C. O. 2008. Materials for hydrogen storage: current research trends and perspectives. *Chemical Communications***,** 668-681.

VERBRUGGEN, A., FISCHEDICK, M., MOOMAW, W., WEIR, T., NADAI, A., NILSSON, L. J., NYBOER, J. & SATHAYE, J. 2010. Renewable energy costs, potentials, barriers: Conceptual issues. *Energy Policy,* 38**,** 850-861.

VEZIROGLU, T. N. & SAHIN, S. 2008. 21st Century's energy: Hydrogen energy system. *Energy Conversion and Management,* 49**,** 1820-1831.

WALKER, P. L., FORESTI, R. J. & WRIGHT, C. C. 1953. SURFACE AREA STUDIES OF CARBON-CARBON DIOXIDE REACTION. *Industrial and Engineering Chemistry,* 45**,** 1703-1710.

WALTON, K. S. & SNURR, R. Q. 2007. Applicability of the BET method for determining surface areas of microporous metal-organic frameworks. *Journal of the American Chemical Society,* 129**,** 8552-8556.

WANG, L. F. & YANG, R. T. 2008. New sorbents for hydrogen storage by hydrogen spillover - a review. *Energy & Environmental Science,* 1**,** 268-279.

WANG, X. S., MA, S. Q., FORSTER, P. M., YUAN, D. Q., ECKERT, J., LOPEZ, J. J., MURPHY, B. J., PARISE, J. B. & ZHOU, H. C. 2008. Enhancing H-2 uptake by "Close-Packing" alignment of open copper sites in metal-organic frameworks. *Angewandte Chemie-International Edition,* 47**,** 7263-7266.

WANG, Q. M., SHEN, D. M., BULOW, M., LAU, M. L., DENG, S. G., FITCH, F. R., LEMCOFF, N. O., SEMANSCIN, J. 2002. Metallo-Organic Molecular Sieve for Gas Separation and Purification, *Microporous Mesoporous Mat*., 55, 217.

WEE J.H. 2007. Applications of proton exchange membrane fuel cell systems, Renewable and Sustainable Energy Reviews, 11, 1720–1738.

WEBB, P. A. 2001. *In:* CORPORATION, Micromeritics Instrument Corporation, 1-16.

WEIDENTHALER, C. & FELDERHOFF, M. 2011. Solid-state hydrogen storage for mobile applications: Quo Vadis? *Energy & Environmental Science,* 4**,** 2495-2502.

WEINBERGER, B. & LAMARI, F. D. 2009. High pressure cryo-storage of hydrogen by adsorption at 77 K and up to 50 MPa. *International Journal of Hydrogen Energy,* 34**,** 3058-3064.

WEITKAMP, J., FRITZ, M. & ERNST, S. 1995. Zeolites as media for hydrogen storage. *International Journal of Hydrogen Energy,* 20**,** 967-970.

WOLVERTON, C., OZOLINS, V. & ASTA, M. 2004. Hydrogen in aluminum: First-principles calculations of structure and thermodynamics. *Physical Review B,* 69**,** 16.

WONG-FOY, A. G., MATZGER, A. J. & YAGHI, O. M. 2006. Exceptional H-2 saturation uptake in microporous metal-organic frameworks. *Journal of the American Chemical Society,* 128**,** 3494-3495.

WORLD COMMISSION ON ENVIRONMENT AND DEVELOPMENT. 1987. *Our common future,* Oxford ; New York, Oxford University Press.

YAGHI, O. M., O'KEEFFE, M., OCKWIG, N. W., CHAE, H. K., EDDAOUDI, M. & KIM, J. 2003. Reticular synthesis and the design of new materials. *Nature,* 423**,** 705-714.

YANG, J., SUDIK, A., WOLVERTON, C. & SIEGEL, D. J. 2010. High capacity hydrogen storage materials: attributes for automotive applications and techniques for materials discovery. *Chemical Society Reviews,* 39**,** 656-675.

YANG, R. T., LI, Y., LACHAWIEC, A.J., . 2006. *Chemical Bridges for Enhancing Hydrogen Storage by Spillover and Methods Forming the Same*.

YANG, Z. X., XIA, Y. D. & MOKAYA, R. 2007. Enhanced hydrogen storage capacity of high surface area zeolite-like carbon materials. *Journal of the American Chemical Society,* 129**,** 1673-1679.

YILDIZ, B. & KAZIMI, M. S. 2006. Efficiency of hydrogen production systems using alternative nuclear energy technologies. *International Journal of Hydrogen Energy,* 31**,** 77-92.

YOSHIZAWA, N., YAMADA, Y., SHIRAISHI, M. 1998. TEM lattice images and their evaluation by image analysis for activated carbons with disordered microtexture, *Journal of Materials Science*, 33, 199–206.

YURUM, Y., TARALP, A. & VEZIROGLU, T. N. 2009. Storage of hydrogen in nanostructured carbon materials. *International Journal of Hydrogen Energy,* 34**,** 3784-3798.

ZECCHINA, A., BORDIGA, S., VITILLO, J. G., RICCHIARDI, G., LAMBERTI, C., SPOTO, G., BJORGEN, M. & LILLERUD, K. P. 2005. Liquid hydrogen in protonic chabazite. *Journal of the American Chemical Society,* 127**,** 6361-6366.

ZEOLITES. 2010. Retrieved April 19, 2013, from Ullmann's Encyclopedia of Industrial Chemistry: http://mrw.interscience.wiley.com.ezp1.bath.ac.uk/emrw/9783527306732/ueic/article/a28_475/current/pdf

ZHANG, C., LU, X. S. & GU, A. Z. 2004. How to accurately determine the uptake of hydrogen in carbonaceous materials. *International Journal of Hydrogen Energy,* 29**,** 1271-1276.

ZHANG, J. S., FISHER, T. S., RAMACHANDRAN, P. V., GORE, J. P. & MUDAWAR, I. 2005. A review of heat transfer issues in hydrogen storage technologies. *Journal of Heat Transfer-Transactions of the Asme,* 127**,** 1391-1399.

ZHAO, X. B., XIAO, B., FLETCHER, A. J. & THOMAS, K. M. 2005a. Hydrogen Adsorption on Functionalized Nanoporous Activated Carbons. *The Journal of Physical Chemistry B,* 109**,** 8880-8888.

ZHAO, Y. F., KIM, Y. H., DILLON, A. C., HEBEN, M. J. & ZHANG, S. B. 2005b. Hydrogen storage in novel organometallic buckyballs. *Physical Review Letters,* 94**,** 4.

ZHOU, L. 2005. Progress and problems in hydrogen storage methods. *Renewable & Sustainable Energy Reviews,* 9**,** 395-408.

ZLOTEA, C., MORETTO, P. & STERIOTIS, T. 2009. A Round Robin characterisation of the hydrogen sorption properties of a carbon based material. *International Journal of Hydrogen Energy,* 34**,** 3044-3057.

ZÜTTEL, A. 2003. Materials for Hydrogen Storage, Materials Today, 24-33.

ZÜTTEL, A. 2004. Hydrogen storage methods. *Naturwissenschaften,* 91**,** 157-172.

ZÜTTEL, A., BORGSCHULTE, A. & SCHLAPBACH, L. 2008. *Hydrogen as a future energy carrier,* Weinheim, Wiley-VCH.

ZÜTTEL, A., NUTZENADEL, C., SUDAN, P., MAURON, P., EMMENEGGER, C., RENTSCH, S., SCHLAPBACH, L., WEIDENKAFF, A. & KIYOBAYASHI, T.

2002. Hydrogen sorption by carbon nanotubes and other carbon nanostructures. *Journal of Alloys and Compounds,* 330**,** 676-682.